Model-based fault detection and diagnosis for the fuel system of a six-cylinder heavy duty diesel engine

Vom Fachbereich
Elektrotechnik und Informationstechnik
der Technischen Universität Darmstadt
zur Erlangung des Grades eines Doktor-Ingenieurs (Dr.-Ing.)
genehmigte Dissertation

von

Patrick Sauer, M.Sc.

geboren am 10 Juli 1986 in Erbach (Odenwald)

Referent:	Prof. Dr. -Ing. Dr. h. c. Rolf Isermann
Korreferent:	Prof. Dr. -Ing. Ulrich Konigorski
Tag der Einreichung:	18. November 2020
Tag der Prüfung:	27. April 2021

D 17 · Darmstadt 2021

Model-based fault detection and diagnosis for the fuel system of a six-cylinder heavy duty diesel engine

Genehmigte Dissertation von Patrick Sauer, M.Sc.

D 17 · Darmstadt 2021

URN: urn:nbn:de:tuda-tuprints-185899
URI: https://tuprints.ulb.tu-darmstadt.de/id/eprint/18589

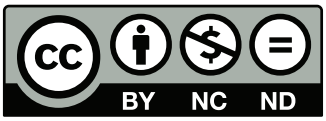

Preface

This research work is an outcome of my employment at the Institute of Drives for Vehicle Technology at the Technical University of Kaiserslautern in cooperation with the research group for Controls and Process Automation at the Technical University of Darmstadt.

First of all I want to thank Prof. Dr.-Ing. Dr. h. c. Rolf Isermann who made this research work possible. I especially want to thank him for his excellent guidance and constructive discussions which made it possible to find the best solution.

I also want to thank my second examiner Prof. Dr.-Ing. Ulrich Konigorski for the interest in my work and the acceptance of this position. Furthermore, I would like to thank Prof. Dr.-Ing. Rudolf Flierl and Prof. Dr.-Ing. Michael Günthner for the possibility to work at the Technical University of Kaiserslautern.

Moreover, I want to thank all my colleagues in Darmstadt and Kaiserslautern for the helpful technical discussions, valuable comments and feedback. Especially Dr.-Ing Thorsten Fuchs supported me in an excellent way with the countless technical discussions and his valuable feedback. I also would like to particularly thank Ilse Brauer for the excellent support and the pleasant atmosphere during the time I was at the Institute. I want to thank Corinna Fischer and in memory Brigitte Hoppe for their great support as well. Furthermore, I want to thank the technical employees for their support when building up the engine test bench in Kaiserslautern and my students who supported this thesis with their useful contributions in terms of student research projects.

Finally, I want to thank my parents for their support during my whole education without whom I would not be where I am today. I also would like to thank my fiancée and friends for the continuous patience and support during the whole work.

Kaiserslautern, May 2021
Patrick Sauer

Contents

Symbols and Abbreviations

Symbols

A	area	cm^2
e	error equation	
f	function, fault, frequency	
F	fault	
G	transfer function	
I	current	A
n	rotational speed	1/min, rpm
J	quadratic norm	
M	torque	Nm
m	mass per cycle	mg/cycle
$\dot{m}$	mass flow	mg/s
m'	mass per CS resolution	mg/°CA
r	residual	
s	symptom	
P	power	W
p	pressure	kPa
T	temperature | time period	°C | s
t	time	s
τ	angle period	°CA
U	voltage	V
u	input variable	
V	volume	cm^3
$\dot{V}$	volume flow	cm^3/s
V'	volume per CS resolution	cm^3/°CA
y	output variable	
$\hat{y}^-$	minimum threshold	
$\hat{y}^+$	maximum threshold	
η	efficiency	
$\mathbf{\Psi}$	data vector	
$\mathbf{\Theta}$	parameter vector	
φ	crank shaft angle	°CA
$\varphi_{cs,res}$	crank shaft sensor resolution	$\frac{360}{78}$°CA
α	flow coefficient	
ρ	density	mg/ cm^3
χ	coefficient	
$\hat{a}$	estimate of variable a	

Subscripts

air	air
baro	barometric
br	brake
cac	charged air cooler
cl	closed loop
cs	crank shaft
cycl	cycle
comp	compressed
d	dead time
dd	discharge duration
del	delivery
des	desired
disc	discharge
ee	equation error
egr	exhaust gas recirculation
el	electric
eng	engine
em	exhaust manifold
emp	exhaust manifold pressure
f	fuel
fol	first order lag
fq	fuel quantity
geom	geometric
ger	gerotor
h	harmonic
hci	hydrogen carbonate injection
hpp	high pressure pump
hyd	hydraulic
id	injection duration
in	inlet
int	integration
inj	injection
lim	limit
lp	low pressure
lpp	low pressure pump
lub	lubrication
main	main
max	maximum
mean	mean
meas	measured

mech	mechanic
mi	main injection
min	minimum
mt	main timing
mv	metering valve (Pressure Relieve Valve)
ndel	non-delivery
oe	output error
of	overflow
ol	open loop
oil	oil
out	outlet
ov	overall
p	period
pcv	pressure control valve
pos	position
prev	previous
prv	pressure relieve valve
pump	pump
pq	pump quantity
q	quantity
rail	common rail system
regv	regulation valve
relv	relieve valve
res	resolution
rm	redundant model
rpc	rail pressure control
rv	return valve
s	supervized period
sa	start angle
smpl	sample
sp	setpoint
th	threshold
vol	volemtric
ua	uniformity analysis
4cyl	4 cylinder diesel engine described in [67]

Abbreviations

AT	Aftertreatment
CA	Crank Angle
CAC	Charged Air Cooler
CAN	Controller Area Network
DAQ	Data Acquisition
DC	Direct Current
d/c	Do not Care
DFT	Discrete Fourier Transformation
DSP	Digital Signal Processor
DT1200	Type designation of dynamometer from Horiba (1200 KW)
ECU	Electronic Control Unit
EGR	Exhaust Gas Recirculation
EKF	Extended Kalman Filter
EMP	Exhaust Manifold Pressure
EOI	End Of Injection
EPA	United Stated Environment Protection Agency
FD	Fuel Delivery
FF	Fault-Free
FFT	Fast Fourier Transformation
FMEA	Failure Mode and Effective Analysis
GT	Gamma Technology
GUI	Graphical User Interface
HCI	Hydrocarbon Injection
HD	Heavy Duty
HF	High Flow
HO	High Offset
HP	High Pressure
HPP	High Pressure Pump
HP6	High Pressure 6 (from Denso)
ICE	Internal Combustion Engine
IO	Input Output
IPP	Inline Plunger Pump
K-NN	K- Nearest Neighbors
LF	Low Flow
LO	Low Offset
LP	Low Pressure
LPP	Low Pressure Pump
LS	Least Squares
MABX	Micro Auto Box
MP	Middle Pressure
MPP	Middle Pressure Pump

NI	National Instruments
OBD	On Board Diagnosis
OP	Operation Point
PC	Personal Computer
PCV	Pressure Control Valve in the HPP
PRedV	Pressure Reducing Valve
PRV	Pressure Relieve Valve
PWM	Pulse Width Modulation
RCP	Rapid Control Prototyping
RDE	Real Driving Emissions
RLS	Recursive Least Squares
RMS	Root Mean Square
RP	Rail Pressure
SA	Start Angle
SAE	Society of Automotive Engineers
SISO	Single Input Single Output
SLCT	Self Lerning Classification Tree
SOI	Start Of Injection
SPARC	Name of common dynamometer controller plattform from Horiba
SVM	Support Vector Machine
SW	Software
UA	Uniformity Analysis
US	United States
VGT	Variable Geometry Turbine

Abstract

Zusammenfassung (German)

Gegenwärtig gewinnt die Fehlerdiagnose in modernen Verbrennungsmotoren zunehmend an Bedeutung. Die stetige Weiterentwicklung der Motoren besonders im Hinblick auf optimale Ausnutzung der im Kraftstoff enthaltenen Energie, sowie die durch die Gesetzgebung stärker regulierten Abgasemissionen, führen zu immer komplexeren Gesamtsystemen. Die Steigerung der Komplexität bringt konventionelle Diagnosesysteme, wie z.B. die Überprüfung von Sensorgrenzwerten, an ihre Grenzen. Die vorliegende Arbeit behandelt die Entwicklung eines Kraftstoff Diagnosesystems für einen Schwerlastmotor mit Hilfe von weiterführenden Signalmodell und Prozessmodell basierten Methoden.

Das Diagnosesystem wurde für den Serienbetrieb entwickelt, was diverse Einschränkungen zur Folge hat. Eine dieser Einschränkungen stellt die fehlende Integration zusätzlicher Sensoren zur Überwachung von Zwischenzuständen dar. Weiterhin arbeiten die Niederdruckpumpe, sowie die Raildruckregelung im geschlossenen Regelkreis, um eine bestmögliche Einhaltung der geregelten Größe zu gewährleisten. Geschlossene Regelkreise kompensieren jedoch zunächst kleinere Fehler.

In der vorliegenden Arbeit wurden physikalische Modelle für diverse Komponenten im Kraftstoffsystem aufgestellt, welche die Grundlage für die modellbasierte Entwicklung darstellen. Mit Hilfe dieser Modelle werden Algorithmen zur Überwachung der Niederdruck- und Hochdruckpumpe, Kraftstofffilter, diverse Leckagen, sowie das Rail-Durchflussventil entwickelt. Weiterhin wurden durch die modellbasiert berechneten Zwischengrößen zusätzliche Informationen generiert, die bei der Fehlerdiagnose zur Fehlercharakterisierung dienen.

Für die Signalmodell basierte Entwicklung wurden die Frequenzanteile der zu überwachenden periodischen Raildruck- und Abgasdrucksignale in einer hohen Auflösung analysiert, um schließlich Algorithmen zur Überwachung von Injektor-Durchflussfehlern, sowie Kompressionsverlusten in Verbrennungszylindern zu extrahieren. Nicht nur bei der Fehlerdetektion, sondern ebenfalls bei der Fehlerdiagnose liefern diese Signalmodell basierten Methoden einen Mehrwert an Information, die es ermöglichen, die exakte Position des beobachteten Fehlers zu bestimmen.

Anhand der entwickelten Algorithmen wurden Residuen aufgestellt, die eine Abweichung des zu überwachenden Systems vom Normalzustand darstellen. Mit den Prozess- und Signalmodell basiert gebildeten Residuen wurden Symptome erzeugt, welche die Eingangsgrößen der Fehlerdiagnose sind. Mit Hilfe einer Schlussfolgerung basierten Fehlerdiagnose wurden anhand der Symptome die Fehlercharakteristiken wie Fehlertyp und Fehlerquelle ermittelt, um somit die Fehler zuzuordnen.

Das Kraftstoffdiagnosesystem wurde am Motorenprüfstand implementiert, parametriert, getestet und zuletzt validiert. Dabei wurden verschiedene möglichst authentische Fehler im Kraftstoffsystem des Motors generiert. Diese wurden durch die Prozess- und Signalmodell basierte Fehlerdetektion detektiert und schließlich wurden die einzelnen Fehler identifiziert und isoliert. Die Werkzeuge zur Identifikation und Isolation stellten hierbei Fehler-Bäume dar, die zur Kategorie der schlussfolgernden Methoden gehören. Ebenfalls hilfreich zur Isolation einzelner Fehler sind Fehler-Symptom-Tabellen, welche die kompletten Symptome aller implementierten Fehler beinhalten. Besonders die Methode zur Isolierung von Injektor-Durchflussfehlern lieferte einen geeigneten Beitrag zur eindeutigen Zuordnung der jeweiligen Fehlerquelle.

Schließlich wurde eine Strategie zur online Kompensation verschiedener Injektor-Durchflussfehler entwickelt, welche die kurzfristige Kompensation des Fehlers ermöglicht. Dies gewährleistet eine zuverlässige Funktionsweise des Motors bis zum nächsten Werkstattaufenthalt. In der Nutzfahrzeugindustrie ist dies von großer Bedeutung, um zusätzlich anfallende Kosten eines Maschinenstillstands zu minimieren.

Abstract

Nowadays, the fault diagnosis in modern internal combustion engines is becoming increasingly important. The constant development of engines, particularly in terms of fuel efficiency, and more stringent regulations of exhaust emissions, are leading to more complex systems. This enormous increase in complexity restricts the efficiency of conventional diagnosis systems, such as the limit checking of sensors. This thesis deals with the development of a fuel diagnosis system for a heavy duty diesel engine using advanced signal model- and process model-based methods.

The diagnosis system has been developed for serial operation, which results in various limitations. One of these limitations is the lack of integration of additional sensors to monitor intermediate states. Furthermore, the low pressure pump, as well as the rail pressure control operate in closed loop control to ensure best possible results for the controlled variable. However, closed loop controls compensate for minor faults.

In this thesis, physical models for various components in the fuel system have been developed which form the basis for model-based development. These models are used for developing algorithms to monitor the low pressure and high pressure pump, fuel filters, various leakages and the rail flow valve. Additionally, the model-based parameters generated additional information to help characterize the faults during the fault diagnosis.

For signal model-based development, the frequency components of the periodic rail pressure and exhaust pressure signals were analyzed in high resolution. With this it is possible to extract algorithms to monitor injector flow and compression losses in internal combustion cylinders. This signal model-based methods provide additional information not only during fault detection but also during fault diagnosis, which allows the exact location of the observed fault to be determined.

Residuals have been created using the developed algorithms, which represent a deviation of the system to be monitored from the normal state. Residuals formed using process and signal models have been created, which represent the inputs of the fault diagnosis. An inference based fault diagnosis was used to determine the fault characteristics, such as the type and location of the fault, in order to isolate these faults.

The fuel diagnosis system was implemented, parameterized, tested and validated at the engine test bench. Various faults in the engine fuel system were generated as authentic as possible. These were detected by the process and signal model-based fault detection and the individual faults were identified and isolated. The tools for identification and isolation were fault-trees, which belong to the category of inference methods. Also useful for isolating individual faults are fault-symptom-tables that contain the full symptoms of all implemented faults. In particular, the method for isolating the injector flow faults provided an appropriate contribution to clearly identify the location of the fault.

Finally, a strategy was developed for the online compensation of various injectors flow faults, which allows the short-term compensation of these faults. This ensures a reliable operation of the engine until the next workshop stay. In the commercial vehicle industry this is of great importance in order to minimize the additional costs of machine downtime.

1 Introduction

Modern engines are carefully engineered to balance the trade-off between efficiency on one side and stringent emissions legislation requirements on the other side [5]. In recent years the stringent legislation requirements on emission have led to an increased development of engine diagnosis. Especially in regards to the upcoming Real Driving Emissions (RDE), the development of advanced On-Board-Diagnostics (OBD) for engines continues to grow in importance. A brief historical background of OBD development is given in the following paragraph:
It began with the introduction of digital controlled systems in diesel engines in the 1980s where diagnosis development became noteworthy for manufacturers [38]. The legislation, especially in California (USA), also noticed the need for OBD which led to the introduction of OBD I to detect malfunctions, specifically causing increased emissions [56].

This research work deals with heavy duty engines where the primary focus is their fault detection capability which is important to ensure a reliable and safe functionality of commercial vehicles. One of the most important aspects is to prevent safety critical situations which can lead to machine damage or even risk of human life. This can sequentially be done with a fail-operational system which use additional redundant elements. An improvement of critical component monitoring and fast reaction to system faults (robust diagnosis management system) can reach this goal. In contrast to safety aspects, one of the main important topics of the fail-operational structures for heavy duty engines is to reduce or even prevent machinery downtime. This may safe large productivity or delivery losses and large amounts of additional costs to the customer.

The engine can be divided into different functional subsystems like the fuel, combustion, intake, cooling, lubrication and exhaust system. Especially for diesel engines, the improvement of the fuel system is a crucial factor to cope with the trade-off between efficiency and tighter emission limits. The development of the common rail fuel system is a result of these efforts, see [40].
Furthermore, the improvement of injectors is one of the main effective elements which can reduce emissions, increase efficiency and also increase comfort by reducing engine noise [40]. All these improvement aspects come with a cost of increased system complexity, which makes it more difficult to monitor the system. Especially the complexity of the engines and cost reduction aspects push conventional fault detection methods to their limit. This opens up an opportunity for more advanced model-based fault detection methods.

It is also important to pay attention to the fact that nowadays, up to 50% of the engines Electronic Control Unit (ECU) software is occupied by diagnosis functions [58]. A further improvement is to implement advanced model-based diagnosis approaches, which can generate deeper system knowledge (expert knowledge) and give the possibility for an enlarged fault detection and diagnosis capability.Also, increased usage of electrification and digital control opens new possibilities to improve diagnosis and contribute to upcoming remote access and cloud data storage.

Finally, an additional improvement of diagnosis is the usage of advanced model-based approaches like signal and process model-based approaches in combination with conventional supervision and diagnosis methods which in turn includes the diagnosis of electrical/electronic components and the diagnosis of different subsystems [58]. Especially the latter two points include open and short circuit detection of sensors and actuators, the monitoring of abnormal control deviations, signal range checks of sensor signals and plausibility checks of different sensors, see [20] and [4]. Model-based fault detection methods were seldom used until now [44].

1.1 State of the art of engine diagnosis

In the following, a short overview of fault detection and diagnosis fundamentals are discussed. The characteristics of an abnormal system behavior can be divided into three sub-definitions, see [63]:

- Fault: "Is an unpermitted deviation of at least one characteristic property (feature) of the system from the acceptable, usual, standard condition."
- Failure: "Is a permanent interruption of a system's ability to perform a required function under specified operation conditions."
- Malfunction: "Is an intermittent irregularity in the fulfillment of a system's desired function."

For an early detection of a possible abnormal system behavior, it is essential to supervise faults which occur initially. The basic concept of fault detection and diagnosis can be divided into three essential tasks [78] [34]:

- Fault detection, i.e. recognition of an unpermitted feature deviation.
- Fault isolation or localization, i.e. the determination of the fault location.
- Fault identification, i.e. the determination of type and size of the fault.
- Fault diagnosis: Fault isolation and fault identification.

Fig. 1.1 gives an overview of a fault detection and diagnosis system structure with a fault management system which can react after a diagnosed fault.

1.1.1 Classical methods of fault detection

[12],[13] and [53] categorize the fault detection of combustion engines into limit checking, active tests and static or dynamic plausibility checks.

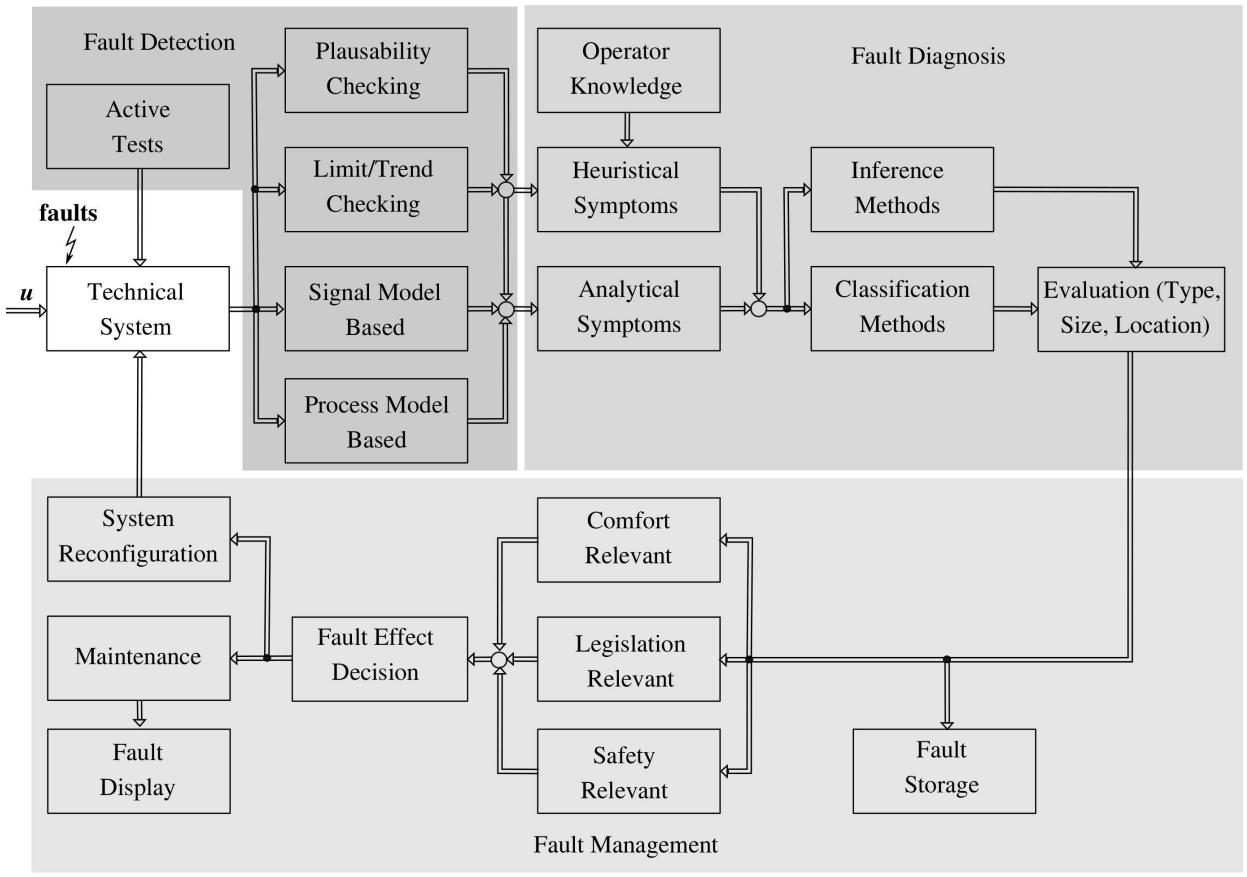

Fig. 1.1: Overall engine diagnosis structure of a technical system, according to [58]

For *limit checking*, upper and lower thresholds for the observed signal are defined. A fault occurs if the monitored signal exceeds these predefined thresholds. In *static plausibility checks*, the correlation between two different signals which are statically correlated is tested. The *dynamical plausibility check* further monitors a value increase or decrease of the observed variable, in a short time interval. *Active tests* have the benefit to check the dynamic system behavior by imprinting specified input signals in known environmental conditions [12]. [34] described in 1988 that fault detection and isolation can be done with these standard diagnosis methods and model-based approaches.

1.1.2 Model-based fault detection

Model-based fault detection methods use process models or signal models which are developed with state observers, parameter estimation, signal analysis models or Fast Fourier Transformation. Herewith one can distinguish additive or multiplicative faults. Multiplicative faults represent model changes (for example parameter changes), whereas additive faults represent system offsets, see [65], [63]. More details of these methods are described in Chap. 2.

1.1.3 Fault diagnosis

A *fault diagnosis* is based on generated features from the fault detection. Here, *analytical symptoms* and *heuristical symptoms* can be generated with these features and operator knowledge. These symptoms are used for the fault evaluation to gather information of the fault type, size and location. The symptom evaluation is for example realized by inference and classification methods, see Fig. 1.1. A fundamental description can be found in [62] [33].

1.1.4 Fault management

A *fault management system* uses the information (fault type, size and location) gained from the fault diagnosis as a basis to first classify the fault relevance, see Fig. 1.1. Then comfort, legislation or safety relevant fault classifications are used to decide the need for actions. Depending on the fault the technical system is reconfigured to compensate the fault, or point out the fault occurrence to the operator indicating a need for maintenance. Fundamentals of the fault management can be found in [62], [58].

1.1.5 Investigated diesel engine

In industrial systems fault detection is mostly based on the classical approaches, see Sect. 1.1.1. The On-Board Diagnosis for the investigated diesel engine mainly depends on conventional methods as well. For fault detection, the approaches utilized are limit and plausibility checks for instance. Some advanced methods with signal model-based fault detection like correlation analysis are already used for injector quantity faults, but are only valid for a small operational range and occupy a large amount of calculation resources. Moreover, some system components are already physically modeled to replace sensors which are exposed to critical environmental conditions.

1.1.6 On-Board Diagnosis (OBD)

The *On-Board Diagnosis* (OBD) for internal combustion engines is a legislative requirement since 1988 for light duty vehicles. For heavy duty vehicles Heavy Duty (HD) OBD was introduced in Europe in 2005, in the US for HD vehicles less then 14000 lbs in 2005-2008 and finally for heavier categories in 2010, see [21]. Similar to OBD for light duty vehicles, HD OBD gained more importance over the past couple of years due to, with every stage, more stringent emission legislation. This legislation driven emission standards can be found in [16] for HD on-road and off-road vehicles. HD OBD regulations have different requirements which are only briefly described in the following (detailed information can be found in [21], [49], [48]):

- **System monitoring:** The OBD has to monitor malfunctions of sensors, actuators, controllers and complete systems, to ensure a proper functionality of these components with one of the main aspects to reduce emissions.

- **Operator and service interface:** This provides the operator an indication that a malfunction occurred with a lightening of the Malfunction Indication Lamp (MIL). The service interface provides a standardized protocol (for HD: SAE J1939) with several defined parameters which can be accessed trough a standard (HD) diagnostic adapter.
- **OBD testing and validation:** This aspect proofs a OBD durability demonstration testing in an emission certification test cell. This test will proof a proper functionality of the OBD monitoring system.

To show the possibility of a future HD OBD coping with continuously growing requirement to diagnose more stringent emissions, this research work deals with model-based fault detection and diagnosis approaches for a HD diesel engine. Fundamentals of these advanced model-based approaches can be found in [33], [62], [30]. For model-based approaches the division into signal model-based and process model-based methods is used.

Signal model-based approaches are spectrum-, frequency-, correlation- and wavelet-analysis methods, see [62]. These approaches are especially suitable for engines where several measurement signals have a periodic oscillating behavior. Most of the injector quantity fault detection approaches in literature are based on signal model-based methods (e.g. [10], [20], [69], [32], [46], [45]). As shown in the upcoming sections, injectors are one of the key elements for improving the engine's efficiency and to comply with the stringent legislation emissions regulations. In order to guarantee a proper functionality the injectors have to be monitored.
[10] and [20] used an implicit version of a uniformity analysis to detect injection quantity faults. The uniformity analysis belongs to the group of signal model-based fault detection and checks a similar periodicity of a periodic oscillating measurement signal. [67] introduced an algorithm which isolates a pump fault from an injector quantity fault with the uniformity analysis of the Rail Pressure (RP). Another method to identify injector faults is shown in [32] with a spectral analysis of the turbocharger Speed. In other research works this was done by a spectral analysis of the RP signal, see [46]. [45] used a wavelet transformation for the RP sensor signal to detect injector quantity fault of a spark ignition engine. An alternative way to identify injector faults is shown in [19] and [1] for a diesel engine using acoustic emissions techniques.

Misfire faults for gasoline engines can be detected with signal model-based approaches as well. These faults have to be detected, according to OBD II [51], because they significantly increase emissions, decrease the engine's efficiency or even cause component damages in the complex exhaust gas regeneration system.

In the automotive area, misfire fault detection is usually done by an analysis of the engine speed, because the angular speed shows oscillations due to the acceleration and decelerations during the piston strokes [58]. [31] described a misfire detection method with the help of a speed analysis for a six-cylinder engine. [74] described misfire detection based on the engine's speed with a Kalman filter approach which can be implemented on-board in the vehicle.
Engine speed might be a good indicator for passenger cars, but has no significant impact in the heavy duty area due to huge drive-line mass, changing load conditions and a large variety of

drive-lines. This is primarily due to the mass damping the amplitudes of the short time engine speed decrease which makes it difficult to detect misfire faults. Furthermore, the calibration effort significantly increases with the number of vehicle variations in which the engine is used, see [37] and [23]. Hence, [37] used the Exhaust Manifold Pressure (EMP) sensor signal to detect a misfire fault which is less dependent on the drive-line mass, whereas [23] used signals which are also less affected by the drive-line like the cylinder pressure, the turbocharger pressure and speed. [51] described a misfire detection with a wavelet transformation and DFT of the EMP signal for a gasoline engine in passenger cars.

Process model-based approaches can be divided into parity equation, parameter estimation and state estimation, see [62]. These techniques create analytical features from the static and dynamic behavior of process models. For example, [67] introduced a mean common RP model-based on parity equations. Hence for the fuel path system, [67] has shown an algorithm for the estimation of the RP mean value and the High Pressure Pump (HPP) fuel delivery.
A state estimation approach with an Extended Kalman Filters (EKF) is used in [3] for the diagnosis of injection fuel quantity, air mass flow and boost pressure faults. The EKF is based on emission models for NO_x and Lambda in combination with their measured sensor values. Furthermore, [79] showed a detailed model of the common rail fuel system of a heavy duty engine with a qualitative injector model. [5] introduced a model-based fault detection and diagnosis to detect different leakages in the intake and exhaust system as well as turbocharger faults on the basis of a turbocharger model. A different model-based fault detection and isolation of air path leakages and sensor faults is shown in [41]. Also, intake leakage detection for a diesel engine on the basis of an adaptive observer approach is described in [57].

With regard to *fault diagnosis*, [51] described two different fault diagnosis approaches for a gasoline 12-cylinder engine which performs a signal model-based detection. The first fault diagnosis uses a classification approach called Nearest Neighbor in combination with a fuzzy-based inference which can exactly locate a cylinder misfire (cylinder number) with the help of spectral amplitudes and phases of the EMP signal. The second diagnosis is an expert-based fuzzy inference approach with a wavelet analysis of the EMP signal as the basis.
[20] used an inference method based fault diagnosis approach which is visualized with fault symptom tables with the developers expert knowledge and fault trees. [67] introduced an overall diagnosis system for a diesel engine which combines the different functional subsystems like the intake air system, exhaust gas system, combustion, mechanics and common rail injection system. Finally, [67] tested different classification and inference methods and concluded that inference methods should be recommended for diesel engines.

1.2 Thesis goals

This research work aims to develop advanced engine diagnosis methods for the fuel system of a heavy duty engine with the least possible changes to the normal operating conditions. It will specifically focus on fault detection with model-based methods as a basis for the fault diagnosis.

The major goals of this project are to implement a fault detection and diagnosis strategy for the fuel system of a heavy duty engine in a way that:

- Faults can be detected, identified and isolated early to reduce downtime.
- The developed engine diagnosis operates in normal operation mode.
- The engine diagnosis is reliable without additional costs for additional components.
- The robustness of the fault detection and fault sensitivity is considered.
- The calibration effort for the diagnosis system is kept minimal.
- The engine diagnosis depth increases compared to the existing system.
- The OBD is real-time capable.

Another goal is to reduce the preparation time and implementation effort for mass production. Also, a combination of a new signal model-based approach for injector fuel quantity faults and misfires will be investigated.

1.3 Thesis outline

Chap. 2 provides a short and broad overview of model-based fault detection, inference and classification based fault diagnosis approaches. Four different fault detection methods, namely change detection with limit checking, fault detection in control loops, signal model-based and process model-based approaches are discussed. For the classification based fault diagnosis the Nearest Neighbor as well as the Bayes classifier are considered. Furthermore, fault symptom tables and fault trees are used which are helpful to design a fault diagnosis system.

Chap. 3 provides an overview of the heavy duty test engine and the fuel system components along with their functionalities. The available sensor infrastructure from the engine and the test bench is visualized. The fuel path is divided into three central domains: The Low Pressure (LP), the Middle Pressure (MP) and the High Pressure (HP) area. Further on, the requirements and constraints for the, to be developed, engine diagnosis are shown. The developed diagnosis system should be able to detect faults or malfunctions without an active change of the engine's Operation Point (OP).

Chap. 4 deals with the development of mathematical equations which form the basis for process model-based fault detection approaches introduced in Chap. 2. Different physical, semi physical, or mean value models for the LP, MP and HP domains were developed in Chap. 4 which are fundamental for the developed fault detection modules.

In Chap. 5, the relevant signals for the introduced signal model-based approaches are analyzed with a Fast Fourier Transformation (FFT) to identify the frequency components induced on the

rail pressure. This is due to the discontinuous volume flow of the HPP fuel delivery and injections or of the Exhaust Manifold Pressure (EMP) by the combustion in each engine cylinder. This behavior causes a normal periodic pressure signal in the rail or the exhaust manifold in a fault-free case. Furthermore, a signal model-based approach, known as uniformity analysis, is described which monitors a periodicity change to the observed variables.

Chap. 6 describes a fuel fault detection system. This chapter illustrates the developed conventional and model-based fault detection modules based on the previously mentioned mathematical equations (Chap. 4) and frequency analysis (Chap. 5). Also, a representative extraction of the investigated faults is described and suitable experiments for each fault are implemented on an engine test bench. The results of the developed fault detection modules are visualized in different residual figures.

Chap. 7 deals with the fuel system fault diagnosis which besides the fault detection is one of the main goals. A new isolation concept based on the uniformity analysis for RP and EMP is discussed which gives the opportunity to isolate an injector fuel quantity from a cylinder misfire fault and furthermore isolate up to 5 injector faults in combination with other features. For the isolation of different faults, symptoms are generated and visualized in fault symptom tables. An inference method-based fault diagnosis is discussed with the help of these fault symptom tables and representative fault trees for visualization. Chap. 7 additionally provides an Operation Point (OP) dependency of the residuals and fault detection in dynamic operation ranges of faults, that are only active in transient engine OPs. This opens up the possibility of a dynamic fault detection and diagnosis with adaptive thresholds.

In Chap. 8, a short description of a fault management system for injector faults is provided. Furthermore, a fault management strategy for an injector quantity fault is discussed to maintain full engine performance until the next workshop visit.

Finally, Chap. 9 gives a conclusion and an outlook for further improvements of engine diagnosis methods.

2 State of the art of fault detection and diagnosis methods

This chapter gives an overview of different fault detection and fault diagnosis approaches. First of all the conventional approaches such as change detection with limit checking are discussed. For an advanced fault detection two different types, the signal- and process model-based approaches are treated as well as fault detection methods in control loops. Further-on three different approaches for adaptive threshold generation will be introduced.
For the fault diagnosis, the inference and classification based methods are discussed. The basis of the classification are pattern recognition methods, whereas the inference approach mainly depends on expert knowledge.

Fault detection

Limit Checking of measured variables are the most commonly used approaches for fault detection. For these approaches the value of a measured variable is compared to their predefined fault-free value or fault-free area.
The more advanced model-based fault detection approaches use mathematical models to generate features with the input signals $\mathbf{u}$ and the output signals $\mathbf{y}$, or only the output signals $\mathbf{y}$. These features can be expressed as residuals $\mathbf{r}$ of parity equations, amplitudes $\mathbf{A}$, frequencies $\mathbf{f}$ or parameter estimates $\boldsymbol{\Theta}$ for example. Residuals visualize the discrepancies of the observed system e.g. measured features to their nominal fault-free features. Ideally the residual of a fault-free case should be zero, because for example for an accurate developed model for the parity equations the modeled output should line up with the process output. In reality there exist modeling errors, stationary/instationary disturbances at the output and unknown input signals [62]. Therefore thresholds have to be introduced which compensate for the above listed issues. They have to be chosen carefully because an overly large threshold hides small faults while the opposite increases the risk of indicating an error in a fault-free state.
Finally the benefits of model-based approaches are obvious by the additional gained signal or system information which can be used to diagnose more faults, to detect smaller faults or even to detect different faults earlier. The following sections discuss these fault detection approaches. The basic concepts can be found in [62],[43],[36],[30].

2.1 Change detection with limit checking

In industry the most commonly used method is a change detection with limit checking of a directly measured variable [62]. There are different possibilities to monitor the health of a process, two are:

- **Limit checking of absolute values:**
  In general two limit values, $Y_{\min}$ and $Y_{\max}$, so called threshold values are used. As long as the observed variable $Y(t)$ is within the tolerance range

  $$Y_{\min} < Y(t) < Y_{\max} \tag{2.1}$$

  the process is fault-free. The threshold values are mostly defined by experience and are a trade-off between robustness of the system and sensibility of the fault detection [62].

- **Trend checking**
  For trend checking a minimum, maximum value of the first derivative $\dot{Y} = \mathrm{d}Y(t)/\mathrm{d}t$ is used for the threshold generation:

  $$\dot{Y}_{\min} < \dot{Y}(t) < \dot{Y}_{\max} \, . \tag{2.2}$$

  This approach is beneficial for earlier detection of faults compared to the limit checking with absolute values [62].

2.2 Process model-based approaches

In process model-based approaches the internal behavior of the observed system is described with an adequate mathematical model. This model represents the relation between the measured input signals $\mathbf{u}$ and the output signals $\mathbf{y}$. With model-based fault detection methods, special features such as state variables $\mathbf{x}$, parameters $\boldsymbol{\Theta}$ or residuals $\mathbf{r}$ can be extracted. Furthermore analytical symptoms $\mathbf{s}$ can be developed with these features, which forms the basis of the fault diagnosis. For a detailed overview, see [62].

2.2.1 Parameter estimation

Parameter estimation belongs to the field of process identification which is a subcategory of model-based approaches. Process identification includes different methods for the estimation of unknown parameters which are needed to design a mathematical process model. One of the most important approaches of parameter estimation is the method of Least Squares for systems which are linear in the parameters. With this method a picture of the internal process can be built using only the input and output signals.

Parameter estimation with least squares method for linear processes

If the process can be described with a linear difference equation

$$y(k) + a_1 \cdot y(k-1) + ... + a_m \cdot y(k-m) = b_1 \cdot u(k-d-1) + ... + b_m \cdot u(k-d-m), \tag{2.3}$$

then the transfer function in z-domain can be described as:

$$G_{\mathrm{FoI}} = \frac{y(z)}{u(z)} = \frac{B(z^{-1})}{A(z^{-1})} \cdot z^{-d} = \frac{b_1 \cdot z^{-1} + ... + b_m \cdot z^{-m}}{1 + a_1 \cdot z^{-1} + ... + a_m \cdot z^{-m}} \cdot z^{-d} \tag{2.4}$$

where

$k = t/T_{\mathrm{smpl}}$	is the discrete time, with T_{smpl} the sample time,
m	is the model order,
a_m	are the output coefficients,
b_m	are the input coefficients and
$d = T_{\mathrm{d}}/T_{\mathrm{smpl}}$	is the discrete process dead time, with T_{d} the dead time.

With the measured input signals $u(k)$ and output signals $y(k)$, the data vector becomes

$$\boldsymbol{\Psi}^T(k) = [-y(k-1) \; ... \; - y(k-m) | u(k-d-1) \; ... \; u(k-d-m)]\,. \tag{2.5}$$

The parameter vector is:

$$\hat{\boldsymbol{\Theta}}^T(k) = \left[\hat{a}_1 ... \hat{a}_m | \hat{b}_1 ... \hat{b}_m\right]. \tag{2.6}$$

Using the equation error (see e.g. [63])

$$\mathbf{e}(k) = y(k) - \hat{y}(k|k-1) \tag{2.7}$$

where $y(k)$ is the measured output signal and $\hat{y}(k|k-1)$ is the one-step ahead prediction of the process model, the cost function $\mathbf{V} = \mathbf{e^T e}$ is minimized. Finally the estimated parameter vector follows after application of the method of least squares, see [63]:

$$\hat{\boldsymbol{\Theta}} = \left(\boldsymbol{\Psi}^T \boldsymbol{\Psi}\right)^{-1} \boldsymbol{\Psi}^T \mathbf{y}. \tag{2.8}$$

With a Recursive Least Squares method (RLS), it is further possible to identify the parameters online.

2.2.2 Parity equations

Parity equations are a relatively simple approach for process model-based fault detection. The roots of this approach goes back to the mid 70s [72],[61] (or the early 80s [17]). With parity equations a residual is calculated with the difference of the process and the process model. This model is mostly developed for the nominal behavior of the system. In this work three main structures for the residuals generation with parity equations are discussed [62],[75]:

a) The output error.

b) The equation error.

c) Redundant models.

These structures are illustrated in Fig. 2.1. Compared to the equation error the output error has a low pass filter characteristic which specifically makes the generated residual robust against noise but with the drawback of a slower reaction. Instead of output or equation errors, redundant models (see Fig. 2.1 c)) are useful if the to-be-observed measured variables aren't available. However, the structure of these two models should be independent (one model should not influence the other model) for a proper fault detection. Depending on the purpose of the application, these characteristics have to be taken into account to choose the optimal structure.

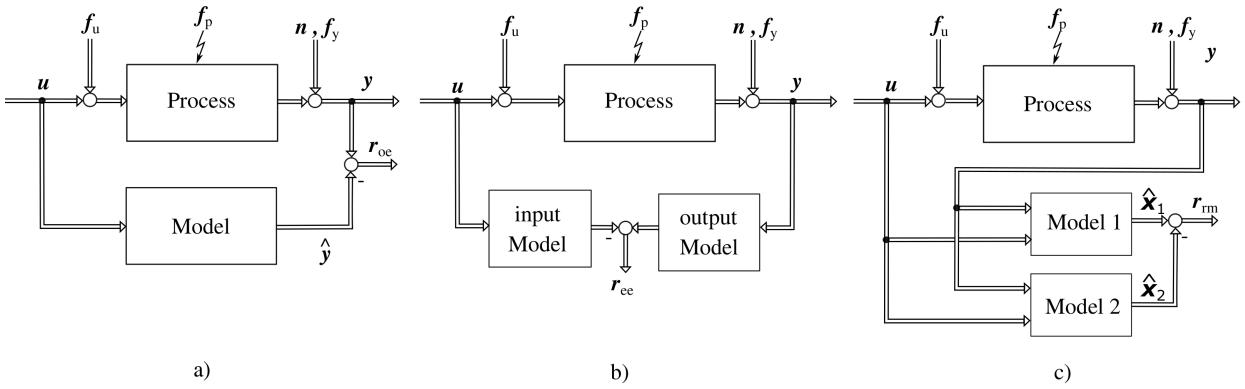

Fig. 2.1: Residual generation using parity equations with: a) Output error. b) Equation error. c) Redundant models [75].

In the following the output error for a SISO (Single Input Single Output) system is used for illustration. If the model is well designed and no fault occurs, the residual

$$r(t) = y(t) - \hat{y}(t), \tag{2.9}$$

should be zero. $y(t)$ represents a process output and $\hat{y}(t)$ represents the model output from the observed system. If now an input fault f_u, process fault f_p, output fault f_y or noise n occurs, the residual r from equation (2.9) differs from its normal behavior of zero, see Fig. 2.1 a).

2.2.3 Observers

The roots of state observers can be traced back to Luenberger in the early 60s [42]. State observers like Luenberger and state estimators like the Kalman filter can be applied when faults can be modeled as state variable changes. Especially the Kalman filter should be used if the initial states, inputs and outputs exhibit stochastic behavior [61]. Another approach involves using output observers. These can be used if the state variables are not important and the inputs are not

precisely known. Additional explanations can be found in [61],[62], [33] and [78]. Furthermore it can be noted that the observers show similarities with parity equations, see [62]. Contrary to parity equations, observers have more disadvantages due to their complex structure, large number of parameters which have to be applied and the computational effort, convergence problems may arise when the model exhibits uncertainties [47].

2.3 Signal model-based approaches

The main goal of signal model-based fault detection is to detect faults out of a signal behavior. In general, many systems have measured signals that behave periodically, stochastically or both. With these measured signals statistical features (residuals) can be calculated. In many cases the measured signals show oscillations or an oscillating behavior. Hence suitable features for these measured signals can be developed with the calculation of amplitudes, phases, correlation functions , uniformity of the signal and spectrum frequencies [62].

2.3.1 Fast Fourier transformation

A standard approach to find the frequencies of an oscillating signal is Fast Fourier Transformation (FFT).
The basis of the FFT is the Discrete Fourier Transformation (DFT) where the measured signal is transformed from the time domain to the frequency domain. In general the FFT results in a faster calculation compared to the DFT which is, for example, beneficial for a quicker residual evaluation in embedded systems. For detailed information see [62] or how to design a FFT algorithm in C-programming language, see [26].
In conclusion, FFT is a strong approach for the detection of faults in oscillating signals. The FFT visualizes a frequency change of the oscillations for the observed system which mostly occurs with an underlying fault. With the FFT it is possible to monitor amplitude and/or phase shift changes of these oscillations.

2.3.2 Uniformity analysis

The uniformity analysis is a signal model-based approach which compares an observed periodic signal to its uniformity repetition e.g. over a specified time period. With uniformity analysis injection quantity faults can be detected (see [10] and [20]). [67] introduced an algorithm which isolates a pump fault from an injector fuel quantity fault with a uniformity analysis of the RP. In the following the mathematical foundation of the uniformity analysis is described.

For undamped periodic signals with time period T_p the following holds true [64]:

$$y(t) = y(t + T_\mathrm{p}). \tag{2.10}$$

This means that a phase shifted signal over the time period should be equal to the basic signal. The periodic signal is also equal for multiple phase shifts of the time period:

$$y(t) = y(t + m \cdot T_\mathrm{p}), \quad m \in \mathbb{N}^*. \tag{2.11}$$

For internal combustion engines the pulsating behavior of different components, such as injectors and High Pressure Pumps (HPP) produce periodic oscillations. It is obvious to check the periodicity of these oscillations to get information about a possible fault in one or more components. In a fault-free case the signal should satisfy equation (2.10) and (2.11). However, a first indication of a possible fault could be detected by the signal changes over time that does not comply with these equations anymore.
According to [67] the basic equation for the uniformity analysis is given by:

$$y(t) - y(t + T_\mathrm{s}) = \begin{cases} 0 & y(t) \text{ is periodic with } T_\mathrm{s} = T_\mathrm{p} \cdot m, \quad m \in \mathbb{N}^* \\ c(t) \in \mathbb{R} & y(t) \text{ is not periodic with } T_\mathrm{s} = T_\mathrm{p} \cdot m \quad m \in \mathbb{N}^* \end{cases} \tag{2.12}$$

2.4 Fault detection in control loops

Output residuals in an open loop (feed forward) controlled systems, as a result of the difference of the observed output variable to a model output variable, have a high degree of system fault information. However, this information vanishes for output residuals in closed loop controlled systems, because the closed loop compensates all kind of external disturbances, parameter changes, actuator or process nonlinearities and stabilize also unstable processes [62]. It results in better control behavior of the system but has less information content, because by proper control it can't detect an occurring fault by only observing the controlled variable y. In this case the manipulated variable has to be considered too, see [62].

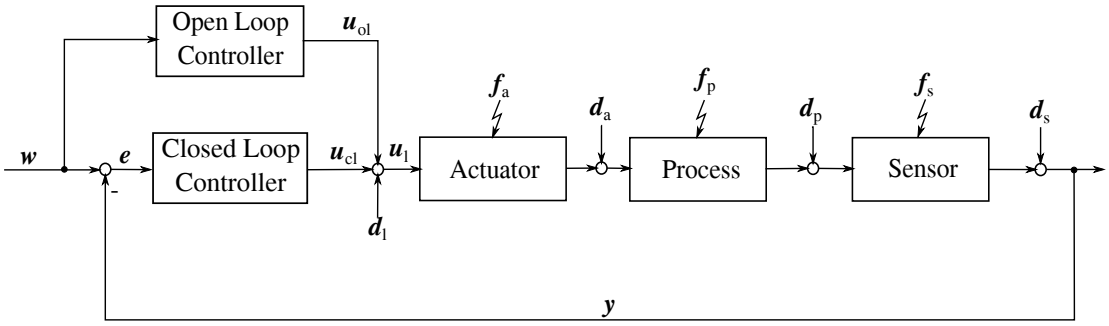

Fig. 2.2: Potential faults in open and closed loop controls

In Fig. 2.2, a combination of an open and closed loop control is shown. The advantage of observing a controlled variable y in open loop controls offers a higher degree of information, whereas closed loop control (also in combination with an open loop control) realizes a more robust control system. The control system which combines an open loop with a closed loop control, where the open loop is designed to provide the whole actuator input variable u_l in a fault-free case, is called a two

degree control in literature (see [54]). With this control, the observation of the output variable of the closed loop u_{cl} is a good indicator for system actuator faults (f_{a}), process faults (f_{p}), sensor faults (f_{s}), disturbances (d_{l}, d_{a}, d_{p}, d_{s}) as well as parameter changes (actuator, process, sensor). However, these faults can only be isolated with a combination of several fault detection methods [62].

2.5 Adaptive thresholds

An adaptive threshold can improve the robustness of fault detection compared to fixed thresholds. In most cases the process model does not fully depict the real process due to model inaccuracies. For a residual this results in a deviation from zero even without a fault. The deviations depend on the amplitude and frequency of the input excitation [62]. Three approaches are presented:

1. A high pass filter method [73].
2. A model prediction based adaption [55].
3. An interval method which evaluates the residual energy [55].

The first approach contains a static part that is proportional to the input value and a dynamic part that depends on the deviation of the input, see [62]. The adaptive threshold is then developed with a first order high pass filter. With this filter only higher frequency signals can enlarge the thresholds which is especially beneficial for transient states. For detailed information see [62] [73].

The second approach uses minimum and maximum values of the model prediction to generate the adaptive threshold:

$$\hat{y}^{-}(t) = \min\left(\hat{y}(t)\right) \quad \hat{y}^{+}(t) = \max\left(\hat{y}(t)\right). \tag{2.13}$$

The only constraint here is that the model should be developed for a fault-free behavior. This approach tries to avoid misclassifications caused by model uncertainties.

The third approach is a norm based residual evaluation which uses the residual "energy" to generate the threshold [78]. The L_2 is a popular evaluation function for residual evaluations. It visualizes the energy of the residual over an infinite time range [15]:

$$L_2 = ||\mathbf{r}(t)||_2^2 = \int_0^{\infty} \mathbf{r}(t)^T \mathbf{r}(t) dt. \tag{2.14}$$

Normally, only a finite residual interval is used so that the L_2 norm has to be updated for finite time ranges $L_{2,[t_1,t_2]}$ to [55]:

$$L_{2,[t_1,t_2]} = ||\mathbf{r}(t)||_{2,[t_1,t_2]}^2 = \int_{t_1}^{t_2} \mathbf{r}(t)^T \mathbf{r}(t) dt. \tag{2.15}$$

In practice, the Root-Mean-Square (RMS) is used instead of the L_2 norm which in turn measures the average energy of the residual [15] [78].

With equation (2.15) the maximum and minimum adaptive threshold is given by:

$$\hat{y}^{+}(t) = \max\left(\sqrt{||\mathbf{r}(t)||^2_{2,[t_1,t_2]}}\right). \tag{2.16}$$

$$\hat{y}^{-}(t) = -\hat{y}^{+}(t). \tag{2.17}$$

Fault diagnosis

The primary focus of fault diagnosis is to determine the characteristics of a fault with as many details as possible, such as fault type, size, location and time of detection [61] [43]. In general, there are two groups of symptoms [61]:

- Analytical symptoms which represent the results in the previously discussed fault detection section. Here the knowledge representation is assumed to be precise [20].
- Heuristic symptoms which represent the observations of human operators. Here the representation is qualitative, e.g. linguistic expressions such as "low", "medium" or "high",see [61].

For determining the characteristics of a fault, the previously discussed residuals in Sect. 2 are transfered to symptoms. These residuals can be categorized as analytical symptoms which occur when exceeding e.g. a previously defined positive or negative threshold.

In a physical system, faults cause events which generate symptoms. The diagnosis is functioning in an inverse manner. Hence the diagnosis uses the observed symptoms to trigger events which reconstruct the underlying faults. Fig. 2.3 illustrates this behavior.

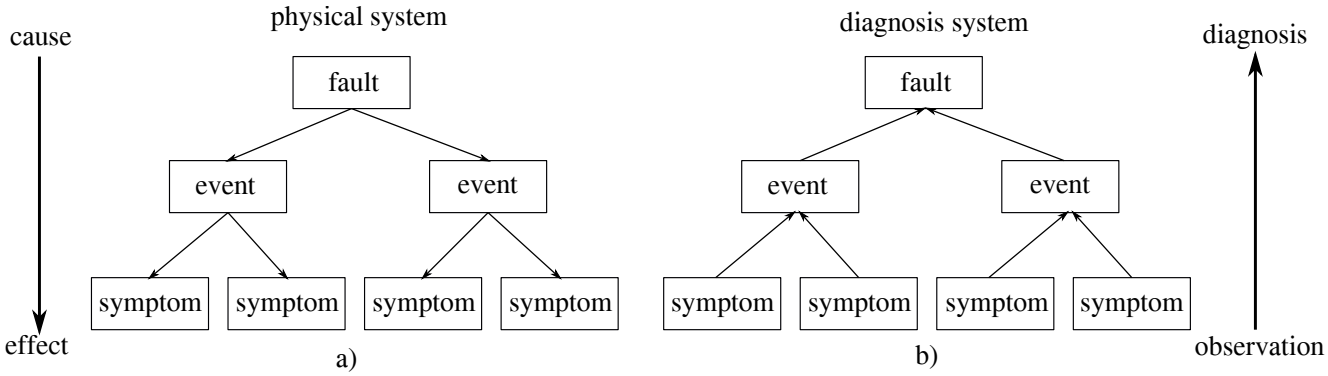

Fig. 2.3: Fault-symptom relationship according to [62]: a) From fault to symptoms for physical system b) From symptoms to faults for diagnosis system

In certain cases, the fault isolation or pinpointing of a specific fault can turn out to be a real challenge for the system developer. This is mainly caused by the complexity of the observed system which strongly depends on [78]:

- The number of possible faults.
- The occurrence and distribution of these faults.
- The available information of faults.
- The characteristic feature of each fault.
- Simultaneously occurring faults.

2.6 Symptom generation

The symptoms can be evaluated from analytical or operator-observed information [62]. The simplest way to generate a symptom is to compare the observed feature to a *static (fixed) threshold* of a simple limit check. Here the trade-off between the sensibility of detection and misclassification has to be taken into account.
With regard to fixed thresholds, residuals depend on the sensor accuracy, model uncertainties which depend on the model quality (could also be OP dependent model uncertainties), inner and outer disturbances [66] [20]. If for example, the residual shows OP dependent uncertainties, the simple limit check to fixed thresholds can cause misclassification. One possibility to cope with this is to combine fixed thresholds with *adaptive thresholds* (described in Sect. 2.5).
The *representation of symptoms* can be realized in different ways see [27] [62]. Here only the binary values and multivalued variables are discussed. For the binary values the symptom occurrence is defined by a 1, whereas the multivalued variables can have different states or characters like small, medium or large. These multivalued symptoms are represented by fuzzy sets with membership functions for linguistic expressions, which are often the representation of operator observed information [60]. For further information see [2] for a general introduction to fuzzy systems and [14] for a Self-Learning Classification Tree (SLCT) approach. The SLCT is capable of extracting a fuzzy classification from system measurement data with the possibility of including prior knowledge.

2.7 Inference methods

Fault diagnosis methods can be categorized into *inference methods* and *classification methods*. In the following section the most common inference and classification approaches are described to solve the above discussed issues. For a detailed fault diagnosis overview, see [61] [62].

The inference approaches use a priori knowledge according to causal relations. Dependent on this qualitative system knowledge, the relationship between symptoms and faults can be described with the following rule:

$$\text{IF} < \text{condition} > \text{THEN} < \text{conclusion} >,$$

where the conditions are the symptoms and the conclusion is the event or fault. The events form an intermediate step. [61]. The following section describes fault symptom trees that demonstrate the above mentioned rule.

2.7.1 Fault symptom trees

Fault trees visualize the relationships between faults and the occurring symptoms. A brief introduction on this topic is provided by [14]. Fault symptom trees visualize the fault situation at the top and symptoms and events at the bottom leading to a particular fault situation. The relationships between the symptoms and events can be represented with binary values and logical operators like AND or OR.

A simple example is shown in Fig. 2.4. The hierarchical structure of fault symptom trees supports

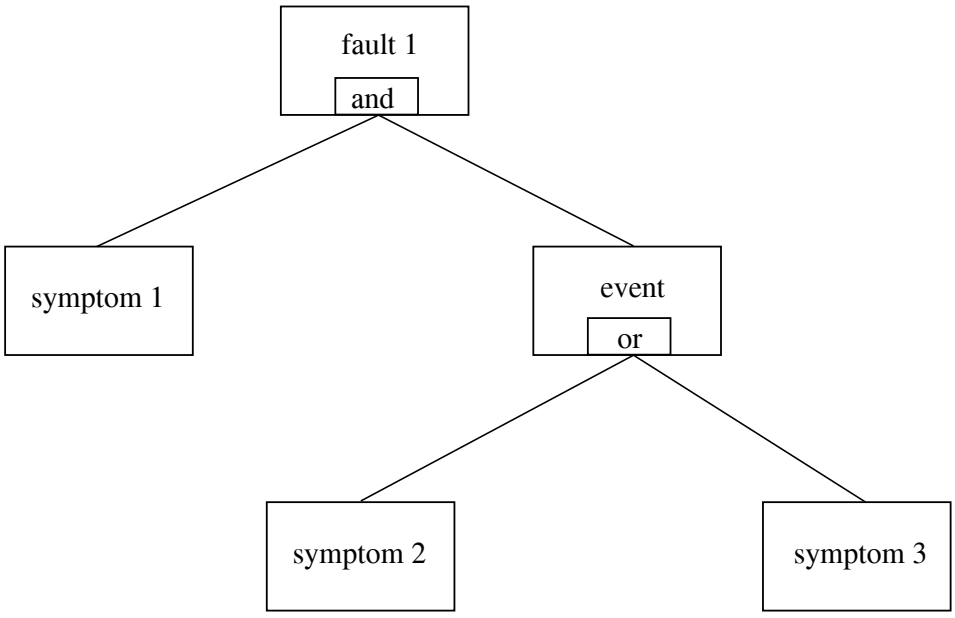

Fig. 2.4: Fault Tree schematic [62] for the following rule: IF < symptom 2 > OR < symptom 3 > AND < symptom 1 > THEN < fault 1 >.

human comprehension [14]. A detailed overview of basic concept and construction fundamentals is shown in [76].

2.7.2 Fault symptom tables

Another method to gain a brief and comprehensive overview of the fault relationships are fault symptom tables. Here, the information of the symptom occurrence for the underlying fault is collected in a table. The collection of this data visualizes the different symptom patterns caused by the introduced faults. An example is shown in Table 2.1 where 3 symptoms and 3 faults are considered with a binary symptom representation. The tables can be categorized two ways, strong and weak isolation. Strong isolation is given if, due to one residual error, no other fault is isolated. Weak isolation is given if, by one residual error, another (wrong) fault is isolated, see [62].

Table 2.1: Fault Symptom Table

	strong isolation				weak isolation		
	s_1	s_2	s_3		s_1	s_2	s_3
f_1	1	1	0	f_1	1	1	0
f_2	0	1	1	f_2	0	1	0
f_3	1	0	1	f_3	1	1	1

2.8 Classification

If there exists no analytical knowledge between symptoms and faults, pattern recognition or classification approaches can be used. Fundamentals of different classification approaches can be found in [62] and [24]. The first step in any classification approach is to generate reference vectors $\mathbf{s}_{\text{ref}}$ for the fault-free case and input vectors $\mathbf{s}$ for different faults $\mathbf{F}$ generated by experiments [65]. For optimal conditions the estimated symptoms show a specific pattern for each fault which can be used to classify the fault properties. Fig. 2.5 illustrates this relation based on a fault-free and two fault cases.

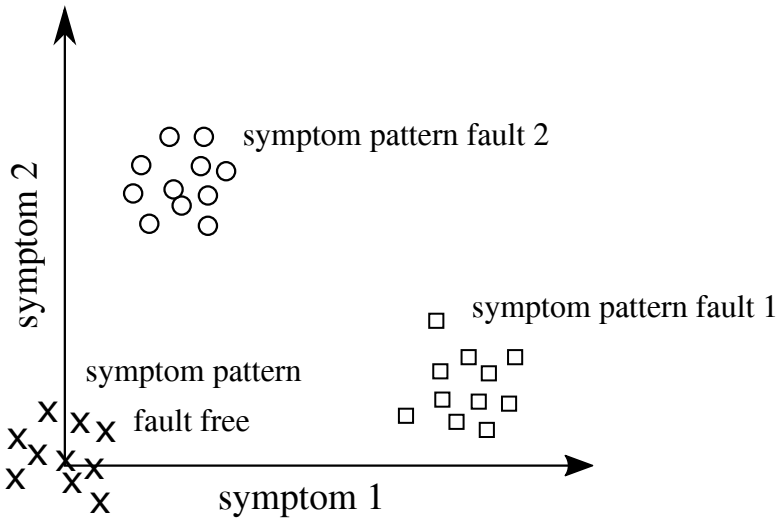

Fig. 2.5: Basic principle of an estimated symptom pattern for a fault-free case, fault 1 and fault 2

In the following sections the most common classification approaches will be discussed.

2.8.1 Bayes classifier

The Bayes classifier approach mainly depends on the probability and statistical distribution of previously established symptoms. With the help of Gaussian probability density functions [62] [67]

$$p(\mathbf{s}) = \frac{1}{(2\pi)^{ns/2}|\Sigma|^{1/2}} \exp\left(-\frac{1}{2}(\mathbf{s}-\mathbf{s_0})^T \Sigma^{-1}(\mathbf{s}-\mathbf{s_0})\right) \tag{2.18}$$

and the Bayes-Law

$$p(F_j|\mathbf{s}) = \frac{p(\mathbf{s}|F_j)P(F_j)}{p(\mathbf{s})} \tag{2.19}$$

the posterior probability can be calculated, where the covariance matrix Σ and the centers $\mathbf{s_0}$ are determined using a likelihood estimation. The class specific densities $p(\mathbf{s}|F_j)$ can be determined using labeled reference data from the corresponding fault F_j. The quality of the algorithm mainly depends on prior probabilities $P(F_j)$, which are generated by the frequency of occurrence assuming there is enough reference data available [62]. One drawback of this approach is that the quality of classification decrease for a huge set of faults [67].

This approach is beneficial if:

- The user has no deep system knowledge.
- Enough reference data from real applications is available.
- The set of faults to be classified is relatively small.

2.8.2 k-Nearest Neighbor

The k-Nearest Neighbor (k-NN) is an approach to classify an actual symptom s_a to it's class membership from the k-nearest reference symptoms $s_{\mathrm{ref},p}$ dependent on the Euclidean distance. To find the class of the actual symptom, the minimum distance of the actual symptom to reference symptom to this actual symptom has to be determined [62]:

$$\min_p (d_p) = \min_p \left(\sqrt{||\ s_\mathrm{a} - s_{\mathrm{ref},p}\ ||^2}\right) \qquad ,\ p \in \{1, ..., n_\mathrm{ref}\} \tag{2.20}$$

n_ref is hereby the number of reference symptoms. If k(NN) = 1, the nearest reference symptom $s_{\mathrm{ref,min}}$ to the actual symptom s_i represents the class membership. Otherwise the majority of the nearest reference symptoms represent the class membership.

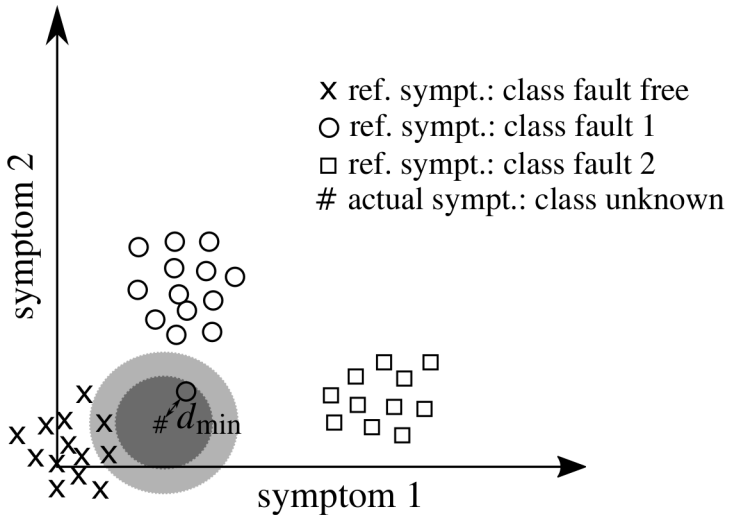

Fig. 2.6: Classification of the actual symptom (unknown class) using the k-NN approach

Fig. 2.6 visualizes the classification of the actual symptom (unknown class) using the k-NN approach. For k=1 the nearest reference symptom to the actual symptom is chosen to define the unknown class membership. In the example of Fig. 2.6 the actual symptom is assigned to the class of fault 1. Now if the three nearest reference symptoms (k = 3) are taken into account, the class membership assignment of the actual symptom will switch to the fault-free class. This is caused by the majority of the three reference symptoms where two belong to the fault-free class and only one to the fault 1.
On the one hand, misclassification could occur if only one nearest neighbor classifies the actual symptom where the nearest reference symptom is caused by noise for example. On the other hand if the number of nearest neighbors increases, there is the possibility that the distance gets too large and therefore a misclassification could occur, due to the distribution of different classes that are linear inseparable. In Fig. 2.6 for example the classes are linear separable. The solution of this is to weigh the reference symptoms according to their distance from the actual symptom [77].
An additional problem for this method is the increased computational effort and storage of all reference symptoms especially for high dimensional issues.

2.9 Summary

This chapter dealt with different fault detection and fault diagnosis approaches. For the fault detection, conventional limit checking, fault detection in closed loop systems, signal model-based approaches with FFT and uniformity analysis and process model-based approaches with parameter estimation, observers and parity equations were discussed. A short overview of the trade-off between small fault detection and misclassification was given which can be improved with adaptive thresholds.
For fault diagnosis different approaches were discussed. On the one hand, it can be expert knowledge based inference methods which can be visualized using fault trees. On the other hand, it can be pattern based classification methods for example with a Bayes or k-NN classifier. Finally fault

symptom tables give a short but broad overview of the faults symptom relationship. In previous research [14],[67] inference methods are recommended for the fault diagnosis of diesel engines. In the following chapters, all discussed fault detection approaches, except the observers are used. Furthermore the dependencies of faults and observed symptoms are shown with fault symptom tables. These tables in combination with a graphical fault tree representation are useful to develop an inference method-based fault diagnosis system, which will be discussed in the following chapters.

3 Heavy duty diesel engine, its components and failure mode analysis

In this chapter, the technical fuel system components of a heavy duty diesel engine are described. The fuel system is divided into three central domains, namely the Low Pressure (LP), the Middle Pressure (MP) and the High Pressure (HP) domains. The primary focus lies on the fuel injectors, the High Pressure Pump (HPP), the Middle Pressure Pump (MPP) and the Low Pressure Pump (LPP). The HPP is described which generates the requested fuel HP with the help of a mechanically driven in-line plunger pump. This guarantees a stable HP fuel supply for sufficient fuel injections. Furthermore, the MPP and the LPP are described. These pumps belong to the type of displacement pumps. The main task of both pumps is the proper fuel supply to the HPP. The primary distinguishing features between these two pump types are the operating pressure range and the type of drive. The MPP is mechanically driven by the crankshaft and the LPP electrically driven by a Direct Current (DC) motor.
In the last section, possible faults of the Internal Combustion Engine (ICE) fuel system are considered. These faults, along with their possible fault origins are discussed in a Failure Mode and Effective Analysis (FMEA) table. Finally, the system requirements and challenges for an optimal integrated fuel system diagnosis is discussed.

3.1 Internal combustion engine with compression ignition (Diesel engine), fuel system and water swirl dynamometer

The test engine is an Internal Combustion Engine (ICE) with compression ignition. The engine is a six-cylinder, in-line heavy duty diesel engine with up to 317kW rated power. The cylinder firing order for this research project is chosen to be 1-5-3-6-2-4 and can be adjusted manually in the ECU. The engine also exhibits a fixed turbocharger, a Variable Geometry Turbine (VGT) turbocharger, an external exhaust gas recirculation and a common rail injection system. A deeper insight including the fundamentals of diesel engines can be found in [39].
Fig. 3.1 shows the schematic of the engine with all integrated sensors, the fuel system and the water swirl dynamometer. The sensors indicated in gray, are serially installed sensors. The sensors labeled in white are additional sensors installed on the test bench. On the left bottom side of Fig. 3.1 the fuel path with a fuel tank on a mass scale, the primary and secondary fuel filter, the LPP and the Denso HP6 fuel pump is shown. This HP6 pump includes the MPP and the HPP. The engine drives a Horiba DT1200 water swirl dynamometer. The brake torque can be adjusted by a variation of the water mass flow which is streaming into swirl chambers. This is achieved by a

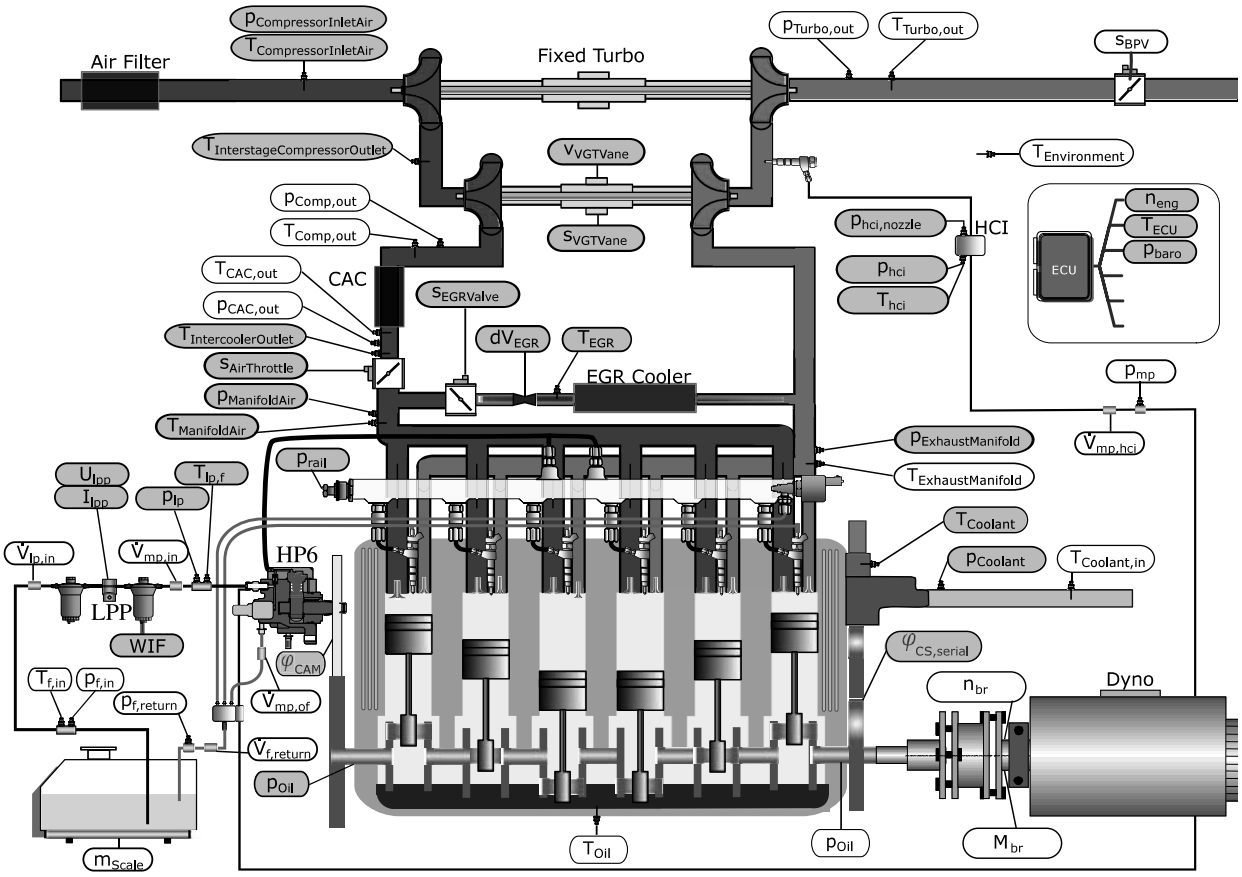

Fig. 3.1: The test engine with serial sensors (gray) and test bench sensors (white), fuel system and water swirl dynamometer

servo controller varying the opening position of the water inlet valve. The brake type belongs to the type of hydraulic brakes. The principle of this brake is to convert mechanical energy from the engine into kinetic energy of the water particles by the swirling of these particles. This conversion will also cause friction and therefore a water temperature increase. The heated water is finally transported out of the brake via the water mass return flow.
The test bench with all additional components is shown in the Appendix A.1.

3.2 Fuel system pressure domains

The engine's fuel system includes different pressure ranges and is divided into three central domains (see Fig 3.2):

- The Low Pressure (LP) fuel system supplies the engine with fuel from the fuel tank. The general pressure in the LP system is about 120 kPa (1.2bar) if the atmospheric pressure is 100 kPa. So, the LPP increases the fuel pressure about 20 kPa above the measured atmospheric pressure. This pressure increase is generated by a LPP with a gerotor displacement pump. The gerotor pump, named Racor and manufactured by Parker Automation, is driven

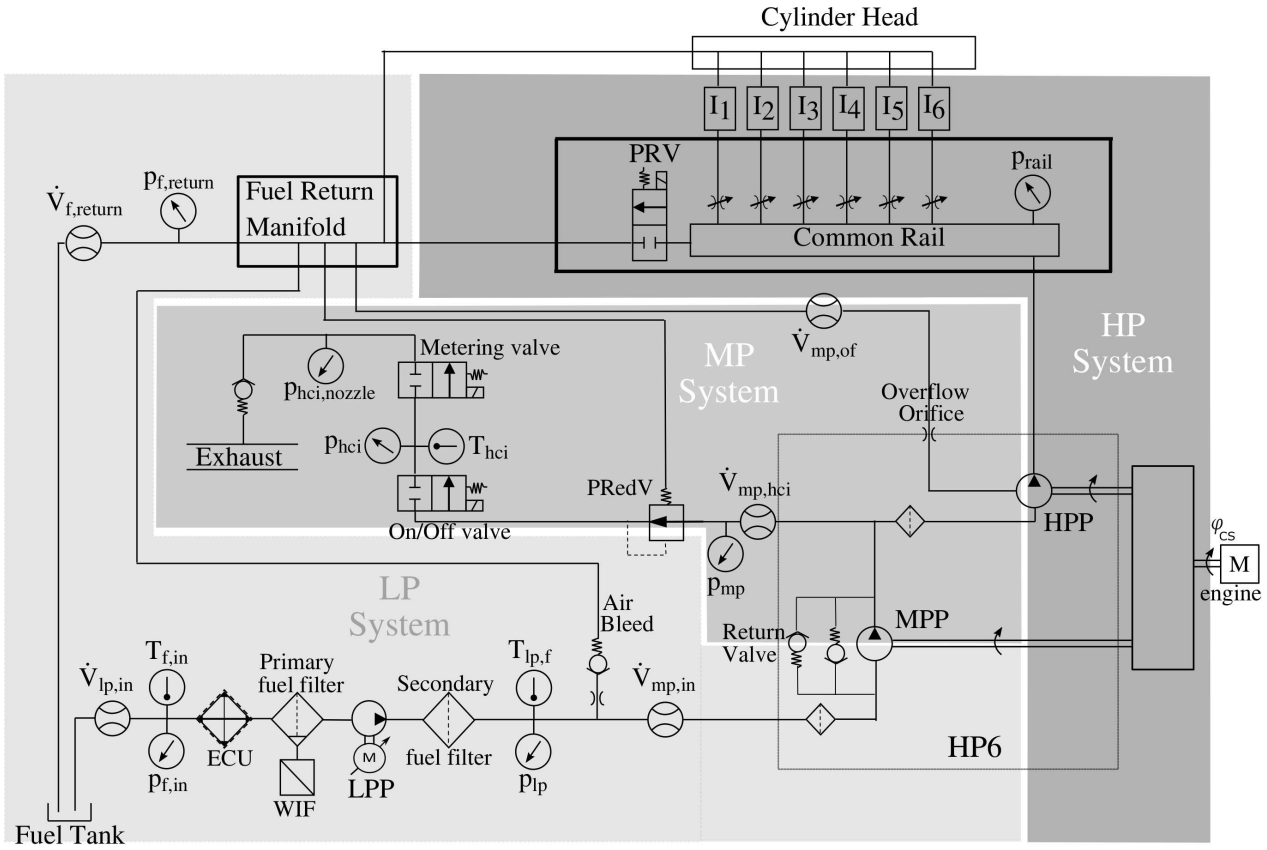

Fig. 3.2: Fuel system diagram with the three pressure domains including all sensors (without HP6 lubrication parts). PRV: PWM controlled on-off valve.

by a brushless DC motor [11]. If an air-fuel mixture gets into the system caused by an empty fuel tank or leakages before the LPP's inlet, a fuel path back flow through the air bleed valve to the fuel tank is generated.

- In the Middle Pressure (MP) fuel system, the pressure goes up to 1600 kPa (16 bar). This pressure is generated by a MPP. Like the LPP, the MPP is a gerotor displacement pump. The main task of the MPP is to supply fuel to the HPP piston chambers, to ensure a constant amount of fuel in each chamber. In addition, the MPP supplies fuel to the external aftertreatment regeneration system. The aftertreatment regeneration system includes a Pressure Reducing Valve (PRedV), an ON/Off valve, a metering valve and an injector for the injection of fuel into the exhaust gas flow to increase the exhaust temperature. The PRedV reduces and stabilizes the pressure to a constant value of about 800 kPa (8 bar) to ensure optimal functionality for the soot filter regeneration cycle.

- The High Pressure (HP) system is the primary component of the fuel system and it includes the HPP, common rail, Pressure Relieve Valve (PRV) and G4S injectors from Denso. In the common rail, the fuel can be compressed by two HPP piston chambers up to 250 MPa (2500 bar). The PRV is the valve, which opens if the pressure exceeds a predefined threshold. Furthermore, there are flow dampers at the inlet of every injector to restrict the fuel mass flow in case of an HP leakage.

Fig. 3.2 shows all fuel paths, their components and the three pressure domains.
The measured variables in the fuel path are:

- Pressure sensors: $p_{\mathrm{f,in}}$, p_{lp}, p_{rail}, p_{hci}, $p_{\mathrm{hci,nozzle}}$, p_{mp}, $p_{\mathrm{f,return}}$
- Temperature sensors: $T_{\mathrm{f,in}}$, $T_{\mathrm{lp,f}}$, T_{hci}
- Volume flow sensors: $\dot{V}_{\mathrm{lp,in}}$, $\dot{V}_{\mathrm{mp,in}}$, $\dot{V}_{\mathrm{mp,of}}$, $\dot{V}_{\mathrm{f,return}}$, $\dot{V}_{\mathrm{mp,hci}}$
- Others: Current and voltage measurement of LPP U_{lpp}, I_{lpp} fuel tank scale m_{sclae}

3.3 Low pressure pump

As mentioned earlier the LPP is a gerotor displacement pump, see Fig. A.5 in the Appendix. Therefore, the pump's volume flow is equal to the mathematical product of the displacement volume and the pump speed. Furthermore, the pump is electrically driven. Therefore, the LP fuel supply can be activated without turning on the engine. To guarantee enough fuel supply for lubrication and optimal functionality of the MPP and the HPP, the pressure is constantly held at about 20 kPa above atmospheric pressure by pressure control.

The LPP control is designed as a cascaded control system, where the inner closed loop is a brushless pump speed control [6], offered by the pump manufacturer Parker. The outer closed loop is a pressure control implemented in the engine's ECU. The inner speed control is implemented on a Digital Signal Processor (DSP) integrated in the pump of Parker, see [11]. Fig. 3.3 shows the cascaded control loop of the LPP.

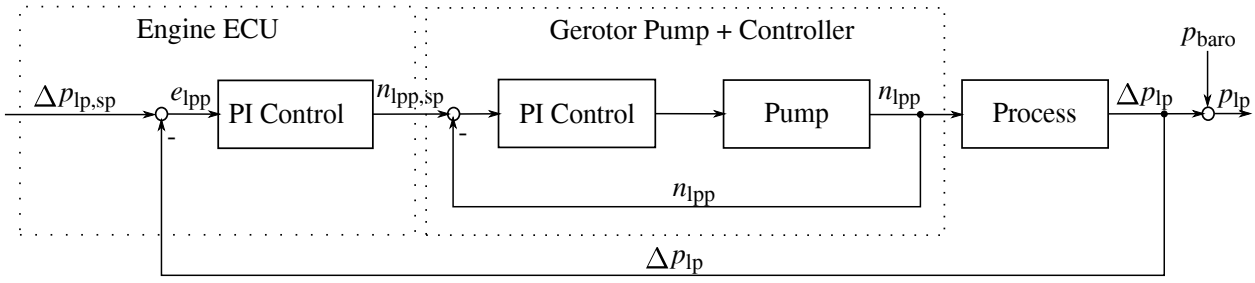

Fig. 3.3: Cascaded closed loop control of the LPP

The communication between the ECU and the LPP speed controller is achieved through a CAN bus. To ensure the functionality of the closed loop control, the ECU must transform the control deviation

$$e_{\mathrm{lpp}} = \Delta p_{\mathrm{lp,sp}} - \Delta p_{\mathrm{lp}} \tag{3.1}$$

to a speed command $n_{\mathrm{lpp,sp}}$ for the internal PI speed controller from Parker.

3.4 Middle pressure pump and system volume flows

The HP6 fuel pump from Denso combines the MPP and the HPP inside a single pump housing. The HP6 pump, and in turn, the MPP and the HPP are mechanically driven by the engine's crankshaft with a 1:1 ratio. As described in Sect. 3.2, the MPP is a gerotor displacement pump (see Fig. A.5 in the Appendix) which preconditions the fuel to a MP up to 1600 kPa (16 bar) mainly depending on engine speed. The MPP has the primary function of supplying a constant amount of fuel for the HPP piston chambers, ensuring a constant fuel pressure. Furthermore, the MPP supplies fuel for the aftertreatment system and lubrication of the very important mechanical pump parts. The inner fuel paths of the HP6 and LP system are important for system modeling and algorithm design in the following chapters. Fig. 3.4 illustrates these volume flows which will be described in the following section.

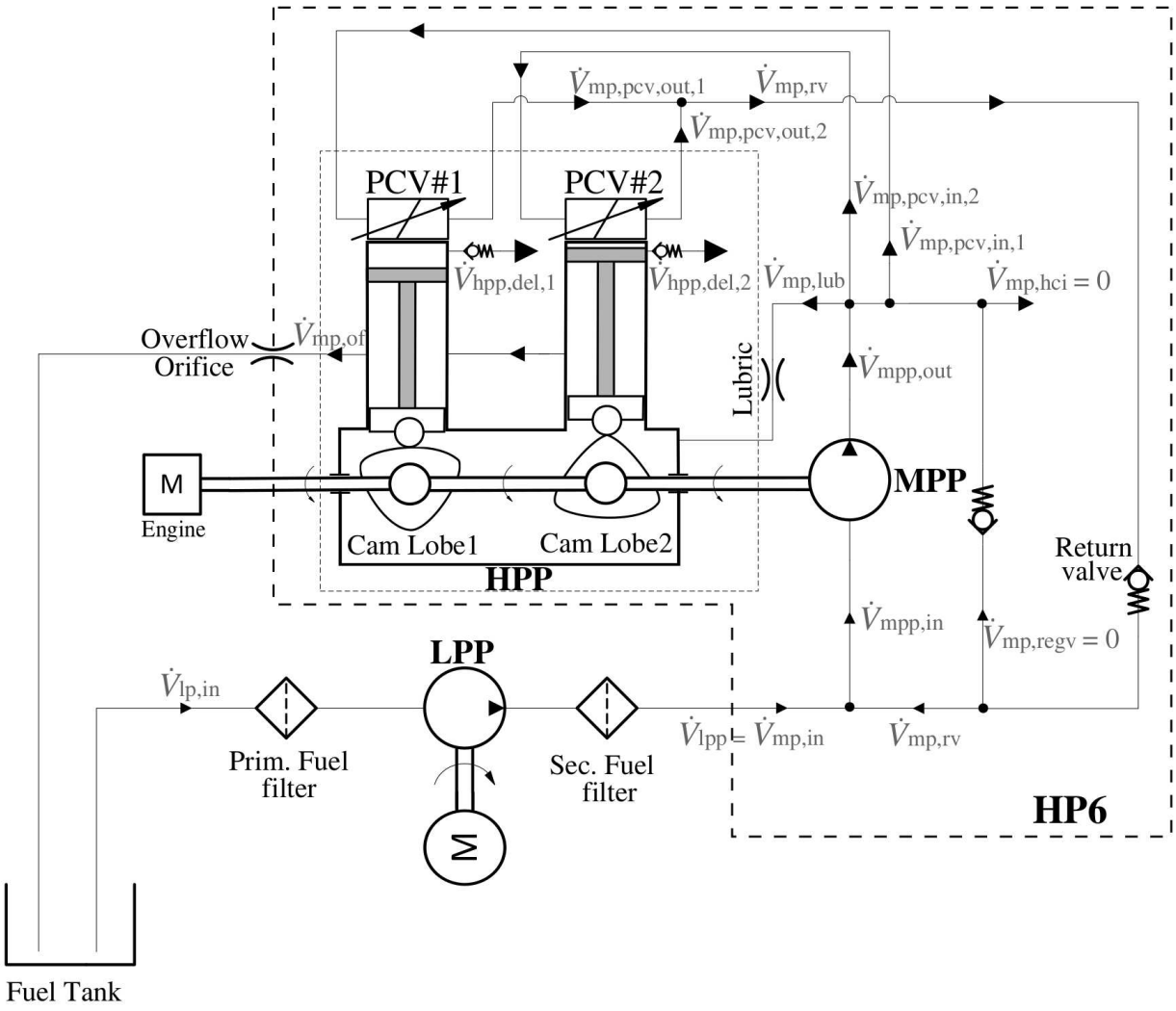

Fig. 3.4: Volume flow paths of the HP6 and LP system with neglected air bleed volume flow

According to Fig. 3.2, the inner fuel path architecture of the HP6 can further be divided into three different pressure areas:

- The fuel inlet area of the HP6 (MPP), where the fuel and fuel pressure is supplied from the LP side. Hence, this area is allocated to the LP area (see also Sect. 3.2). In Fig. 3.4 this area is shown with small arrows (at the fuel lines) before the MPP. For this area, the MP gerotor pump and the return valve describe the connection between the LP and the MP system.
- The second area is located after the MP gerotor pump in the HP6. In Fig. 3.4 this area is shown with medium sized arrows in between the MPP and the HPP. In this area, the fuel is compressed with the MP gerotor pump from LP to MP.
- The third area is the HP area of the HP6 which includes the HPP. In Fig. 3.4 this area is shown with large arrows which define the fuel output of the HP6 or the HPP to the common rail.

3.5 High pressure pump

Another important component in common rail fuel systems is the High Pressure Pump (HPP). The HPP is a part of the HP6 and it is mechanically driven by a camshaft with a 1:1 ratio from the engine's crankshaft. The HPP falls into the category of outlet metered in-line plunger pumps. The HPP compresses the fuel up to the desired RP value ($p_{\text{rail}} \leq$ 250MPa (2500bar)) depending on the engine's OP. The two in-line plunger chambers are shown in Fig. 3.4 and Fig. 3.8.
The pre-compressed fuel from the MPP supplies the HPP's two plunger pump chambers with fuel. These pump chambers are driven by a pump camshaft via cam lobes, with one lobe dedicated per pump chamber. The cam lobes profile has three profile peaks per lobe, whereas the angle between the peaks is phase-shifted over 120°CA (see Fig. 3.8). Hence, in every full revolution of the crank shaft each pump chamber has 3 pumping cycles. Fig. 3.4 and Fig. 3.8 show the two pump chambers with cam lobes and Fig. 3.5 illustrates the functionality of the pump.
Furthermore, the cam lobe of pump chamber 'one' compared to the cam lobe of pump chamber 'two' is designed with an offset of 60°CA on the camshaft (see Fig. 3.4 or Fig. 3.8). With this design, it is possible to supply fuel every 60°CA and hence the two plungers can supply fuel sequentially into the common rail. The fuel delivery is regulated by the HPP fuel quantity control and is described in the following section. Due to the firing distance of 120°CA which in turn decreases the RP and the fuel supply of 60°CA increasing the RP, a stepped common RP curve is imprinted (see Sect. 4.6).

HPP fuel delivery functionality

To supply a desired amount of fuel from the HPP pump chamber into the rail, the ECU activates a Pressure Control Valve (PCV). The PCV consists of a poppet valve, a valve spring and a coil, see Fig. 3.5.
If the HPP's plunger now moves upwards, the starting point is the electrical activation of the PCV. This activation closes the PCV's poppet valve and thereby cuts off the back-flow of fuel to the MP system. This means that during the compression stroke (plunger's upward movement) the poppet

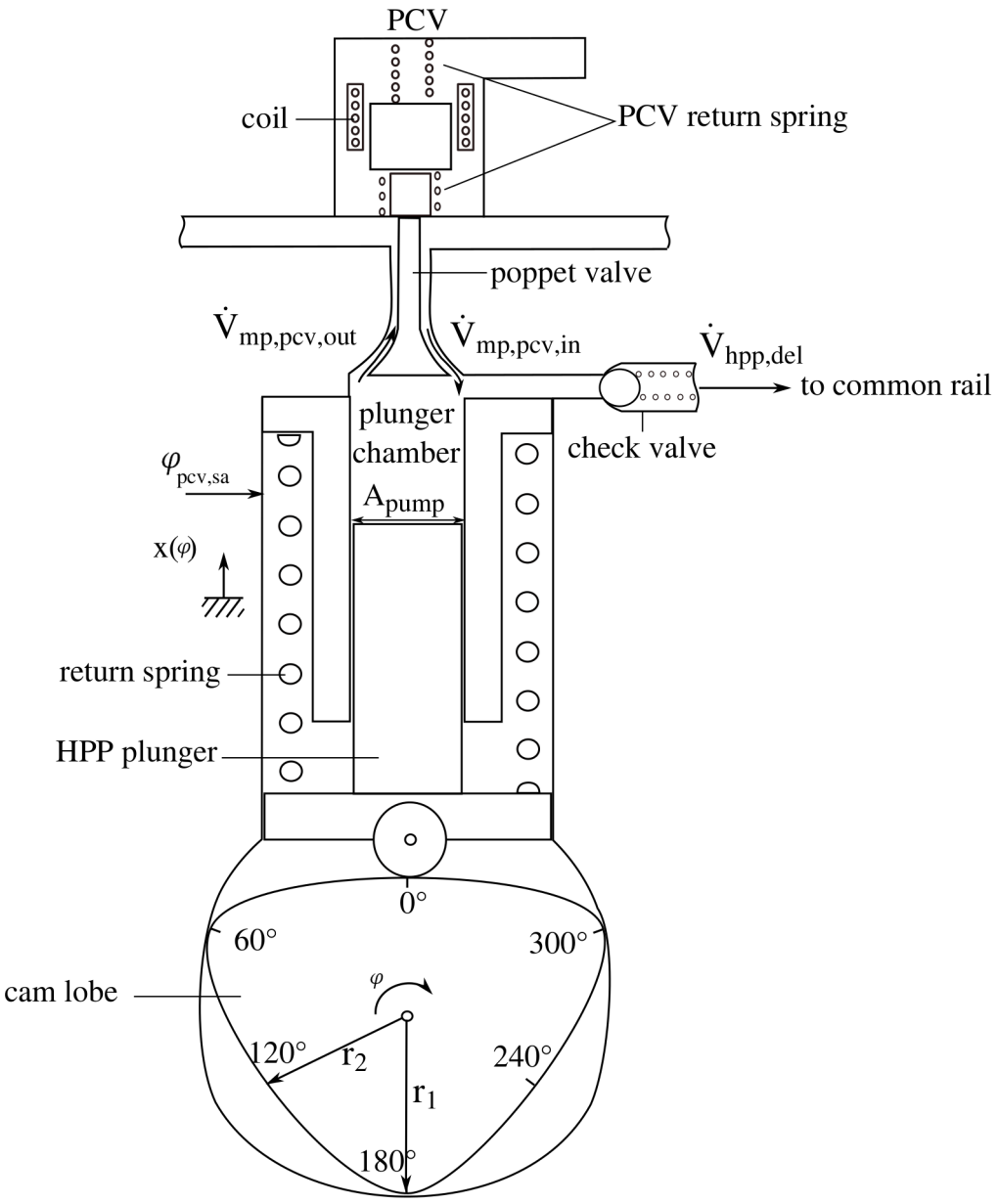

Fig. 3.5: HPP function diagram (for plunger chamber 1) showing only the main volume flows

valve remains open until the position $\varphi_{pcv,sa}$ and thereby delivering no fuel into the rail until then. This closing position $\varphi_{pcv,sa}$ of the poppet valve is calculated by the HPP fuel quantity control, see Fig 3.7. When $\varphi > \varphi_{pcv,sa}$ condition is met, the plunger starts compressing the fuel mass that is left in the plunger chamber up to the RP value.

The principle of a defined starting position of fuel delivery can be described with a phase angle control for the PCV which is shown in Fig. 3.6 for two different commanded closing positions $\varphi_{pcv,sa}$. For detailed information on phase angle control for hydraulic pumps see [8] [7]. With this principle, the exact amount of fuel needed for fuel injections can be delivered by the HPP when the following holds true: When the poppet valve is closed at a specific PCV start angle $\varphi_{pcv,sa}$, there is a defined pump chamber volume with a defined amount of fuel in this chamber (see Fig.

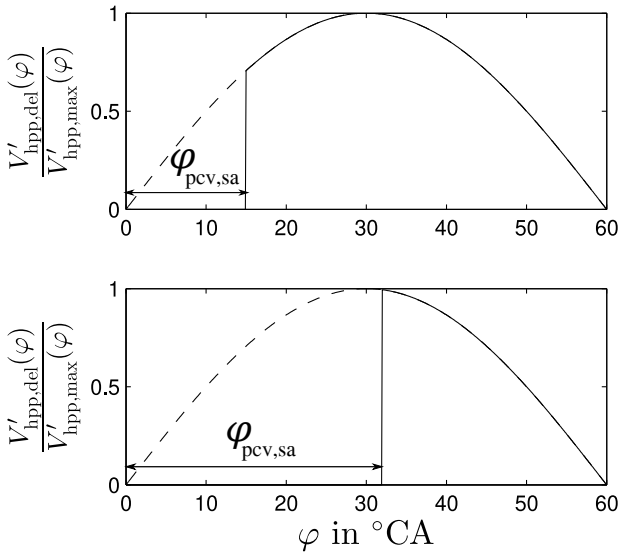

Fig. 3.6: Simulated HPP fuel delivery described with a phase angle control for two different PCV start angle $\varphi_{\mathrm{pcv,sa}}$ commands

3.5).

The assumption of a defined amount of fuel (at a specific PCV start angle) results in the downstream of the plunger in a continuous fuel mass supply from the MPP into the plunger chambers for an assumed constant MP. With this definition and since the pump is 1:1 gear driven, the precise amount of fuel delivered by the HPP can be estimated with:

- The actual volume of the HP plunger chamber (volume in between actual plunger position and top dead center of HP plunger chamber) when the PCV is closed (at specific $\varphi_{\mathrm{pcv,sa}}$).
- The fuel density and fuel compressibility dependent on the actual RP.

Additionally, the following rules apply for the compression phase ($\varphi > \varphi_{\mathrm{pcv,sa}}$), upstream of the plunger chamber and when the poppet valve is closed. If the hydraulic force in the HPP's plunger chamber, generated by the compressed fuel in this chamber, is a little higher than the RP plus the check valve spring opening force, the chamber continues to supply fuel into the rail until this force imbalance is not fulfilled anymore. This is the case if the plunger is changing direction (downstream). If the poppet valve is open, which means that the PCV is not activated in the upstream of the plunger, then there is no pressure build up in the common rail. This is the case because the complete amount of fuel left in the plunger chamber is pumped back to the MP system and flows in a fuel circle. Fig. 3.5 visualizes this behavior. A detailed description with all phases will follow in Sect. 4.3.

HPP fuel quantity control

The control of the in-line plunger pump fuel quantity (HPP fuel quantity control) is a combination of an open loop and closed loop control implemented in the engine ECU, see Fig. 3.7.

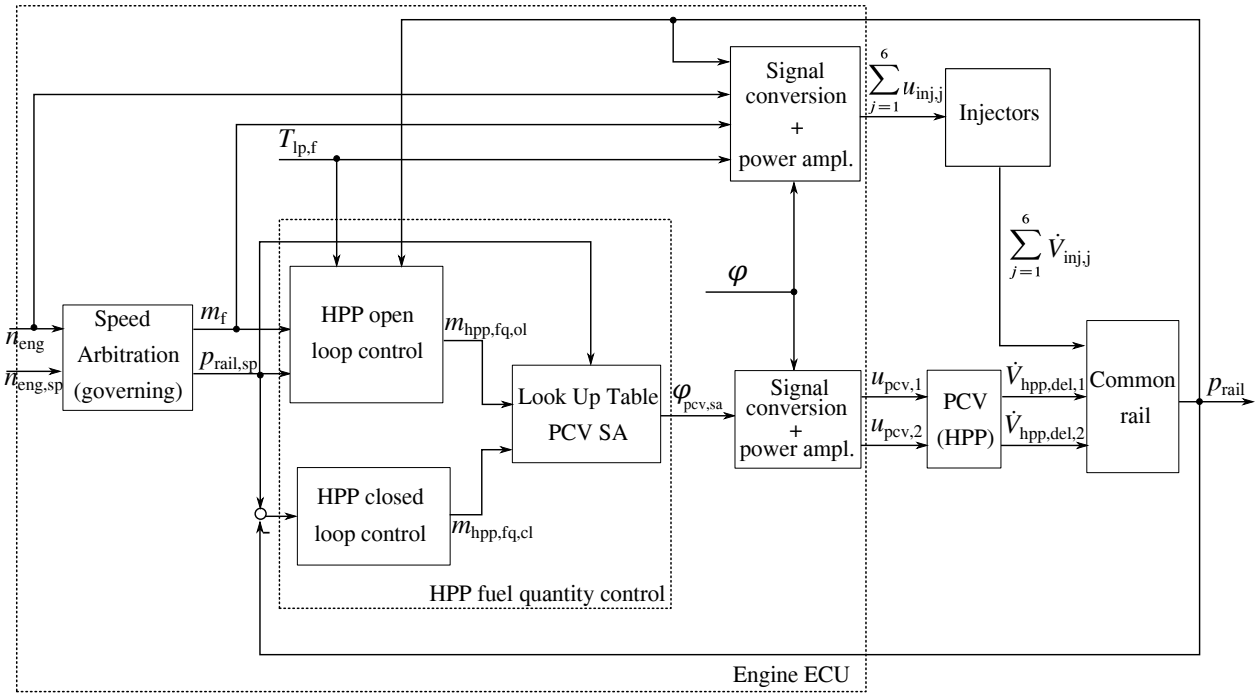

Fig. 3.7: High level overview HPP fuel quantity control for a simplified speed arbitration (governing) neglecting the PRV

With the HPP's fuel quantity open loop control, the ECU initially calculates the amount of fuel mass ($m_{\mathrm{hpp,fq,ol}}$) that is needed for a desired RP setpoint at the current OP. Next, the HPP fuel quantity closed loop control (fuel mass $m_{\mathrm{hpp,fq,cl}}$) compensates for all kind of faults, parameter variations or disturbances influencing the RP. The HPP (actuator) input variable, named PCV start angle $\varphi_{\mathrm{pcv,sa}}$, is calculated as a function of the HPP fuel quantity open loop control's fuel mass $m_{\mathrm{hpp,fq,ol}}$, HPP fuel quantity closed loop control's fuel mass $m_{\mathrm{hpp,fq,cl}}$ and a desired RP setpoint $p_{\mathrm{rail,sp}}$ (see Fig. 3.7).
In an HPP fault-free state, the entire value of the actuator input variable ($\varphi_{\mathrm{pcv,sa}}$) is provided by the open loop control's fuel mass $m_{\mathrm{hpp,fq,ol}}$ for a desired RP setpoint. This means, that in a fault-free case, it can be assumed that the open loop control will pre-calculate the complete amount of fuel mass needed for fuel injections. This leads to $p_{\mathrm{rail,sp}} - p_{\mathrm{rail}} = 0$, where the difference between the actual RP and the RP setpoint is the input variable of the HPP fuel quantity closed loop control (see Fig. 3.7). Finally, only the pre-calculated fuel mass will then be delivered by the plunger chambers of the HPP into the rail.

From Fig. 3.7, it can be noticed that the HPP and the injectors form the main components influencing the RP. In this combination, the PRV is neglected because it is only active in extreme transient engine operating point changes with a huge RP to RP setpoint mismatch.

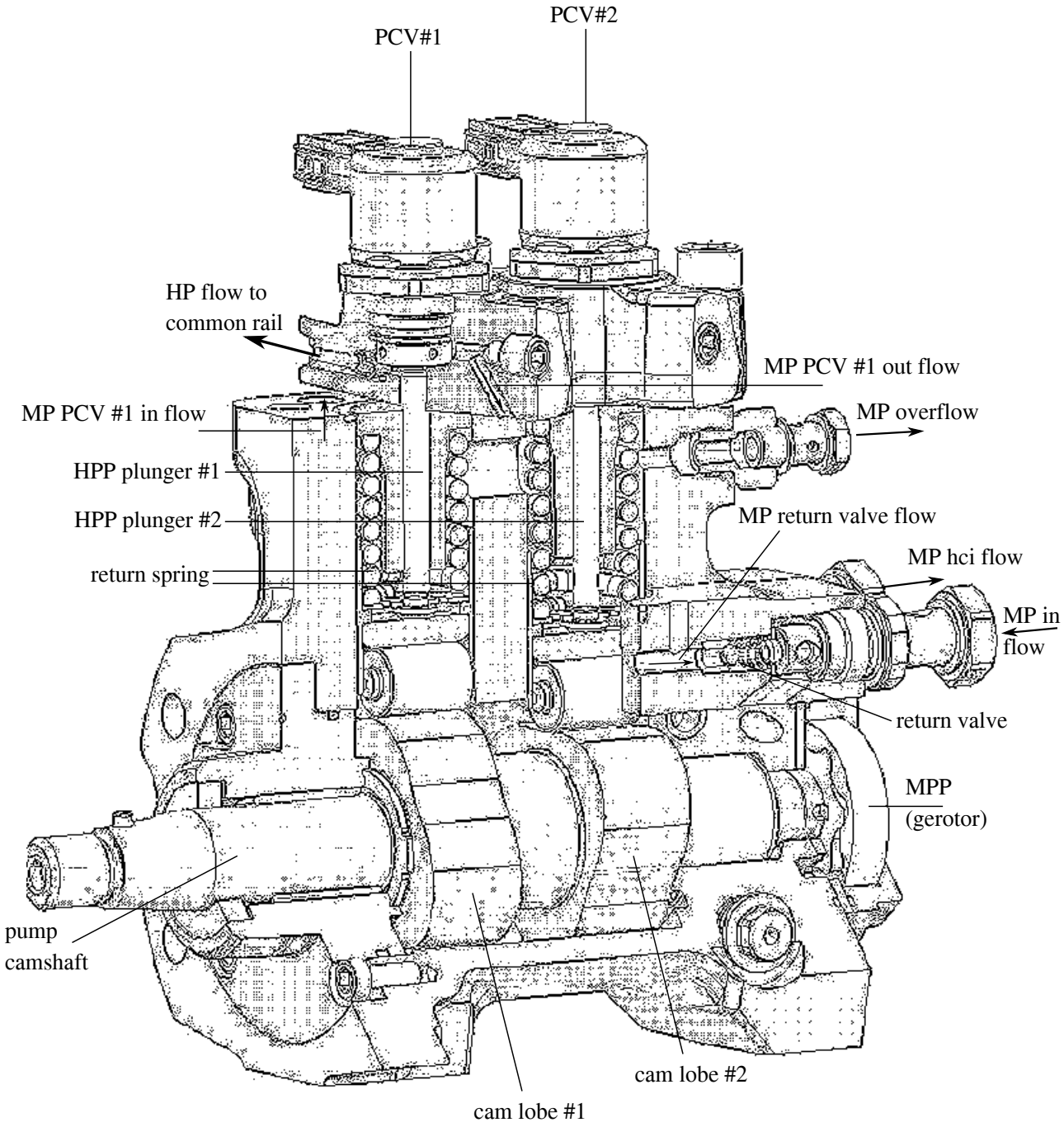

Fig. 3.8: HP6 sectional view showing the HPP and the MPP (Figure according to [71])

In conclusion, the HPP fuel delivery is controlled by the HPP fuel quantity control and the RP is the controlled output variable of the HPP fuel quantity control, see Fig. 3.7.
This outlet metered concept and especially the phase angle control has a crucial advantage, that the amount of fuel needed for a desired RP setpoint can be precisely controlled without an activation

of the PRV. This leads to lower energy losses and an improvement of fuel consumption. Higher energy losses and fuel consumption occurs when the fuel is compressed up to the RP and then relieved by the PRV in the common rail system.

3.6 Injectors

The injectors are one of the most important elements in engine fuel systems. They have several functions, such as increasing the efficiency of the engine, reducing the emissions and optimizing the engine's noise by an efficient optimization of fueling time and parameters. For detailed information see [40].
The injectors also must withstand a high pressure of up to 250MPa and seal the combustion chamber from the highly compressed fuel. There are two different types of injectors, namely solenoid and piezo based injectors. The piezo based injectors have the characteristic of a quick activation but they are sensitive to wear, whereas the solenoid injectors are less susceptible to wear but not as fast in activation. In the past few years the optimization of solenoid injectors resulted in faster actuation of this type of injectors reducing the weakness of this concept and therefore solenoid injectors are used as the first choice for different applications. However, the abrupt closing of the injectors in general causes pressure waves with high frequencies in the rail. This phenomenon is called the "water hammer effect" [9].
In heavy duty applications, solenoid injectors are often used because of their reliability and lower costs. The test engine has six solenoid G4S injectors from Denso introduced in 2013 [28], one for each cylinder. These injectors allow a RP up to 250MPa. Furthermore, they reduce switching leakage (needed for injector activation) and avoid clearance leakages. This leads to less power losses due to reduced mechanical power needed to drive the HPP, for detailed information see [28].

Fig. 3.9 describes the three functional states of the injector:

- The first state is the inactive closed position of the injector labeled "Before Injection". In this state, the pressure in the control chamber is equal to the RP because the control valve is closed. This results in a force imbalance where the control chambers hydraulic force at the top area and the spring force of the nozzle needle is higher than the hydraulic force at the nozzle needle surface in the fuel supply area. As a result, the nozzle needle is pressed to the outer surface of the injector and the injector is therefore closed.

- The second state is labeled "Start Of Injection" (SOI). Here, the control valve is opened by a solenoid activation. The fuel in the control chamber flows out through an 'out-orifice' which is integrated in the control plate. The control plate avoids the incoming fuel flow from the fuel supply area into the control chamber. The pressure in the control chamber decreases and results in a reversed force imbalance compared to the first state which moves the nozzle needle upwards. Now the nozzles are open and the fuel from the supply area is injected into the cylinder via the injector nozzles.

- The third state, with the label "End Of Injection" (EOI), represents the closing mode of the injector after injection. In this state, the solenoid is deactivated resulting in a closure of the control valve by a spring. The high pressure groove circle and the increasing pressure at the intermediate chamber evokes a force imbalance at the control plate, which moves the control plate in the direction of the nozzle needle closing position. The fuel flows through 'in-orifice' from the fuel supply area into the control chamber and causes a pressure increase in the control chamber up to the supply pressure (RP). Similar to the first state, the same force imbalance closes the nozzle needle and stops the fuel supply to the cylinder. The state then switches again to the first state and the injection cycle is finished.

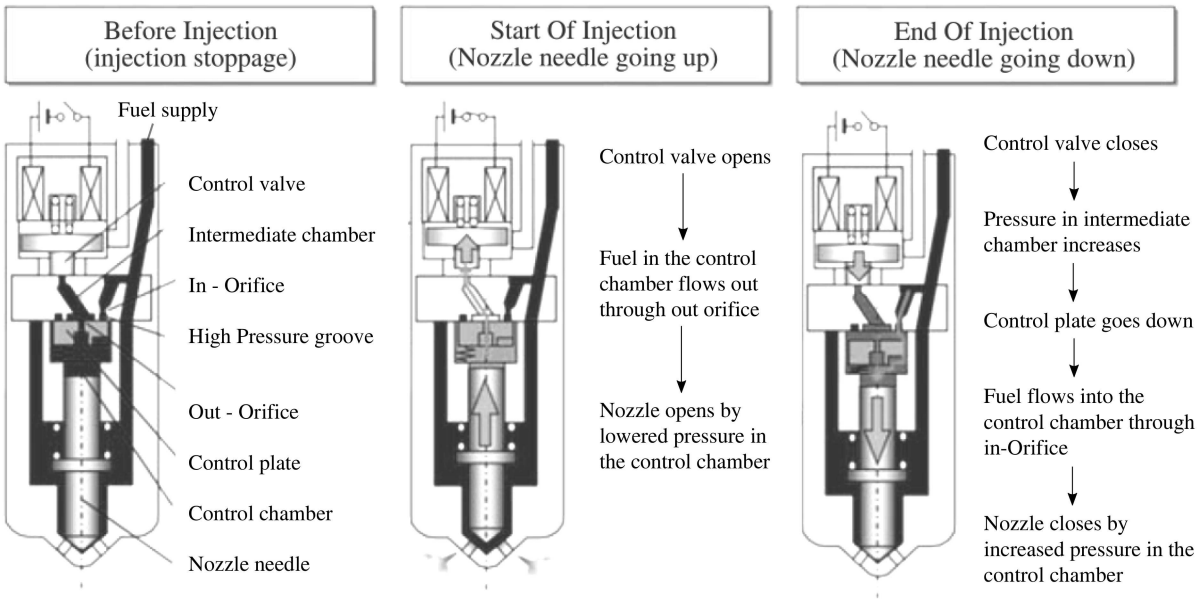

Fig. 3.9: Denso G4S injector function description (picture source [28])

3.7 Failure mode and effective analysis / requirements for the diagnosis of the diesel engine

The Failure Mode and Effective Analysis (FMEA) is an analytical method to list all possible system faults or malfunctions and their effects considering all components, fault causes and their effects on the unit where they occur as well as on the complete system (for a detailed description see [62]).

3.7.1 System requirements

One of the main goals of this work is to develop a diagnosis system for the fuel path with least restrictive conditions on the normal operation of the engine as already stated in Sect. 1.2. In other words, the intervention for diagnosis on the normal operation process should be kept as small as possible. Adding additional sensors should be avoided, mainly because of costs, but also because of compatibility reasons with already produced engines.
With model-based approaches and production sensors, physical models are used to avoid additional sensor implementation. But these methods pose a few challenges such as:

- Accuracy of used models.
- The detection and isolation of faults in closed loop controls.
- Model uncertainties caused by low resolution of the production sensors (e.g. discretization error for the RP sensor).
- Loss of observed variable's dynamic behavior when using production sensors caused by low sensor resolution.
- Missing intermediate variables for system observations.

To cope with these challenges, additional methods like signal based and model-based approaches, described in Chap. 2, are used.

3.7.2 Failure mode and effective analysis

This section is an excerpt of possible faults for the fuel system of the described Internal Combustion Diesel Engine in Sect. 3.1. With an inspection of the system, an FMEA is designed in Table 3.1 for different components with their possible faults. This table is the basis for the treated faults of the developed fault diagnosis.

Table 3.1: Failure Mode and Effective Analysis of the fuel path of the ICE

System	Component	Fault	Fault cause	Fault/Failure effects
HPP	PCV	Valve not closing/opening	Missing power supply, valve debris	HP drop at high load OPs
		Valve close not commanded	Spring wear, spring broken	Excessive/ low pump fuel delivery
LP system	Prim. fuel filter	Clogged	Aging/ polluted fuel	Critical LPP/ HPP lubrication, LP not sufficient
	Sec. fuel filter	Clogged	Aging/ polluted fuel	Critical HPP lubrication, LP not sufficient
	LPP	No fuel delivery	Missing power supply, broken pump windings	Critical LPP/ HPP lubrication, LP not sufficient
Injector	Injector nozzle	Clogged (Low Flow)	Nozzle coking	Less fuel injections
		Fuel growth (High Flow)	Nozzle erosion	More fuel injections
LP leakage	Fuel line before prim. filt.	Leakage	Aging, loosen connection	LPP pull air/fuel mixture, less fuel supply to LPP
	Fuel line behind sec. filt.	Leakage	Aging, loosen connection	Fuel reaches the environment
HP leakage	Side feed tube	Leakage	Loosen conn.	HP drop, increase of energy loss
	PRV	PRV leakage	Broken return spring	HP drop, increase of energy loss
		Valve not opening	Valve stuck/ shortcut	Uncontrolled RP in dynamic mode
Pressure sensors	RP sensor	High offset	Aging, disturbance	RP value undersized
		Low offset	Aging, disturbance	RP value oversized
	LP sensor	High offset	Aging, disturbance	LP value undersized
		Low offset	Aging, disturbance	LP value oversized
Cylinder misfire	Piston ring, In-/outlet valve	Less compression	Wear	Fuel not burned, change in emissions
			Incorrect clearance	Air path fault
				Turbocharger fault

3.8 Summary

In this chapter, the test bench and the ICE with its fuel system components were described in technical detail. As a first step, the fuel system is divided into three pressure domains. In a fuel path diagram, the production and additional installed sensors were described.
The LPP and its cascaded control loop for the LP along with the importance of its electric drive were discussed. Specifically, the engine independent propulsion offers additional possibilities to improve fault detection.
The fuel paths for the HP6, which includes the HPP and the MPP in a single pump housing, additionally the LP fuel paths were discussed. The characteristics of the mechanically driven HPP and MPP in contrast to the electrically driven LPP were described. Furthermore, the function of the MPP was explained with its diverse tasks.
Then the main components for the HP system, the injector and the HPP were described and their functionality were discussed in detail. In addition, the advantages of a precise open and closed loop control for the HPP were discussed.
Finally, the requirements for the fuel path diagnosis of the diesel engine were described and an FMEA of all important fuel path faults was discussed.

4 Modeling of the diesel engines fuel system

In this chapter, basic models for the process model-based approaches are developed. These models reproduce the monitored process with a mathematical model using the measured input signals $u(t)$ and the output signals $y(t)$. The different fuel system components of the LP, MP and HP systems are modeled with physical, semi-physical or look up table-based mean value models. In the LP system, the primary focus is on the development of a volume flow and a power model for the LPP. In the MP system, volume flow models for the inlet of the HP6 (before MPP) are developed with the help of a mass flow balance. Also, intermediate state models for the HP6 (behind the MPP and before the HPP), which include the MP volume flow models and a semi physical MP model, are developed using mass flow balance. These MP models provide an interface between the LP and HP system. The HP system is developed from the mass flow balance of the common rail, where the pump fuel mass delivery is physically modeled and the injections and the fuel discharge for the PRV are modeled using a mean value model.

4.1 Fuel path signals representation

There are two possibilities to represent engine signals and physical engine models. The first possibility is a conventional discrete time-based representation, where the variables are represented with a fixed sample time. The second possibility is a crank shaft angle-based representation, by use of a crank shaft sensor. This sensor determines the actual position of the crank shaft. This is essential for injecting fuel into the engine cylinders precisely and controlling the internal combustion of the diesel engine.
In general, the RP signal can be represented crank angle resolved using the crank shaft position sensor. This crank angle-based representation has a benefit for the fault diagnosis, its high resolution allows it to capture additional information like different pressure oscillations. A deviation of these oscillations can indicate system faults for instance.
The equation to transfer time-based signals into crank angle-based signals is given by:

$$\varphi = t \cdot n_{\text{eng}} \cdot \frac{360}{60}. \tag{4.1}$$

For the following chapters, all representations of HP signals and models are crank angle-based with the engine's crank shaft sensor as an interrupt generator. This means that the HP models were updated with the crank shaft sensor resolution of $\varphi_{\text{cs,res}} = \frac{360}{78} \approx 4.6154°\text{CA}$. This resolution results in the fact that the inductive sensor samples 78 teeth per crank shaft turn.
In contrast to the HP system, the signals and models of the LP system are calculated time-based due to the following two reasons:

- The LPP is independent from the engine speed (crank angle position) because it is electrically driven.
- The communication between the ECU and the LPP is based on a CAN-bus, as described in Sect. 3.3. This implies a very slow signal transmission compared to the synchronous update of the crank angle resolution.

For similar reasons, and since some residuals are calculated in combination of the LP and MP models, the MP system is also represented time-based.

4.2 Physical rail pressure model

The RP in the common rail is modeled by means of a mass flow balance. To define the different mass flows and especially the rail mass flow, the common rail is regarded as a closed system with the rail volume as the system boundary. In this closed system, the HPP increases the rail mass flow, whereas the injectors and the PRV decrease the rail mass flow. Fig. 4.1 illustrates the mass flows into and out of the rail.

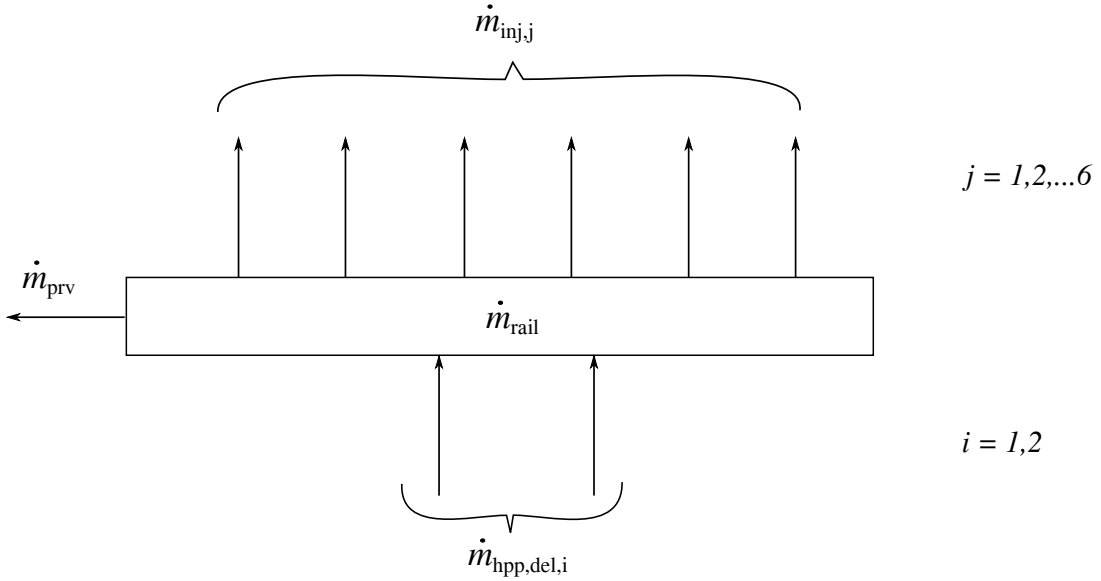

Fig. 4.1: Mass flows into and out of the rail

As shown in Fig. 4.1, the mass balance of the rail system can be developed in the time domain:

$$\frac{\mathrm{d}m_{\mathrm{rail}}}{\mathrm{d}t} = \sum_{i=1}^{2} \dot{m}_{\mathrm{hpp,del},i}(t) - \dot{m}_{\mathrm{prv}}(t) - \sum_{j=1}^{6} \dot{m}_{\mathrm{inj},j}(t). \tag{4.2}$$

The rail mass balance equation (4.2) can also be represented in a crank angle-based domain with a substitution of time. In the following, this will be derived with the help of equation (4.1):

$$\frac{\mathrm{d}\varphi}{\mathrm{d}t} = n_{\mathrm{eng}} \cdot \frac{360}{60}. \tag{4.3}$$

The crank angle-based mass balance equation is then given by:

$$\frac{\mathrm{d}m_{\mathrm{rail}}}{\mathrm{d}\varphi} \cdot \frac{60}{n_{\mathrm{eng}} \cdot 360} = \left(\sum_{i=1}^{2} \frac{\mathrm{d}m_{\mathrm{hpp,del},i}}{\mathrm{d}\varphi} - \frac{\mathrm{d}m_{\mathrm{prv}}}{\mathrm{d}\varphi} - \sum_{j=1}^{6} \frac{\mathrm{d}m_{\mathrm{inj},j}}{\mathrm{d}\varphi} \right) \frac{60}{n_{\mathrm{eng}} \cdot 360} \tag{4.4}$$

and with $m'_{\mathrm{rail}}(\varphi) = \mathrm{d}m_{\mathrm{rail}}/\mathrm{d}\varphi$

$$m'_{\mathrm{rail}}(\varphi) = \sum_{i=1}^{2} m'_{\mathrm{hpp,del},i}(\varphi) - m'_{\mathrm{prv}}(\varphi) - \sum_{j=1}^{6} m'_{\mathrm{inj},j}(\varphi). \tag{4.5}$$

This has the benefit of calculations being independent of the engine speed.
For the rail mass follows

$$m_{\mathrm{rail}} = V_{\mathrm{rail}} \cdot \rho_{\mathrm{rail}} \tag{4.6}$$

where ρ_{rail} is the rail pressure dependent fuel density.

The rail mass flow can then be described with equation (4.6) and the chain rule as rail volume- or density change (see also [70])

$$m'_{\mathrm{rail}}(\varphi) = \frac{\mathrm{d}m_{\mathrm{rail}}}{\mathrm{d}\varphi} = V_{\mathrm{rail}} \cdot \frac{\mathrm{d}\rho_{\mathrm{rail}}}{\mathrm{d}\varphi} + \frac{\mathrm{d}V_{\mathrm{rail}}}{\mathrm{d}\varphi} \cdot \rho_{\mathrm{rail}} = V_{\mathrm{rail}} \cdot \frac{\mathrm{d}\rho_{\mathrm{rail}}}{\mathrm{d}\varphi} \tag{4.7}$$

as the rail volume: $V_{\mathrm{rail}} = const.$

In fuel pressure areas up to 250 MPa, the compressibility module can not be neglected, see [29]. The pressure change caused by the density change can be formulated as

$$\frac{\mathrm{d}p_{\mathrm{rail}}}{\mathrm{d}\varphi} = \frac{\kappa}{\rho_{\mathrm{rail}}} \cdot \frac{\mathrm{d}\rho_{\mathrm{rail}}}{\mathrm{d}\varphi} \tag{4.8}$$

where κ is the compressibility module.

Combining equation (4.7) and (4.8) lead to

$$m'_{\mathrm{rail}}(\varphi) = V_{\mathrm{rail}} \cdot \frac{\mathrm{d}\rho_{\mathrm{rail}}}{\mathrm{d}\varphi} = V_{\mathrm{rail}} \cdot \frac{\rho_{\mathrm{rail}}}{\kappa} \cdot \frac{\mathrm{d}p_{\mathrm{rail}}}{\mathrm{d}\varphi}. \tag{4.9}$$

With the expression of the mass flow equation (4.5) with its corresponding component volume flows it follows with equation (4.6):

$$m'_{\mathrm{rail}}(\varphi) = \sum_{i=1}^{2} V'_{\mathrm{hpp,del},i}(\varphi) \cdot \rho_{\mathrm{rail}} - V'_{\mathrm{prv}}(\varphi) \cdot \rho_{\mathrm{rail}} - \sum_{j=1}^{6} V'_{\mathrm{inj},j}(\varphi) \cdot \rho_{\mathrm{rail}} \tag{4.10}$$

with $V' = \mathrm{d}V/\mathrm{d}\varphi$.

Combining equation (4.9) and (4.10) finally lead to the physical RP change model equation in crank angle-based representation:

$$\begin{aligned} \rho_{\text{rail}} \cdot \frac{V_{\text{rail}}}{\kappa} \cdot \frac{\mathrm{d}p_{\text{rail}}}{\mathrm{d}\varphi} &= \rho_{\text{rail}} \left(\sum_{i=1}^{2} V'_{\text{hpp,del},i}(\varphi) - V'_{\text{prv}}(\varphi) - \sum_{j=1}^{6} V'_{\text{inj},j}(\varphi) \right) \\ \frac{\mathrm{d}p_{\text{rail}}}{\mathrm{d}\varphi} &= \frac{\kappa}{V_{\text{rail}}} \left(\sum_{i=1}^{2} V'_{\text{hpp,del},i}(\varphi) - V'_{\text{prv}}(\varphi) - \sum_{j=1}^{6} V'_{\text{inj},j}(\varphi) \right). \end{aligned} \tag{4.11}$$

Equation (4.11) represents the RP gradient, which can be calculated crank angle-based with the HPP volume flows $\sum_{i=1}^{2} V'_{\text{hpp,del},i}(\varphi)$, the PRV volume flow $V'_{\text{prv}}(\varphi)$ and the injector volume flows $\sum_{j=1}^{6} V'_{\text{inj},j}(\varphi)$.
The following sections now determine the different volume flows per crank-angle $V' = \mathrm{d}V/\mathrm{d}\varphi$ into the rail, see input signals in Fig. 4.2.

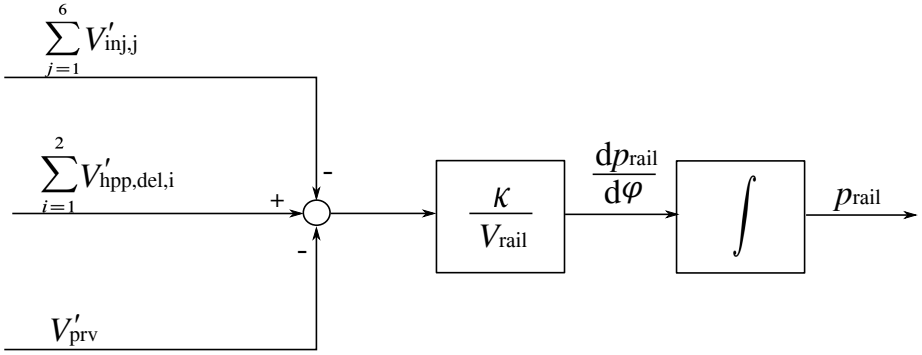

Fig. 4.2: Mass flows into and out of the rail

4.3 High pressure pump volume flow

The general HPP type and functionality is described in Sect. 3.5. As mentioned in Sect. 3.5, the HPP is mechanically driven by the engines crank shaft with a cam-/crankshaft transmission ratio of 1:1. The HPP consists of 2 in-line plunger chambers, each driven by a cam lobe with three profile peaks per lobe phase shifted over 120°CA. The two lobes are fitted with a relative offset of 60°CA to each other on the camshaft.
Furthermore, the HPP fuel quantity control (for HP in-line plunger pumps), calculates a precise amount of fuel to reach a desired RP setpoint. The desired amount of fuel delivered by the HPP for setting a specific RP setpoint is regulated by the Pressure Control Valve (PCV). The PCV start angle ($\varphi_{\text{pcv,sa}}$) defines the closing point where the PCV is activated. For a detailed description see Sect. 3.5.
If the PCV is not active, the in-line plunger chamber is open and the HPP delivers fuel in a fuel circle back-flow to the MP system, which holds true upstream of the plunger. However, if the PCV is activated at a predefined PCV start angle ($\varphi_{\text{pcv,sa}}$), the in-line plunger chamber is closed and the back-flow to the MP system is interrupted. With the upstreaming plunger and the closed

plunger chamber, the cycle of common rail fuel delivery begins. In the following a detailed HPP functionality description is illustrated in Fig. 4.3 in three steps:

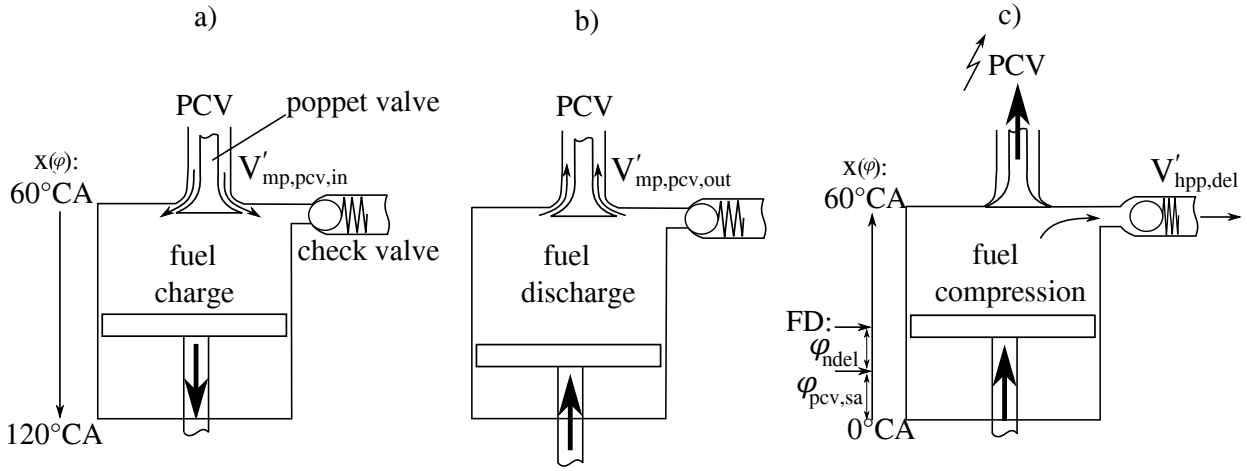

Fig. 4.3: HPP fuel delivery functionality with:
a) Plunger 1 downstream step and the fuel charge of plunger chamber 1.
b) Plunger upstream step without the PCV activation and fuel discharge into MP system.
c) Plunger 1 upstream step with the PCV coil activation for plunger chamber 1 and common rail fuel delivery.

a) **Plunger chamber fuel charge downstream:** In the downstream step of the HP in-line plunger pump, the plunger chamber is charged with fuel due to the open poppet valve. The fuel comes from the MP system where it is pressurized up to 1600 kPa. The chamber is now charged with fuel from the MP system due to the increased inlet volume by the plunger's downward movement. Fig. 4.3 a) visualizes this fuel charge for plunger chamber one with the volume flow $V'_{\mathrm{mp,pcv,in}}(\varphi)$.

b) **Plunger chamber fuel discharge upstream (PCV coil inactive):** This illustration shows the HPP functionality in case of an inactive PCV (no command from the ECU). Upstream of the plunger, the poppet valve spring force is higher than the hydraulic force, which is generated on the poppet valve's bottom surface due to the fuel upstream. Therefore the valve remains open and the plunger discharges the fuel out of the plunger chamber back into the MP system. For the case that the PCV stays inactive the fuel is delivered in a fuel circle. The outgoing volume flow is $V'_{\mathrm{mp,pcv,out}}(\varphi)$, see Fig. 4.3 b).

c) **Common rail Fuel Delivery upstream (PCV coil active):** If the PCV is activated, an electro-mechanical force is generated on the poppet valve by the coil (see Fig. 4.3 c) and Fig. 3.5) in the upstream direction. This force, in combination with the hydraulic force on the poppet valve's bottom surface, exceeds the valve spring force which holds the poppet valve open during the upstream flow. Then the poppet valve closes at a specified PCV start angle ($\varphi_{\mathrm{pcv,sa}}$) and the compression of fuel from the MP to the HP (up to 250MPa) begins.

As the fuel is compressible (see [29]) the Fuel Delivery (FD) into the rail happens later than the $\varphi_{\text{pcv,sa}}$ position when the PCV (poppet valve) closes. The angle between $\varphi_{\text{pcv,sa}}$ and FD is called non-delivery angle $\varphi_{\text{n,del}}$. Finally, the FD to the rail starts when the fuel pressure in the chamber exceeds the actual RP plus the spring opening force of the check valve. In the upstream flow, the poppet valve stays closed due to the high hydraulic pressure on the bottom surface of the valve until the plunger reaches the top dead center. $V'_{\text{hpp,del}}(\varphi)$ is the resulting FD volume flow into the common rail through the check valve, see Fig. 4.3 c). When the plunger has reached the top dead center, the pump cycle is finished and begins again with a).

Fig. 4.4 a) depicts the resulting normalized plunger chamber volume for a crank angle from 0 to 120°CA of chamber 1 and 2 according to the HPP lobes profile (see Fig. 3.5 and Fig. 3.4). Fig. 4.4 b) shows the normalized delivery volume of pump chamber 1. From 0 to 60°CA, the start angle $\varphi_{\text{pcv,sa}}$ and the non-delivery angle φ_{ndel} determine the beginning of fuel delivery into the rail. Fig. 4.4 c) illustrates the normalized volume flow of the HPP plunger chamber 1.

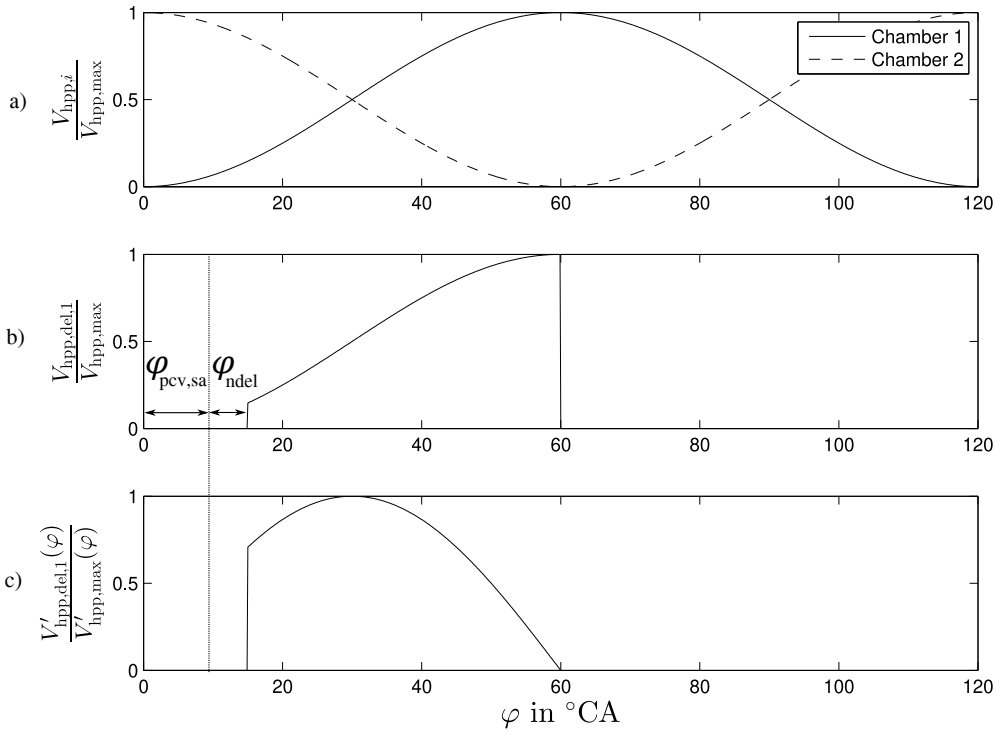

Fig. 4.4: Modelled normalized delivery volume and volume flow of HPP for plunger chamber 1 and 2 for 0 to 120°CA

a) Volume of pump chamber 1 and 2 for 0 to 120°CA, $\varphi_{\text{pcv,sa}} = 0$ and $\varphi_{\text{n,del}} = 0$.

b) Delivery volume of pump chamber 1 for 0 to 120°CA, $\varphi_{\text{pcv,sa}} \neq 0$ and $\varphi_{\text{n,del}} \neq 0$.

c) Delivery volume flow of pump chamber 1 for 0 to 120°CA, $\varphi_{\text{pcv,sa}} \neq 0$ and $\varphi_{\text{n,del}} \neq 0$.

The HPP, with its two in-line plunger pump chambers, two cam lobes on the camshaft, three profile peaks for each lobe and the offset in between the two lobes on the camshaft results in an

alternating common rail fuel delivery of 60°CA if both PCVs are active. Fig. 4.5 depicts the crank angle-based normalized volume in pump chamber 1 and 2 for 360°CA camshaft(crankshaft) turn. The volume flow of both pump chambers for this cycle follows as described in Fig. 4.4, where every 60°CA one pump chamber delivers fuel into the rail.

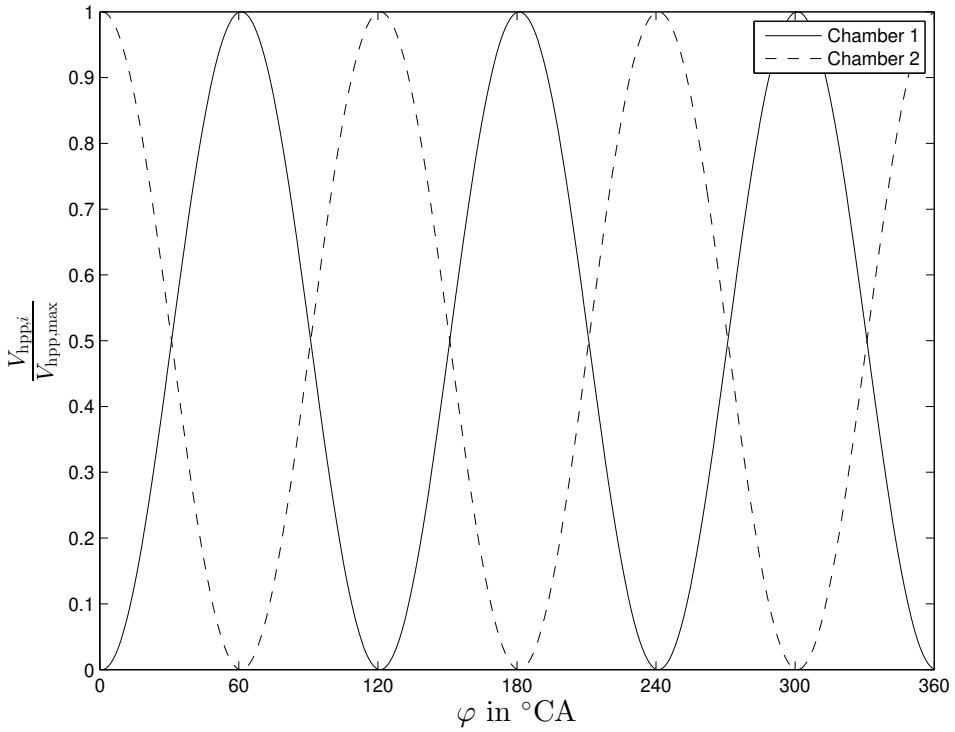

Fig. 4.5: Modelled normalized volume of the HPP for plunger chamber 1 and 2 for one camshaft period 0 to 360°CA for $\varphi_{\mathrm{pcv,sa}} = 0$ and $\varphi_{\mathrm{n,del}} = 0$

The parameters A_{pump} and $x(\varphi)$ are needed to calculate the plunger chamber's volume. A_{pump} is the plunger area and $x(\varphi)$ is the plunger position dependent on the CA position. As illustrated in Fig. 3.5, the maximum volume of one pump chamber can be calculated with the minimum r_2 and maximum r_1 lobes radius:

$$V_{\mathrm{hpp,max}} = A_{\mathrm{pump}} \cdot x_{\mathrm{max}}(\varphi) = A_{\mathrm{pump}} \cdot (r_1 - r_2) \tag{4.12}$$

where the parameters A_{pump}, r_1 and r_2 are provided by the HPP manufacturer.

Volume flow model pump chamber 1

According to [68], the volume dependent on the actual crank angle of one HPP chamber can be approximated with a cosine function if $\varphi_{\mathrm{pcv,sa}} = 0$ and $\varphi_{\mathrm{n,del}} = 0$:

$$V_{\mathrm{hpp},1}(\varphi) = \frac{V_{\mathrm{hpp,max}}}{2}\left(1 - \cos\left(2\pi\frac{\varphi}{T_\varphi}\right)\right) \tag{4.13}$$

where the periodic angle $T_\varphi = 120°\text{CA} = \frac{2\pi}{3}$. The volume flow is then given by the derivative of the volume function (4.13):

$$\frac{\mathrm{d}V_{\mathrm{hpp},1}(\varphi)}{\mathrm{d}\varphi} = V'_{\mathrm{hpp},1}(\varphi) = \frac{V_{\mathrm{hpp,max}}}{2}\left(\frac{2\pi}{T_\varphi}\sin\left(2\pi\frac{\varphi}{T_\varphi}\right)\right). \tag{4.14}$$

As shown in Fig. 4.4, the volume flow depends on the desired start angle $\varphi_{\mathrm{pcv,sa}}$ which is a table-based calculation from the ECU and the non-delivery angle $\varphi_{\mathrm{ndel}}(p_{\mathrm{rail}}(\varphi))$ which is also a table-based function dependent on the fuel RP. The table-based function of the non-delivery angle is estimated empirically on the test bench with the help of the phase delay of the measured common RP increase after the HPP pumping event which starts with the desired start angle $\varphi_{\mathrm{pcv,sa}}$ for different constant RP OPs. The volume flow for one plunger therefore is:

$$V'_{\mathrm{hpp,del},1}(\varphi) = \begin{cases} 0 & \text{for} \quad 0° \le \varphi < \varphi_{\mathrm{pcv,sa}} + \varphi_{\mathrm{ndel}}(p_{\mathrm{rail}}(\varphi)) \\ \dfrac{\pi V_{\mathrm{hpp,max}}}{T_\varphi}\left(\sin\left(2\pi\dfrac{\varphi}{T_\varphi}\right)\right) & \text{for} \quad \varphi_{\mathrm{pcv,sa}} + \varphi_{\mathrm{ndel}}(p_{\mathrm{rail}}(\varphi)) \le \varphi < 60° \\ 0 & \text{for} \quad 60° \le \varphi < 120° \end{cases} \tag{4.15}$$

Volume flow model pump chamber 2

Analogous to model of pump chamber 1, the volume flow model of plunger chamber 2 results in a phase shift of 60°CA caused by the mechanical constructed cam lobes offset from cam lobe 1 (HPP chamber 1) to cam lobe 2 (HPP chamber 2) on the camshaft. Then it follows:

$$V'_{\mathrm{hpp,del},2}(\varphi) = \begin{cases} 0 & \text{for} \quad 0° \le \varphi < 60° + \varphi_{\mathrm{pcv,sa}} + \varphi_{\mathrm{ndel}}(p_{\mathrm{rail}}(\varphi)) \\ \dfrac{\pi V_{\mathrm{hpp,max}}}{T_\varphi}\left(\sin\left(2\pi\dfrac{\varphi}{T_\varphi} + \pi\right)\right) & \text{for} \quad 60° + \varphi_{\mathrm{pcv,sa}} + \varphi_{\mathrm{ndel}}(p_{\mathrm{rail}}(\varphi)) \le \varphi < 120° \end{cases} \tag{4.16}$$

With equation (4.15) and (4.16) the HPP volume flows $\sum_{i=1}^{2} V'_{\mathrm{hpp,del},i}(\varphi)$ for equation (4.11) are calculated.

4.4 Injector volume flow

The diesel engine under consideration has 6 cylinders and therefore 6 injectors, one for each cylinder. Regarding Sect. 3.6 with the function of the G4S injectors, the injector volume flow can be described with a throttle equation with:

$$\dot{V}_{\mathrm{inj}} = \alpha A_{\mathrm{inj}}\sqrt{\frac{2}{\rho_{\mathrm{rail}}}\left(p_{\mathrm{rail}} - p_{\mathrm{air,comp}}\right)} \tag{4.17}$$

where,

α is the discharge coefficient including all losses,
A_{inj} is the injector blind hole area and
ρ_{rail} is the RP fuel density.

For equation (4.17) only the RP p_{rail} and the RP fuel density ρ_{rail} is known. The injection hole area A_{inj}, the discharge coefficient α and the compressed air pressure $p_{\text{air,comp}}$ are unknown variables. Since the dynamic of the injector can not be captured with the crank shaft sensor resolution (see Sect. 4.1), which results in a model update rate of $\Delta\varphi_{\text{cs,res}} = 360/78°\text{CA}$, see Fig. 4.7 additionally the unknown variables must be determined. Therefore a second possibility to calculate the injector volume flow is described.
This second possibility shows a volume flow mean value model developed with the input signals from the ECU: Engine speed n_{eng}, main injection fuel mass m_{mi}, crank angle position φ, the RP p_{rail} and the fuel temperature $T_{\text{lp,f}}$. In order to keep the complexity small, the pilot and post injection fuel mass is included in the main injection fuel mass. Also, the timing of the pilot and post injections is neglected. As it is described in Sect. 3.7, one of the main restrictions of model-based development is that the developed models must work in production engines and therefore use input signals which already exist or can be determined from the engine ECU. This leads to the input signals for an injector volume flow model as shown in Fig. 4.6.

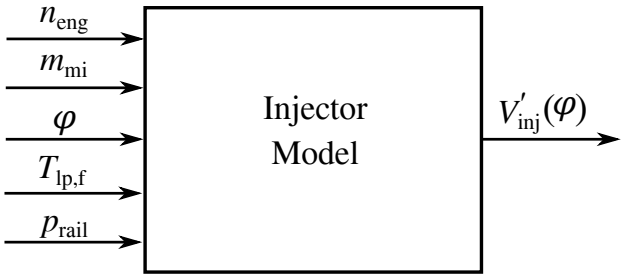

Fig. 4.6: Mean value model for the injector volume flow

The model calculates the volume flow of the injectors with the crank angle-based SOI (φ_{mi}) and the crank angle-based injection duration ($\Delta\varphi_{\text{id}}$) until the EOI ($\varphi_{\text{mi}} + \Delta\varphi_{\text{id}}$) (see Fig. 3.9). The SOI is calculated using a look up table with the engine speed and main injection fuel mass

$$\varphi_{\text{mi}} = f(n_{\text{eng}}, m_{\text{mi}}). \tag{4.18}$$

This is a look up table function resulting from the calibration of the ECU. The injection duration ($\Delta\varphi_{\text{id}}$) is also look up table-based dependent on the actual RP and the main injection fuel mass rounded to full crank shaft resolutions $\Delta\varphi_{\text{cs,res}}$:

$$\Delta\varphi_{\text{id}} = f(m_{\text{mi}}, p_{\text{rail}}, n_{\text{eng}}, \Delta\varphi_{\text{cs,res}}). \tag{4.19}$$

This is because the model is sampled with $\Delta\varphi_{\text{cs,res}}$, see Fig 4.7. The look up table also results from the ECU calibration.

The mean value model of the crank angle-based injector volume flow is formulated with equation (4.6), the main injection mass, the RP fuel density and the injection duration to:

$$V'_{\mathrm{inj}}(\varphi) = \frac{\mathrm{d}V_{\mathrm{inj}}}{\mathrm{d}\varphi} = \begin{cases} \dfrac{m_{\mathrm{mi}}}{\rho_{\mathrm{rail}}(T_{\mathrm{lp,f}},\, p_{\mathrm{rail}}) \cdot \Delta\varphi_{\mathrm{id}}} & \text{for} \quad 0° + \varphi_{\mathrm{mi}} \leq \varphi \leq \varphi_{\mathrm{mi}} + \Delta\varphi_{\mathrm{id}} \\ 0 & \text{for} \quad \varphi_{\mathrm{mi}} + \Delta\varphi_{\mathrm{id}} < \varphi < 120° + \varphi_{\mathrm{mi}} \end{cases} \tag{4.20}$$

Fig. 4.7 a) shows a real crank angle-based injection sequence (injector volume flow) with opening and closing dynamics of an injector according to [28]. Fig. 4.7 b) visualizes an ideal model of the crank angle-based (with the model update rate $\Delta\varphi_{\mathrm{cs,res}}$) injection sequence (developed in equation (4.20)) without any dynamics of the injector. This means that in the model the injector opening and closing delays are not considered, because with the model update rate these dynamics can not be captured (see Fig. 4.7). Furthermore, in the mass balance, equation (4.5), only the exact mass is important for a calculation of the RP without high resolution. It is sufficient to use the main injection mass calculated by the engine's ECU and normalize it over the injection duration. This is done in the injector volume flow model in equation (4.20).
Further on, for the real injection sequence the injector volume flow sharply increases after the opening of the injector (first few crank angle degrees) and then only slowly increases until the closing of the injector, see Fig. 4.7 a). More details on a real injector sequence can be found in [28] and [35].

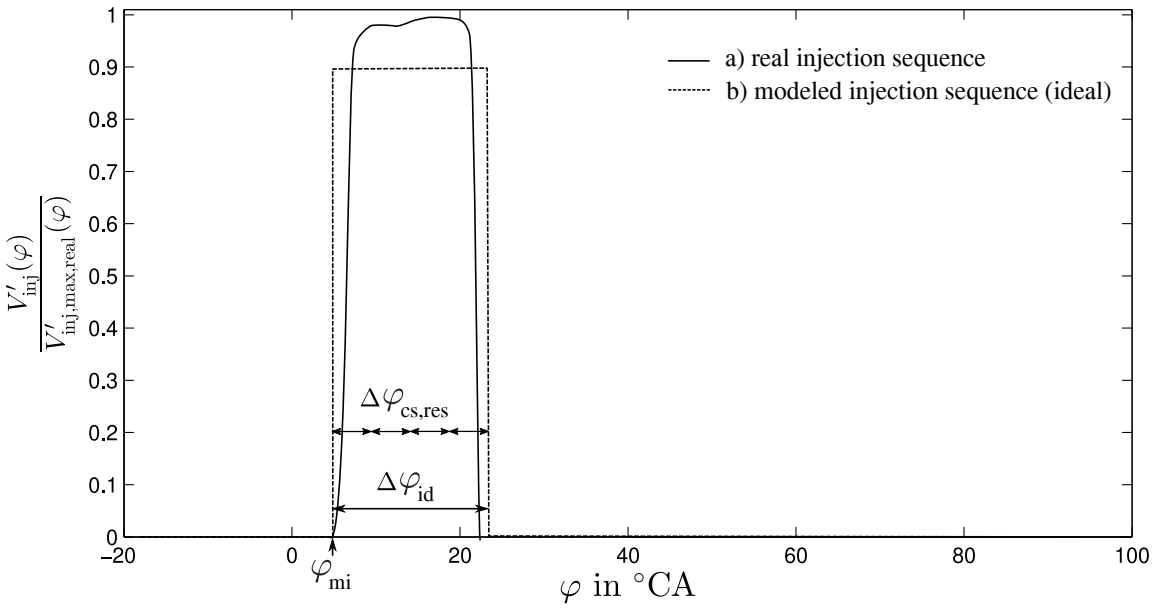

Fig. 4.7: Injection sequence with the injector volume flow for one injector with the assumption m_{mi} =const., p_{rail} =const., $T_{\mathrm{lp,f}}$ =const. and n_{eng} =const. for:
a) The real injection sequence according to [28].
b) The (ideal) modeled injection sequence, see equation (4.20).

Comparing the injection sequences in Fig. 4.7 for a) and b) shows:

- That for both injection sequences the injected mass for one injection cycle is the same, since for both injection sequences an identical enclosed injector volume flow area and an identical fuel density is assumed.
- The injector dynamics is neglected in the developed model b).

The model simulates the volume flow of each injector (6 injectors) and is therefore sequentially repeated every 120°CA over an engine cycle (720°CA). Equation (4.20) is now used for the calculation of the injector volume flow $\sum_{j=1}^{6} V'_{\mathrm{inj},j}(\varphi)$ in equation (4.11).

4.5 Pressure relieve valve volume flow

Analogous to Sect. 4.4, a mean value model for the PRV volume flow from the rail to the tank is developed with the input signals: Engine speed n_{eng}, the HPP discharge mass $m_{\mathrm{prv,disc,q}}$, the crank angle φ, the RP p_{rail} and the fuel temperature $T_{\mathrm{lp,f}}$, see Fig. 3.2.

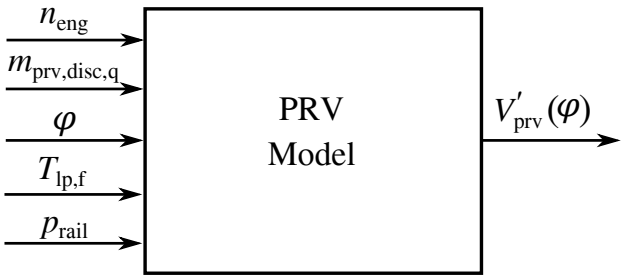

Fig. 4.8: Mean value model for the PRV volume flow

The PRV is an on/off valve that is actuated via a Pulse Width Modulation (PWM) and is fully open when the coil of the PRV is activated. Similar to the injector volume flow model, the crank angle duration of PRV activation is calculated based on a look up table as a function of the RP and the HPP discharge mass rounded to full crank shaft resolutions $\Delta\varphi_{\mathrm{cs,res}}$:

$$\Delta\varphi_{\mathrm{prv,dd}} = f(p_{\mathrm{rail}}, m_{\mathrm{prv,disc,q}}, n_{\mathrm{eng}}, \Delta\varphi_{\mathrm{cs,res}}). \tag{4.21}$$

Analogous to the main injection mass for the injector, the HPP discharge mass is received from the ECU. The PRV discharge duration $\Delta\varphi_{\mathrm{prv,dd}}$ is a function resulting from the calibration of the ECU look up tables. The PRV volume flow model is also dependent on the crank angle and therefore updated with the model sample rate of $\Delta\varphi_{\mathrm{cs,res}}$. The equation is given by:

$$V'_{\mathrm{prv}}(\varphi) = \frac{\mathrm{d}V_{\mathrm{prv}}}{\mathrm{d}\varphi} = \begin{cases} \dfrac{m_{\mathrm{prv,disc,q}}(\varphi)}{\rho_{\mathrm{rail}}(T_{\mathrm{lp,f}}, p_{\mathrm{rail}}) \cdot \Delta\varphi_{\mathrm{prv,dd}}} & \text{for} \quad 0° < \varphi \leq \Delta\varphi_{\mathrm{prv,dd}} \\ 0 & \text{for} \quad \Delta\varphi_{\mathrm{prv,dd}} < \varphi \leq 120° \end{cases} \tag{4.22}$$

Fig. 4.9 shows the PRV volume flow model of equation (4.22) with the assumption of a constant HPP discharge mass.

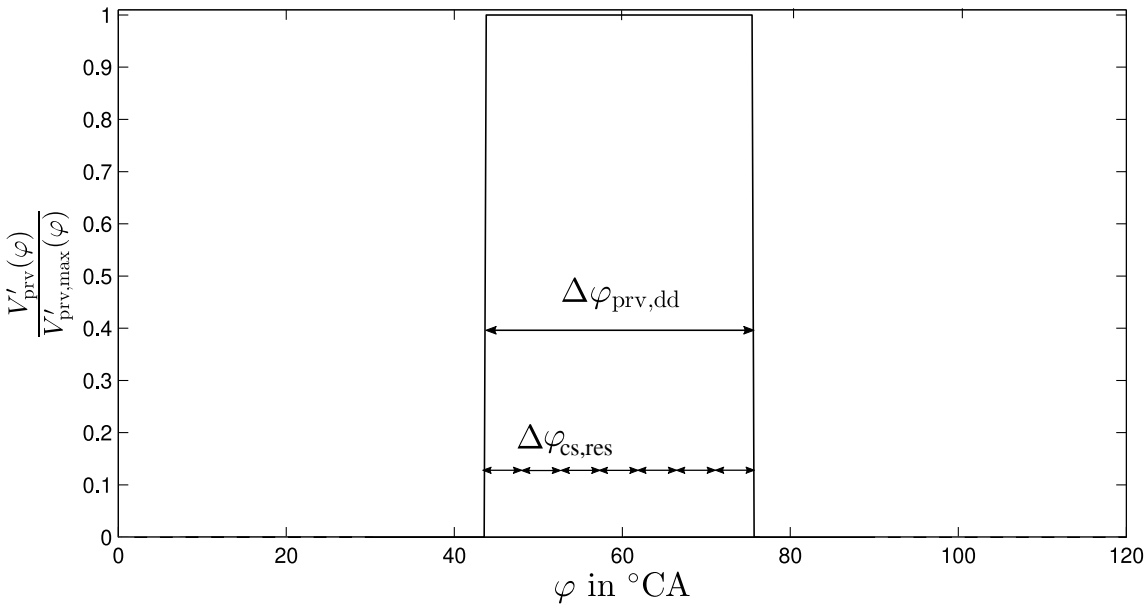

Fig. 4.9: Modelled normalized PRV volume flow with the assumption $m_{\mathrm{prv,disc,q}}$ =const., p_{rail} =const., $T_{\mathrm{lp,f}}$ =const. and n_{eng} =const.

With the developed equations (4.15), (4.16), (4.20) and (4.22) now the RP behavior $\mathrm{d}p_{\mathrm{rail}}/\mathrm{d}\varphi$ according to equation (4.11) and Fig. 4.2 can be determined.

4.6 Simulation of the physical rail pressure model

Fig. 4.10 d) shows the results of the RP model from equation (4.11) integrated over one engine cycle (720°CA). This RP model is calculated with:

- The alternating HPP volume flow models from equation (4.15) and (4.16) (see Fig. 4.10 a)).
- The injector volume flow model equation (4.20) in cylinder firing order (see Fig. 4.10 b)).
- The PRV volume flow model equation (4.22) (see Fig. 4.10 c)).

The simulation parameters chosen for a stationary engine OP are:

$n_{\mathrm{eng}} = 1600$ rpm.
$M_{\mathrm{eng}} = 800$ Nm.
$m_{\mathrm{mi}} = 90$ mg/str.
$p_{\mathrm{rail}} = 233$ MPa.
$\Delta p_{\mathrm{rail,max}} = 6$ MPa.
$m_{\mathrm{prv,disc,q}} = 0$ mg/str.

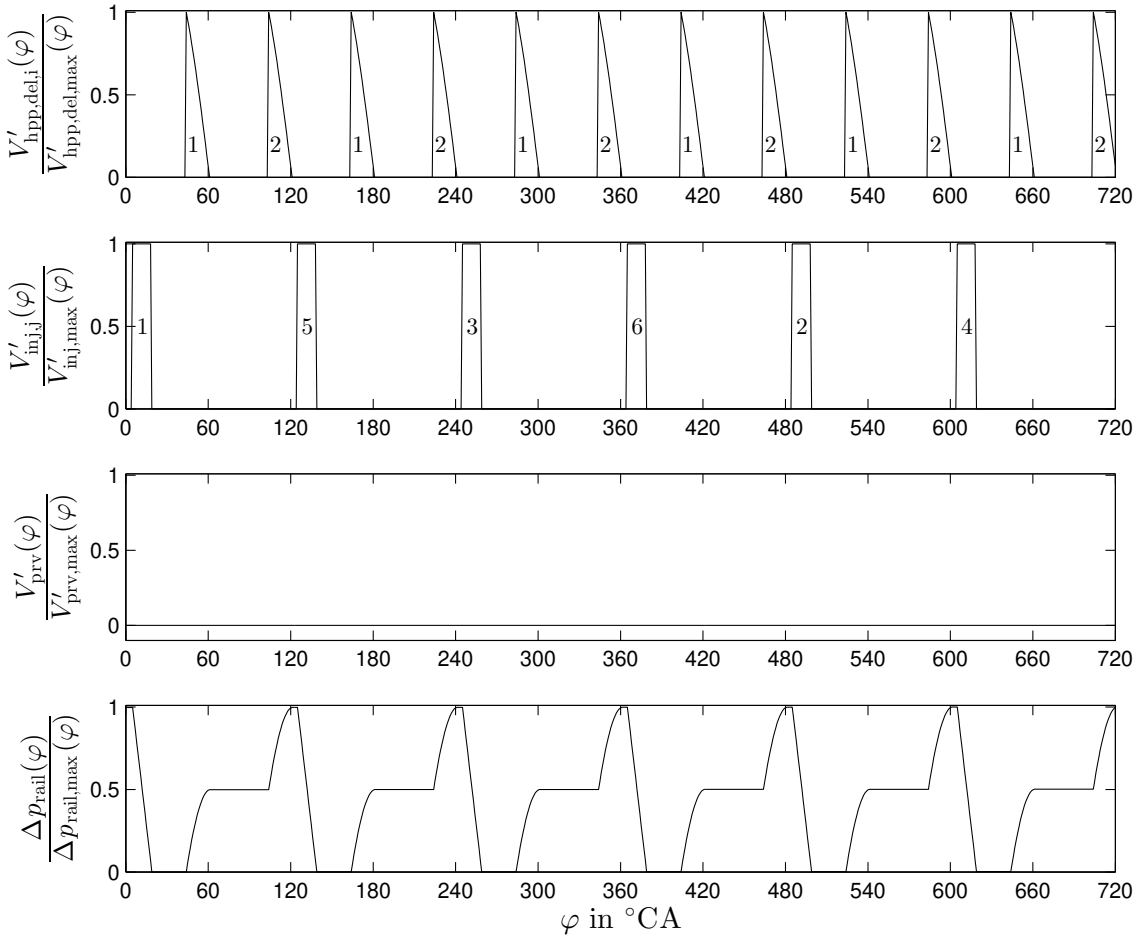

Fig. 4.10: Normalized RP model simulation for engine OP $n_{\mathrm{eng}} = 1600$ rpm and $m_{\mathrm{mi}} = 90$ mg/str with:
a) The alternating HPP volume flow of pump chamber 1 and 2.
b) The injector volume flows in cylinder firing order.
c) The PRV volume flow model.
d) The resulting RP model.

Conclusion for the simulation of the physical rail pressure model

Fig. 4.10 a) visualizes the alternating HPP volume flow behavior of the HPP in-line plunger chambers with a fuel delivery every 60°CA for both pumps and 120°CA for each HPP in-line plunger chamber.

Because the engine OP is stationary the injections shown in Fig. 4.10 b) are equal for every injector. Due to this fact, the HPP volume flow is equal for every HPP cycle. The engine is a six-cylinder engine with six injectors, the injector volume flow visualized in Fig. 4.10 b) shows that the injector volume flow model repeats the injection sequence every 120°CA.

The PRV has no volume flow, see Fig. 4.10 c), which is the result of a stationary engine OP. The PRV only opens if the actual RP compared to the RP setpoint exceeds a predefined limit, which only happens in high dynamical engine OP changes (for high engine OP: big torque or speed value to low engine OP: small torque and speed value). There also has to be a large dynamical engine OP change because the HPP fuel quantity control can compensate small pressure drops with the suspension of fuel delivery.

The RP curve is shown in Fig. 4.10 d) where every 120°CA the HPP increases two times the RP with pumping events and the injector decreases one time the RP due to the injection. Overall the HPP causes the RP angle frequency of 1/60°CA and the injectors the RP angle frequency of 1/120°CA. Finally looking at the RP curve in Fig. 4.10 d) shows that the RP distribution is uniform with the angle period of 120°CA.

4.7 Physical low pressure pump models

4.7.1 LPP displacement volume flow model

The basis of the physical LPP displacement inlet volume flow model is an equation of the LP fuel supply pump as described in Sect. 3.3. First, the LP inlet volume flow is modeled for the outlet of the LPP. For a fault-free case, the secondary fuel filter is neglected and the volume flow location is assumed to be at a position behind the secondary fuel filter and in front of the air bleed valve, see Fig. 3.2.
The pump belongs to the category of displacement pumps. This type of pump is a gerotor pump where the displacement volume is constant and given by [25]:

$$V_{\mathrm{lpp}} = z \cdot (A_{\max} - A_{\min}) \cdot b \tag{4.23}$$

with the tooth width b, the number of the inner teeth z, the maximum $A_{\max}$ and minimum $A_{\min}$ displacement area. All these parameters are provided by the LPP manufacturer. A schematic of the gerotor pump is shown in the Appendix A.2. With the constant displacement volume, the physical LP volume flow is calculated as follow:

$$\dot{V}_{\mathrm{lpp}}(U_{\mathrm{lpp}}, I_{\mathrm{lpp}}, n_{\mathrm{lpp}}) = \frac{V_{\mathrm{lpp}} \cdot n_{\mathrm{lpp}} \cdot \eta_{\mathrm{lpp,vol}}(U_{\mathrm{lpp}}, I_{\mathrm{lpp}}, n_{\mathrm{lpp}})}{60}. \tag{4.24}$$

The volume flow is mainly dependent on the pump speed n_{lpp} and in order to cope with all losses, for example inner leakages or cavitation, a volumetric efficiency $\eta_{\mathrm{lpp,vol}}$ is introduced. This volumetric efficiency is based on a look up table obtained from the LPP manufacturer.

4.7.2 LPP power models

According to [59], the power of a system can be described in different ways. This means, that the physical power equation can be designed with a flow variable multiplied with a potential difference

variable for the electrical, mechanical or hydraulic system.
The LPP is electrically driven, therefore the hierarchy of the LPP is given by:

- LPP DC motor (electrical LPP part) drives a LPP gerotor (mechanical LPP part).
- The LPP gerotor displaces fuel (hydraulic LPP part).

With these facts, the mechanical LPP power model can be derived with an electrical and a hydraulic equation.

Mechanical LPP power model derived with the electrical power

Mechanical power is needed to drive the gerotor in the LPP. This power is provided by a fuel-lubricated brush- and sensor-less DC motor (see [6]). The electrical LPP power model is calculated with the LPP voltage U_{lpp} and current I_{lpp} provided by the ECU:

$$P_{\mathrm{el}}(U_{\mathrm{lpp}}, I_{\mathrm{lpp}}) = U_{\mathrm{lpp}} \cdot I_{\mathrm{lpp}}. \tag{4.25}$$

The ECU receives the LPP current from the pump controller via CAN-bus communication (see [6]). In addition to the volumetric losses introduced in 4.7.1, there are also mechanical losses, for example bearing frictions, which are described with the mechanical efficiency $\eta_{\mathrm{lpp,mech}}$.
The mechanical LPP power model derived by the electrical equation is given by the electrical power (equation (4.25)) and the mechanical efficiency $\eta_{\mathrm{lpp,mech}}$:

$$P_{\mathrm{mech,el}}(U_{\mathrm{lpp}}, I_{\mathrm{lpp}}, n_{\mathrm{lpp}}) = \eta_{\mathrm{lpp,mech}} \cdot P_{\mathrm{el}} = \eta_{\mathrm{lpp,mech}}(U_{\mathrm{lpp}}, I_{\mathrm{lpp}}, n_{\mathrm{lpp}}) \cdot U_{\mathrm{lpp}} \cdot I_{\mathrm{lpp}}. \tag{4.26}$$

Similar to the volumetric efficiency, the mechanical efficiency is also a look up table-based parameter provided by the LPP manufacturer.

Mechanical LPP power model derived with the hydraulic power

The basis of the hydraulic power model is the physical LPP displacement inlet volume flow model as described in Sect. 4.7.1. The hydraulic LPP power model is given by:

$$P_{\mathrm{hyd}}(U_{\mathrm{lpp}}, I_{\mathrm{lpp}}, n_{\mathrm{lpp}}, \Delta p_{\mathrm{lp}}) = \frac{\dot{V}_{\mathrm{lpp}}(U_{\mathrm{lpp}}, I_{\mathrm{lpp}}, n_{\mathrm{lpp}}) \cdot \Delta p_{\mathrm{lp}}}{1000} \tag{4.27}$$

where, Δp_{lp} is the pressure increase from inlet to outlet of the gerotor pump.
The mechanical LPP power model derived by the hydraulic equation is given by the hydraulic power (equation (4.27)) in combination with the pump's volumetric efficiency $\eta_{\mathrm{lpp,vol}}$:

$$P_{\mathrm{mech,hyd}}(U_{\mathrm{lpp}}, I_{\mathrm{lpp}}, n_{\mathrm{lpp}}, \Delta p_{\mathrm{lp}}) = \frac{1}{\eta_{\mathrm{lpp,vol}}} \cdot P_{\mathrm{hyd}} = \frac{\dot{V}_{\mathrm{lpp}}(U_{\mathrm{lpp}}, I_{\mathrm{lpp}}, n_{\mathrm{lpp}}) \cdot \Delta p_{\mathrm{lp}}}{\eta_{\mathrm{lpp,vol}}(U_{\mathrm{lpp}}, I_{\mathrm{lpp}}, n_{\mathrm{lpp}}) \cdot 1000}. \tag{4.28}$$

4.7.3 Low pressure control model

As described in Sect. 3.3 the LP at the inlet of the MPP is closed loop controlled. This complicates the detection of different faults such as filter restrictions, leakages or LP sensor offset faults, because disturbances acting on the LP are compensated by the closed loop control itself. With the development of the LP model $\Delta\hat{p}_{\mathrm{lp}}$, these faults can be detected comparing the LP model to the LP measurement Δp_{lp} , due to the dynamic behavior change of the LP measurement in case of a fault.
The LP model is developed with

$$\Delta\hat{p}_{\mathrm{lp}} = G_{\mathrm{fol}}(z) \cdot \Delta p_{\mathrm{lp,sp}} \tag{4.29}$$

where, $G_{\mathrm{fol}}(z)$ is a discrete transfer function whose parameters are estimated with a Least Squares (LS) algorithm for dynamic systems (for description see Sect. 2.2.1). The transfer function $G_{\mathrm{fol}}(z)$ represents the cascaded LPP control loop, see the gray shaded area in Fig. 4.11. The order of the

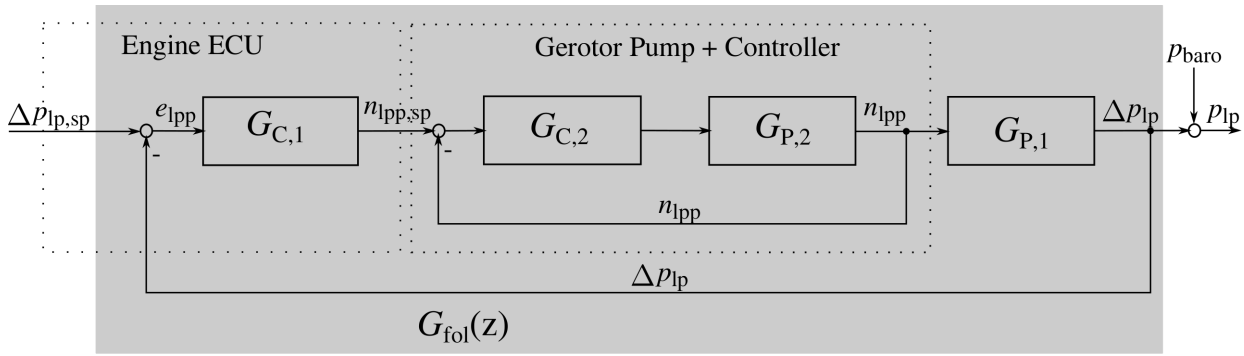

Fig. 4.11: The gray area show the discrete transfer function $G_{\mathrm{fol}}(z)$ for the cascaded LPP closed loop control

transfer function can be determined establishing the equations of the LPP cascaded closed loop:

$$G_{\mathrm{fol}}(z) = \frac{G_{\mathrm{C,1}}(z) \cdot G_{\mathrm{C,2}}(z) \cdot G_{\mathrm{P,2}}(z) \cdot G_{\mathrm{P,1}}(z)}{1 + G_{\mathrm{C,2}}(z) \cdot G_{\mathrm{P,2}}(z) + G_{\mathrm{C,1}}(z) \cdot G_{\mathrm{C,2}}(z) \cdot G_{\mathrm{P,2}}(z) \cdot G_{\mathrm{P,1}}(z)}. \tag{4.30}$$

Equation (4.30) shows that the transfer function has a higher order (dependent on the individual transfer functions in between), but experiments have shown that the modeling of a first order for this transfer function is sufficient.
According to this, the discrete time transfer function of the type equation (2.4) with the desired LP $\Delta p_{\mathrm{lp,sp}}$ as input and the measured LP Δp_{lp} as output is described as a first order system with dead time:

$$G_{\mathrm{fol}}(z) = \frac{\Delta p_{\mathrm{lp}}(z)}{\Delta p_{\mathrm{lp,sp}}(z)} = \frac{\hat{B}(z^{-1})}{\hat{A}(z^{-1})} \cdot z^{-d} = \frac{\hat{b}_1 \cdot z^{-1}}{1 + \hat{a}_1 \cdot z^{-1}} \cdot z^{-d} = \frac{0.0878}{z - 0.9123} \cdot z^{-2}. \tag{4.31}$$

The parameters $\hat{a}_1$ and $\hat{b}_1$ of the transfer function (4.31) are estimated with the LS estimation equation (2.8). The resulting parameters are $\hat{a}_1 = -0.9123$, $\hat{b}_1 = 0.0878$ for a sample time of $T_0 = 0.1\mathrm{s}$. The dead time is the process response time of the measured LP Δp_{lp} output signal

change in case of a changed input signal ($\Delta p_{\mathrm{lp,sp}}$). Dependent on the sample time, the dead time coefficient finally results in $d = 2$.
The accuracy of the first order and thus no need of a second or higher order transfer function can be seen in Fig. 4.12 comparing the b) LP measured with the c) LP model response in case of a) a step signal input.

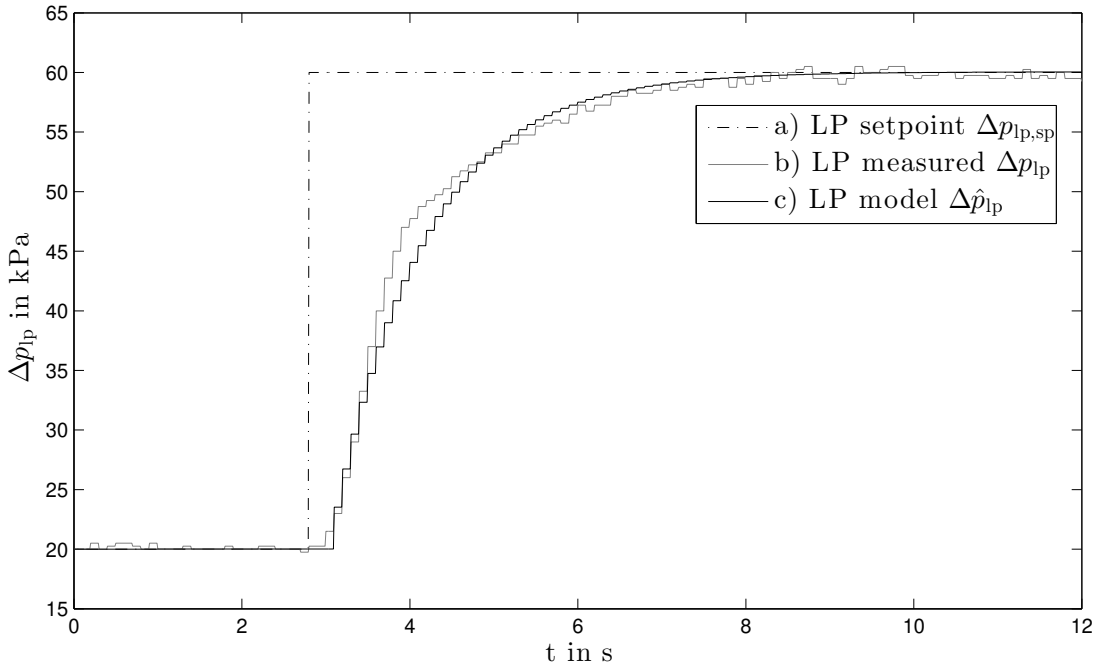

Fig. 4.12: LP signal responses for step input from 20 to 60 kPa with a) LP setpoint signal b) Measured LP and c) LP model

4.8 Physical middle pressure path models

In this section, physical volume flow models of the MP components as well as a semi physical MP model are developed, considering the location of the volume flows of the HP6. The functionality and the inner fuel path architecture with the three pressure areas of the HP6 are already discussed in Sect. 3.4 and 3.5. In Fig. 4.13 this inner fuel path architecture of the HP6 is again visualized. The most important models can be developed by using the mass conservation laws for the volume knots, see Fig. 4.13 a) through d). Since the LP and MP fuel densities are assumed to be constant, the volume flow equations can be derived directly from the mass flow equations. For example with the mass conservation law at the inlet of the MPP, see Fig. 4.13 a), it follows:

$$\dot{V}_{\mathrm{mpp,in}}(n_{\mathrm{eng}}) = \dot{V}_{\mathrm{mp,in}}(n_{\mathrm{eng}}, p_{\mathrm{lp}}, p_{\mathrm{mp}}) + \dot{V}_{\mathrm{mp,rv}}(p_{\mathrm{lp}}, p_{\mathrm{mp}}). \tag{4.32}$$

This provides the physical MP inlet volume flow used for primary, secondary or leakage fault detection in the following chapters. Herewith it holds $p_{\mathrm{lp}} = \Delta p_{\mathrm{lp}} + p_{\mathrm{baro}}$ where p_{baro} is the

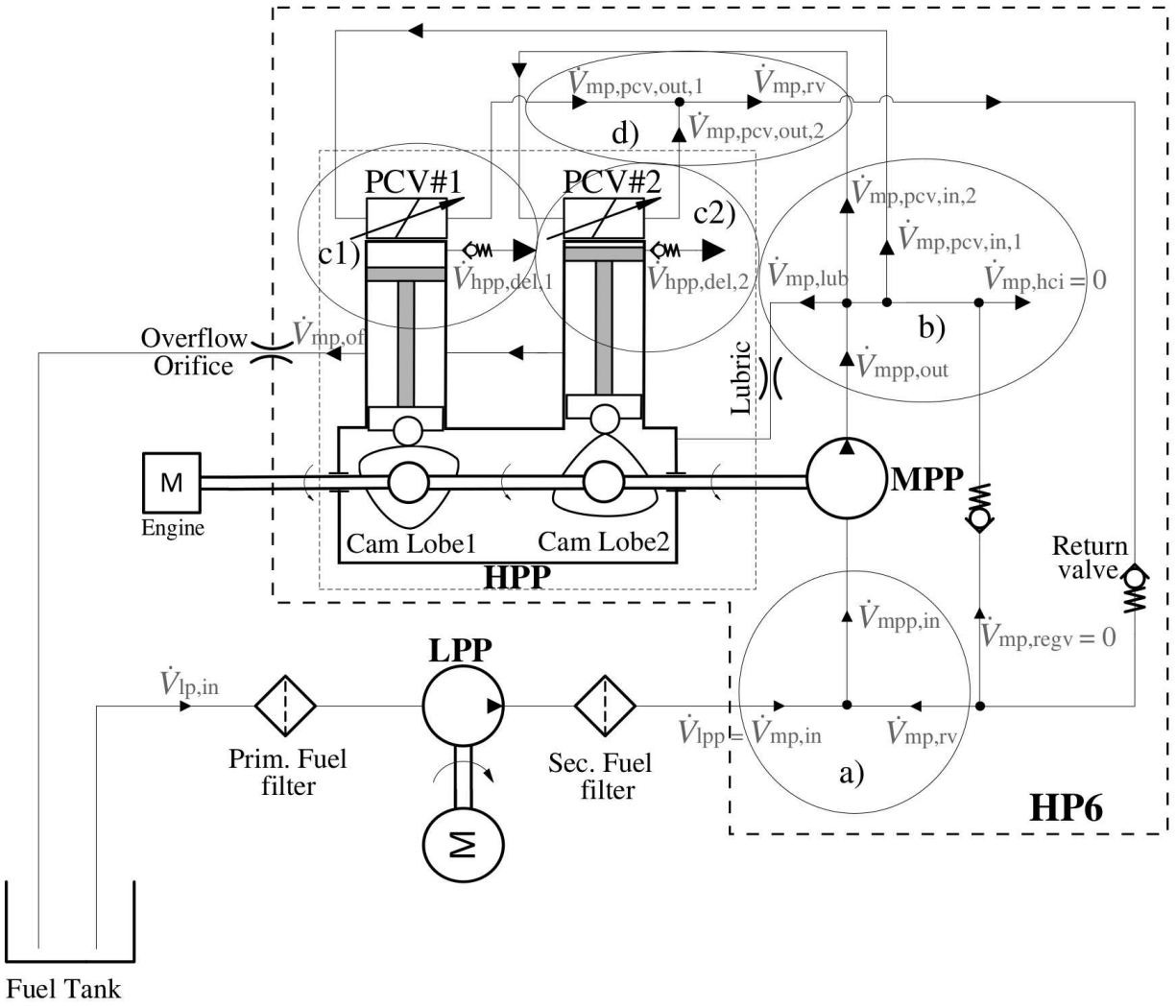

Fig. 4.13: Volume flow paths of the HP6 and LP system including the three pressure domains: Small arrows describe the volume flows for the LP system, medium arrows visualizes the volume flows for the MP system and large arrows show the volume flow for the HP system

environmental pressure measured in the ECU. The same can be applied for the outlet of the MPP, see Fig. 4.13 b):

$$\dot{V}_{\mathrm{mpp,out}}(n_{\mathrm{eng}}) = \dot{V}_{\mathrm{mp,lub}}(p_{\mathrm{lp}}, p_{\mathrm{mp}}) + \sum_{i=1}^{2} \dot{V}_{\mathrm{mp,pcv,in},i}(\varphi_{\mathrm{pcv,sa}}, \varphi_{\mathrm{ndel}}, \varphi) \tag{4.33}$$

where $\dot{V}_{\mathrm{mp,hci}} = 0$ and $\dot{V}_{\mathrm{mp,regv}} = 0$ is assumed. Equation (4.33) can be used for the development of a semi physical MP model. Out of the mass conservation law the inlet volume flow of the HPP pump chambers, see Fig. 4.13 c1), c2) is given by:

$$\sum_{i=1}^{2} \dot{V}_{\mathrm{mp,pcv,in},i} = \sum_{i=1}^{2} \dot{V}_{\mathrm{hpp,del},i} + \sum_{i=1}^{2} \dot{V}_{\mathrm{mp,pcv,out},i} \tag{4.34}$$

and finally the MP return valve volume flow, see Fig. 4.13 d) follows with:

$$\dot{V}_{\mathrm{mp,rv}} = \sum_{i=1}^{2} \dot{V}_{\mathrm{mp,pcv,out},i}\,. \tag{4.35}$$

MPP volume flow model

Analogous to the LPP from Sect. 4.7.1, the MP gerotor pump belongs to the category of volume displacement pumps. But unlike the LP gerotor pump, it is mechanically driven (see Sect. 3.4). According to Sect. 4.7.1, the inlet volume flow of this pump is described by:

$$\dot{V}_{\mathrm{mpp,in}}(n_{\mathrm{eng}}) = \frac{V_{\mathrm{mpp}} \cdot n_{\mathrm{eng}}}{60} \tag{4.36}$$

and the outlet volume flow of the MPP to:

$$\dot{V}_{\mathrm{mpp,out}}(n_{\mathrm{eng}}) = \dot{V}_{\mathrm{mpp,in}}(n_{\mathrm{eng}}) \cdot \eta_{\mathrm{mpp,vol}}(n_{\mathrm{eng}}) = \frac{V_{\mathrm{mpp}} \cdot n_{\mathrm{eng}} \cdot \eta_{\mathrm{mpp,vol}}(n_{\mathrm{eng}})}{60} \tag{4.37}$$

where the efficiency factor $\eta_{\mathrm{mpp,vol}}$ is provided by the MPP pump manufacturer.

Return valve volume flow model

The return valve returns fuel that is not required for the HPP plunger chambers in the fuel circuit, see Fig. 4.13. The volume flow can be developed by means of a throttle equation and a look up table-based coefficient χ_{pos}. The coefficient size depends on the actual pressure difference at the inlet and outlet of the return valve. The volume flow is given by the equation:

$$\dot{V}_{\mathrm{mp,rv}}(p_{\mathrm{lp}}, p_{\mathrm{mp,prev}}) = \alpha_0 A_{\mathrm{mp,rv}} \chi_{\mathrm{pos}}(p_{\mathrm{mp}}, p_{\mathrm{lp}}) \sqrt{\frac{2}{\rho}\left(p_{\mathrm{mp}} - p_{\mathrm{lp}}\right)} \tag{4.38}$$

where,

α_0	is the discharge coefficient,
$A_{\mathrm{mp,rv}}$	is the orifice area of the return valve,
ρ	is the constant fuel density and
χ_{pos}	is the table-based opening position of the return valve.

For this pressure area the fuel density ρ is assumed to be constant. The table-based coefficient χ_{pos} and the discharge coefficient α_0 are gained by a GT-Power fluid simulation and the orifice area of the return valve is given by the MPP manufacturer.

Lubrication volume flow model

The HPP is fuel-lubricated, which is possible because of the good lubrication properties offered by low-sulfur diesel containing chemical additives [22].

The fuel lubrication is realized with an orifice from the MP fuel path to the pump case, see Fig. 4.13. The pressure inside the pump case is assumed to be equal to the LP, since there is a direct connection to the LP system. To retain clarity this is not drawn in Fig. 4.13. Analogous to the return valve and without the ball valve, the volume flow is modeled with the throttle equation to:

$$\dot{V}_{\mathrm{mp,lub}}(p_{\mathrm{lp}}, p_{\mathrm{mp}}) = \alpha_0 A_{\mathrm{mp,lub}} \sqrt{\frac{2}{\rho}\left(p_{\mathrm{mp}} - p_{\mathrm{lp}}\right)} \tag{4.39}$$

where,

α_0	is the discharge coefficient,
$A_{\mathrm{mp,lub}}$	is the lubrication orifice area and
ρ	is the constant fuel density.

Here, the lubrication orifice area is given by the MPP manufacturer.

4.8.1 Semi physical MP model

For the basic equation of the semi physical MP model, the mass conservation equation (4.33) of the inner fuel path architecture is used, see Fig. 4.13 b). The model is denoted as semi physical, because it is derived with the help of a look up table-based opening position angle of the return valve, which is obtained from the GT-Power fluid simulation.
Since the fuel density is assumed to be constant in this pressure area, the volume flow equation can be formulated using the mass flow equations. Furthermore, it is assumed that:

- There are no exhaust gas regeneration injections $\dot{V}_{\mathrm{mp,hci}} = 0$.
- There is no volume flow through the air bleed valve (see Fig. 3.2).
- The pump is not in its initial state $\dot{V}_{\mathrm{mp,regv}} = 0$ (no pre-fueling).
- The pressure of the pump case is equal to the LP.
- The flow coefficients are constant.

The volume flow equations (4.33) to (4.35) lead to:

$$\dot{V}_{\mathrm{mpp,out}}(n_{\mathrm{eng}}) = \dot{V}_{\mathrm{mp,lub}}(p_{\mathrm{lp}}, p_{\mathrm{mp}}) + \dot{V}_{\mathrm{mp,rv}}(p_{\mathrm{lp}}, p_{\mathrm{mp}}) + \sum_{i=1}^{2} \dot{V}_{\mathrm{hpp,del},i}(\varphi_{\mathrm{pcv,sa}}, \varphi_{\mathrm{ndel}}, \varphi). \tag{4.40}$$

The $\sum_{i=1}^{2} \dot{V}_{\mathrm{hpp,del},i}$ is the volume flow delivery of both plunger chambers, which are described by $\mathrm{d}V/\mathrm{d}\varphi$ in equation (4.15), equation (4.16) and transformed by means of equation (4.1) to a time

domain. This is done by an integration of these equations leading to:

$$\sum_{i=1}^{2} V_{\mathrm{hpp,del},i}(\varphi_{\mathrm{pcv,sa}}, \varphi_{\mathrm{ndel}}, \varphi) = \sum_{x=0}^{\lfloor T_{\varphi,\mathrm{int}}/T_\varphi \rceil} \left[\int_{\varphi_{\mathrm{pcv,sa}}+\varphi_{\mathrm{ndel}}+x\cdot T_\varphi}^{T_\varphi(1/2+x)} \frac{\pi V_{\mathrm{hpp,max}}}{T_\varphi} \left(\sin\left(2\pi \frac{\varphi}{T_\varphi} \right) \right) \cdot \mathrm{d}\varphi \right.$$
$$\left. + \int_{T_\varphi(1/2+x)+\varphi_{\mathrm{pcv,sa}}+\varphi_{\mathrm{ndel}}}^{T_\varphi(1+x)} \frac{\pi V_{\mathrm{hpp,max}}}{T_\varphi} \left(\sin\left(2\pi \frac{\varphi}{T_\varphi} + \pi \right) \right) \cdot \mathrm{d}\varphi \right] \tag{4.41}$$

with $T_\varphi = 120°\mathrm{CA}$ and equation (4.1) over $\Delta t_{\mathrm{int}} = 1\mathrm{s}$

$$T_{\varphi,\mathrm{int}} = \Delta\varphi_{\mathrm{int}} = n_{\mathrm{eng}} \cdot \frac{360}{60} \Delta t_{\mathrm{int}} \tag{4.42}$$

and finally a derivation of equation (4.41) with $\Delta t_{\mathrm{int}} = 1\mathrm{s}$ it follows the time-based HPP volume flow:

$$\sum_{i=1}^{2} \dot{V}_{\mathrm{hpp,del},i}(\varphi_{\mathrm{pcv,sa}}, \varphi_{\mathrm{ndel}}, \varphi) = \frac{\sum_{i=1}^{2} V_{\mathrm{hpp,del},i}(\varphi_{\mathrm{pcv,sa}}, \varphi_{\mathrm{ndel}}, \varphi)}{\Delta t_{\mathrm{int}}}. \tag{4.43}$$

With the basic volume flow equation (4.40), equations (4.37) to (4.39) and equation (4.43) it follows:

$$\dot{V}_{\mathrm{mpp,out}}(n_{\mathrm{eng}}) = \alpha_0 A_{\mathrm{mp,lub}} \sqrt{\frac{2}{\rho}\left(p_{\mathrm{mp}} - p_{\mathrm{lp}}\right)} + \alpha_0 A_{\mathrm{mp,rv}} \chi_{\mathrm{pos}}(p_{\mathrm{mp,prev}}, p_{\mathrm{lp}}) \sqrt{\frac{2}{\rho}\left(p_{\mathrm{mp}} - p_{\mathrm{lp}}\right)}$$
$$+ \sum_{i=1}^{2} \dot{V}_{\mathrm{hpp,del},i}(\varphi_{\mathrm{pcv,sa}}, \varphi_{\mathrm{ndel}}, \varphi) \tag{4.44}$$

transformed to

$$\sqrt{\frac{2}{\rho}\left(p_{\mathrm{mp}} - p_{\mathrm{lp}}\right)} \alpha_0 \left(A_{\mathrm{mp,lub}} + A_{\mathrm{mp,rv}} \chi_{\mathrm{pos}} \right) = \dot{V}_{\mathrm{mpp,out}}(n_{\mathrm{eng}}) - \sum_{i=1}^{2} \dot{V}_{\mathrm{hpp,del},i}(\varphi_{\mathrm{pcv,sa}}, \varphi_{\mathrm{ndel}}, \varphi) \tag{4.45}$$

which is further transformed to

$$\sqrt{\frac{2}{\rho}\left(p_{\mathrm{mp}} - p_{\mathrm{lp}}\right)} = \frac{\dot{V}_{\mathrm{mpp,out}}(n_{\mathrm{eng}}) - \sum_{i=1}^{2} \dot{V}_{\mathrm{hpp,del},i}(\varphi_{\mathrm{pcv,sa}}, \varphi_{\mathrm{ndel}}, \varphi)}{\alpha_0 \left(A_{\mathrm{mp,lub}} + A_{\mathrm{mp,rv}} \chi_{\mathrm{pos}}(p_{\mathrm{mp,prev}}, p_{\mathrm{lp}}) \right)}. \tag{4.46}$$

Finally the semi physical MP model is developed by solving for p_{mp} :

$$p_{\mathrm{mp}}(\varphi, \varphi_{\mathrm{ndel}}, \varphi_{\mathrm{pcv,sa}}, p_{\mathrm{lp}}, n_{\mathrm{eng}}) = \left(\frac{\dot{V}_{\mathrm{mpp,out}}(n_{\mathrm{eng}}) - \sum_{i=1}^{2} \dot{V}_{\mathrm{hpp,del},i}(\varphi_{\mathrm{pcv,sa}}, \varphi_{\mathrm{ndel}}, \varphi)}{\alpha_0 \left(A_{\mathrm{mp,lub}} + A_{\mathrm{mp,rv}} \chi_{\mathrm{pos}}(p_{\mathrm{mp,prev}}, p_{\mathrm{lp}}) \right)} \right)^2 \frac{\rho}{2} + p_{\mathrm{lp}}. \tag{4.47}$$

4.8.2 Physical MP inlet volume flow model

As shown in Fig. 4.13, the volume flows for the outlet of the LPP and the inlet of the MP system (HP6) have the same volume flow ($\dot{V}_{\mathrm{lpp}} = \dot{V}_{\mathrm{mp,in}}$) if the volume flow through the air bleed valve is neglected. Especially with different propulsions of both pumps (MPP mechanically and LPP electrically driven), it is possible to develop the same volume flow first with a MP volume flow and secondly with the LPP volume flow. It follows that:

- For the LP system, this volume flow can be described with the gerotor pump model ($\dot{V}_{\mathrm{lpp}}$) of the LPP.
- The mass conservation law leads to the inlet mass flow of the MP system. Assuming that the fuel density is constant due to the MP fuel incompressibility, the MP inlet mass flow can then be directly converted to a MP inlet volume flow. The MP inlet volume flow ($\dot{V}_{\mathrm{mp,in}}$) can further be described with the help of the return valve model ($\dot{V}_{\mathrm{mp,rv}}$) and the MPP inlet volume flow model ($\dot{V}_{\mathrm{mpp,in}}$), see Fig. 4.13 a).

With equation (4.36) for the MPP inlet volume flow model, equation (4.38) for the return valve volume flow model, the semi physical MP model equation (4.47) and the MPP inlet volume flow (from mass conservation law) equation (4.32) the physical MP volume flow equation is given by:

$$\dot{V}_{\mathrm{mp,in}}(n_{\mathrm{eng}}, p_{\mathrm{lp}}, p_{\mathrm{mp}}) = \dot{V}_{\mathrm{mpp,in}}(n_{\mathrm{eng}}) - \dot{V}_{\mathrm{mp,rv}}(p_{\mathrm{lp}}, p_{\mathrm{mp}}). \tag{4.48}$$

Both volume flows ($\dot{V}_{\mathrm{lpp}}$ and $\dot{V}_{\mathrm{mp,in}}$) can then be used to observe a proper system functionality by the design of a parity equation with a redundant model.

4.9 Overall signal flow diagram of the LP, MP and HP models

The overall signal flow diagram of the developed LP, MP and HP models is shown in Fig. 4.14 with the input signals from the engine ECU and the resulting model output signals used for the process model-based residual generation in Chap. 6. These residuals gained from the physical system modeling are further used for the fault isolation in the following Chap. 7.

4.10 Summary

In this chapter, the physical equations for the fuel system were developed. These models are required for the following process model-based fault detection algorithms. Due to the different drives, the LP system is presented by using a time-based and the HP system by using a crank angle-based representation.
For the HP system, a physical RP model was introduced on the basis of a mass flow balance with the main components: The HPP- , the injector- and the PRV volume flows. A simulation of the

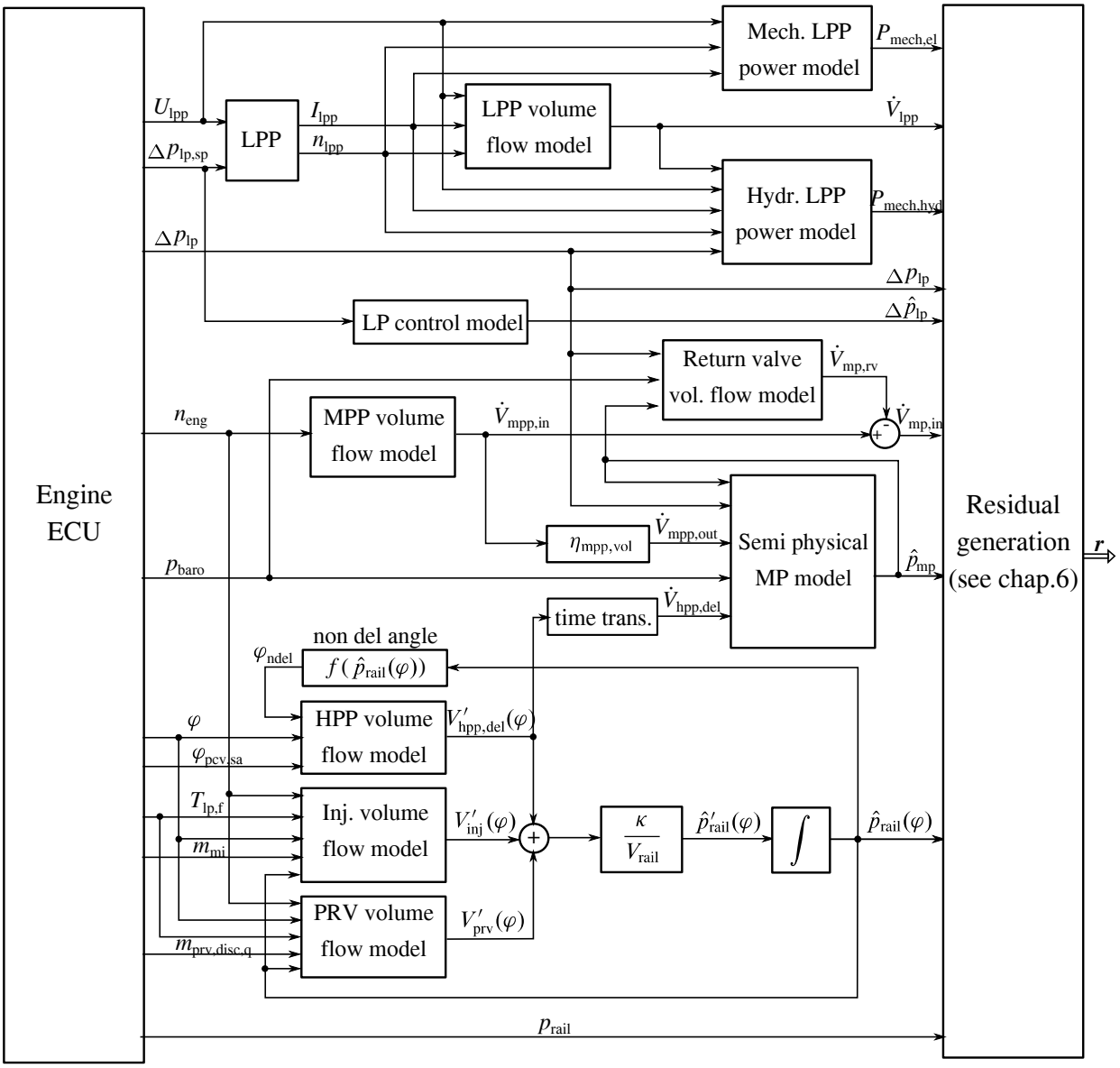

Fig. 4.14: Signal flow diagram of the developed LP, MP and HP models with input signals from the ECU and resulting model signals which are used for the Residual generation

RP with these volume flows was shown. Especially the representation of the RP model is crank angle-based in order to capture injector and HPP faults due to their fast crank angle synchronous activation.

For the MP and LP system, the equations for the LPP displacement volume flow model, the LPP power model, the LP model, the semi physical MP model and the MP inlet volume flow were derived. The overall signal flow diagram in Fig. 4.14 for the LP, MP and HP models gives an overview of the engine ECU input signals and the modeled output signals used for the following process model-based fault detection.

5 Signal analysis of the common rail pressure and the exhaust manifold pressure

The HPP and the injectors cause oscillations in the common rail and the combustion of fuel causes oscillations in the exhaust manifold. In the following sections, Rail Pressure (RP) and Exhaust Manifold Pressure (EMP) signals are analyzed and the pressure oscillation frequencies for these system components are shown in a fault-free and a faulty state. The analyzed frequencies are the basis for the signal model-based fault detection. To visualize the RP oscillation frequencies, different test run scenarios are analyzed using a FFT of the RP Signal. Such test scenarios are considered for the case, that the HPP is active, the HPP and injector operate in normal state, one HP plunger chamber has a fault and one injector has a fault. For a FFT analysis of the exhaust pressure oscillations, test runs with a fault-free state and an injector fault state show the frequencies of the exhaust pressure oscillations. Additionally, two different signal model-based fault detection approaches are discussed, a fault detection with the help of a FFT and a fault detection with the help of an uniformity analysis. Finally, the RP signal characteristics for a multiple and equal HPP fuel delivery to fuel injection frequency are discussed.

5.1 Rail pressure sensor signal analysis

The RP sensor signal has a special oscillating characteristic which can be attributed to the discontinuous fuel delivery and injections. The HPP is 1:1 gear driven by the crank shaft, whereas the cam shaft contains two lobes, with each lobe having three profile peaks with the pump itself having two plunger chambers (see Sect. 3.5). Additionally, the cam lobe mounting position of the pump chamber one is designed with an offset of 60°CA to the cam lobe of pump chamber two. As a result, this constellation causes discontinuous fuel deliveries every $360°\text{CA} \div (2 \cdot 3) = 60°\text{CA}$. The 6 injectors themselves have discontinuous fuel injections which add an additional signal characteristic every $720°\text{CA} \div 6 = 120°\text{CA}$. In the following paragraph, these signal characteristics are investigated with different test runs.

The first case shows the oscillations caused by the HPP. Therefore, only the HPP is active without any fuel injections. To guarantee an HPP fuel delivery, a continuous fuel flow out of the rail has to be generated. This is achieved by an HP leakage on the side feed tube of the injectors which allows fuel flow through the cylinder head back to the fuel tank. In detail, these side feed tubes in combination with fuel lines are the connection between the common rail and the injectors. The fuel lines are mounted to the common rail and the side feed tubes are mounted to the fuel lines on one side and on the other side to the cylinder head. Finally, the side feed tubes are, due to

the installation on the cylinder head, pressed with a side connection to the injector's openings for supplying fuel to these injectors (note that these pressed connections work because the injectors are also mounted on the cylinder head). The engine dyno with its water brake (see attachment A.1) can only decelerate the engine. This implies that the test case, where only the HPP fuel delivery is active and no fuel injections occur, can only be achieved in an engine overrun state.

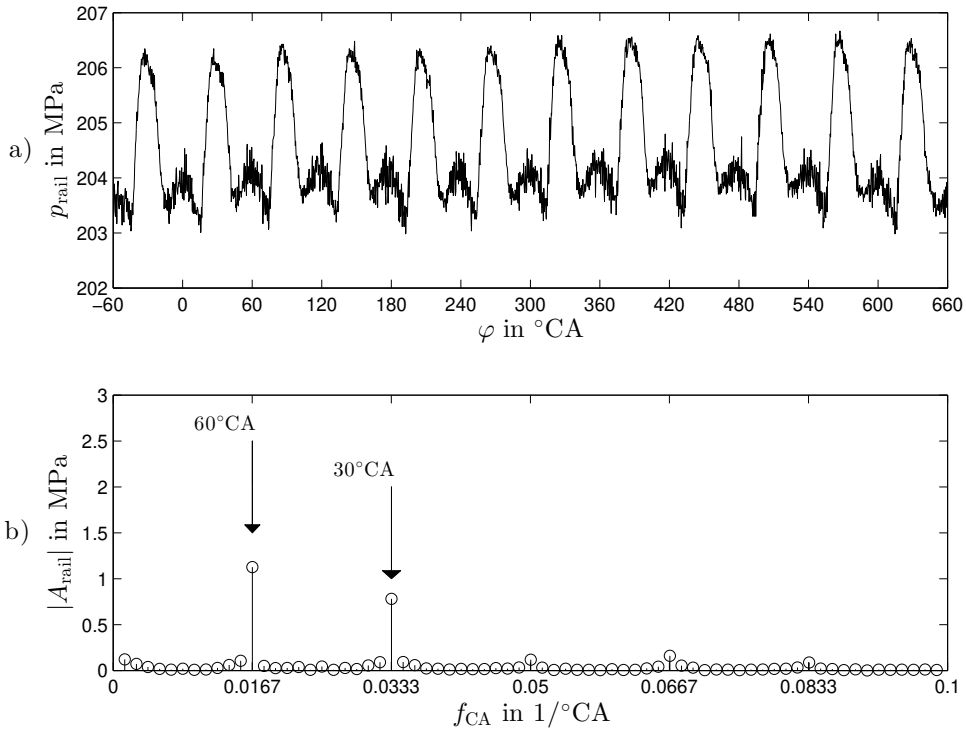

Fig. 5.1: HPP only active, no fuel injections (OP: $n_{\mathrm{eng}} \approx 1200$ rpm, $m_{\mathrm{mi}} = 166$ mg/str) with:
a) Measured RP signal.
b) Amplitude spectrum calculated with FFT of the measured RP signal.

In Fig. 5.1 a) the RP signal for the above described case, with only the HPP activity, is shown. Note that the engine speed decreases in the overrun state, but is assumed to be nearly constant for one engine cycle as the energy storage of the large mass of the drive train nearly maintains the engine speed. Therefore in Fig. 5.1 the shown RP is only a small section captured at about $n_{\mathrm{eng}} \approx 1200$rpm of the whole overrun state. It can clearly be seen that the HPP has a discontinuous fuel delivery every 60°CA which causes a RP rise at every pumping event. The main HPP period

$$\tau_{\mathrm{hpp,main}} = 60°\mathrm{CA} \tag{5.1}$$

is shown in the RP amplitude spectrum, as depicted in Fig. 5.1 b). It is calculated with a FFT analysis of the RP signal (see Sect. 2.3.1). Also the first order higher harmonic of the HPP $\tau_{\mathrm{hpp,h1}} = 30°\mathrm{CA}$ occurs in the RP amplitude spectrum. This first harmonic is caused by the discontinuous fuel delivery of both pump chambers.

The second test case shows the engine in a fault-free state. The HPP and the injectors operate in normal condition with no HP leakage. An OP with $n_{\mathrm{eng}} = 1600$ rpm and $M_{\mathrm{eng}} = 800$ Nm is

chosen because the injectors have only main injections in this case. In Fig. 5.2 the RP signal and

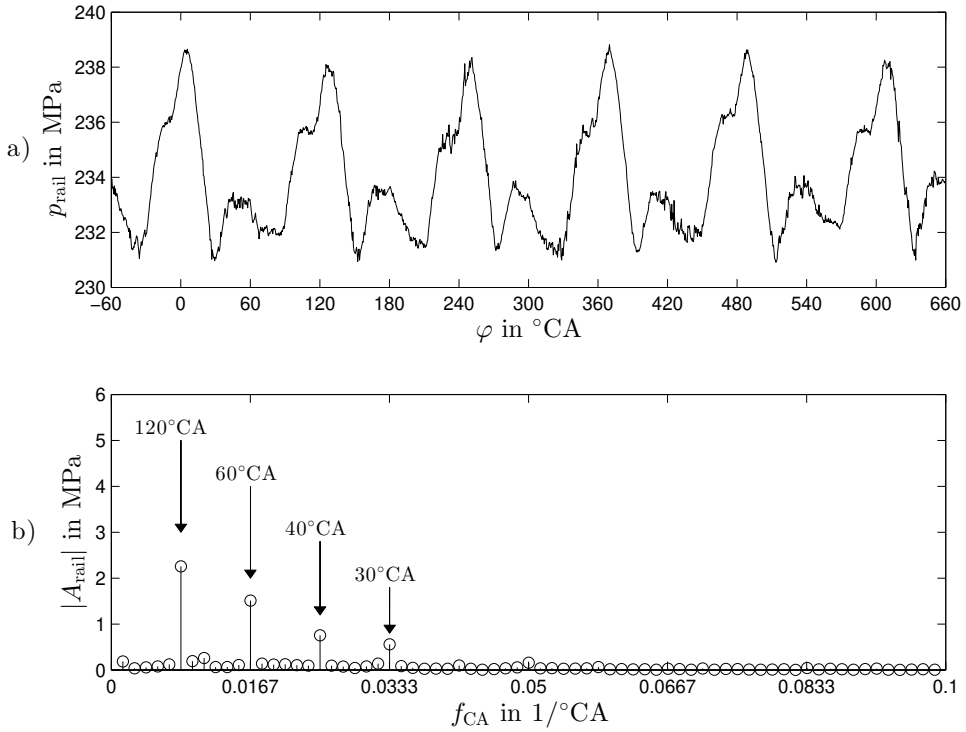

Fig. 5.2: Normal fault-free state, HPP and injectors active (OP: $n_{\text{eng}} = 1600$ rpm, $M_{\text{brake}} = 798$ Nm, $m_{\text{mi}} = 93\text{mg/str}$) with:
a) Measured RP signal.
b) Amplitude spectrum calculated with FFT of the measured RP signal.

the RP amplitude spectrum for a fault-free state is visualized, where the HPP and the injectors are active. The RP signal shows two pressure increases caused by both HPP plunger chamber elements. Now the RP signal doesn't decrease after the first pumping event, because due to the injection timing there is no fuel mass flow out of the system. This corresponds to equation (4.2) with $m_{\text{inj}} = 0$. The timing of the second pumping event overlaps with the timing of injection. This results in a pressure decrease due to the start of injection and therefore the fuel mass flow out of the rail. In Fig. 5.2 b), the amplitude spectrum shows the frequencies of the RP signal. The main amplitude for the injections is now

$$\tau_{\text{inj,main}} = 120°\text{CA}, \tag{5.2}$$

whereas the HPP period is the same as for the first test scenario $\tau_{\text{hpp,main}} = 60°\text{CA}$. Compared to the first test case, the amplitude of 60°CA increase caused by the super imposed main amplitude of the HPP with the first harmonic of the injector $\tau_{\text{inj,h1}} = 60°\text{CA}$. Furthermore, a second harmonic of the injections which is given by $\tau_{\text{inj,h2}} = 120°/3 = 40°\text{CA}$ can be observed.

Table 5.1 shows the RP amplitude spectrum for the HPP and the injectors in a fault-free state.

In the third test case, an HPP fault is implemented with a disconnected power supply of one PCV. Apart from this, all other conditions are the same as in the second test scenario. This means that

Table 5.1: RP amplitude spectrum for HPP and injectors in a fault-free state

Main HPP angle period:	60°CA
1st harmonic of HPP:	30°CA
Main injector angle period:	120°CA
1st harmonic of inject.:	60°CA
2nd harmonic of inject.:	40°CA

one HPP plunger chamber element is pumping fuel in the fuel circuit and not into the rail (for details see Sect. 4.3). The analysis of Fig. 5.3 b) compared to the fault-free state in Fig. 5.2 b) shows the increase of the 120°CA period in the amplitude spectrum. The HPP is now supplying

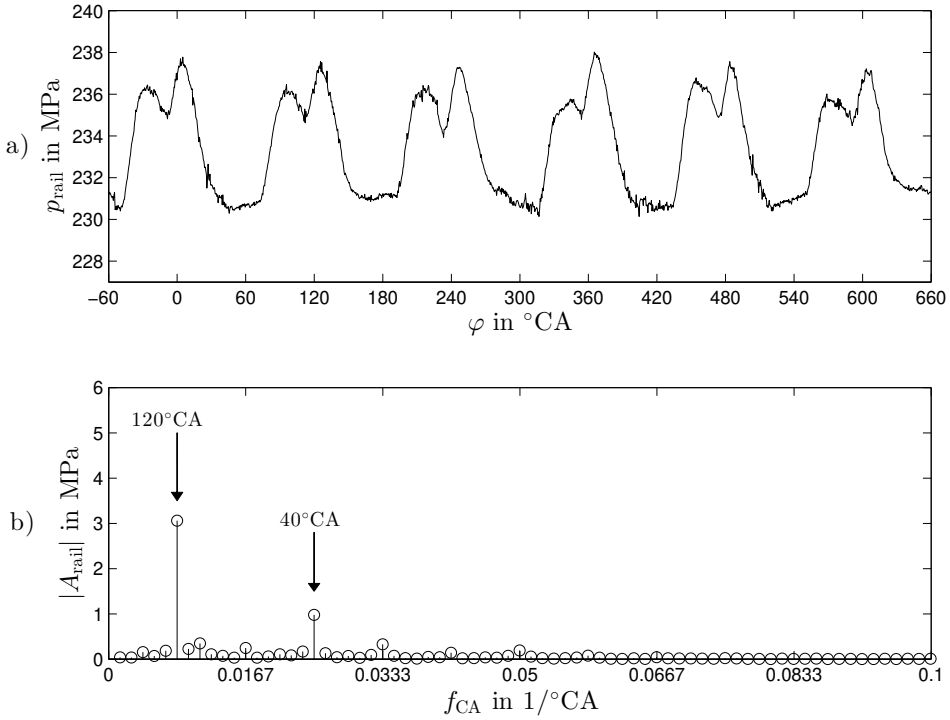

Fig. 5.3: PCV HPP fault, one plunger doesn't deliver fuel (OP: $n_{\mathrm{eng}} = 1600$ rpm, $M_{\mathrm{brake}} = 801$ Nm, $m_{\mathrm{mi}} = 94$ mg/str) with:
a) Measured RP signal.
b) Amplitude spectrum calculated with FFT of the measured RP signal.

every 120°CA fuel into the rail, instead of every 60°CA. The reason for this is the missing pumping event of the disconnected power supply of one PCV. Additionally, the insufficient fuel delivery from the faulted chamber is compensated by the HPP fuel quantity control which adjusts the fuel delivery in the healthy pump chamber. This results in the amplitudes of the injector and the HPP frequencies at 120°CA to overlap.
In Fig. 5.3 a) there is also a small pressure decrease in the pumping event, which is caused by overlapping injection during fuel delivery. This in combination with a harmonic of the occurred 120°CA causes an additional angle period of 40°CA. Finally, the second HPP period which occurs

in a faulty case of one HPP element is equal to the main injector period:

$$\tau_{\text{hpp,sec}} = 120°\text{CA}. \tag{5.3}$$

Table 5.2 shows the RP amplitude spectrum for an HPP fault, when one plunger doesn't supply fuel.

Table 5.2: RP amplitude spectrum for HPP fault

Second HPP angle period:	120°CA
2nd harmonic of HPP:	40°CA
Main injector angle period:	120°CA
2nd harmonic of inject.:	40°CA

In the fourth case, an injector fault in injector 1 with 40% less fuel mass quantity is implemented. All other conditions are equal to the fault-free state in the second test scenario. Compared to

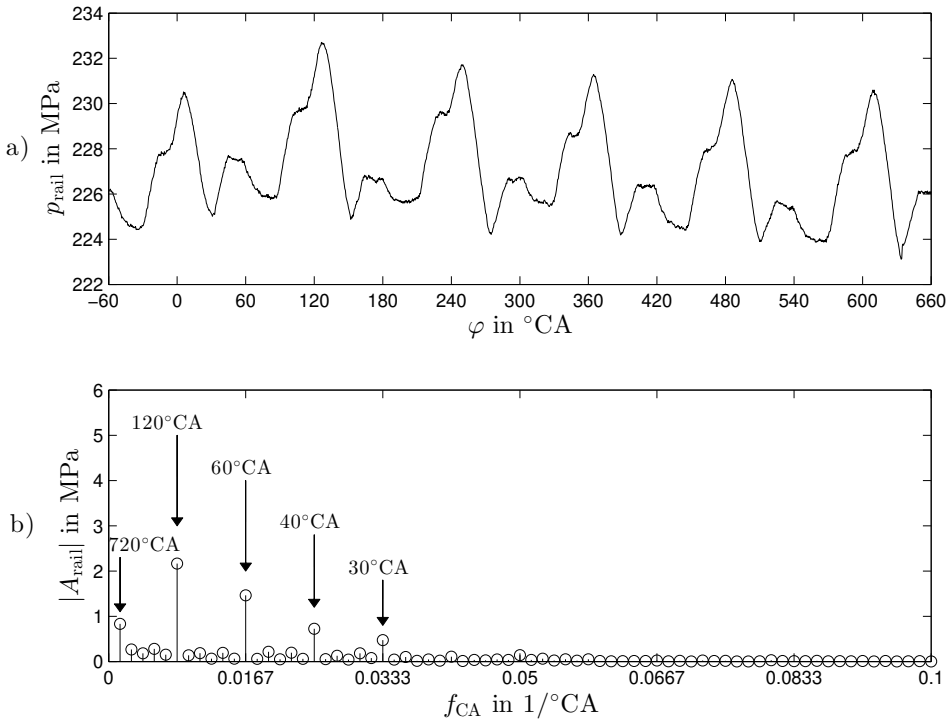

Fig. 5.4: Injector 1 fault (40% less fuel quantity, OP: $n_{\text{eng}} = 1600$ rpm, $M_{\text{brake}} = 804$ Nm, $m_{\text{mi}} = 101$ mg/str) with:
a) Measured RP signal.
b) Amplitude spectrum calculated with FFT of the measured RP signal.

Fig. 5.2, Fig. 5.4 shows the same RP behavior with the exception of an additional frequency which occurs due to the faulted injector. This frequency has the angle period of 720°CA which is visualized in the amplitude spectrum of the RP signal in Fig. 5.4 b). This means that one injector

fault results in a period of 720°CA:

$$\tau_{\text{inj,sec}} = 720°\text{CA}. \tag{5.4}$$

Table 5.3 shows the RP amplitude spectrum for an injector fault, injector 1 with 40% less fuel mass flow.

Table 5.3: RP amplitude spectrum for an injector fault

Main HPP angle period:	60°CA
1st harmonic of HPP:	30°CA
Second injector angle period	720°CA
Main injector angle period:	120°CA
1st harmonic of inject.:	60°CA
2nd harmonic of inject.:	40°CA

Summary of rail pressure signal analysis

For the shown OP, an injector fault can be detected with the occurrence of a second injector angle period of $\tau_{\text{inj,sec}} = 720°\text{CA}$, see Table 5.3 in comparison to Table 5.1. Furthermore, for the shown OP an HPP fault can be detected with the vanished main HPP angle period $\tau_{\text{hpp,main}} = 60°\text{CA}$, the vanished first harmonic of the HPP $\tau_{\text{hpp,h1}} = 30°\text{CA}$ and the increased amplitude at 120°CA as well as 40°CA, see Table 5.2 compared to Table 5.1. The RP amplitudes and the occurring frequencies are OP dependent, the reasons for this dependency along with a possible solution will be discussed in Sect. 5.3.

Finally, the figures show that all relevant signal angle frequencies, which are equal or higher than $\frac{1}{30°\text{CA}}$, should be captured. This means that with the Shannon theorem (see [18]) frequencies up to $\frac{1}{15°\text{CA}}$, or higher, should be sampled to represent the required frequencies.

The results for the recorded RP tests and their frequency occurrences are shown in Table 5.4.

Table 5.4: RP frequency occurrences for recorded tests

Test	720°CA	120°CA	60°CA	40°CA	30°CA
HPP only active			x		x
Fault-free (or misfire fault)		x	x	x	x
HPP fault (PCV unplugged)		x		x	
Injector 1 fault	x	x	x	x	x

5.2 Exhaust manifold pressure sensor signal analysis

[52] investigated misfire detection using a FFT analysis of the EMP in the time domain for a gasoline engine. Further investigations of misfire detection in heavy duty diesel engines were made by [37] with an amplitude check of the EMP signal.

Analogous to the previous section, the EMP signal is also analyzed with a FFT in a crank angle synchronous representation. The EMP signal characteristic is shown in Fig. 5.5 a). Over one en-

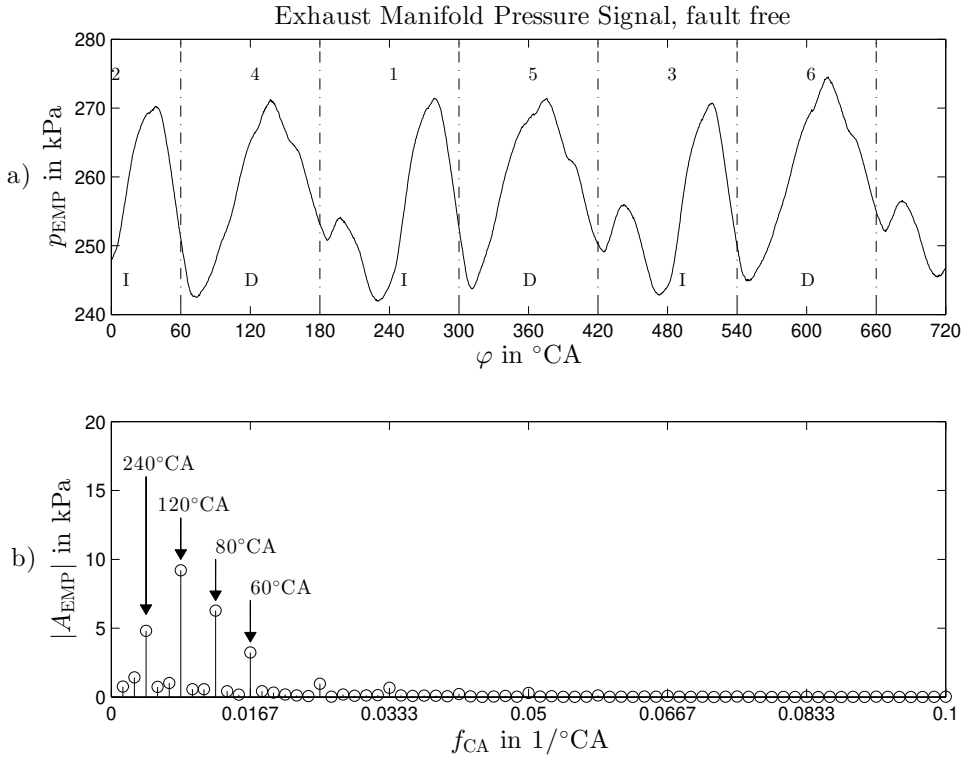

Fig. 5.5: EMP signal fault-free (OP: $n_{eng} = 1600$ rpm, $M_{brake} = 798$ Nm, $m_{mi} = 93$ mg/str) with:
a) Measured exhaust pressure signal.
b) Amplitude spectrum calculated with FFT of the measured exhaust pressure signal.

gine cycle (720°CA) there are 6 pressure oscillations due to the combustion sequence. This results in a basic angle period of:

$$\tau_{cyl,main} = 120°CA. \tag{5.5}$$

Furthermore, the signal shows 3 identical pressure oscillations phase shifted by 240°CA (see Fig. 5.5 a) twice, where the interval is labeled as D for Direct and as I for Indirect pressure waves. This pressure oscillation characteristic results due to:

- The EMP sensor location.
- The separated exhaust manifolds for cylinder 1,2,3 and 4,5,6.

- The injection sequence (cylinder firing order) which is 1-5-3-6-2-4 (see Sect. 3.1).

Fig. 5.6 visualizes the geometry of the exhaust manifold. Therefore the directly measured EMP waves are shown in Fig. 5.5 a) with D in the intervals for cylinder:

$$\text{Cyl}: \quad 4, 5, 6 \qquad \text{at} \qquad \Delta\varphi_{\text{D},4}\,[60°... 180°],\ \Delta\varphi_{\text{D},5}\,[300°... 420°],\ \Delta\varphi_{\text{D},6}\,[540°... 660°]$$

and indirectly measured EMP waves with I in the intervals for cylinder:

$$\text{Cyl}: \quad 1, 2, 3 \qquad \text{at} \qquad \Delta\varphi_{\text{I},1}\,[180°... 300°],\ \Delta\varphi_{\text{I},2}\,[660°... 60°],\ \Delta\varphi_{\text{I},3}\,[420°... 540°]$$

In Fig. 5.5 a), the cylinder firing order is labeled with the upper index and the direct and indirect

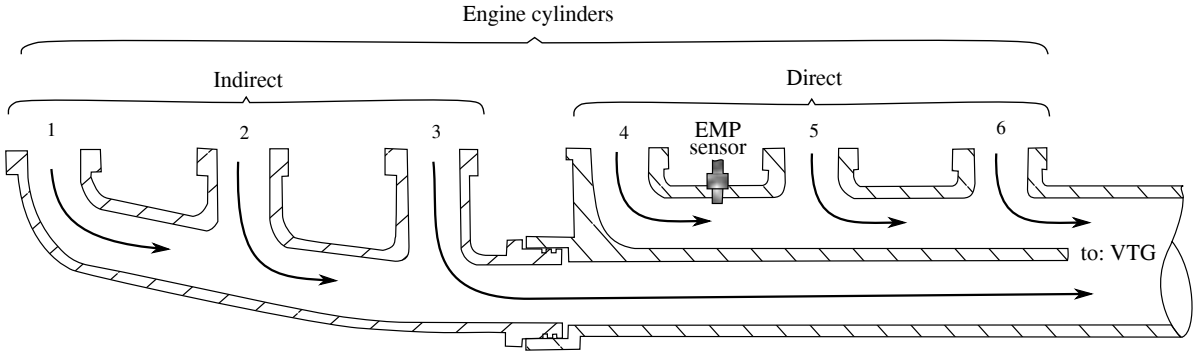

Fig. 5.6: Exhaust manifold geometry with EMP sensor position

EMP waves with the lower index. As it can be seen in Fig. 5.5 a) and the interval $\sum_{j=4}^{6} \Delta\varphi_{\text{D,j}}$ the direct pressure waves repeat every 240°CA. The same applies for the indirect pressure waves. This direct and indirect pressure oscillations at the EMP sensor in combination with the cylinder firing order induces a signal periodicity over 240°CA. With the signal periodicity, due to the EMP sensor location, it follows the geometrical angle period:

$$\tau_{\text{geom,main}} = 240°\text{CA}. \tag{5.6}$$

The spectrum of the EMP frequencies is visualized in Fig. 5.5 b). Table 5.5 shows the EMP amplitude spectrum for a fault-free case. Here the first harmonic of the EMP geometry angle

Table 5.5: EMP amplitude spectrum for the fault-free case

Main EMP angle period:	120°CA
1st harmonic of EMP:	60°CA
Main EMP geometry angle period	240°CA
1st harmonic of geom.:	120°CA
2nd harmonic of geom.:	80°CA

period is 120°CA and the second harmonic is 80°CA.

If now an injector fault occurs, similar angle period changes can be observed in Fig. 5.7 b) compared to Fig. 5.4 b) in the amplitude of 720°CA (see also Table 5.6 and Table 5.3). The changed

combustion, due to less fuel injection from one injector, results in an EMP decrease for cylinder 1 (see EMP signal in Fig. 5.7 a) in the interval $\Delta\varphi_{\mathrm{I},1}$). The injector fault (less fuel quantity injected) has a similar behavior on the EMP signal as a compression loss of the intake air which results in an engine cylinder misfire fault. The results of cylinder misfire faults will be shown in the following chapters.

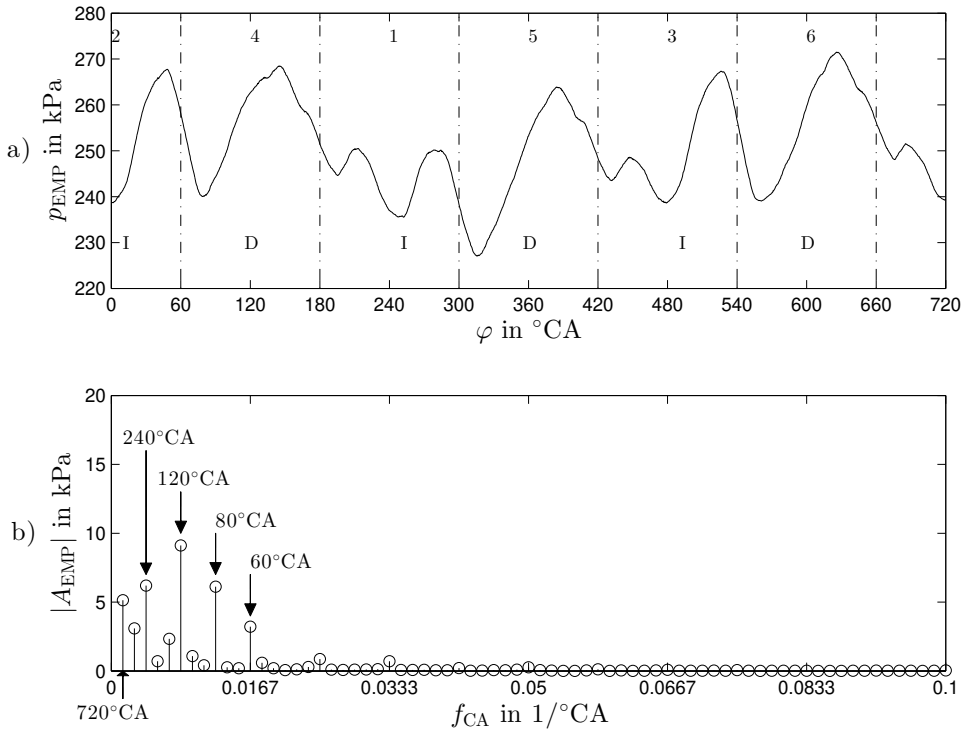

Fig. 5.7: EMP signal with injector 1 fault (40% less fuel quantity, OP: $n_{\mathrm{eng}} = 1600$ rpm, $M_{\mathrm{brake}} = 804$ Nm, $m_{\mathrm{mi}} = 101$ mg/str) with:
a) Measured exhaust pressure signal.
b) Amplitude spectrum calculated with FFT of the measured exhaust pressure signal.

Table 5.6 shows the EMP amplitude spectrum for a injector 1 fault (40% less fuel quantity).

Table 5.6: EMP amplitude spectrum for an injector fault or a cylinder misfire fault

Second EMP angle period (misfire)	720°CA
Main EMP angle period:	120°CA
1st harmonic of misfire:	60°CA
Main EMP geometry angle period	240°CA
1st harmonic of geom.:	120°CA
2nd harmonic of geom.:	80°CA

Summary of EMP signal analysis

With the observation of the EMP signal, either a single injector fuel quantity or a single cylinder misfire fault can be detected with the occurrence of the second cylinder misfire angle period of

720°CA (see Table 5.6 compared to Table 5.5). The root cause of a single cylinder misfire fault could be insufficient compression in one cylinder, due to wrong valve clearance or piston ring wear for instance.
By observing the occurrence of an angle period of 720°CA for the RP, as well as the EMP signal, the isolation between a misfire and injector fault can be performed. This is because in the case of a misfire, only the EMP signal is influenced. This means, that in the case of a misfire fault the angle period of 720°CA will occur for the EMP signal, whereas it won't occur in the RP signal. While comparing Table 5.7 with Table 5.4 the angle period of 720°CA will occur for an injector fault in both signals (EMP as well as RP).

The final results for the recorded EMP tests and their frequency occurrences are shown in Table 5.7.

Table 5.7: EMP frequency occurrences for recorded tests

Test	720°CA	240°CA	120°CA	80°CA	60°CA
Fault-free		x	x	x	x
Injector 1 fault (or misfire fault)	x	x	x	x	x

5.3 Fast Fourier Transformation

The FFT is an effective method to visualize the frequency components of an observed signal. In the current work, it is advantageous to represent the FFT in a crank angle synchronous domain since the occurring frequencies can be directly allocated to the mechanical functionality frequencies of the fuel system, independent of the engine speed. In Sect. 5.1, it can be seen that different oscillation periods occur or vanish with an injector fault or an HPP fault. With an online calculation of the FFT, these faults can be detected by comparing the actual calculated amplitude spectrum against an amplitude spectrum stored in a fault-free state. Fig. 5.8 demonstrates this implementation.

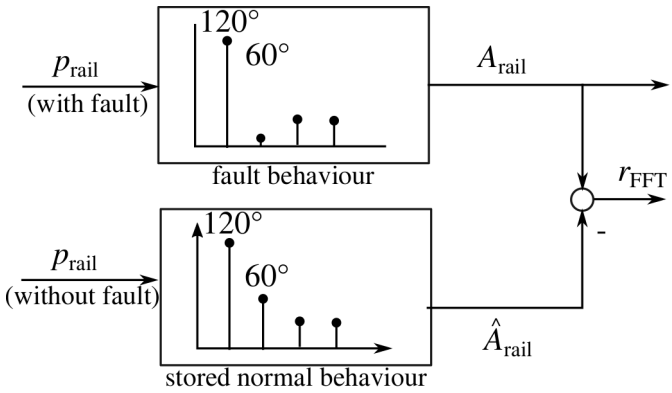

Fig. 5.8: FFT residual

As described in Sect. 5.1, an injector fault can be detected by observing the occurrence of the 720°CA amplitude (see Table 5.3 compared to Table 5.1). In addition, comparing the amplitude spectrums of Fig. 5.3 b) and 5.2 b), a pump fault can be detected by monitoring a missing 60°CA amplitude and it's harmonic 30°CA (see Table 5.2 compared to Table 5.1). Both are valid for the OP shown in Sect. 5.1.

The amplitude of the frequency components is strongly OP dependent. One of the most important elements which causes this OP dependency is the highly variable closing angle called PCV start angle (see Sect. 4.3) that is used to vary the amount of fuel delivery into the rail depending on the actual engine OP. This is a typical characteristic of an outlet metered pump system. As a result, the calibration for the fault-free FFT reference data must be done for different engine OPs. There are two ways to cope with this issue:

- Generate and store different fault-free reference data over the whole engine OP range (application).
- Allocate different subspaces which classify the online calculated data. This could be accomplished with a machine learning approach called Support Vector Machines (SVM) [50] which has the benefit of reducing manual application. For this work a short investigation has been done in [82].

Furthermore, the FFT is very sensitive to system noise such as a periodic RP sensor voltage increase caused by an insufficient injector electro-magnetic compatibility (i.e. high injector currents induce additional voltages in the RP sensor). This sensitivity to system noise, increased evaluation effort and a high degree of online calculation is a challenge for the FFT implementation. The uniformity analysis requires less computations. This approach is discussed in the next section.

5.4 Uniformity residual calculation

The uniformity residual can be calculated with the basis equation (2.12). As described in Sect. 2.10, a periodic signal can be observed to monitor its periodicity. This condition is fulfilled if equation (2.12) is equal to 0. However, to reduce noise effects, the mean value is calculated and the residual is represented in a crank angle domain. According to [67], the equation is given by:

$$r_{\mathrm{u}} = \frac{1}{\tau_{\mathrm{u}}} \int_{\varphi}^{\varphi+\tau_{\mathrm{u}}} [y(\varphi) - y(\varphi - \tau_{\mathrm{s}})]\,\mathrm{d}\varphi \tag{5.7}$$

with

r_{u} uniformity residual,
τ_{u} angle period for mean value generation and
τ_{s} supervised angle period.

5.5 RP signal characteristics for a multiple and equal HPP fuel delivery frequency to fuel injection frequency

In this section the periodicity of the RP signal over the angle period $\tau_{\text{eng,cycl}} = 720°\text{CA}$ of one engine cycle is investigated with a RP simulation for the fault-free case. Here the HPP fuel delivery frequency is a multiple ($1/60°\text{CA}$) or an equal ($1/120°\text{CA}$) fuel injection frequency. This RP signal characteristic description will be essential for the injector fault isolation, which is discussed in Sect. 7.2.1. It is furthermore shown how the RP signal characteristics change for both frequencies in case of an HPP fault (i.e. one elements does not supply fuel):

- **HPP fuel delivery frequency is a multiple integer of the fuel injection frequency** $f_{\text{inj,main}} = \frac{1}{120°\text{CA}}$, where the HPP delivers fuel with a harmonic frequency (multiple integer x) of the fuel injection frequency $f_{\text{hpp,main}} = f_{\text{inj,main}} \cdot x$. This is the case for the investigated system, where $f_{\text{hpp,main}} = \frac{1}{\tau_{\text{hpp,main}}} = \frac{1}{60°\text{CA}}$ and therefore $x = 2$. In an HPP fault case, where one plunger chamber does not supply fuel, the healthy chamber (activation of the HPP closed loop fuel quantity control) will compensate this fault by delivering the double amount of fuel. For the investigated system with its specific fuel system design, the second HPP period lines up with the main injector period $\tau_{\text{inj,main}} = \tau_{\text{hpp,sec}} = 120°\text{CA}$ (see Sect. 5.1). Fig. 5.9 illustrates a simulated RP signal derived by an integration of equation (4.11) similar to Sect. 4.6. The RP characteristics (oscillations) caused by the HPP fuel delivery are shown for a) a fault-free case and b) fault in chamber 1. It can be seen that, in a fault-free

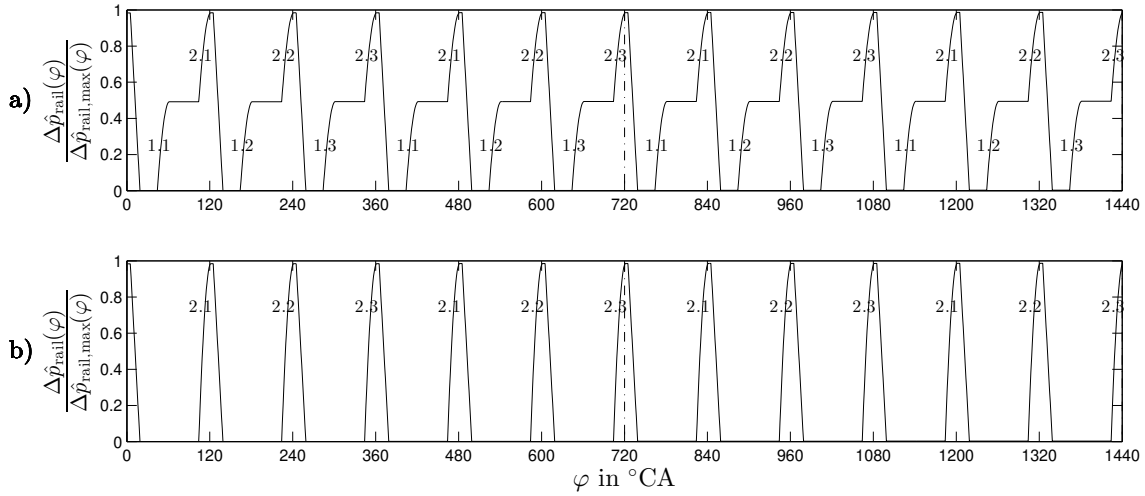

Fig. 5.9: Simulated RP oscillation signal for a multiple HPP fuel delivery frequency to fuel injection frequency with:
a) A fault-free case (the first number in the upper index show the pump element and the second number show the actual profile peak. The same holds true for the lower index).
b) HPP fault in chamber 1, where RP oscillations caused by pump chamber 2 are visualized.

case and in an HPP fault case, the RP signal remains periodic over the engine cycle period

of 720°CA as well as over the period of 120°CA (injector main period). However, the HPP fuel delivery imprints a stepwise RP increase for the fault-free case, see Fig. 5.9 a).

- **HPP fuel delivery frequency is equal to the fuel injection frequency**
  $f_{\text{hpp,main}} = f_{\text{inj,main}}$, where the HPP delivers fuel with an equal frequency of the fuel injection frequency. Similar to the first case the system also uses two HPP chambers to supply fuel into the rail, but with the difference that the HPP delivery frequency is halved. In the case of an HPP fault it is obvious, that due to this design the HPP fuel delivery frequency is halved which results in a doubled angle period $\tau_{\text{inj,main}} \neq \tau_{\text{hpp,sec}} = 2 \cdot \tau_{\text{inj,main}} = 240°\text{CA}$. Similar to the previous case Fig. 5.10 illustrates the simulated RP signal characteristics (oscillation) caused by the HPP fuel delivery in a) a fault-free case and b) a fault in chamber 1. For an

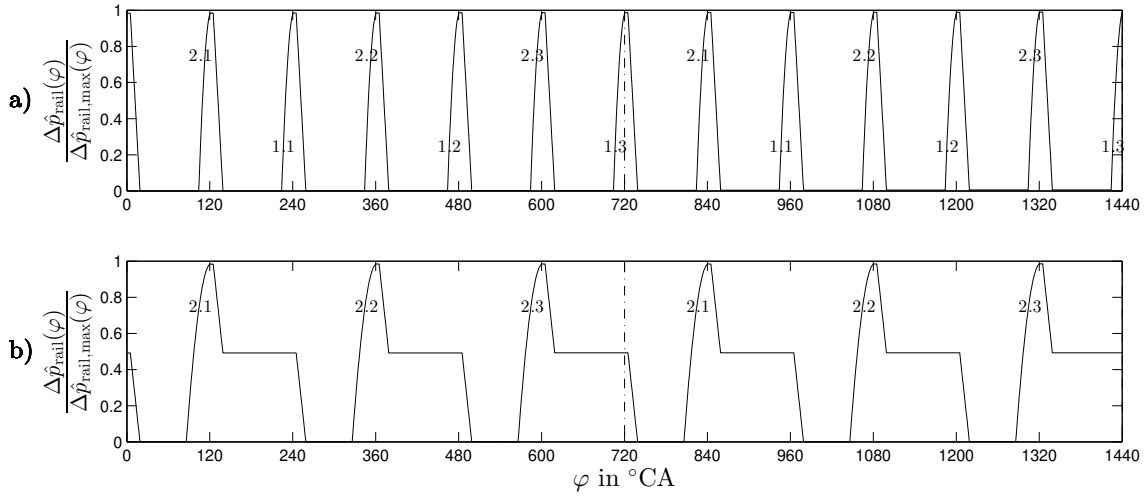

Fig. 5.10: Simulated RP oscillation signal for an equal HPP fuel delivery frequency to fuel injection frequency with:
a) A fault-free case (the first number in the upper index show the pump element and the second number show the actual profile peak. The same holds true for the lower index).
b) HPP fault in chamber 1, where RP oscillations caused by pump chamber 2 are visualized.

HPP fault case the RP signal still remains periodic over the engine cycle period of 720°CA, but the periodicity vanishes for the period of 120°CA (injector main period). Instead the signal is periodic over $\tau_{\text{hpp,sec}} = 240°\text{CA}$, see Fig. 5.10 b). Contrary to the first case, the injector imprints a stepwise RP decrease in case of an HPP fault, see Fig. 5.10 b).

For both cases it can be seen that a fault-free state and an HPP fault have no influence on the periodicity of the RP signal over one engine cycle period. It can also be seen in the RP signal of Fig. 5.9 a) and b) that the RP signal is periodic over 120°CA with and without an HPP fault. Different to the first case, the signal is now only periodic with and without an HPP fault over 240°CA for the second case, see Fig. 5.10 a) and b).

5.6 Summary

This chapter analyzed the signal characteristic of the RP sensor for various test scenarios by using a FFT approach. The test scenarios were explained to show the frequency components that each fuel system part impresses on the RP signal due to its activation. The primary test scenario included an exclusive function of the HPP without any injections or faults. The next test case was a fault-free scenario followed by an HPP chamber fault. Finally, for the last test scenario an injector fault (40% less fuel quantity) was implemented. For each test, the signal amplitudes of the FFT have clearly shown the frequencies in the RP signal of each component. This is the basis for the signal model-based residual development and injector isolation of the following sections.
Similarly, the EMP signal was also analyzed with a FFT just like the RP signal. However, only the fault-free case and an injector or misfire fault (the behavior is similar for the EMP) was shown. The HPP fault has no direct correlation to the EMP signal.
Two approaches for the signal model-based fault detection were discussed, namely the FFT and the uniformity residual calculation. Fault detection using FFTs is a useful approach with two main disadvantages, a large application effort for different engine OPs and being sensitive to system noise. Hence, the uniformity residual is introduced which can solve these issues.
Finally, the RP signal characteristics for a multiple and equal HPP fuel delivery to fuel injection frequency was discussed. This shows the capability of a robust injector fault detection with the help of the uniformity analysis and forms the basis for injector fault isolation.

6 Diesel engine fuel system fault detection

This chapter presents different fuel system fault detection algorithms, such as process- and signal model-based approaches, as well as limit checking approaches for the HP and LP system. The basic equations for process model-based methods are already discussed in Chap. 4 and for signal model-based approaches in Chap. 5. In the beginning, a signal model-based fault detection, namely the uniformity residual, is discussed. With the help of a uniformity analysis of the RP and EMP signal, different uniformity residuals are developed to detect an injector fault and a cylinder misfire fault. In the following section the fault detection algorithms are presented. Additionally, different investigated HP and LP faults are discussed and the results from the developed fault detection algorithms are visualized. These results are gained from test runs, performed on an engine test bench, with the goal to reproduce the investigated HP and LP faults as precisely as possible. The combination of all fault detection approaches forms the basis of a solid diesel engine fuel system fault diagnosis.

6.1 General fault detection structure

As discussed in Chap. 1, the diagnosis system can be divided into three different phases: Fault detection, fault diagnosis and fault management, see Fig. 6.1.
This chapter deals with fault detection algorithms with process- and signal model-based, as well as limit checking approaches using the equations from Chap. 2. Specifically, the advanced approaches, namely signal or process model-based give a deeper technical insight into the system. With this additionally obtained information, different physical variables or measured sensor signals can be observed to check for plausibility with a modeled physical behavior.
Finally, with a combination of all the algorithms, the fault detection can be improved significantly. In Fig. 6.1, the general structure of this fault detection is highlighted.

6.2 RP and EMP uniformity analysis for injector and misfire fault detection

In this section a signal model-based approach, namely the fault detection by uniformity residuals, is discussed. The basis for this was described in Chap. 5. The following two sections show the fault detection for:

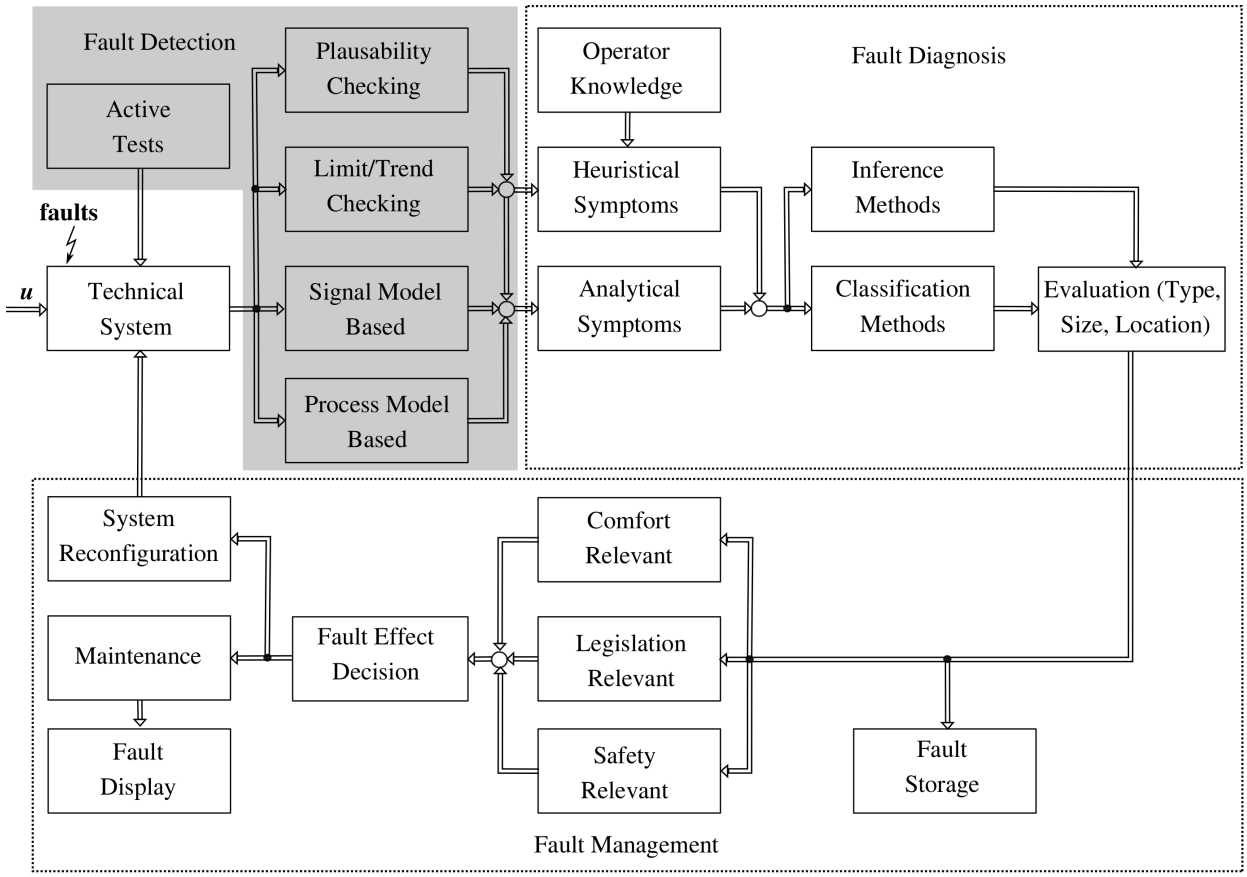

Fig. 6.1: Overall diagnosis structure with the primary focus on fault detection, according to [58]

- An HPP and an injector fault with uniformity residuals using different periodicities of the RP signal.
- The misfire fault detection with uniformity residuals using different periodicities of the EMP signal.

6.2.1 RP uniformity analysis for an HPP and injector fault

Sect. 5.1 already described how the HPP and injectors cause specific pressure frequencies in the common rail. In the following paragraph, the periodicity of the RP signal over an angle period of one engine cycle $\tau_{\mathrm{eng,cycl}} = 720°\mathrm{CA}$ is investigated with the help of a simulation similar to Sect. 4.6.

As it is described in Sect. 5.1 the injector fault causes an additional angle period of $\tau_{\mathrm{inj,sec}} = 720°\mathrm{CA}$ (see Table 5.4), whereas an HPP fault causes an increase of the $\tau_{\mathrm{hpp,sec}} = 120°\mathrm{CA}$ RP amplitude (see Fig. 5.3 b) compared to the fault-free case in Fig. 5.2 b)). Now with these angle periods, the uniformity residuals are calculated to observe an HPP fault r_{hpp} and an injector fault r_{inj}.

For the first uniformity residual r_{inj} the periodic angle τ_{u} and the supervised periodic angle τ_{s} (see equation (5.7)) are chosen to be the second HPP period $\tau_{\text{hpp,sec}} = \tau_{\text{u}} = \tau_{\text{s}} = 120°\text{CA}$). This period is chosen because the residual is thus not sensitive to HPP faults, due to the fact that the RP stays periodic with and without an HPP fault over 120°CA, see Sect. 5.5. With equation (5.7) it follows for the uniformity residual:

$$r_{\text{inj}} = \frac{1}{120[°\text{CA}]} \int_{\varphi}^{(\varphi+120[°\text{CA}])} [\hat{p}_{\text{rail}}(\varphi) - \hat{p}_{\text{rail}}(\varphi - 120[°\text{CA}])]\,\mathrm{d}\varphi. \tag{6.1}$$

Analog to the first uniformity residual the second residual r_{hpp} is calculated with the second injector period $\tau_{\text{inj,sec}}$ which occurs in case of a single injector fault. With equation (5.7) it follows:

$$r_{\text{hpp}} = \frac{1}{720[°\text{CA}]} \int_{\varphi}^{(\varphi+720[°\text{CA}])} [\hat{p}_{\text{rail}}(\varphi) - \hat{p}_{\text{rail}}(\varphi - 720[°\text{CA}])]\,\mathrm{d}\varphi \tag{6.2}$$

where $\tau_{\text{u}} = \tau_{\text{s}} = \tau_{\text{inj,sec}} = 720°\text{CA}$.

The different columns in Fig. 6.2 visualize a fault-free state, an HPP fault, an injector fault (40% less fuel quantity) and an HPP in combination with an injector fault. It is assumed that for the simulation in Fig. 6.2 the PRV volume flow is 0, then the RP is calculated with the integration of equation (4.11) mainly dependent on the HPP and injector volume flows.

In Fig. 6.2, column two illustrates the system behavior in case of an HPP fault. In the first row, the HPP fuel quantity control activity can clearly be seen in the amplitude changes of the HPP volume flows. In case of an HPP fault the double amount of fuel is delivered by the healthy pump chamber, see first row second (fourth) column. In case of a single injector Low Flow fault the HPP fuel quantity closed loop control decreases the fuel supply, because less fuel is needed to hold a RP setpoint, see first row third and fourth column. Furthermore, the HPP volume flows directly influence the RP signal characteristic (third row). In the fault-free case, see column one, these volume flows impress a step wise pressure increase. This stepwise behavior vanishes in case of an HPP fault shown in column two.

The single injector 3 Low Flow fault can be seen in the decreased third injector volume flow (40% less fuel quantity), see Fig. 6.2 row two column three and four. Also, the occurrence of an additional lower frequency ($1/720°\text{CA}$) in the RP signal can be seen, see row three column three and four. The vertical dash-pointed line shows the window of the r_{inj} and the vertical dash line shows the window of the r_{hpp} uniformity residual calculation. An observation of the residual r_{inj}, row four, shows the occurrence of the injector 3 Low Flow fault over 120°CA with a phase shift of again 120°CA (caused by the residual calculation, see equation (6.1)).

It can also be seen in Fig. 6.2 that the RP signal, row three column one and two, is periodic over 120°CA with and without an HPP fault. For the same graphs the RP signal is furthermore periodic over one engine cycle 720°CA. The periodicity over 120°CA vanishes in case of an injector fault, see third row column three and four, but is still periodic over one engine cycle of 720°CA. Due to the fact that the RP signal is periodic over 120°CA with and without an HPP fault, only an

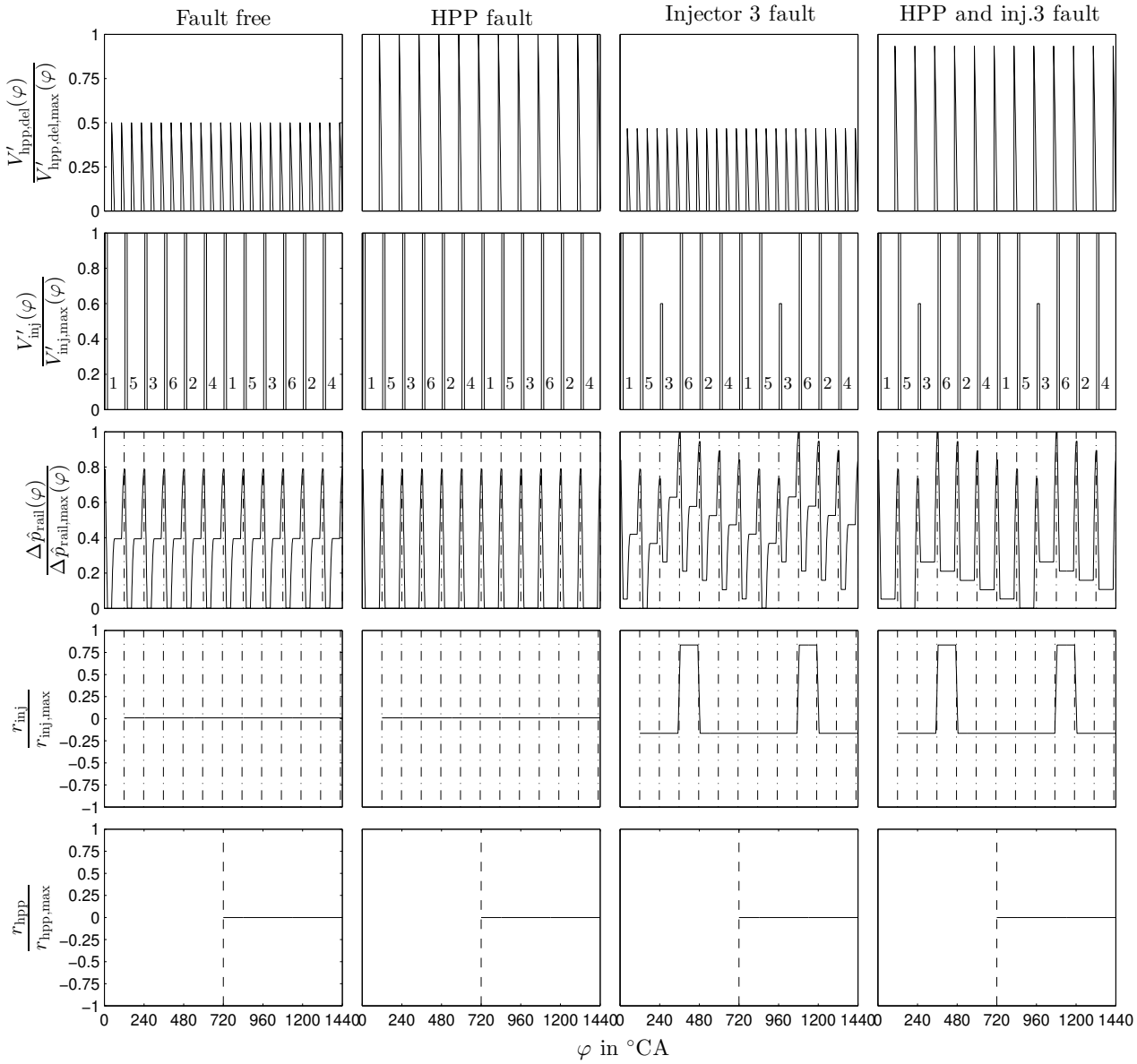

Fig. 6.2: Simulated RP signal and uniformity residuals for **column one:** A fault-free state, **column two:** An HPP fault (no fuel delivery from pump chamber 1), **column three:** Injector 3 fault (40% less fuel quantity) and **column four:** An HPP in combination with injector 3 fault.

injector fault can disturb this periodic behavior. This results in the possibility to detect the injector fault with the observation of the RP periodicity over 120°CA. This means that the residual r_{inj} is able to monitor the occurrence of an additional angle period of 720°CA, which occurs in the case of an injector fault. For multiple injector faults and therefore additional frequencies other than 720°CA, the residual r_{inj} can furthermore detect the occurrence of these frequencies. This uniformity residual r_{inj} for an injector fault, can be seen in Fig. 6.2 row four, third and fourth column. Here the occurrence of the residual r_{inj} is also periodic with the engine cycle period of 720°CA (stays also periodic for multiple injector faults). Furthermore, the residual r_{hpp} in the fifth

row shows that the residual does not occur at any time, which makes it impossible to separate an injector and an HPP fault. This is due to the fact that the RP signal stays periodic over 120°CA and 720°CA with and without an HPP fault. A system where a separation between an injector and an HPP fault is possible, is shown in [67] and the difference between the investigated system and the system in [67] is described in the Appendix A.4.

The final conclusion is, that an injector fault can be detected with the uniformity residual r_{inj}, see Fig. 6.2 fourth row, but an HPP fault can not be detected with the uniformity residual r_{hpp}, see fifth row. Also, the occurrence of the residual r_{inj} is periodic, which opens up the possibility to isolate the injector fault. This will be discussed in the following Sect. 7.2.1. A comparison between the simulated RP signal, third row in Fig. 6.2, to the measured RP signal (see Fig. 5.2, Fig. 5.3 and Fig. 5.4) for the fault-free, HPP fault and injector fault shows a similar RP behavior. This implies a reliable approximation for the physical RP model developed in Sect. 4.2.

6.2.2 EMP uniformity analysis for a cylinder misfire

Analog to the previous case a cylinder misfire induces an additional frequency of $1/720°\text{CA}$ (see Fig. 5.7), which makes the EMP signal periodic over $\tau_{\text{cyl,sec}} = 720°\text{CA}$, see Table 5.7. In Sect. 5.2 it was shown that the cylinder misfire fault has a similar behavior on the EMP signal as an injector fault.

Instead of the RP signal, the EMP signal is not periodic over 120°CA, due to geometry of the exhaust manifold (separated manifolds) and the sensor position, see Fig. 5.6. The EMP signal periodicity over $\tau_{\text{geom,main}} = 240°\text{CA}$ is visualized in Fig. 5.5. Two different residuals are now calculated to visualize the detection of a cylinder misfire fault (injector fault).

According to equation (5.7) the first residual is given with $\tau_{\text{u}} = \tau_{\text{s}} = \tau_{\text{geom,main}} = 240°\text{CA}$ by:

$$r_{\text{ua,emp,1}} = \frac{1}{240[°\text{CA}]} \int_{\varphi}^{(\varphi+240[°\text{CA}])} |p_{\text{em}}(\varphi) - p_{\text{em}}(\varphi - 240[°\text{CA}])| \, \text{d}\varphi \tag{6.3}$$

and the second residual with $\tau_{\text{u}} = \tau_{\text{s}} = \tau_{\text{cyl,sec}} = 720°\text{CA}$ by

$$r_{\text{cyl,sec}} = \frac{1}{720[°\text{CA}]} \int_{\varphi}^{(\varphi+720[°\text{CA}])} |p_{\text{em}}(\varphi) - p_{\text{em}}(\varphi - 720[°\text{CA}])| \, \text{d}\varphi. \tag{6.4}$$

Fig 6.3 visualizes both residuals calculations with a measured EMP signal for a fault-free (column one) and a cylinder misfire fault (column two). A misfire fault detection with residual $r_{\text{ua,emp,1}}$ can clearly be seen in row two, column two. Similar to the previous case in Sect. 6.2.1 the residual calculation $r_{\text{cyl,sec}}$ can not detect a cylinder misfire fault, see row three column two in Fig 6.3. This is due to the fact that the periodicity of the EMP signal remains periodic over one engine cycle.

Finally, an injector fault or a misfire fault caused by a compression loss in one cylinder can be detected with the uniformity residual $r_{\text{ua,emp,1}}$.

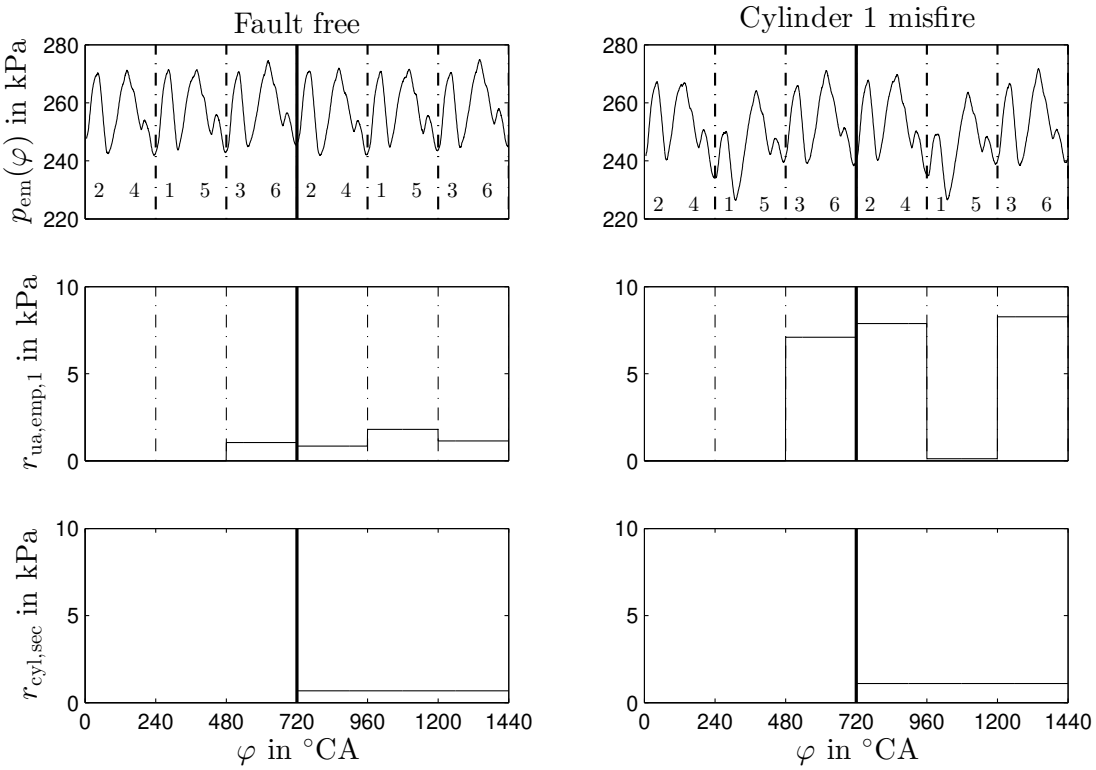

Fig. 6.3: EMP uniformity residual calculation $r_{\mathrm{ua,emp,1}}$ and $r_{\mathrm{cyl,sec}}$ for measured cylinder 1 misfire

6.3 Fuel system fault detection algorithms

The fault detection algorithms are implemented for an online calculation on a Rapid Control Prototyping (RCP) system, the Micro Auto Box II from dSPACE. This platform guarantees real time testing on the test bench (test bench description see Appendix A.1). The structure of the advanced fault detection and fault diagnosis approaches implemented in the RCP is visualized in Fig. 6.4. In this figure, the signal model-based fault detection approaches only depend on the output signals, whereas the process model-based approaches depend on both input and output signals of the real process. The outputs of these fault detection algorithms are the basis for fault diagnosis. In the next sections, the development of these fault detection algorithms is discussed. The fundamental models or equations for the residual development are already described in Chap. 4 for process model-based and Chap. 5 for the signal model-based approaches.

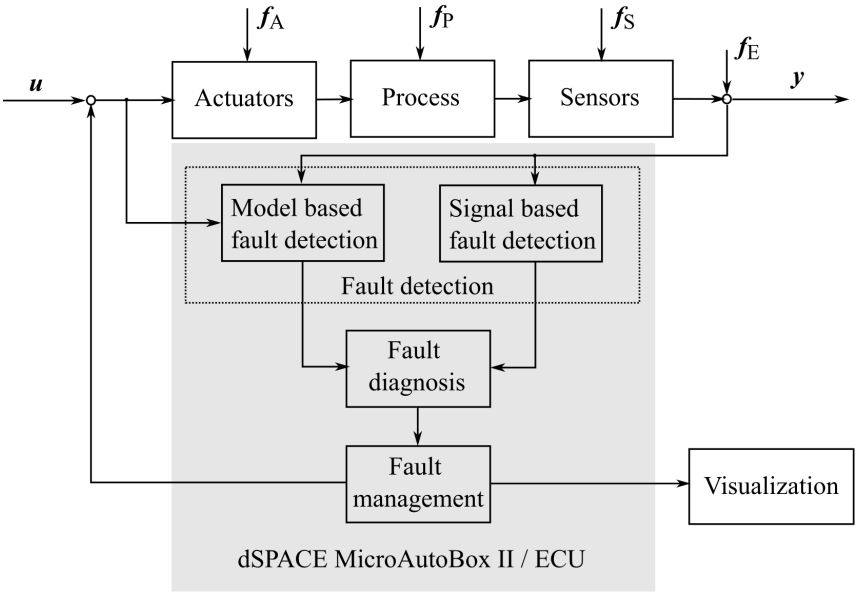

Fig. 6.4: Schematic for advanced fault detection and fault diagnosis, according to [62]

6.3.1 Residual r_1: Physical rail pressure model

The physical RP model residual is developed with the mathematical integration of equation (4.11). This equation includes the HPP physical volume flow model, the injector and PRV volume flow mean value model (see also Fig. 4.14):

$$\hat{p}_{\text{rail}}(\varphi) = \int \frac{\kappa}{V_{\text{rail}}} \left(\sum_{i=1}^{2} V'_{\text{hpp,del},i}(\varphi) - V'_{\text{prv}}(\varphi) - \sum_{j=1}^{6} V'_{\text{inj},j}(\varphi) \right) \mathrm{d}\varphi. \tag{6.5}$$

The volume flow models are described in Sect. 4.3 to 4.5. For static OPs, the PRV volume flow V'_{prv} (see Fig. 3.2, PRV from common rail to the fuel tank) can be neglected because the HPP's fuel quantity control with PCV is very efficient. However, for large RP-to-RP setpoint changes in dynamic engine OPs, the fuel quantity control needs a PRV activation to reach a specific RP setpoint by decreasing the RP.

Fig. 6.5 represents the residual r_1 of an output parity equation approach calculated with the input

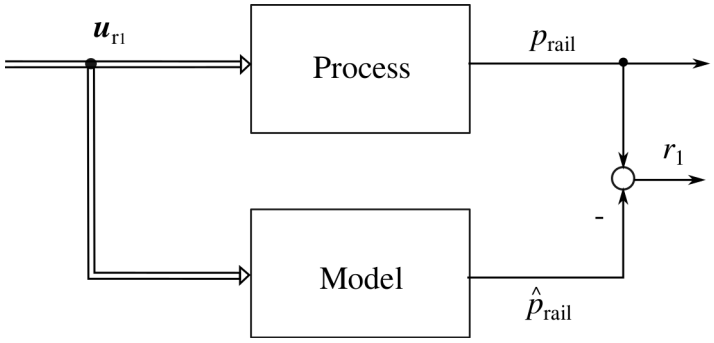

Fig. 6.5: Parity equation with a physical rail pressure model

signal vector

$$\mathbf{u}_{r_1} = \begin{bmatrix} \varphi & \varphi_{\mathrm{pcv,sa}} & T_{\mathrm{lp,f}} & n_{\mathrm{eng}} & m_{\mathrm{mi}} & m_{\mathrm{prv,disc,q}} \end{bmatrix}^T, \tag{6.6}$$

which is required to build the volume flow models in equation (6.5). Fig. 4.14 shows a block diagram depicting how the input signals are derived from the engine ECU. With this RP model output and the measured RP, a process model-based output error parity equation, as shown in Fig. 2.1 a), is calculated by:

$$r_1 = p_{\mathrm{rail}}(\varphi) - \hat{p}_{\mathrm{rail}}(\varphi). \tag{6.7}$$

This residual is useful for the detection of HPP faults, PRV faults or HP leakages.

6.3.2 Residual r_2: HPP fuel quantity closed loop control

As described in Sect. 3.5, the HPP fuel quantity control structure is a two degree control, where the open loop control provides the entire fuel quantity mass for the actuator input variable in a fault-free case. Therefore the closed loop control is only active in case of a fault, disturbance or parameter change (see Sect. 2.4 for additional information on fault detection in control loops) and can be interpreted as a direct indicator for these changes.

The residual r_2 is based on an observation of the output signal of the HPP closed loop control which is basically the HPP fuel quantity closed loop mass $m_{\mathrm{hpp,fq,cl}}$. The general control structure is shown in Fig. 2.2 and explicitly for the HPP fuel quantity control in Fig. 3.7. This HPP closed loop fuel quantity control is implemented as a PI controller in the engine's ECU. The input variable is the RP setpoint minus the measured RP and the output variable the HPP fuel quantity closed loop mass $m_{\mathrm{hpp,fq,cl}}$ (see Fig. 3.7). The residual r_2 is finally the HPP fuel quantity closed loop mass which is calculated in the engine ECU:

$$r_2 = m_{\mathrm{hpp,fq,cl}}. \tag{6.8}$$

With other residuals in combination, it is possible to identify different HPP faults, RP sensor faults, PRV and HP leakages faults. Furthermore, with the help of this residual, it is possible to isolate multiple injector fuel quantity faults, which will be discussed in Chap. 7.

6.3.3 Residual r_3: RP uniformity residual

This residual belongs to the category of signal model-based approaches and is especially developed to detect injector faults. The basic oscillations of the RP signal imprinted by the different fuel system components are already analyzed in Sect. 5.1. It can be seen that the RP signal is periodic with 120°CA in the fault-free and the HPP fault case (see Fig. 5.2 and 5.3). The simulation with the HPP and injector volume flows in Sect. 6.2.1 show the same behavior.

The main RP characteristics are caused by the discontinuous fuel delivery and injections, as described in Sect. 5.1. In contrast to an HPP fault, a single injector fault causes an additional periodic angle of $\tau_{\mathrm{Inj,sec}} = 720°\mathrm{CA}$. As described in 6.2.1 the occurrence of this additional periodic angle can be further observed with a uniformity residual based on equation (6.1).
Therefore, the supervised angle period τ_{s} and the periodic angle for the mean value generation τ_{u} are assumed to be equal. Finally, with a supervised angle $\tau_{\mathrm{s}} = \tau_{\mathrm{hpp,sec}} = \tau_{\mathrm{inj,main}} = 120°\mathrm{CA}$, for detailed description see Sect. 6.2.1, an injector fault can be detected. This period is chosen, because the RP signal remains periodic over 120°CA with and without an HPP fault. Hence, the residual is only sensitive on injector faults. Fig. 6.6 visualizes that this residual only needs the measured RP sensor signal, in a crank angle domain, as an input.

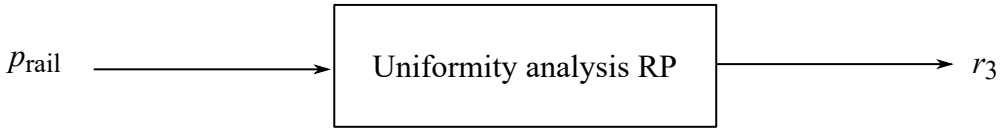

Fig. 6.6: Rail pressure uniformity analysis

According to equation (6.1) with the difference of a measured RP as an input, the RP uniformity residual is given by:

$$r_3 = \frac{1}{120[°\mathrm{CA}]} \int_{\varphi}^{(\varphi+120[°\mathrm{CA}])} [p_{\mathrm{rail}}(\varphi) - p_{\mathrm{rail}}(\varphi - 120[°\mathrm{CA}])]\,\mathrm{d}\varphi. \tag{6.9}$$

With the help of this residual, injector faults can be detected. This residual (in combination with other described residuals) can also be used to directly isolate different injector faults. The idea behind this will be discussed in Chap. 7, specifically in Sect. 7.2. This will significantly improve the diagnosis with minor effort and low computational resources.

6.3.4 Residual r_4: EMP uniformity residual

Analogous to residual r_3, another signal model-based uniformity residual for the EMP is developed. This residual is influenced by the combustion (misfire) of the engine cylinders and therefore depends on the degree of inlet air mass in the cylinders or the injected fuel quantity. The fault-free case can be seen in Fig. 5.5. As described in Sect. 5.2 the EMP sensor signal is periodic over 240°CA. The periodicity over 240°CA is caused by the EMP sensor position, as shown in Fig. 5.6, which has an indirect and direct pressure increase resulting in a periodic signal of 240°CA.
When a cylinder misfires, caused by a cylinder air quantity fault (e.g. compression loss) or an injector fault occurs, the EMP signal shows an additional periodicity of $\tau_{\mathrm{cyl,sec}} = 720°\mathrm{CA}$. In Sect. 6.2.2 it is described how this additional periodicity and therefore the cylinder misfire fault can be detected with the residual in equation (6.3). Similar to residual r_3, Fig. 6.7 visualizes that only the EMP sensor signal is needed, in a crank angle domain, for the input of residual r_4.

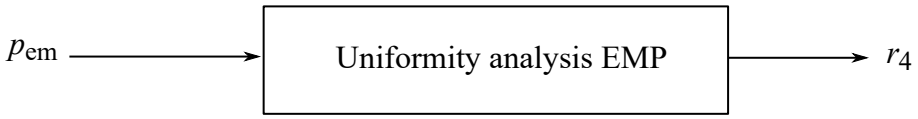

Fig. 6.7: Exhaust manifold pressure uniformity analysis

According to equation (6.3), the EMP uniformity residual is calculated with an absolute value:

$$r_4 = \frac{1}{240[^\circ\text{CA}]} \int_{\varphi}^{(\varphi+240[^\circ\text{CA}])} |p_{\text{em}}(\varphi) - p_{\text{em}}(\varphi - 240[^\circ\text{CA}])| \text{d}\varphi. \tag{6.10}$$

r_4 is used to detect an injector fault or a cylinder misfire fault, which is caused by a cylinder air quantity fault. Using a combination of residual r_3 and r_4 a misfire fault can be separated from an injector fault.

6.3.5 Residual r_5: Physical volume flow models LPP / MP inlet

This residual is developed by comparing two different volume flow models. The foundation of this residual is a process model-based parity equation approach with redundant models as described in Sect. 2.2.2. The first volume flow model is the physical LPP displacement volume flow model equation (4.24) from Sect. 4.7.1. Since the system has no integrated volume flow sensor and it is necessarily that the standard production equipped engine is used (see Sect. 3.7), a second independent volume flow model is needed.
This second independent volume flow is the physical MP inlet volume flow model described with equation (4.48) shown in Sect. 4.8.2. Here, the assumption of neglecting the air bleed volume flow, see Fig. 3.2, has to be taken into account. The second volume flow is independent because the MPP is mechanically driven, whereas for the first volume flow the LPP is electrically driven. For a detailed flow structure with input and output signals for both volume flow models see Fig. 4.14 from Sect. 4.9.

Fig. 6.8 visualizes the calculation of the parity equation with these volume flow models and the input vectors $\mathbf{u}_{\text{r}_{5,1}}$ and $\mathbf{u}_{\text{r}_{5,2}}$. The input vectors are generated from the models of equation (4.48), which is the physical MP inlet volume flow model and from equation (4.24), which is the physical LPP displacement volume flow model as:

$$\begin{aligned} \mathbf{u}_{\text{r}_{5,1}} &= \begin{bmatrix} \hat{p}_{\text{mp}} & n_{\text{eng}} & p_{\text{lp}} \end{bmatrix}^T, \\ \mathbf{u}_{\text{r}_{5,2}} &= \begin{bmatrix} n_{\text{lpp}} & U_{\text{lpp}} & I_{\text{lpp}} \end{bmatrix}^T. \end{aligned} \tag{6.11}$$

Finally, the process model-based residual equation is given by:

$$r_5 = \dot{\hat{V}}_{\text{mp,in}} - \dot{\hat{V}}_{\text{lpp}}. \tag{6.12}$$

This residual is useful for the detection of different faults like primary and secondary fuel filter restrictions, leakages in the LP, MP and HP systems and LP sensor faults.

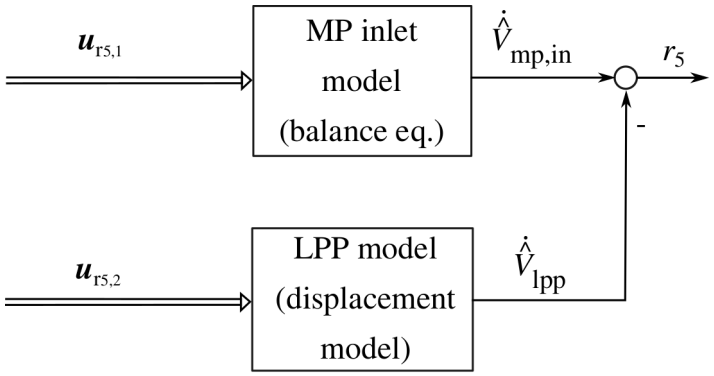

Fig. 6.8: Physical volume flow models LPP/ MP inlet

6.3.6 Residual r_6: Physical power model LPP

Sect. 4.7.2 covers how the mechanical LPP power model can be described with an electrical equation (4.26) or with a hydraulic equation (4.28), including known efficiency factors. Fig. 4.14 from Sect. 4.9 illustrates a detailed flow structure with input and output signals of these models. For the mechanical power model derived by the hydraulic equation, it is further assumed that the delta pressure of the LPP inlet to the outlet is equal to the pressure rise from the environmental pressure to the LP Δp_{lp}. This is assumed, because there is no direct pressure measurement at the inlet and the outlet of the LPP (see Fig. 3.2).

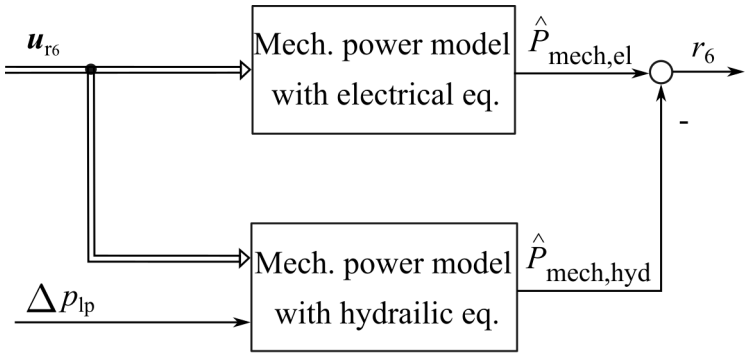

Fig. 6.9: Physical power model LPP

Fig. 6.9 shows the structure of the process model-based parity equation with physical LPP power models. Residual r_6 is given by:

$$r_6 = \hat{P}_{\text{mech,el}} - \hat{P}_{\text{mech,hyd}}. \tag{6.13}$$

The input vector $\mathbf{u}_{r_6}$ is generated out of the models of equation (4.26) and (4.28):

$$\mathbf{u}_{r_6} = \begin{bmatrix} U_{\text{lpp}} & I_{\text{lpp}} & n_{\text{lpp}} \end{bmatrix}^T. \tag{6.14}$$

With the help of this residual, primary and secondary fuel filter restrictions and pump drive faults can be detected.

6.3.7 Residual r_7: Low pressure model

The closed loop control of the LP, as described in Sect. 3.3, has a special dynamic behavior which can be described as a first order lag as shown in Sect. 4.7.3. A deviation between the dynamic behavior of the measured LP sensor signal and the first order lag model will point to a changed LP closed loop control behavior e.g. caused by a fault. This fault can be detected with a special mode, where the desired LP setpoint is stimulated, for example, with a step input, see Fig. 4.12. For example, fuel filter restrictions can cause a changed LP control dynamic behavior, which results in a delayed pressure rise of the measured LP sensor value.

As shown in Fig. 6.10, the parity equation is developed by a process model-based approach. The

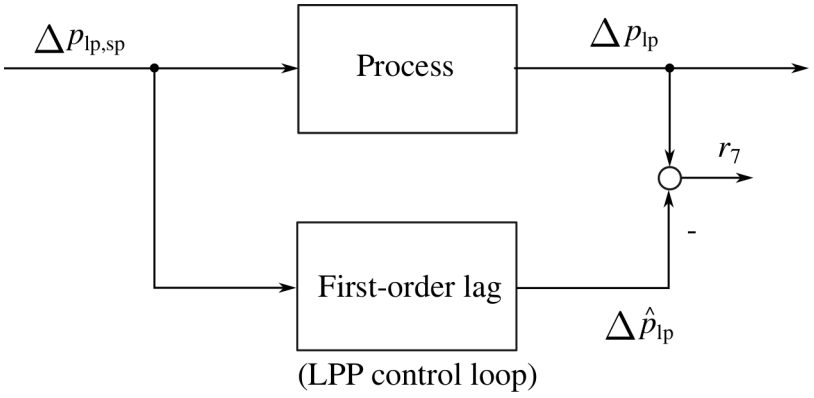

Fig. 6.10: Low pressure model

first order lag transfer function is derived by a parameter estimation with LS, see Sect. 4.7.3. The residual r_7 is calculated with the equations (4.29), (4.31) for the LP model $\Delta \hat{p}_{\mathrm{lp}}$ and the measured LP sensor value Δp_{lp}:

$$r_7 = \Delta p_{\mathrm{lp}} - \Delta \hat{p}_{\mathrm{lp}} \tag{6.15}$$

where the input signal for the process and model is the desired LP setpoint $\Delta p_{\mathrm{lp,sp}}$.

6.3.8 Residual r_8: Hydro carbon injection pressure limit check

Regeneration of the aftertreatment system uses a post injection of fuel into the exhaust path between the VGT and the fixed turbocharger (see Fig. 3.1). In the Hydro Carbon Injection (HCI) module, there are two integrated pressure sensors and one temperature sensor. The first HCI pressure sensor can be used to monitor possible leakage in the HCI system, when the regeneration cycle is not active. To measure the HCI pressure, the On/Off valve in front of the sensors has to be switched on (see Fig. 3.2). The second sensor, the HCI nozzle pressure sensor, can further be used to monitor an active regeneration cycle.

The residual which monitors a sufficient fuel supply to the HCI dosing system is developed by a limit checking approach:

$$r_8 = p_{\mathrm{hci}} - p_{\mathrm{hci,lim}}. \tag{6.16}$$

In a fault-free case the HCI pressure is reduced with the help of the Pressure Reducing Valve (PRedV) from the MP to a p_{hci} pressure, which is assumed to be constant. The pressure $p_{\mathrm{hci,lim}}$ is the limiting pressure which is empirically gained on the test bench.

6.3.9 Residual r_9: ECU HPP fuel quantity open/closed loop comparison

This residual compares the open loop with the closed loop ECU signals of the HPP fuel quantity control (see Fig. 3.7). The HPP has two plunger chambers that deliver fuel into the rail. In a fault-free case the HPP fuel quantity open loop control calculates the total amount of fuel mass needed for a specific RP setpoint (for a detailed description see Sect. 3.5).

HPP fuel quantity control behavior in case of HPP fault

If, for instance, one chamber is faulty and does not supply enough fuel, the HPP fuel quantity closed loop control will be activated due to a mismatch of the measured RP to RP setpoint (see Fig. 3.7).
In case of two existing plunger chambers, the closed loop control mass will adapt to the same size of the open loop control mass ($m_{\mathrm{hpp,fq,cl}} = m_{\mathrm{hpp,fq,ol}}$) to compensate the insufficient fuel supply of the faulty pump chamber.
In general this increased mass ($m_{\mathrm{hpp,fq,ol}} + m_{\mathrm{hpp,fq,cl}}$) results in a changed PCV start angle. This results in increased fuel delivery due to an earlier requested PCV closing angle for both HPP plunger chambers (decreased $\varphi_{\mathrm{pcv,sa}}$ see Fig. 3.5). Since one pump chamber has a fault and does not deliver fuel, only the healthy pump chamber will deliver the increased amount of fuel. In case of two pump chambers this is the doubled fuel mass, which will correct the fault. This holds true if the amount of fuel request does not exceed the maximum possible fuel delivery of the healthy pump chamber.

Residual r_9 calculation

The residual r_9 equation is given by:

$$r_9 = m_{\mathrm{hpp,fq,ol}} - m_{\mathrm{hpp,fq,cl}}. \tag{6.17}$$

The HPP fuel quantity open loop control is calculated using a look-up-table in the ECU (see Fig. 3.7) with the following input signals: Measured RP p_{rail}, RP setpoint $p_{\mathrm{rail,sp}}$, fuel temperature $T_{\mathrm{lp,f}}$ and the desired fuel injection mass m_{f}.
This residual will directly show if one plunger chamber does not supply fuel into the rail for low and medium engine OPs.

6.3.10 Residual r_{10}: Physical volume flow models LPP / MP inlet trend checking

Residual r_{10} is an extension of residual r_5. As described in Sect. 2.1, the trend checking approach is used for an earlier detection of faults. With residual r_5 as the basic signal residual, r_{10} is given by:

$$r_{10} = \dot{r}_5 = \ddot{\hat{V}}_{\mathrm{mp,in}} - \ddot{\hat{V}}_{\mathrm{lpp}}. \tag{6.18}$$

This residual is useful for the detection of volume flow or pressure oscillations in the LP system.

6.3.11 Residual r_{11}: PCV start angle offset detection

Residual r_{11} detects a wrong HPP camshaft to crankshaft assembly. The model in general calculates a desired PCV start angle only considering the HPP fuel quantity open loop mass and compares it with the ECU calculated PCV start angle. In Fig. 3.7 the calculation of the PCV start angle is shown.

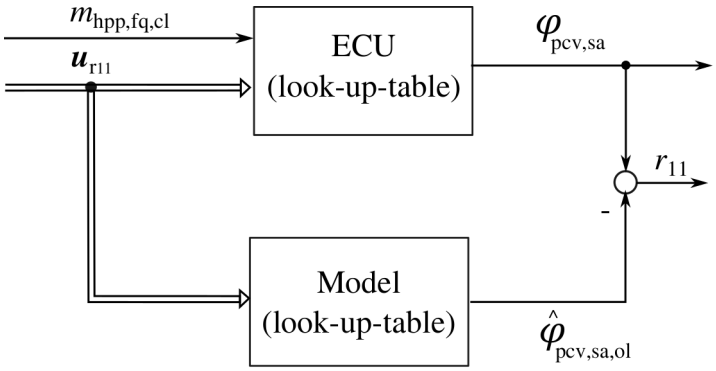

Fig. 6.11: PCV start angle offset detection

Figure 6.11 shows this residual structure and the calculation follows with

$$r_{11} = \varphi_{\mathrm{pcv,sa}} - \hat{\varphi}_{\mathrm{pcv,sa,ol}} \tag{6.19}$$

where the input vector for the model and the ECU calculation is

$$\mathbf{u}_{\mathrm{r_{11}}} = \begin{bmatrix} m_{\mathrm{hpp,fq,ol}} & p_{\mathrm{rail,sp}} \end{bmatrix}^T. \tag{6.20}$$

If now r_{11} has e.g. a constant offset in the amount of the CS tooth resolution $\varphi_{\mathrm{cs,res}}$ over different engine OPs, this could be an indication of a wrong HPP camshaft to crankshaft assembly. This holds also true for a constant offset in the amount of several CS tooth resolutions.

6.4 Investigated fuel system faults

In the following sections, different investigated faults are described. These faults are extracted from the FMEA information, as shown in Table 3.1. They are separated into HP crank angle synchronous and LP time-domain faults.

6.4.1 Investigated HP faults

Important faults in the HP system are HPP, or PCV faults. PCV faults lead to an unclosed poppet valve of the plunger pump chamber, resulting in a fault where the plunger pump chamber will not supply fuel to the rail. Two cases are distinguished:

1. An HPP fault for low/medium engine OPs (e.g. low/medium engine torque OPs), the HPP fuel quantity control compensates this insufficient fuel supply. For a general HPP fuel quantity control description see 3.5 and an explicit HPP fuel quantity control behavior in case of an HPP fault see Sect. 6.3.9. This fault is labeled in the following as F_1 low engine OPs.
2. An HPP fault for high engine OPs (high engine torque OPs), the fuel delivery of only one plunger chamber element has an insufficient fuel supply to the rail. Here, the requested amount of fuel exceeds the maximum possible fuel delivery of the healthy pump chamber. The HPP fuel quantity control fails to compensates the fault. This fault is labeled with F_2 high engine OPs.

Consequently, the insufficient fuel delivery for high engine OPs causes a decreased RP, which can lead to insufficient fuel injections and lowered engine power generation. Both investigated faults F_1 and F_2 are implemented by unplugging the PCV power supply connection on the test bench.

Some residuals from Sect. 6.3 are developed using signal model-based approaches including single input information of the measured sensor signals. One of the important sensors in the fuel system is the RP sensor. The first investigated fault is therefore a positive (high) offset fault F_3 and the opposite is a negative (low) offset fault F_4. Both faults are implemented by a manipulation of the conversion factor of the voltage to RP conversion in the ECU.

Another important fault is a Pressure Relief Valve (PRV) leakage or a side feed tube leakage F_5. The latter can occur when the side feed tube connection to the injector is loose and the fuel flows into the cylinder head, before returning to the fuel tank. A test setup description for the loose side feed tube can be found in Sect. 5.1, where the RP frequency oscillations by the HPP activation is analyzed. This results in rapid local fuel temperature increase and energy losses by the HPP, since mechanical energy of the engines crank shaft is used to compress the fuel to a specified RP setpoint. This mechanical energy is now converted to thermal energy and consequently results in an increase of the fuel temperature by the expansion from RP back to the fuel tank pressure. This investigated fault is implemented by loosening an injector side feed tube connection, to generate an inner HP leakage fuel flow back to the tank.

Pursuing, mechanical and fluidic injector faults, can not be detected with an electrical injector signal observation. The origin of these faults could be coked injector nozzles for example. This causes a lower injector fuel mass flow quantity into the cylinders, labeled as F_6. In contrast, nozzle erosions cause a higher mass flow quantity, labeled as F_7. Both faults F_6 and F_7 are implemented by an increased or decreased injection time for one injector, manipulating a scaling factor in the ECU software.

Cylinder misfire, labeled as F_8, can cause one of the most inefficient states for the engine. These faults are mostly caused by a loss of compression leading to partially or even unburned fuel. This implies less engine power, efficiency and increased emissions. The root cause of this cylinder misfire, or compression loss, could be worn/broken piston rings, worn/broken inlet or outlet valves, or wrong clearance adjustments for these inlet/outlet valves. The implementation of a small cylinder misfire fault was made with an opening of the cylinder pressure indication hole. This reduces the compression in one cylinder. For a bigger cylinder misfire fault an inlet valve in one cylinder was removed.

Table 6.1: Investigated HP faults

Fault index	Fault description
F_1	HPP one plunger chamber does not supply fuel (low OP)
F_2	HPP one plunger chamber does not supply fuel fails to build up RP (high OP)
F_3	RP sensor High Offset
F_4	RP sensor Low Offset
F_5	PRV or HP (side feed tube) leakage
F_6	Lower injector mass flow quantity (single injector Low Flow)
F_7	Higher injector mass flow quantity (single injector High Flow)
F_8	Engine misfire by compression loss

Table 6.1 summarizes all above described investigated HP faults.

6.4.2 Investigated LP faults

In the LP system, fuel filter restrictions are one of the most important faults to observe. The proper functionality of both fuel filters (primary and secondary fuel filter see Fig. 3.2) has to be guaranteed to protect the fuel system from damage caused by fuel pollution or insufficient fuel supply. This will result in poor lubrication or even fails to comply with the stringent EPA (United States Environment Protection Agency) emission standard, see[11]. The primary fuel filter acts as a fuel pre-filter and helps to avoid damage on the LPP. The fault of the primary fuel filter restriction F_9 could originate from a high degree of polluted fuel or an aged filter. The investigated fault F_9 is implemented with a throttle valve at the inlet of the primary fuel filter, to regulate the fuel flow rate. Similar to the primary fuel filter restriction, the secondary fuel filter restriction F_{10} has the same fault origins. The difference between the secondary and primary fuel filter is that the secondary filters out finer fuel particles due to a finer mesh. The fault F_{10} is implemented with a throttle valve at the inlet of the secondary fuel filter, just like F_9.

The other investigated faults of the LP system are fuel leakage faults. These faults can occur at the fuel line connection before the primary fuel filter and the fuel line connection behind the secondary fuel filter, see Fig. 3.2. The primary fuel filter inlet leakage F_{11} causes the LPP to pull an air/fuel mixture into the fuel system if the fuel tank position is below the LPP and fuel lines. This fault is implemented by adding an additional opened fuel line connection, where the opening area is regulated with a throttle valve at the inlet of the primary fuel filter. The result is an inefficient fuel supply with the possibility of lubrication demolition.

The leakage at the fuel line connection behind the secondary fuel filter F_{12} causes pollution into the environment and an increased fuel consumption. Similar to F_{11}, F_{12} is implemented with an additional opened fuel line connection, where the opening area is regulated with a throttle valve at the outlet of the secondary fuel filter.

Table 6.2: Investigated LP faults

Fault index	Fault description
F_9	Primary fuel filter restriction
F_{10}	Secondary fuel filter restriction
F_{11}	Primary fuel filter inlet leakage
F_{12}	Secondary fuel filter outlet leakage

Table 6.2 shows the list of the investigated LP faults.

6.5 Threshold generation for the fuel system fault detection

There are two possibilities to implement thresholds for the fuel system fault detection with:

a) **Stationary operation points:**

Stationary engine OPs are constant in engine torque and speed. Here the thresholds have a fixed value. For the investigated HP faults, the need of stationary OPs is mainly driven by the uniformity analysis which compares the periodicity of the observed sensor signal output.

The advantage of this case is the proper calculation of the uniformity residuals, due to the stationary operation mode and a simplified implementation of the thresholds. The thresholds are chosen to be constant and empirically estimated from the different recorded test runs. Here, attention must be paid to the trade-off between early fault detection and fault misclassification. The disadvantage of stationary OPs is, that the fault detection must be turned off for transient engine states. This requires a reinitialization of the initial conditions. An example for this is the uniformity calculation, which requires stationary or quasi stationary engine cycles to prevent fault misclassification. Non-periodical RP changes, which result from transient RP OP changes, can cause this misclassification. The solution is to disengage the fault detection in transient RP changes, to reinitialize the buffer with new sensor output signals when the fault detection is engaged again. This specifically concludes an increased time contingent to detect faults.

To proof that the engine is in a stationary OP, the change of the engine torque and speed has to be monitored. This stationary OP could be reached in heavy duty applications, where the engine is speed controlled and mostly operated in a constant speed setpoint with an application requesting a constant workload (engine torque). There are several possible applications for the heavy duty area, where a constant speed and torque value is requested. E.g. an engine which is used for the propulsion of a ship, harvesting with a combine or a self-propelled forage harvester, or a tractor implement combination, like plowing, where the implement requests a constant workload.

b) **Quasi-stationary operation points:**

The quasi-stationary OPs are constant in engine speed, but varying for the engine torque, or vice versa. For this second possibility, the thresholds are implemented with a fixed and an adaptive component. On the one side, the advantage of this threshold generation is an earlier fault detection as a result of the missing fault detection engagement/disengagement. On the other side, the disadvantage is that the adaptive threshold generation is more complex compared to the fixed threshold generation. In Sect. 2.5, different adaptive approaches are described.

Applications for the quasi-stationary OPs could be Excavators for the construction area, or tractor implement combinations, for example a large square baler used for hay baling. Here, a constant engine speed is requested. Due to the working principle of the baler there are peak torques in a specific frequency, when the baler is compressing the material.

Both assumptions a) and b) only hold true, if the maximum power the engine could deliver is not exceeded. If that is the case the engine speed as well as the engine torque will decrease.
For the investigated faults the stationary OPs are chosen, because on the one hand most applications for the heavy duty area operate at constant engine OPs. On the other hand, it is not necessary to detect the faults immediately. Also, the uniformity analysis residual needs a stationary OP to avoid misclassification, due to a signal uniformity change caused by a transient state. Furthermore, there is only one component in the investigated fuel system, the PRV, which is only active in high transient engine OPs. Even the activation for the PRV is very seldom, because this only holds true for big RP-setpoint changes from a high to a low pressure level. Here, the HPP can not change the RP fast enough. Finally, at the end of Chap. 7 (see Sect. 7.8), the implementation of quasi stationary OPs with adaptive thresholds is shown, which gives the possibility to detect a PRV fault. This is done for the completeness of the fuel system fault detection.

6.6 Fuel system fault detection residual results

This section deals with the residual results for the investigated faults from Sect. 6.4. The fault detection modules from Sect. 6.3 have been implemented into a dSPACE rapid prototyping system, the Micro Auto Box II, for an simultaneous to the engine ECU calculation on the test bench.

The residuals from Sect. 6.3 are divided into HP relevant residuals and LP relevant residuals. This implies, that for the actual observed faults the none visualized residuals are not relevant. Furthermore, the different investigated faults from Sect. 6.4 are implemented and executed sequentially on the test bench. All important signals for the fault-free states are recorded previously for different engine OPs. The tests are performed in the following chronological order:

1. Proof that the diesel engine is in its original condition (fault-free).
2. Implementation of previously defined fault (see Sect. 6.4).
3. Conduction of tests while recording all important data.
4. Repeat tests with different engine OPs, if required.
5. Restore original fault-free state.
6. Beginning of the next test.

All tests are made with an unmodified production engine to comply with the requirements of Sect. 3.7. Some parts are controlled by closed loop rather than open loop, e.g. LPP and HPP. In open loop controlled systems, the output residuals have a high degree of fault information. This information vanishes in closed loop, because the closed loop attempts to compensate for any disturbance or system uncertainties (see Sect. 2.4), if only the controlled variable is observed. When the system is designed with a two degree control (i.e. with an open loop and a closed loop control in combination), additional information can be gathered by the observation of the closed loop control output in addition to the controlled output. This closed loop control observation, described with residual r_2 (HPP fuel quantity closed loop control) from Sect. 6.3, will be performed for the HPP.

For all investigated test runs, a fault-free measurement was made with identical OPs for reference. For similar faults, the same OPs were chosen to illustrate the differences in their behavior. Hence, in every figure, the fault-free case and the different faults are visualized and the important characteristics for each fault are shown. The relevant variables for the test runs are:

- Estimated engine torque $\hat{M}_{\mathrm{eng}}$.
- Applied test cells water brake torque M_{br}.
- Engine speed n_{eng}.
- Actual fault F_{x}.
- Different relative (%) and absolute (Δ) fault sizes.

6.6.1 HP residual results

Fig. 6.12 shows the residuals for the fault-free state and the different faults F_1 as well as F_6 to F_8 for 30 engine cycles (each engine cycle with 720°CA), i.e. 60 crank shaft rounds.

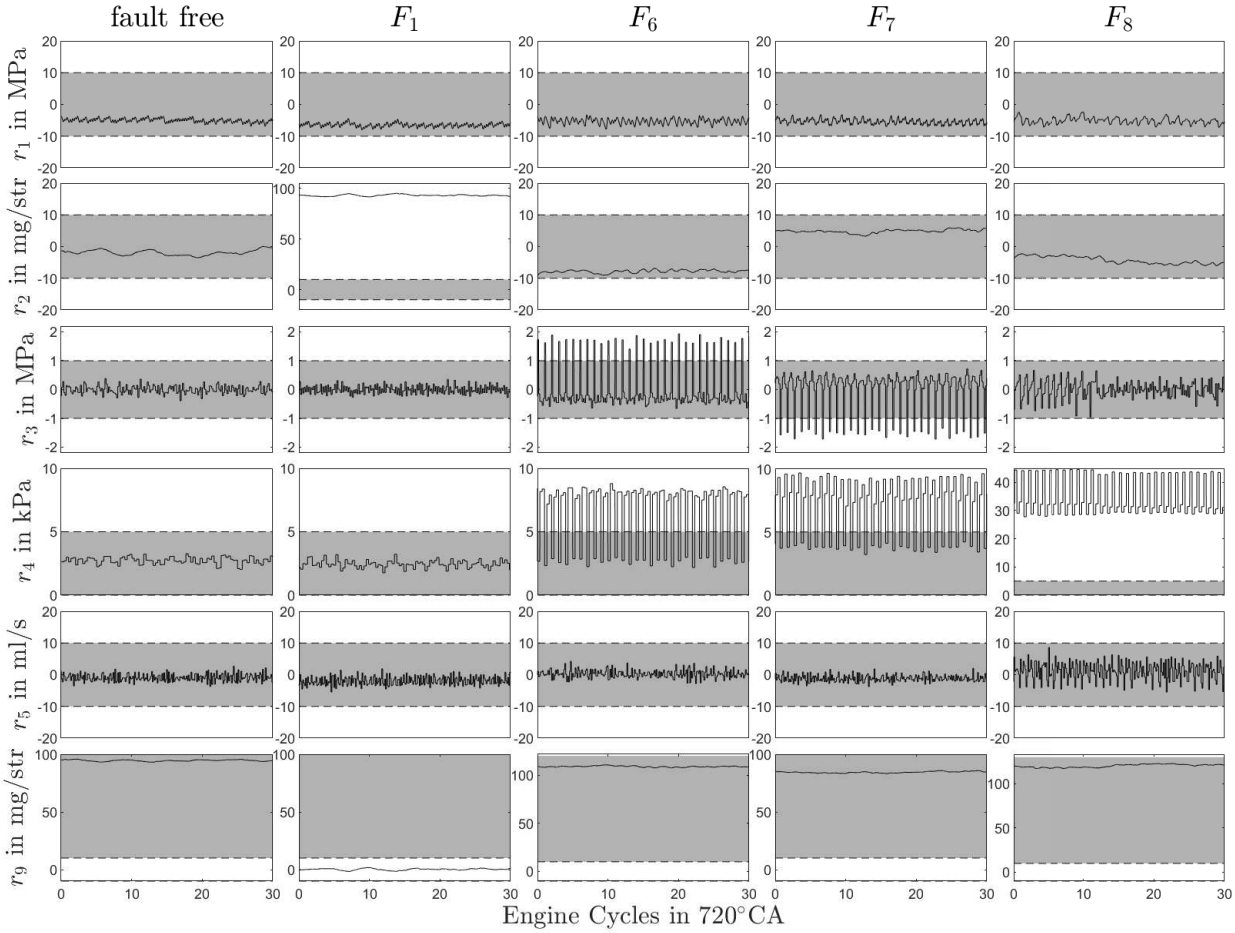

Fig. 6.12: HP residuals calculated from measured signals for a fault-free state and with faults (OPs according to Table 6.3): F_1 : HPP one plunger chamber does not supply fuel (low OP), F_6: Less injector mass flow quantity (Low Flow), F_7: Higher injector mass flow quantity (High Flow) and F_8: Engine misfire by compression loss.

Table 6.3: OPs and important parameters

graphs	n_{eng}	M_{br}	$\hat{M}_{\text{eng}}$	fault (parameter)	fault size in %	fault size in Δ
fault-free	1604 rpm	798 Nm	771 Nm	-	-	-
F_1	1600 rpm	799 Nm	774 Nm	PCV #1 unplugged	50	46,4 mg/str
F_6	1600 rpm	802 Nm	841 Nm	inj. 1 LF, q_{mi}	40	37,2 mg/str
F_7	1598 rpm	797 Nm	736 Nm	inj. 1 HF, q_{mi}	40	37,2 mg/str
F_8	1603 rpm	801 Nm	975 Nm	compression loss	100	0% air intake

The system is assumed to be in a fault-free state, if all residuals are in the gray shaded area, see first column in Fig. 6.12. To show proper functionality and stability of the residuals, they

are visualized over several engine cycles. The positive and negative thresholds (limits), which separates a fault-free from a faulty case, are determined experimentally from fault-free cases and different investigated faults. The limits are specifically chosen to detect small fault sizes on the one hand and to prevent fault misclassification on the other hand. As it is described in Sect. 6.5 a), the recorded faults are performed in stationary operation points.

In the graphs of the first column of Fig. 6.12 it can be seen that all residuals are in the gray shaded area, indicating that the system is in a fault-free state.
The second column shows the graphs for a PCV pump fault F_1, where the residuals r_2 (HPP fuel quantity closed loop control) and r_9 (ECU HPP fuel quantity open/closed loop comparison) occur. Especially residual r_9 only occurs for this fault, because the HPP has two pumping elements (see Sect. 3.5). In the case of one element having a fault, the closed loop HPP fuel quantity control compensates for the fault by requesting the double amount of fuel from the healthy pump chamber (see Sect. 6.3.9). In this case, the closed loop and the open loop pump quantity become equal and the residual r_9 occurs. This is because the occurrence of r_9 is reversed, see the gray shaded area in Fig. 6.12 column two, sixth row (zero means the residual occurs).

In the graphs of the third column, the residual of an injector less fuel quantity (Low Flow) fault F_6 in one cylinder is shown. As mentioned in Sect. 6.4.1, these faults can not be observed from the electrical system of the injector. This implies that the signal must be observed with process or signal model-based approaches rebuilding a physical system behavior or a pattern. Residual r_3 (RP uniformity residual) and r_4 (EMP uniformity residual) show the results of a signal model-based approach. The sign tendency of residual r_3 is also important to identify the difference between an injector Low Flow F_6 and High Flow F_7 fault and to isolate the different injector faults (see Sect. 7.2). Also, the graphs in the second row of Fig. 6.13 indicates that the direction of r_2 (HPP fuel quantity closed loop control) is recognizable for F_6 and F_7, but stays within the threshold. The reason behind the changed r_2 is a decreased or increased fuel mass injection caused by the injector Low Flow F_6 or High Flow F_7 faults, resulting in a decreased or increased HPP fuel quantity closed loop control fuel mass (fault compensation). Furthermore, residual r_3 and r_4 show a periodic occurrence (see Fig. 6.12 column three and four). The origin of this is mainly caused by the residual calculation and was described in Sect. 6.2.1 and 6.2.2 for two engine cycles (see Fig. 6.2 and Fig. 6.3 each row four column three). Identical to Sect. 6.2.1 the residual r_3 occurs for F_6 every 720°CA for an interval of 120°CA. This points to a faulted injector.

Analogous to the Low Flow injector fault, a higher fuel quantity (High Flow) fault F_7 shows the same occurrence of residuals with the difference of the direction of r_3 and the tendency of r_2. Summarized for single injector Low Flow F_6 or High Flow F_7 faults, only the tendency of r_2 is recognizable. This changes for multiple simultaneous injector faults. Then r_2 will occur in the direction of the respective specific injector fault (see Sect. 7.6). Similar to F_6 the residual r_3 and r_4 show also a periodic occurrence for F_7.

In the last column of Fig. 6.12 a misfire F_8 with a compression loss is inserted. In this case only r_4 (EMP uniformity residual) occurs and directly indicates a misfire fault. Here the residual r_4 shows a periodic occurrence.

Fig. 6.13 visualizes the faults from F_2 through F_5.

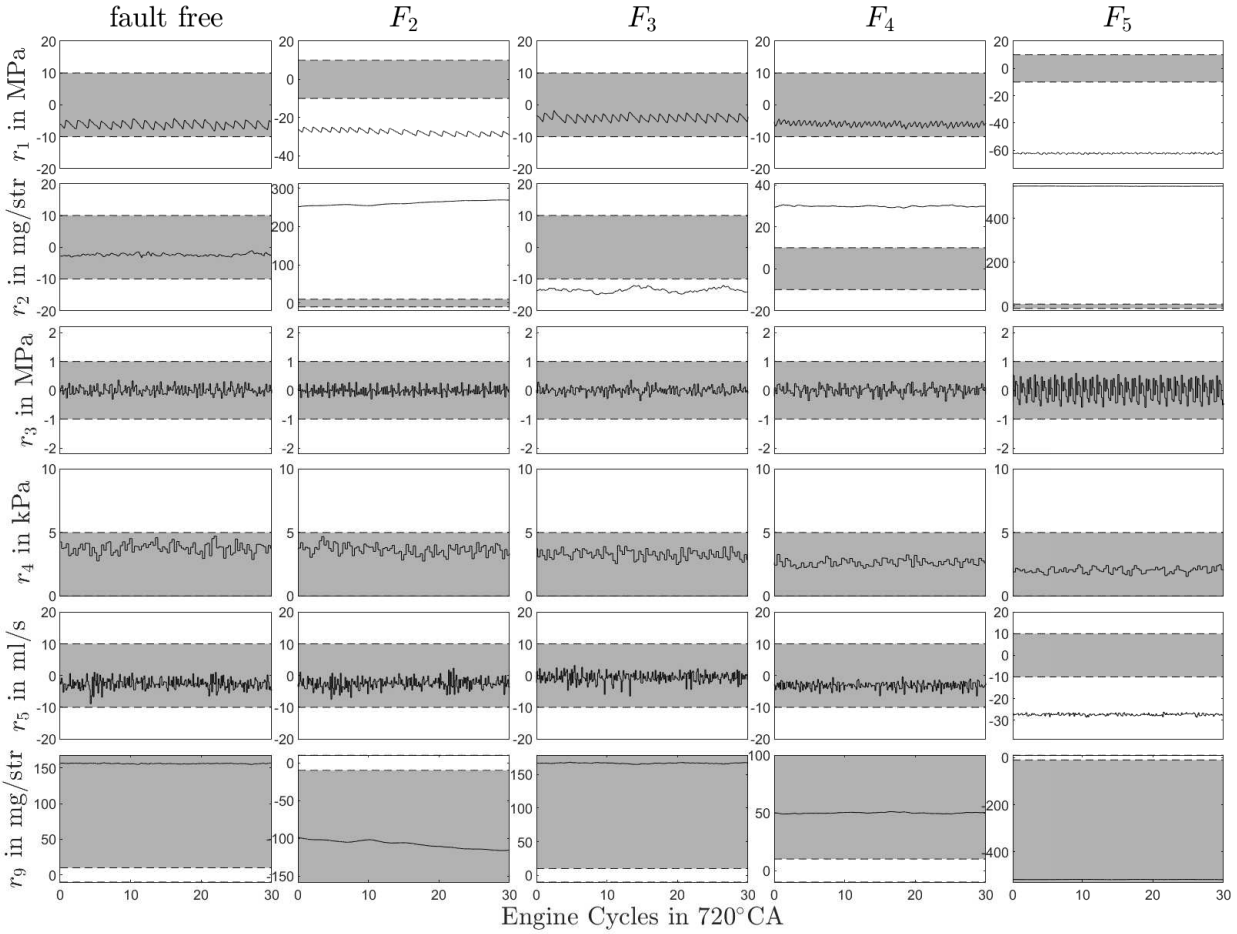

Fig. 6.13: HP residuals calculated from measured signals for a fault-free state and with faults (OPs according to Table 6.4): F_2: HPP fails to build up RP (high OP), F_3: RP sensor High Offset, F_4: RP sensor Low Offset and F_5: PRV or HP Leakage.

Table 6.4: OPs and important parameters

graphs	n_{eng}	M_{br}	$\hat{M}_{\text{eng}}$	fault (parameter)	fault size in %	fault size in Δ
fault-free	1600 rpm	1341 Nm	1300 Nm	-	-	-
F_2	1597 rpm	1342 Nm	1302 Nm	PCV #1 unpl./saturation	50	77 mg/str
F_3	1599 rpm	802 Nm	881 Nm	p_{rail}	10	35 MPa
F_4	1401 rpm	798 Nm	667 Nm	p_{rail}	10	35 MPa
F_5	1604 rpm	396 Nm	1301Nm	PRV/HP Leakage	100	300 mg/str

Fault F_2 (column two) shows a PCV pump fault, where the healthy pump chamber can not compensate the missing amount of requested fuel for a specific RP setpoint. This means that the healthy pump chamber already delivers fuel with its maximum capacity (saturation of healthy pump chamber exceeded). In this case r_2 (HPP fuel quantity closed loop control) occurs, but not r_9 (ECU HPP fuel quantity open/closed loop comparison) because the HPP fuel quantity control

requests more pump quantity then one pump element can deliver. As a result, the closed loop part increases compared to the open loop part. Furthermore, the RP can not be held and the residual r_1 (Physical rail pressure model) occurs.

The next two faults F_3 and F_4 illustrate the most challenging faults to detect, RP sensor offset faults, because r_1 (Physical rail pressure model) does not occur due to the HPP fuel quantity control fault compensation. This means that the HPP fuel quantity closed loop control, due to the RP mismatch, acts similar for F_3 and F_4 for an HPP fault F_1 (see description for HPP fault in Sect. 6.3.9). In the real system this will force the real RP to a lower value for F_3 and a higher value for F_4 compared to the RP setpoint. This is challenging to detect, because the measured RP value will still be equal to the RP setpoint. Here, only residual r_2 (HPP fuel quantity closed loop control) occurs and makes it difficult to distinguish these faults from HPP faults (see fault F_3 and F_4 in Fig. 6.13 compared to F_1 in Fig. 6.12). This is the reason of the development of the additional residual r_9 (ECU HPP fuel quantity open/closed loop comparison), which only occurs for an HPP fault F_1, see Fig. 6.12.

For the HP Leakage fault F_5 (fifth column), three residuals occur r_1 (Physical rail pressure model), r_2 (HPP fuel quantity closed loop control) and r_5 (Physical volume flow models LPP / MP inlet). Both pumping elements are fault-free and there is an inner leakage from the injector line five to the cylinder head back into the fuel tank. Specifically r_5 is a good indicator for any leakage faults in the fuel system.

In the Appendix A.3 additional injector residual results for smaller fault sizes and multiple injector faults are shown.

In summary, all implemented HP faults can be detected.

6.6.2 LP residual results

In Fig. 6.14 the residual results for the LP faults are visualized.

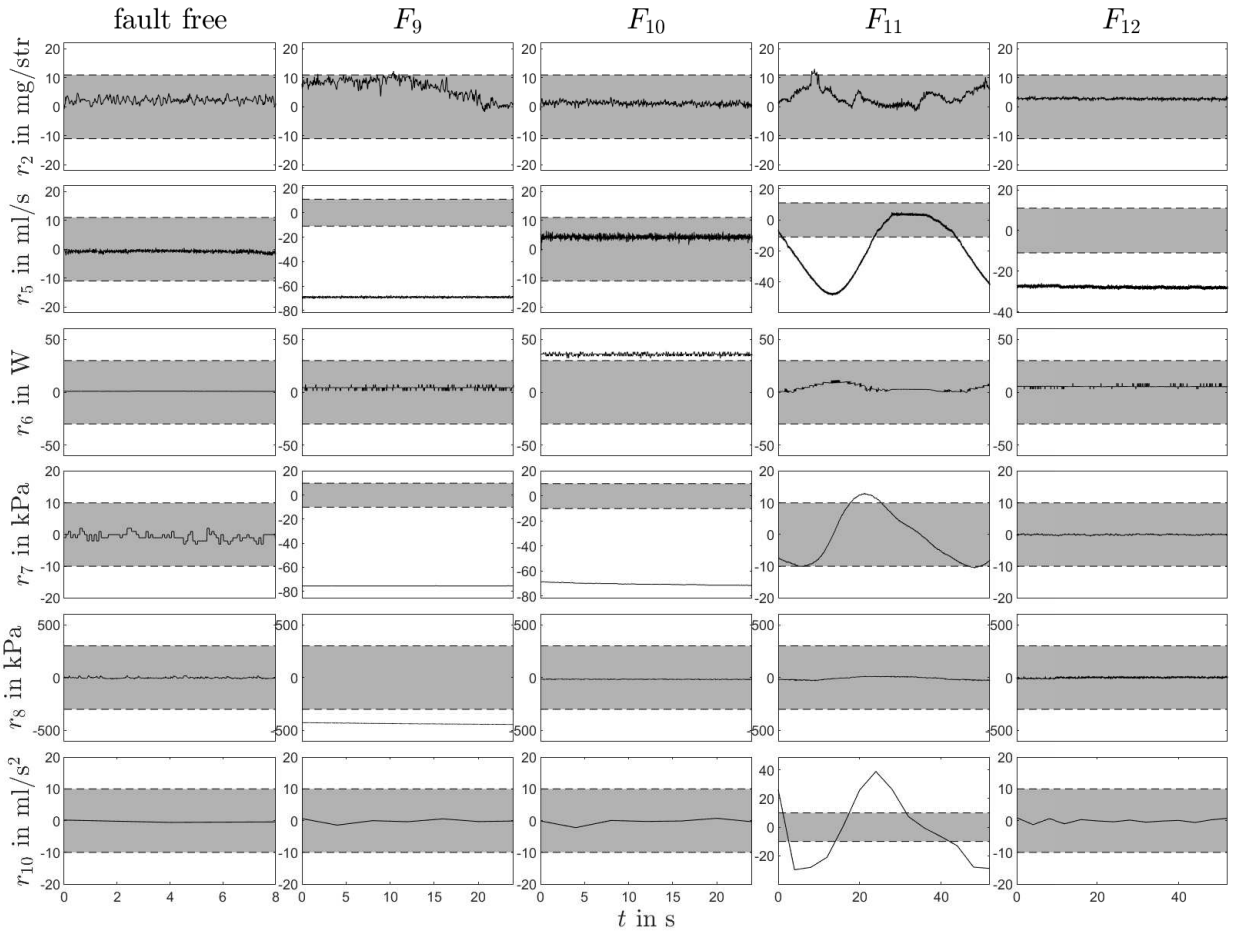

Fig. 6.14: LP residuals calculated from measured signals for a fault-free state and with faults (OPs according to Table 6.5): F_9: Primary fuel filter restriction, F_{10}: Secondary fuel filter restriction, F_{11}: Primary fuel filter inlet leakage and F_{12}: Secondary fuel filter outlet leakage.

Table 6.5: OPs and important parameters

graphs	n_{eng}	M_{br}	$\hat{M}_{\text{eng}}$	fault (parameter)
fault-free	1601 rpm	66 Nm	79 Nm	-
F_9	1600 rpm	69 Nm	81 Nm	Primary fuel filter restricted
F_{10}	1601 rpm	402 Nm	418 Nm	Secondary fuel filter restricted
F_{11}	1599 rpm	66 Nm	79 Nm	Primary fuel filter inlet leakage
F_{12}	1602 rpm	65 Nm	77 Nm	Secondary fuel filter outlet leakage

Analogous to the HP fault visualization, the first column shows a fault-free state. In contrast to the HP residuals, which are represented in a crank angle-based domain, the LP residuals are represented in a time-based domain (see Sect. 6.4).

The first introduced fault of the LP system is a primary fuel filter restriction F_9 (location of the different fuel parts see Fig. 3.2), where the fuel filter has a restriction e.g. caused by polluted fuel. The graphs of the second column in Fig. 6.14 show the residual results of this fault. It can clearly be seen that the residuals r_5 (Physical volume flow models LPP / MP inlet), r_7 (Low pressure model) and r_8 (HCI pressure limit check) decrease. The big LP pressure decrease observed with r_7 (LP falls under atmospheric pressure) is caused by a restriction, extremely reducing the fuel supply. The LPP is closed loop controlled with the LP sensor signal (see Sect. 3.3). In case the pressure does not react on an increased pump speed, the pump will rise the speed signal until its speed saturation. In other words, the LPP tries to compensate for the LP decrease by pulling more fuel into the system with an increased pump speed. In the condition of a fault-free case, this pump speed rise of the LP displacement pump generates an increased inlet volume flow (see Sect. 4.7.1). Finally the modeled volume flow of the LPP and the inlet of the MP system differs and the residual r_5 occurs. A third indicator for this fault is the occurrence of r_8, which illustrates a HCI pressure decrease caused by an insufficient fuel delivery.

The graphs in the third column illustrates the LP residuals results for a secondary fuel filter restriction F_{10}. In case of a closed loop LPP activation, the pressure $\Delta p_{\mathrm{lpp,out}}$ at the outlet of the LPP increases in case of a secondary fuel filter restriction. Contrary to this pressure increase for $\Delta p_{\mathrm{lpp,out}}$, the LP Δp_{lp} decreases. The pump needs more mechanical torque to generate a higher delta pressure to push the fuel through the secondary fuel filter. The amount of fuel stays the same (as for a fault-free case) because the LPP already supplied fuel to the outlet of the LPP (inlet of secondary fuel filter). As a result, the electrical power rises and gives a difference compared to the hydraulic model which stays the same. Finally, residual r_6 (Physical power model LPP) rises and r_7 (Low pressure model) falls.

The graphs in the fourth column of Fig. 6.14 show the LP residual results for a primary fuel filter inlet leakage F_{11}. For this special fault, the LPP pulls a fuel/air mixture into the LP fuel system, which results in a pressure oscillation visualized in residual r_7 (Low pressure model). It is already described above, that the LPP is closed loop controlled on the LP, which evokes an oscillation in pump speed and LP inlet volume flow. The cause of this phenomenon is the density change of the fuel/air mixture and additionally the compressibility change of this mixture compared to the pure diesel fuel. To detect this fault, an additional residual r_{10} (Physical volume flow models LPP / MP inlet trend checking) is generated out of residual r_5 (Physical volume flow models LPP / MP inlet) with a gradient check.

The secondary fuel filter outlet leakage fault F_{12} is shown in the fifth column of Fig 6.14. Here the residual r_5 (Physical volume flow models LPP / MP inlet) occurs. This points to a deviation between the LP inlet volume flow and the MP inlet volume flow due to a leakage fuel flow out of the additional fuel line connection behind the secondary fuel filter into the environment.

Finally, it can be seen that all faults from Table 6.2 can be detected.

6.7 Summary

In this chapter different signal and process model-based fault detection algorithms in combination with conventional algorithms, like limit checking, were discussed.
In the beginning a uniformity analysis of the RP and EMP signal was described to gain suitable uniformity residuals for the fault detection. In the same section it was shown that it is possible to detect an injector fault, as well as a cylinder misfire fault.
For the process model-based fault detection, the modeled physical behavior is the foundation for the analytical residuals, which contain a higher degree of system information. This can specifically be seen for the leakage detection with residual r_5. The basis for this residual is the physical volume flow models for the LPP and the MP inlet. These process models can only be generated by combining the inner physical relationships. E.g. for the MP inlet volume flow, combining the mass balance equation of the MPP outlet with the mass balance equation of the MPP inlet, including an estimation of the MP.
Also, the uniformity analysis residuals, which are signal model-based approaches, contain a higher degree of information.
Further on a set of the most important HP and LP faults were described and the root cause of each fault was discussed. The separation of the HP and the LP residuals, due to their independent propulsion, significantly reduces the complexity of the fault detection. For the fault detection, stationary OPs and therefore fixed thresholds were chosen. This was mainly driven by the applications, where the heavy duty engine is used and the proper calculation of the uniformity analysis itself. Furthermore, the fault test insertion was discussed.
Finally, the fault detection results were shown for HP and LP residuals. Here, the gray shaded area highlighted the fault-free condition. In the following chapter, it will be seen that the developed residuals give the possibility to isolate and diagnose most underlying faults.

7 Diesel engine fuel system fault diagnosis

In this chapter an inference system-based fault diagnosis concept is discussed, which includes a new isolation concept for injector and misfire faults. Based on the uniformity analysis of the RP and EMP sensor signals, in a crank angle synchronous representation, additional information for the fault isolation can be gathered. With the help of operator knowledge and the collected system information, an inference method-based fault diagnosis system is developed and visualized with fault symptom tables as well as fault trees. Further on the faults OP dependency is discussed and an active fault test for the LP system is described. The active test gives the possibility of isolating additional faults with an increased level of system information. Finally, a short overview of a fault detection in transient operation states is given. This can be used for an enlarged fault detection of components only active in transient OPs, like the PRV.

7.1 General fault diagnosis structure

The limit checking, trend checking, signal- and process model-based fault detection algorithms were already discussed in the previous Chap. 6. These algorithms and especially the generated residuals are the basis for the symptom generation and evaluation, which is furthermore the foundation of fault diagnosis. Fig. 7.1 visualizes this context, where specifically in this chapter the fault diagnosis is highlighted. With the information of the fault detection, system or operator based heuristic symptoms as well as analytical symptoms can be generated. Based on these symptoms, inference and classification methods lead to the evaluation results of the underlying faults. Hence, the fault diagnosis provides the information of the fault type, size and location. These characteristics in turn form the basis for the fault management system.

This chapter introduces an inference method-based fault diagnosis system for the fuel path of a heavy duty diesel engine. The developed diagnosis works in normal engine operation mode. The following inference method-based fault diagnosis is developed with the help of fault symptom tables and the developer's knowledge in IF-condition-THEN-conclusion rules. Finally, the fault diagnosis representation is visualized with a fault tree for a few representative examples to show the structure and relationship between the symptoms and faults.

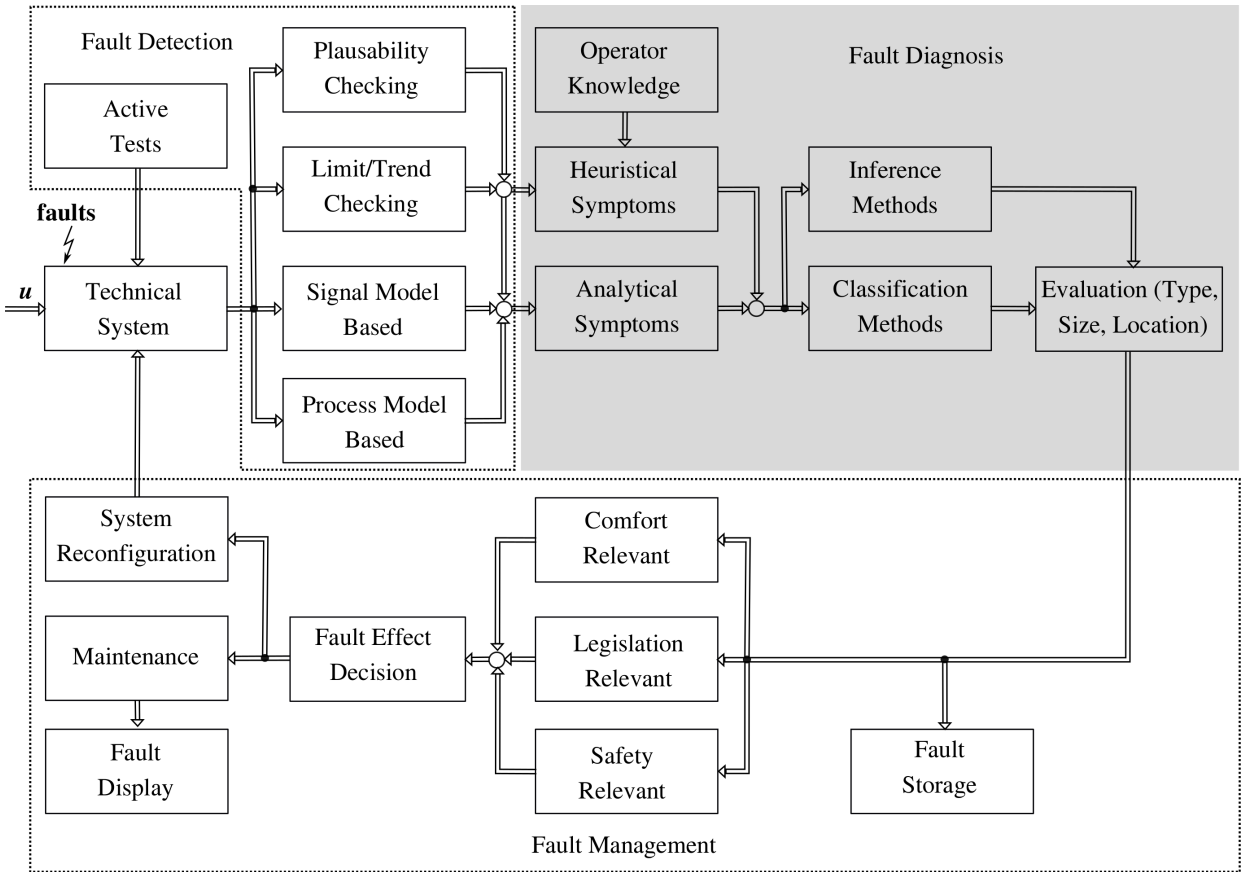

Fig. 7.1: Overall diagnosis structure with the main focus on fault diagnosis, according to [58]

7.2 RP and EMP uniformity analysis for injector and misfire fault isolation

In Sect. 6.2.1 the concept of an injector fault detection with the help of the uniformity residuals was previously described. The same holds true for the concept of a misfire fault detection explained in Sect. 6.2.2. In the following sections the injector and misfire fault isolation will be discussed.

7.2.1 RP uniformity analysis for the injector fault isolation

For the calculation of the RP uniformity residual additional information, i.e. the injector fault location, can be gathered with a skillful choice of the periodic angle of residual r_3 (see also equation (5.7)). Therefore, two main conditions have to be ensured:

- The HPP fuel quantity control should operate in closed loop control.
- The HPP fuel delivery frequency has to be designed for a multiple fuel injection (firing distance) frequency, see Sect. 5.5.

Specifically the closed loop HPP fuel quantity control is needed to stabilize the system due to the compensation of HPP or injector faults. For these faults the HPP fuel quantity control activity was analyzed i.a. in Sect. 6.2.1. The second condition of a multiple HPP fuel delivery to fuel injection frequency (firing distance) is needed to directly allocate the injector number to a faulted injector. The assumption that in the fault-free case the HPP fuel delivery should be a multiple instead of an equal frequency of the fuel injection frequency (see Sect. 5.5) will be shown in the next two figures. Both illustrations are simulated with the basic equation (4.11), which was developed in Sect. 4.2. The variation of the injector or HPP volume flows show the different influences of a possible injector fault on the RP signal. Also, a crucial advantage is the injector isolation with the help of the uniformity analysis will be shown. The different columns in Fig. 7.2 visualize a fault-free state, an HPP fault, an injector fault and an HPP plus injector fault.

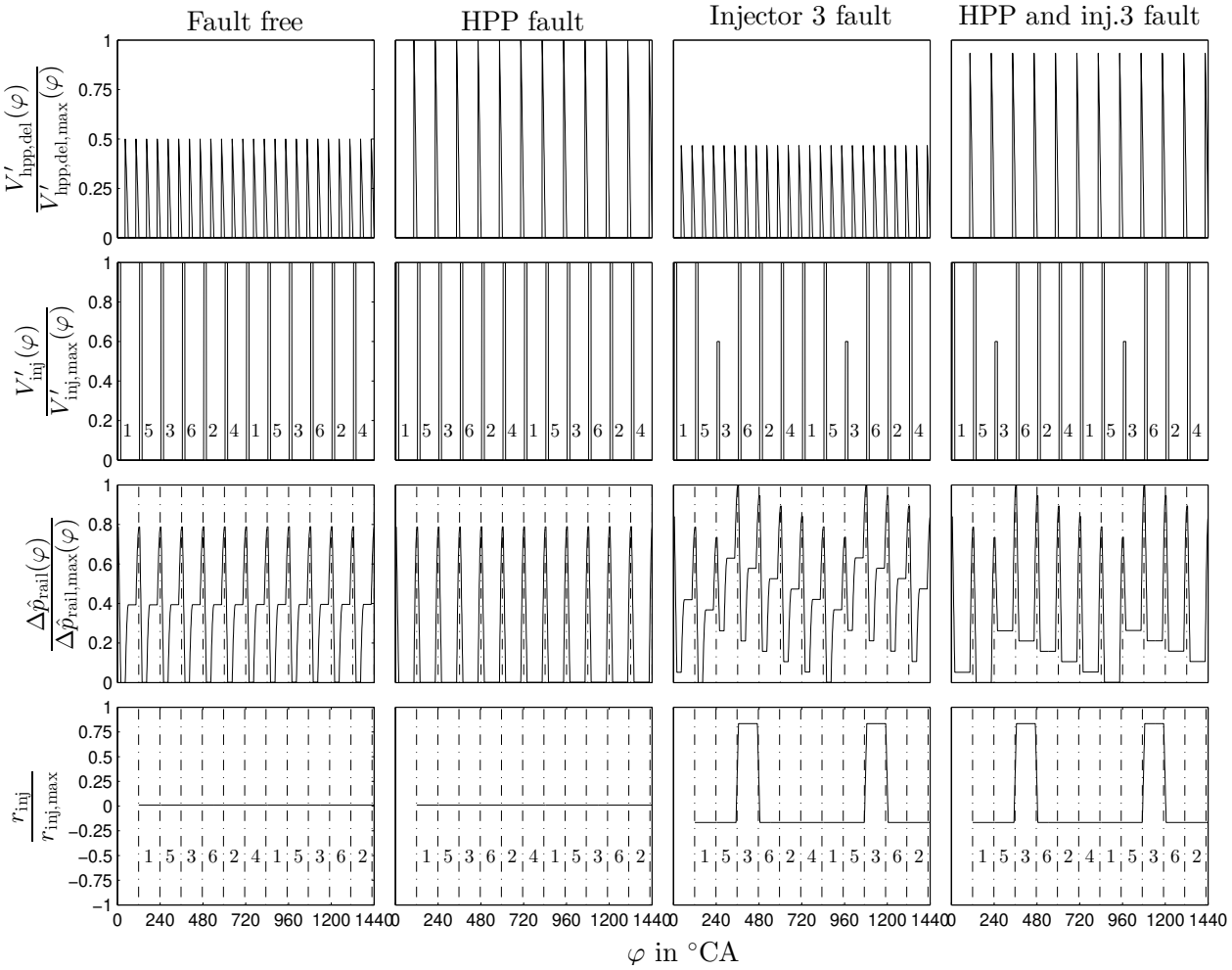

Fig. 7.2: Simulated RP signal for multiple HPP fuel delivery to fuel injection frequency and uniformity residuals for **column one:** A fault-free state, **column two:** An HPP fault (no fuel delivery from pump chamber 1), **column three:** Injector 3 fault (40% less fuel quantity (LF)) and **column four:** An HPP in combination with injector 3 fault.

In Sect. 6.2.1 it was already described that the uniformity residual r_{inj} can detect an injector fault. Furthermore, it was described that the residual signal itself is again periodic over 720°CA. In Fig.7.2 an observation of the injector residual (row four) shows the occurrence of the injector 3 Low Flow fault over 120°CA, with a phase shift of again 120°CA. This is caused by the residual calculation, see equation (6.1). Furtherer, an index is introduced which counts up in the cylinder firing order for the injector residual (see 2. and 4. row of Fig. 7.2). With a correlation between the index and the occurring injector residual r_{inj}, the injector location can be directly identified. The direction of occurrence of the injector residual provides the information whether it is a high or low flow injector fault (see Fig. 6.12). This is because the mean RP either increases or decreases for the faulted injector after its injection cycle. With this new information the injector fault type and location can directly be isolated.

Further on, a combination of the HPP fuel quantity control closed loop activation (residual (6.8) monitors this behavior), the direction of the r_2 occurrence, the direction of the r_3 (RP uniformity residual which represents the residual r_{inj}) occurrence and the injector fault numbers, up to five multiple Low or High Flow injector faults can be isolated simultaneously. Fig. 6.12 shows this r_2 tendency and Fig. A.6 in the Appendix shows the residuals for up to 3 simultaneously injector Low Flow faults. A deeper analysis and the isolation of all injector faults will be discussed in the following sections.

Fig. 7.3 illustrates the system behavior for an equal HPP fuel delivery to fuel injection frequency described in the second case of Sect. 5.5. Analog to the previous scenario the same faults are imprinted. The closed loop HPP fuel quantity control has the same behavior compared to Fig. 7.2. The main difference is, that the HPP activation supplies fuel every 120°CA in a fault-free case, whereas in an HPP fault the second HPP period $\tau_{\text{hpp,sec,eq}} = 240°\text{CA}$ occurs. The injector second period which occurs in case of a fault, stays equal to the previous case. Analog to the previous case, the multiple frequency scenario, the second period $\tau_{\text{hpp,sec,eq}}$ is used for the residual calculation. With this period change to 240°CA, the information of the injector fault location vanishes. This is because two injector fault numbers will occur for a single injector fault, see in Fig. 7.3 row four. Here, a fault in injector 3 ends up in an occurrence of the injector fault numbers 3 and 6. Hence, in this case it is not possible to isolate the location of a single injector fault.

The final comparison of the two scenarios (Fig. 7.2 and 7.3) illustrates smoother fuel delivery for a multiple injector frequency to HPP fuel delivery frequency. This can also be seen in a comparison of the RP signals for both scenarios. Comparing the residual r_{inj} signals of both scenarios in case of an injector fault, see Fig. 7.2 and 7.3 row four, column three (four), shows that for residual r_{inj} the positive amplitude is larger and the negative amplitude is smaller for the first scenario. This is due to the fact, that the residual calculated over 240°CA compared to the residual calculated over 120°CA has an enlarged filtering behavior.
Finally, this implies a stronger residual sensitivity for an injector fault in the first scenario.

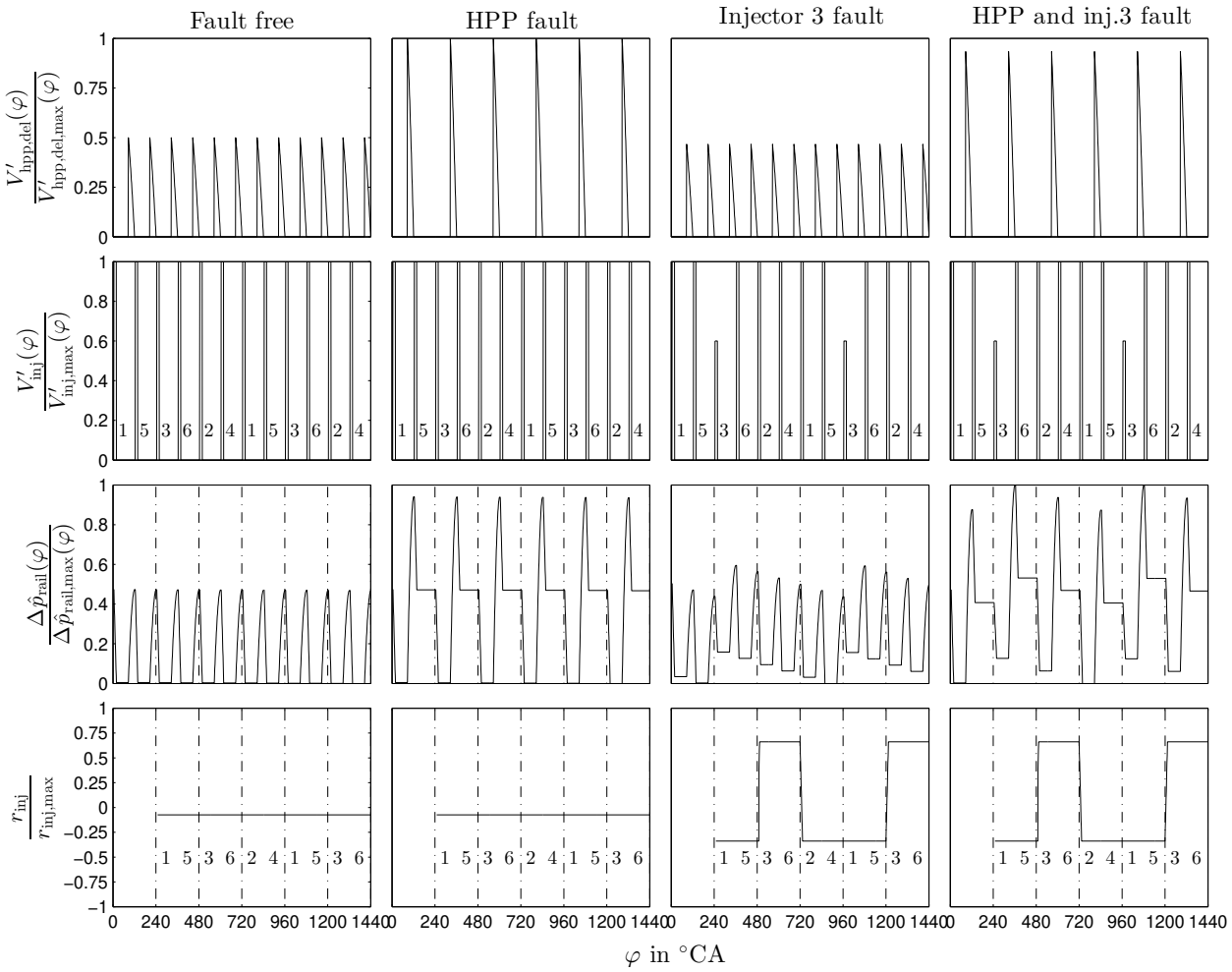

Fig. 7.3: Simulated RP signal for equal HPP fuel delivery to fuel injection frequency and uniformity residuals for **column one:** A fault-free state, **column two:** An HPP fault (no fuel delivery from pump chamber 1), **column three:** Injector 3 fault (40% less fuel quantity (LF)) and **column four:** An HPP in combination with injector 3 fault.

7.2.2 EMP uniformity analysis for the misfire fault isolation

In Sect. 5.2 it is mentioned that the combustion, the EMP sensor location and the separated exhaust manifolds (see Fig. 5.6) are the main characteristics influencing the pressure oscillations for the EMP sensor signal. However, these characteristics give the possibility to calculate the uniformity residual for the EMP signal (with equation (5.7)) in two ways:

1. $r_{\mathrm{ua,emp,1}}$: With the periodic angle equal to the supervised angle period $\tau_{\mathrm{u}} = \tau_{\mathrm{s}} = 240°\mathrm{CA}$ in the following called UA-EMP-1.

2. $r_{\mathrm{ua,emp,2}}$: With the periodic angle not equal to the supervised angle period $\tau_{\mathrm{u}} = 120°\mathrm{CA}$ and $\tau_{\mathrm{s}} = 240°\mathrm{CA}$ in the following called UA-EMP-2.

The UA-EMP-1 case represents the residual (6.10) which is calculated with an absolute value, whereas the calculation of UA-EMP-2 yields signed values. With this signed evaluation the cylinder position of a misfire fault can be identified, similar to the injector fault isolation.

Fig. 7.4 illustrates the calculation of UA-EMP-1 and UA-EMP-2 for a measured EMP signal.

The principle of the UA-EMP-1 is based on a uniformity calculation every 240°CA (τ_u) with its phase shifted signal of 240°CA (τ_s), residual calculation see equation (6.3). This means, that in case of a single misfire fault one cylinder of each exhaust manifold group (I-Indirect: 1-3 and D-Direct: 4-6 see Fig. 5.6) can have a misfire in the actual calculated interval, if the uniformity residual occurs. The cylinder index in both graphs in Fig. 7.4 show the activation of each cylinder at different intervals. Also, the direct and indirect pressure signal of the EMP sensor is recognizable. In Fig. 7.4 a) the full arrow (line) shows the sequence (or intervals) for the calculation of residual $r_{\mathrm{ua,emp,1}}$.

The principle of the UA-EMP-2 is based on a uniformity calculation with $\tau_u = 120°\mathrm{CA}$ with its phase shifted signal over $\tau_s = 240°\mathrm{CA}$. According to equation (5.7) the residual is given by:

$$r_{\mathrm{ua,emp,2}} = \frac{1}{120[°\mathrm{CA}]} \int_{\varphi}^{(\varphi+120[°\mathrm{CA}])} [p_{\mathrm{em}}(\varphi) - p_{\mathrm{em}}(\varphi - 240[°\mathrm{CA}])]\,\mathrm{d}\varphi. \tag{7.1}$$

This provide the benefit of a pressure signal comparison for each cylinder in the same group. E.g. for the direct exhaust manifold group (4-6, see Fig. 5.6) to another cylinder in the same group. The same applies to the indirect exhaust manifold group. Fig. 7.4 b) visualizes the sequence of alternating calculation for the residual $r_{\mathrm{ua,emp,2}}$ with the dotted arrow (lines) for the intervals of the direct group and the full arrow (lines) for the indirect group. This sequence guarantees a comparison of direct to direct and indirect to indirect pressure waves.

Fig. 7.5 illustrate a measured cylinder one misfire example (here shown with an injector 1 fault, which has a similar behavior on the EMP signal, see Sect. 5.2) and the difference between UA-EMP-1 and UA-EMP-2. In the first row the EMP signal for a fault-free and a misfire in cylinder 1 is visualized. The residual in the second row shows the results for UA-EMP-1. The residual is not influenced in a fault-free state, whereas in case of a misfire the residual deviates. Analog to Sect. 7.2.1 with the difference of two indexes in cylinder firing order are introduced. The upper index shows the activation of the actual cylinders with a delay caused by the calculation. The lower index hereby illustrates the previous active cylinders. These were active in the previous signal segment with a phase shift over 240°CA. This directly show the difference to the RP uniformity calculation from the previous section having, in case of a single injector fault, only one residual occurrence over one engine cycle. The reason for this lies in the accurate HPP fuel quantity control functionality compensating different fuel delivery or injection faults immediately. In case of a single injector fault, there is only one significant RP change (for details see previous Sect. 7.2.1). In contrast to this and in the case of a single misfire fault the missing compensation led the EMP sensor signal to deviate two times with alternating signs, see UA-EMP-2 calculation in the third row, second column of Fig.7.5. The residual $r_{\mathrm{ua,emp,1}}$ shows only positive values caused by an absolute value calculation.

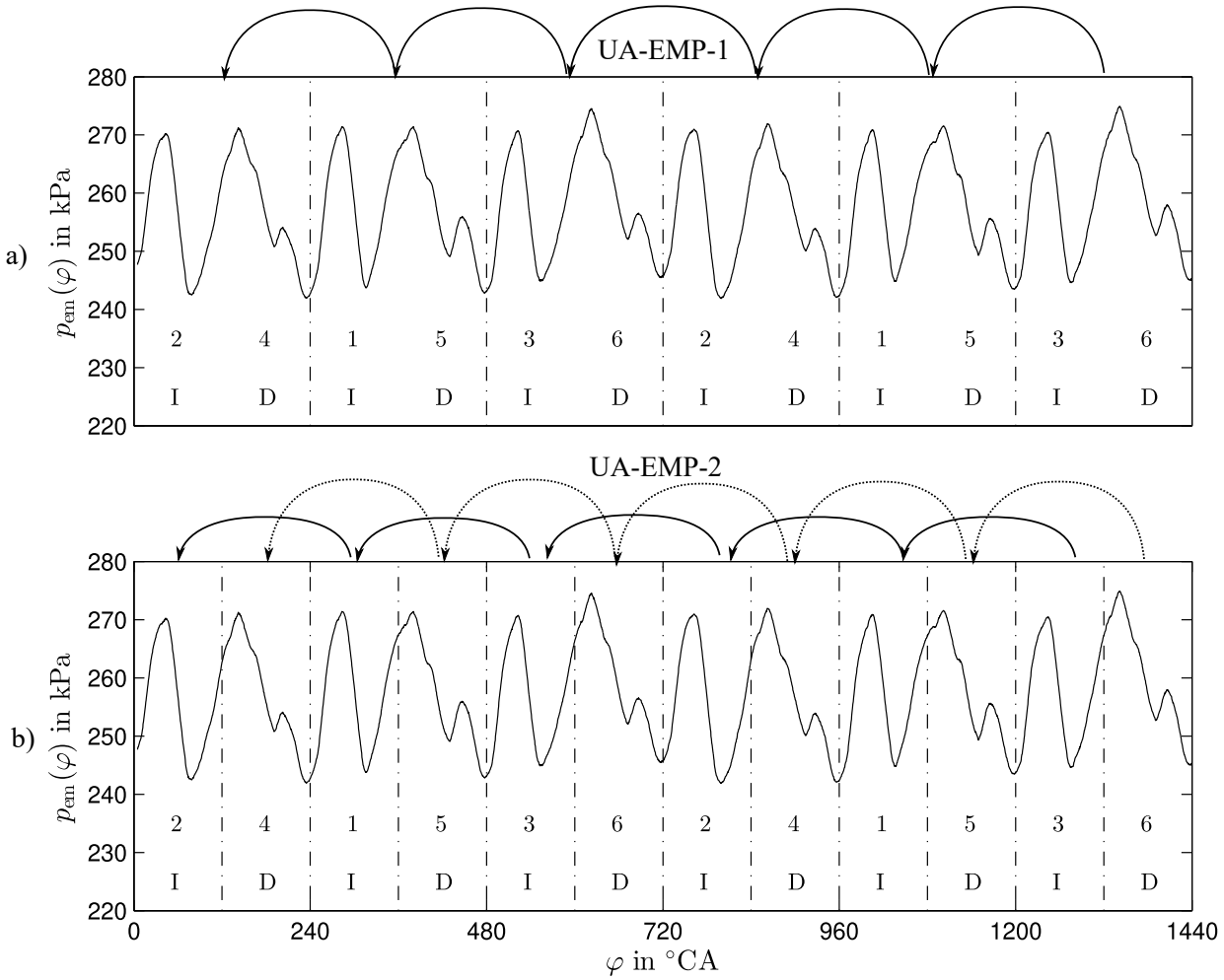

Fig. 7.4: Principle of uniformity residual UA-EMP-1 and UA-EMP-2 calculation shown for an EMP measurement

The upper and lower indexes point to the location of a misfire fault in a cylinder pair. The cylinder pair is defined by the section of calculation in terms of UA-EMP-1 over 240°CA. If the residual occurs two times, over one engine cycle, with the same cylinder pair numbers for the upper and lower index, the cylinder pair numbers with the misfire fault is found (in this example 1 and 5). With the UA-EMP-1 only two cylinder (pair) numbers can be identified in a single cylinder misfire fault as well as a multiple cylinder misfire fault. This makes it impossible to differentiate between a single misfire in this specified cylinder pair (1 or 5), or even in the case that both have a misfire (1 and 5).

To cope with this issue the residual calculation can be made with UA-EMP-2, see equation (7.1). As it is described above, the calculation of this residual is made over 120°CA with the supervised angle period of 240°CA. This has the background of comparing only the direct EMP signals (cylinder 4,5,6) and only the indirect EMP signals (cylinder 1,2,3) with each other. It ensures furthermore a correct signal comparison in the matching cylinder groups. Now the upper cylinder misfire index shows the actual cylinder activation in the current calculated interval. The lower index shows the previously active cylinder. With this combination it is possible to allocate a single

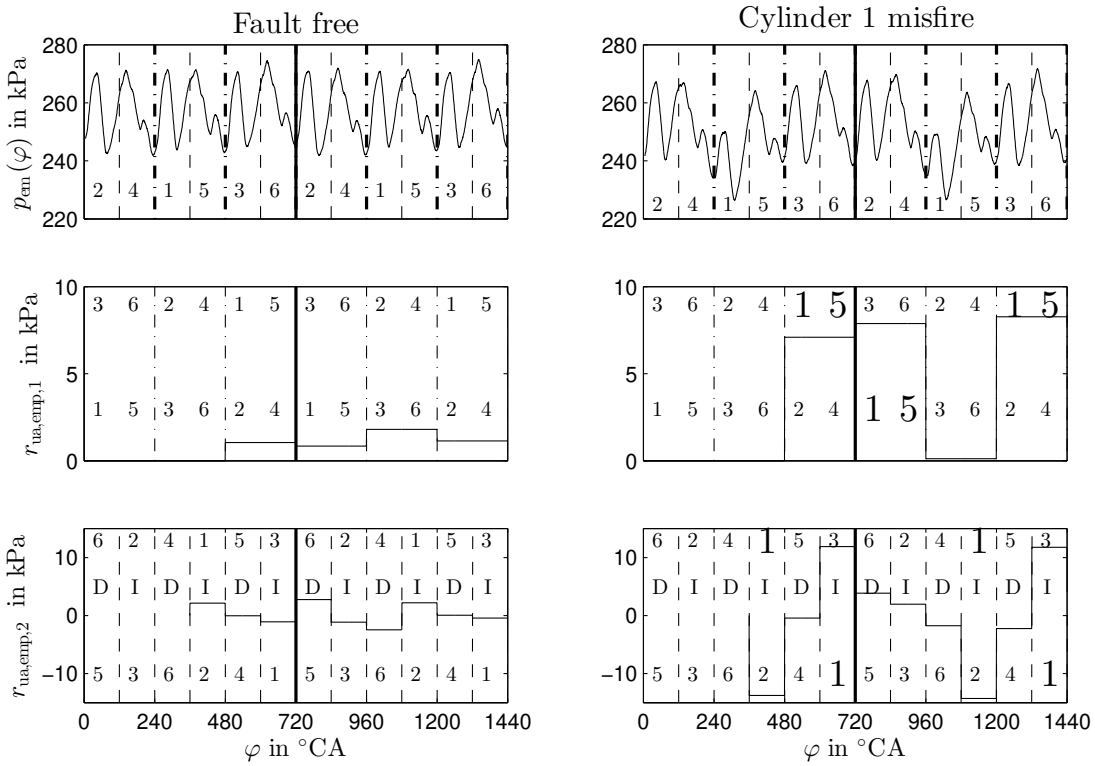

Fig. 7.5: Principle of EMP uniformity residual calculation UA-EMP-1 and UA-EMP-2 for measured cylinder 1 misfire

cylinder misfire fault to its fault location, if the residual $r_{ua,emp,2}$ occur two times over one engine cycle with the same number for the upper and lower index (here cylinder 1, see third row, second column in Fig. 7.5).

In a final conclusion, an injector or a misfire fault can be isolated with the uniformity residual UA-EMP-2 $r_{ua,emp,2}$.

7.2.3 Conclusion for the uniformity analysis isolation concepts

The uniformity analysis has the benefit of a simple implementation with robust results due to its noise resistance. The computational effort is small and can be easily applied to modern ECUs. An additional advantage is that the uniformity residual does not need to be applied for different engine OPs. This behavior concludes in the statement, that in a stationary engine OP the signal characteristic of the observed signal can change drastically over different engine OPs. The uniformity residual calculation is not influenced by the changed signal characteristic, if the signal is periodic for the supervised angle period.
Summarized, it was shown in Sect. 7.2.1 that a single injector fault type and location can be isolated with the help of (see Sect. 6.3 for residual descriptions):

- The occurrence of r_3 (RP uniformity residual).

- The direction of the r_3 occurrence.
- The occurrence of r_4 (EMP uniformity residual).
- The injector fault number.

With the same methodology from Sect. 7.2.1 it is possible to isolate the type and location of up to 5 injector High or Low Flow faults with:

- The occurrence of r_2 (HPP fuel quantity closed loop control).
- The direction of the r_2 occurrence.
- The occurrence of r_3 (RP uniformity residual).
- The direction of the r_3 occurrence.
- The occurrence of r_4 (EMP uniformity residual) in combination with r_3.
- The injector fault number(s).

Note, the conditions in Sect. 7.2.1 with the closed loop control and the multiple HPP fuel delivery to fuel injection frequency must be fulfilled.

A single misfire in one cylinder (caused by a compression loss) can be isolated with the discussed second residual UA-EMP-2 in Sect. 7.2.2 with:

- The occurrence of $r_{\text{ua,emp,2}}$.
- The disappearance of r_3.
- The lower and upper index fault numbers.

Further investigations have shown that the fault location for multiple misfire faults can not be isolated for every cylinder misfire fault combination. It must be investigated whether this issue can be solved with an update of the EMP sensor position. Hence in the following section, only the fault type of misfire faults is isolated from injector faults with the residual r_4 and r_3, without any cylinder fault location isolation.

7.3 Symptoms generation

For the analytical symptom generation, the calculated residuals from the fault detection have to be compared to a threshold defining a fault-free area from a faulted area. The reason of this threshold is already discussed in Sect. 2 and can primary be attributed to model uncertainties (static or OP dependent uncertainty), disturbances or even unknown input signals. As it is already described in Sect. 6.5 there are two possibilities for the threshold generation in

- Stationary OPs (fixed thresholds).
- Quasi-stationary OPs (adaptive thresholds).

Out of the previous mentioned reasons in Sect. 6.5, the fixed thresholds have been used for symptom generation. The analytical symptoms are calculated with the residuals r_k, from Sect. 6.3, with empirically chosen upper thresholds $r^+_{\text{th},k}$ and lower thresholds $r^-_{\text{th},k}$ to:

$$s_k = \begin{cases} +1 & \text{for} \quad r_k > r^+_{\text{th},k} \\ 0 & \text{for} \quad r^-_{\text{th},k} < r_k < r^+_{\text{th},k} \\ -1 & \text{for} \quad r_k < r^-_{\text{th},k} \end{cases} \qquad \text{for } k = [1, ...8, 10] \tag{7.2}$$

The empirically chosen lower $r^-_{\text{th},k}$ and upper thresholds $r^+_{\text{th},k}$ values can be seen in Fig. 6.12 to Fig. 6.14 from Sect. 6.6. The occurrence of the residuals can be seen in Fig. 6.12, 6.13 and 6.14. The dashed lines show the boarder between an assumed fault-free (gray) and fault area (white). Furthermore, the symptoms s_h have a binary representation:

$$s_h = \begin{cases} 1 & \text{for} \quad r^-_{\text{th},h} < r_h < r^+_{\text{th},h} \\ 0 & \text{for} \quad \text{otherwise} \end{cases} \qquad \text{for } h = [9, 11] \tag{7.3}$$

This binary representation is due to the fact that the direction of occurrence for these residuals is not important.

7.4 Fuel system fault diagnosis

There are many aspects which reflects the importance of a solid fault diagnosis:

- Prevent safety critical accidents.
- Prevent component damage.
- Monitor emissions.
- Increase environmental protection.

- Reduce downtime and maintenance costs.

In the fuel system of a diesel engine for example an HP Leakage can result in human life-threatening situations, caused by pressure up to 2500 bar in combination with a loose HP line connection. Also, the monitoring of different functionalities, for example the LP fuel supply, is important to prevent engine damage caused by an insufficient fuel lubrication. This itself results in wear of components and a poor or even loss of functionality. It can end in various engine component damages usually involving very high repair or downtime costs. Also unbalanced fuel injections or cylinder misfire can cause bearing damages and may even cause component breaks on the one side and increase environmental pollution on the other side. Another fault which can cause a contamination of the environmental is a LP Leakage.
A detailed fault isolation additionally gives another important improvement, the possibility to exactly localize the faulted components resulting in a reduction of downtime and repair costs. However, these are only a few examples clarifying the importance of a solid fault diagnosis.

As earlier discussed, there are two different types of fault diagnosis systems, fault diagnosis with inference or classification approaches, described in Sect. 2.5. For classification methods the symptom space is used as the input, whereas the fault space visualizes the outputs. The classification of the different classes is developed with pattern recognition approaches. The rule-based inference approaches are mainly stated with expert knowledge in IF-condition-THEN-conclusion rules. In both cases fault symptom tables can provide sufficient fault pattern information.

Faults may cause intermediate events, which then form features. These features are captured with the fault detection and result in symptoms. The fault diagnosis uses this information backwards to estimate a fault out of the occurred symptoms. The relationship from fault to symptoms and the backward chain for the development of the fault diagnosis system is visualized in Fig. 7.6.

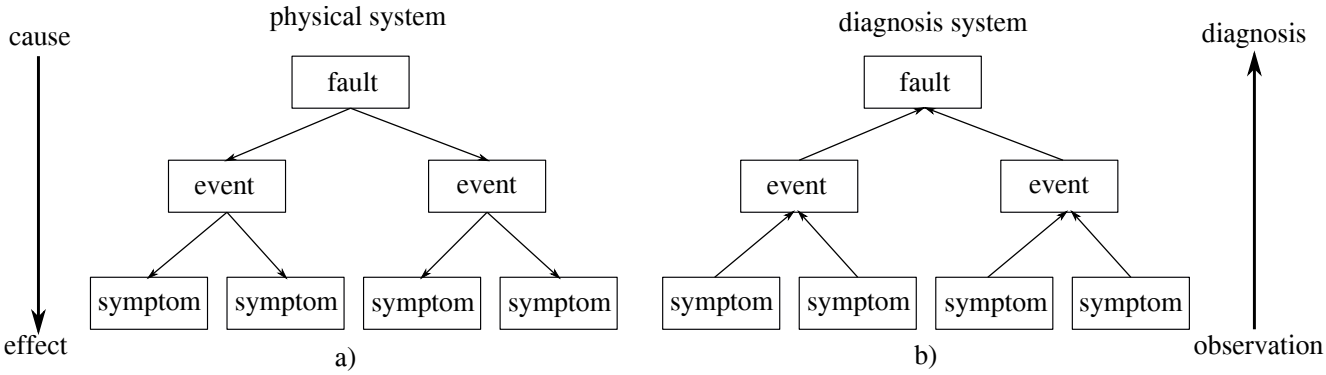

Fig. 7.6: Fault-symptom relationship according to [62]: a) From fault to symptoms for physical system b) From symptoms to fault for diagnosis system

It is not difficult to see that a robust fault detection and symptom generation can significantly improve fault diagnosis. Especially a solid fault detection with a high degree of system information can improve fault isolation. This is due to the fact, that with deeper system knowledge residuals can be developed to observe specific fault characteristics. With this basic idea, the advantages of complex fault isolation or pattern recognition approaches decrease.

In the next sections an expert based inference fault diagnosis system will be discussed. It can be noticed that the requirements of Sect. 3.7.2, especially the fault detection and diagnosis in regular operation mode is fulfilled without a hardware change of the engine's fuel system. The fault patterns are visualized in fault symptom tables and two different fault tree structures are shown, to visualize the software development of the fault diagnosis system.

7.4.1 Fuel system fault symptom tables

As mentioned in the previous sections, the LP system can be separated from the HP system. This also takes affect for the symptoms generated in Sect. 7.3. They can separately be displayed in two fault symptom tables. The different fault behavior for the HP faults, shown in Sect. 6.6.1, can be seen in Table 7.1. The LP fault patterns, shown in Sect. 6.6.2, can be seen in Table 7.2.

Table 7.1: Fault symptom table for the HP faults

Faults	Description	s_1	s_2	s_3	s_4	s_5	s_9
F_1	HPP one plunger chamber does not supply fuel (low OP)	0	+	0	0	0	**1**
F_2	HPP fails to build up RP (high OP)	-	+	0	0	0	0
F_3	RP sensor High Offset	0	-	0	0	0	0
F_4	RP sensor Low Offset	0	+	0	0	0	0
F_5	PRV or HP leakage	-	+	0	0	-	0
F_6	Lower injector mass flow quantity (single injector Low Flow)	0	0	+	+	0	0
F_7	Higher injector mass flow quantity (single injector High Flow)	0	0	-	+	0	0
F_8	Engine misfire by compression loss	0	0	0	+	0	0

Table 7.2: Fault symptom table for the LP faults

Faults	Description	s_2	s_5	s_6	s_7	s_8	s_{10}
F_9	Primary fuel filter restriction	0	-	0	-	-	0
F_{10}	Secondary fuel filter restriction	0	0	+	-	0	0
F_{11}	Primary fuel filter inlet leakage	0	-	0	+	0	+/-
F_{12}	Secondary fuel filter outlet leakage	0	-	0	0	0	0

A short overview of the generated symptoms is given as follow (for residual description see Sect. 6.3):

- s_1 calculated with residual $\mathbf{r_1}$ (Physical RP model).
- s_2 calculated with residual $\mathbf{r_2}$ (HPP fuel quantity closed loop control).
- s_3 calculated with residual $\mathbf{r_3}$ (RP uniformity residual).
- s_4 calculated with residual $\mathbf{r_4}$ (EMP uniformity residual).
- s_5 calculated with residual $\mathbf{r_5}$ (Physical volume flow models LPP/MP inlet).
- s_6 calculated with residual $\mathbf{r_6}$ (Physical power model LPP).
- s_7 calculated with residual $\mathbf{r_7}$ (Low pressure model).
- s_8 calculated with residual $\mathbf{r_8}$ (HCI pressure limit check).
- s_9 calculated with residual $\mathbf{r_9}$ (ECU HPP fuel quantity open/closed loop comparison).
- s_{10} calculated with residual $\mathbf{r_{10}}$ (Physical volume flow models LPP/MP inlet trend checking).

Because of the separated propulsion of the HP and LP system, the LP symptoms are assumed to not be significantly influenced by the HP system and vice versa. This was also empirically observed for all investigated test runs from Sect. 6.6. Therefore a combined fault symptom table for the LP and HP faults with a don't care (d/c) structure is shown in Table 7.3.

It can clearly be seen in Table 7.1, Table 7.2 and finally in Table 7.3, that all inserted faults have a unique pattern. This makes it possible to separate all described faults from Sect. 6.4.
In Sect. 2.7.2 the characteristics of a strong and a weak isolation of fault symptoms was described. Regarding Table 7.1, when one symptom has a deflection, a weakly isolation for the HP faults can be seen. For example s_5 has a residual error, then it can not be distinguished between fault F_2 and F_5. Unlike the case with the HP faults, Table 7.2 shows a strong isolation for the LP faults. Here it is still possible to distinguish between the different faults if any symptom has an error.
By a combination of these two tables, the characteristics of the strong isolation for the LP faults transfer to a weak overall isolation shown in Table 7.3. This is due to the weak isolation characteristic for the HP faults.

Table 7.3: Fault symptom table for LP/HP faults

Faults	Description	s_1	s_2	s_3	s_4	s_5	s_6	s_7	s_8	s_9	s_{10}
F_1	HPP one plunger chamber does not supply fuel (low OP)	0	+	0	0	0	d/c	d/c	d/c	**1**	d/c
F_2	HPP fails to build up RP (high OP)	-	+	0	0	0	d/c	d/c	d/c	0	d/c
F_3	RP sensor High Offset	0	-	0	0	0	d/c	d/c	d/c	0	d/c
F_4	RP sensor Low Offset	0	+	0	0	0	d/c	d/c	d/c	0	d/c
F_5	PRV or HP leakage	-	+	0	0	-	d/c	d/c	d/c	0	d/c
F_6	Lower injector mass flow quantity (single injector Low Flow)	0	0	+	+	0	d/c	d/c	d/c	0	d/c
F_7	Higher injector mass flow quantity (single injector High Flow)	0	0	-	+	0	d/c	d/c	d/c	0	d/c
F_8	Engine misfire by compression loss	0	0	0	+	0	d/c	d/c	d/c	0	d/c
F_9	Primary fuel filter restriction	d/c	0	d/c	d/c	-	0	-	-	d/c	0
F_{10}	Secondary fuel filter restriction	d/c	0	d/c	0	0	+	-	0	d/c	0
F_{11}	Primary fuel filter inlet leakage	d/c	0	d/c	d/c	-	0	+	0	d/c	+/-
F_{12}	Secondary fuel filter outlet leakage	d/c	0	d/c	d/c	-	0	0	0	d/c	0

d/c : don’t care

7.4.2 Fuel system fault diagnosis structure

In this section, the inference method-based fault diagnosis is shown for the examples of four faults:

- F_1: HPP one plunger chamber does not supply fuel (low OP).
- F_2: HPP fails to build up RP (high OP).
- F_6: Lower injector mass flow quantity (single injector Low Flow).
- F_7: Higher injector mass flow quantity (single injector High Flow).

With the fault symptom tables from Sect. 7.4.1 the inference rule for F_1 is given by:

IF < Symptom s_2 positive > **AND**
< Symptom s_9 > **THEN** <F_1: HPP one plunger chamber does not supply fuel >.

Especially the symptom s_2, evaluated from r_2 (HPP fuel quantity closed loop control), occurs for every fault increasing or decreasing the HPP closed loop fuel quantity. In combination with s_9 an HPP one plunger chamber fault F_1 can be isolated. s_9 occurs if the calculated HPP closed loop control fuel quantity is equal to the HPP open loop control fuel quantity.
The simplified foundation of the fault diagnosis software implementation, for the RCP system, is visualized with a fault tree structure in Fig. 7.7. F_1 is shown with the first fault tree a).
A similar fault F_2 has the inference rule:

IF < Symptom s_2 positive > **AND**
< Symptom s_1 negative > **THEN** <F_2: HPP fails to build up RP >.

In general F_1 and F_2 are the same fault, one HPP chamber does not supply fuel to the rail caused e.g. by a failure of the PCV. The difference between both faults lies in the engine's OP, high torque value for F_2. As described in the previous sections the HPP fuel quantity control tries to compensate the insufficient fuel supply with the healthy pump element. In this case the proper function is only guaranteed if the compensated amount of fuel in the healthy pump chamber does not exceed the chambers max fuel delivery capacity. This is the case for F_1. F_2 occurs when the max fuel delivery of one pump element exceed this limit. The result is a vanished symptom s_9, caused by the increasing HPP closed loop control fuel quantity. The insufficient fuel delivery furthermore results in a decreased system RP or a negative s_1 (evaluated with the physical RP model r_1). F_2 is visualized in the second fault tree b) in Fig. 7.7.

The following two faults F_6 and F_7 are injector faults, which are similar faults with different root causes. Fault F_6 occurs from a coked injector nozzle. F_7 occurs from an increased injector nozzle diameter, caused for instance by fuel pollution.
The inference rules for F_6 is given by:

IF < Symptom s_3 positive > **AND**
< Symptom s_4 positive > **THEN** <F_6: Lower injector mass flow quantity in one injector >

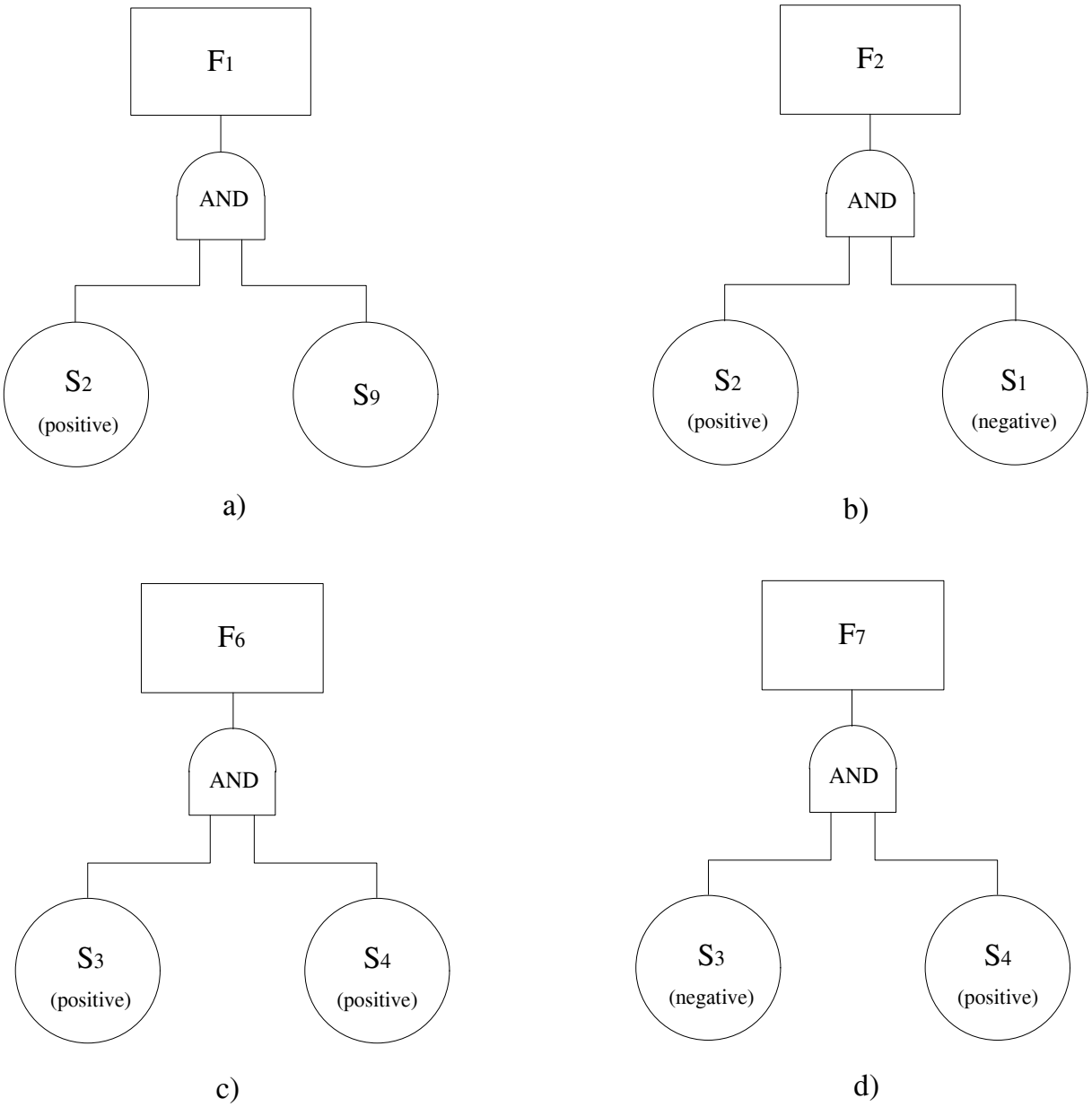

Fig. 7.7: Fault tree for a) F_1: HPP one plunger chamber does not supply fuel (low OP), b) F_2: HPP fails to build up RP (high OP) c) F_6: Lower injector mass flow quantity (single injector Low Flow) and d) F_7: Higher injector mass flow quantity (single injector High Flow)

and for F_7:

IF < Symptom s_3 negative > **AND**
< Symptom s_4 positive > **THEN** <F_7: Higher injector mass flow quantity in one injector >.

The difference of both faults can be seen in the occurrence of the symptom s_3 tendency. s_3 and s_4 are developed from the uniformity analysis of the RP or EMP signal. With the additional information of the injectors fault number, gained from Sect. 7.2.1, the type and location of the fault can be precisely isolated. Also the HPP fuel delivery increases or decreases in case of an injector fault, see Fig. 7.2 from Sect. 7.2.1. This is not recognized by the symptom s_2, because the amount

of fuel increase or decrease is too small for a single injector fault. Hence, the trade-off between a small fault detection and misclassification is the root cause of the vanished s_2 for a single injector fault. Both faults are visualized in the simplified fault tree c) and d) in Fig. 7.7.

Finally, the shown fault trees in Fig. 7.7 are implemented in the software. Each positive or negative symptom is represented with a binary variable. Furthermore, only the above discussed faults are shown because the fault diagnosis structure of the other faults is similar.

7.5 Fuel system operation point dependency

Symptoms which can only be observed in certain operation ranges are already described in different research works, for example [45], [4], [20] and [67]. Specifically, this research work copes with different OP dependent faults for the HP system. The need of an engine OP dependent fault detection has different reasons such as:

- OP dependent model uncertainties.
- OP dependent noise.
- Small fault sizes resulting in small residuals, especially for low engine OPs.
- Exceeding actuator saturation limits, e.g. in higher engine OPs.

One way to cope with the first two issues are larger thresholds resulting in a more robust fault diagnosis, but interferes with the detection of smaller fault sizes. This can be critical in areas where the observed residual is not large enough to clearly separate the fault from a fault-free case. A possible solution could be an adaptive threshold dependent on the engine OP.

In this section the described residuals r_1 to r_{10} from Sect. 6.3 (and symptoms s_1 to s_{10}) are recorded for different engine OPs over the complete engine map, in equidistant torque and speed increments (200 Nm and 200 rpm). The fault detection algorithms are active for every approached engine OP and the following test runs are performed:

- Fault-free reference data (Fig. 7.8).
- Fault F_1 and F_2 (Fig. 7.9).
- Fault F_6 (Fig. 7.10).

Fig. 7.8 visualizes the approached engine OPs in a fault-free case. Here, all residuals or symptoms are in a fault-free state for every approached engine OP. It is obvious that in the fault-free case every engine OP within the maximum engine power can be approached.

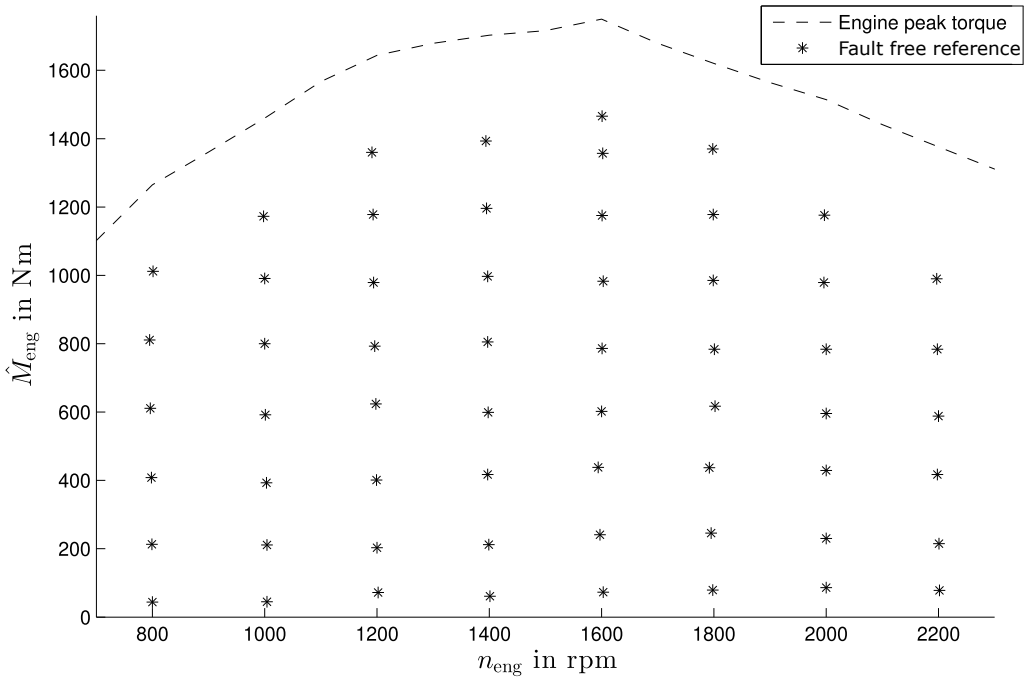

Fig. 7.8: Approached measured engine OPs for the record of fault-free reference data

The following faults F_1, F_2 and F_6 are detected with fault trees which were discussed in Sect. 7.4.2. Fig. 7.7 shows these fault trees and the faults occurring for a specific symptom combination. Fig. 7.9 visualizes the occurrence of fault F_1 and F_2 for the approached engine OPs. Especially a result of F_2 is the decreasing RP (negative s_1). In extreme cases this will cause the engine to stall. It is obvious that the high engine torque OPs above the occurrence of F_2 can not be reached. This is because the amount of fuel, to generate the requested torque, can not be delivered with one remaining healthy HPP chamber.

The actuator saturation limits define an upper torque boundary, where the fault detection for the HPP is active. One example can be seen for the HPP fault in pump chamber one. For fault F_1 the healthy pump chamber does not exceed the saturation limit and can therefore compensate for the missing amount of fuel delivery from the second pump chamber. If now the saturation limit is reached, fault F_2 occurs in a small area of high engine torque OPs. The OPs where the fault F_2 occurs draw the line of the maximum possible HPP fault detection, see Fig. 7.9.

Moreover, a 40% lower injector fault in injector 1 is shown in Fig. 7.10. As described in Sect. 7.2, the detection and isolation is made with the uniformity analysis. The accuracy of the concept with the uniformity fault detection primary depends on the measured sensor signal quality. Stochastic noise is an important factor, whereas system noise with periodic behavior has only a small influence on this concept. An example for system noise with periodic behavior is voltage induction of the injector actuation. Especially a larger threshold copes with the influence of stochastic noise and therefore make the detection more robust, but less sensitive to small faults.

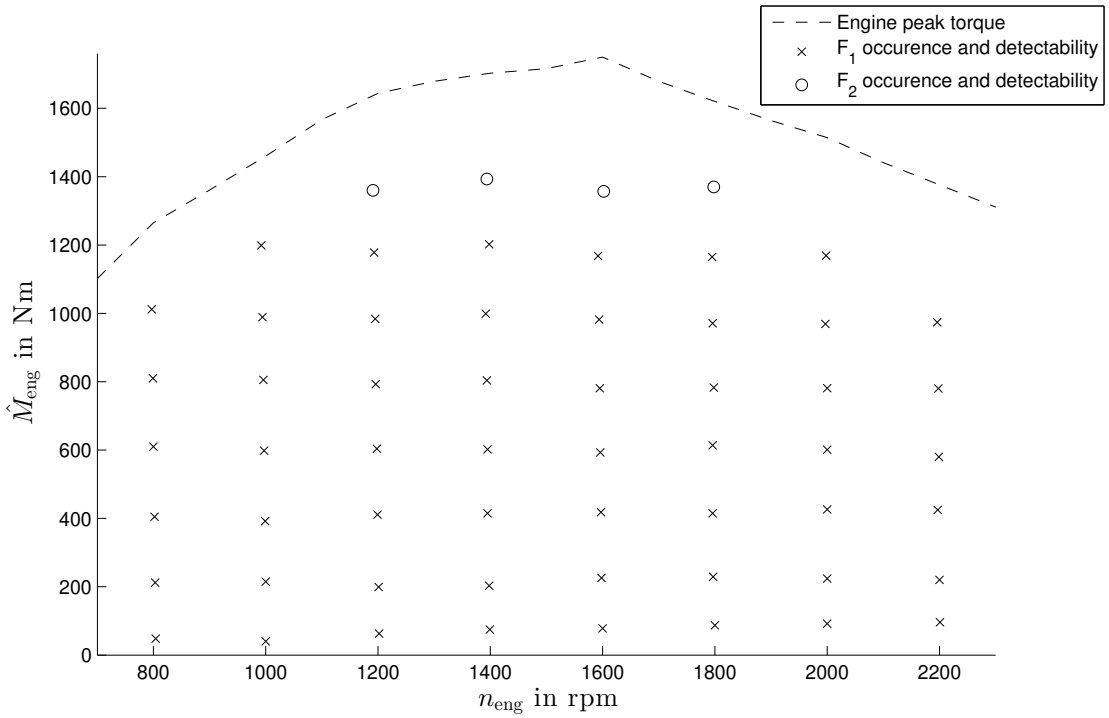

Fig. 7.9: Occurrence and detectability of F_1: HPP one plunger chamber does not supply fuel (low torque OPs) and F_2: HPP fails to build up RP (high torque OPs) for approached measured engine OPs

In Fig. 7.10 it can be seen that for small engine torque OPs (below 400 Nm) an injector quantity fault with 40% less mass flow can not be detected. This is caused by the total amount of injected fuel, which is less for small torque OPs. This results out of the case, that the residual does not exceed the, from Sect. 6.5 described, fixed thresholds.
It is furthermore obvious, that the area of detection decreases with a smaller fault size. On the test bench up to 20% less injector faults can be detected, but the line of detection rises to the border of 800 Nm for a minimal engine OP (see Fig. A.6 in the Appendix).

Summarized, the faults F_1, F_2 and F_6 were performed for the same approached engine OPs shown in the fault-free reference data test runs in Fig. 7.8.
It can be seen that F_1 can be detected for lower engine torque OPs (1200 Nm or less) and F_2 can be detected for high engine torque OPs (1400 Nm). Fig. 7.9 shows the occurrence of both faults and approached engine OPs. Above the torque limit of 1400 Nm no HPP fault can be detected.
The area where the injector fault F_6 occurs is mainly dependent on the fault size. In the performed tests, the fault size is 40% less fuel mass flow for injector 1. This results in a possible fault detection for most engine torque OPs of 400 Nm or above. Fig. 7.10 illustrate the possible injector fault detection. For injector High Flow faults F_7 the behavior is similar to F_6.
Overall it can be seen, that either the HPP faults or the injector faults can not be detected in every engine OP. This makes the fault detection OP dependent.

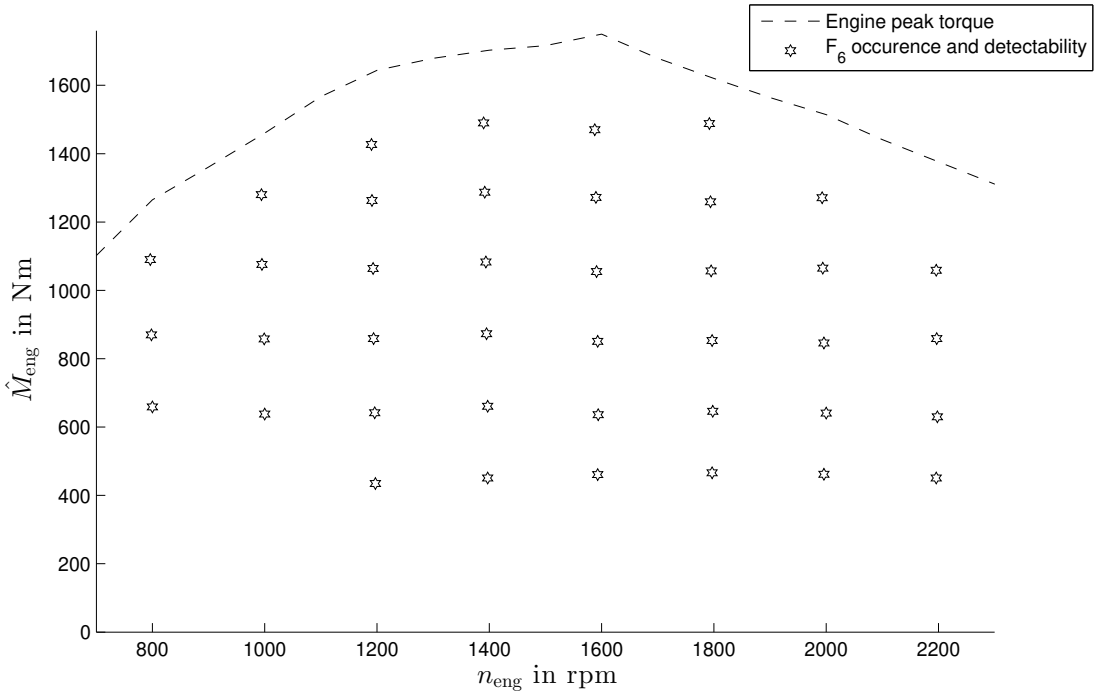

Fig. 7.10: Occurrence and detectability of F_6: 40% Lower injector mass flow quantity (single injector 1 Low Flow) for approached measured engine OPs

7.6 Overall fuel system fault diagnosis

In the previous sections, only a few investigated faults are discussed. In order to keep the expense small, additional faults are only shortly discussed in this section. These additional faults are listed in Table 7.4.

Table 7.4: Additional investigated faults

Fault index	Fault description
F_{13}	Leakage HCI dosing system (HPP fails to build gerotor pressure)
F_{14}	LP sensor High Offset
F_{15}	LP sensor Low Offset
F_{16}	Return flow restriction
F_{17}	PCV High start angle Offset
F_{18}	PCV Low start angle Offset
F_{19}	Two injector faults Low Flow
F_{20}	Three injector faults Low Flow
F_{21}	Four injector faults Low Flow
F_{22}	Five injector faults Low Flow
F_{23}	Two injector faults High Flow
F_{24}	Three injector faults High Flow
F_{25}	Four injector faults High Flow
F_{26}	Five injector faults High Flow

The LPP and especially its control is the most important part in the LP system. The controlled variable of the LPP control is the LP and the fault detection therefore primary depends on the LP sensor signal. It is obvious, that it is important to monitor the sensor, to cope with a possible changed behavior. This for example could be an increased resistance, which can be the reason of an aged sensor. Due to the sensor's principle, the voltage is used to calculate a pressure value. This results for a changed resistance in an offset fault of the sensors signal. The associated faults are F_{14} (LP sensor High Offset) and F_{15} (LP sensor Low Offset).

An additional monitored fault is the fault F_{16} (Fuel return flow restriction). The fuel return flow restriction occurs when the fuel back flow line from the fuel return manifold to the fuel tank is restricted, see Fig. 3.2. This fault can cause significant damage to the engine when the lubrication fuel back flow to the fuel tank is restricted. It will increase the pressure in the HPP housing compared to the engines crank housing pressure. The HPP is directly driven by a gear from the engine crank shaft and the HPP housing is therefore directly coupled with the engines crank housing. This pressure increase can break the sealing ring in between the HPP and the engines crank housing. The broken sealing ring will then cause a mixture of fuel and oil, since the HPP is fuel lubricated and the engine components (like engine driveline and cylinders) are oil lubricated. This will change the lubrication properties of the engine oil. Most likely the result is higher friction and a temperature increase of the engine cylinders and pistons. Finally, it could cause a friction welding of both components.

Many HPP faults can be caused by an incorrect assembly of the HPP. Due to the HPP functionality (see Sect. 3.5), a misalignment of the HPP's cam shaft to the engine's crank shaft will cause a decrease or increase of the HPP fuel quantity closed loop control fuel mass. This results in the fact, that the poppet valve will close too early or too late. In an open loop control, these faults F_{17} (PCV High start angle Offset) and F_{18} (PCV Low start angle Offset) result in an increased or decreased fuel delivery. The faults will be corrected by the HPP fuel quantity closed loop control and r_2 occurs. To differentiate between the faults F_3 and F_{17} or F_4 and F_{18} (see patterns in Table 7.5), the residual r_{11} (PCV start angle offset detection) is taken into account. The residual r_{11} calculates a fault for the case of an HPP misalignment over 1 crank shaft tooth. The basis of the residual r_{11} is described in Sect. 6.3.11 and the evaluation of r_{11} lead to the symptom s_{11}.

One of the big topics of this research work is the detection and isolation of different injector faults. With the basis of Sect. 7.2, it was already mentioned that up to five injector High and Low Flow faults can be isolated with the help of r_2, r_3, r_4 and the injector fault numbers. For multiple injector fault, a vector $\mathbf{v}_{s_3}$ storing the occurrence of symptom s_3 (s_{inj}) over one engine cycle is introduced. Fig. 7.11 shows a simulation with up to four injector Low Flow faults (F_6, F_{19}, F_{20} and F_{21}). The figure shows in the first row the HPP volume flows, in the second row the injector volume flows and in the third row the RP signal. The fourth row shows the simulated uniformity residual r_{inj}. r_{inj} is equal to r_3 which is calculated with the measured RP signal. The vector $\mathbf{v}_{s_3}$ shows the index of the occurred faulted injectors over one engine cycle. Due to the fact that the residual r_3 (r_{inj}) and therefore s_3 (s_{inj}) is calculated every 120°CA, the vector $\mathbf{v}_{s_3}$ contains 6 elements for one engine cycle (see upper index in Fig. 7.11 row four). If now s_3 (s_{inj}) occurs for one or two elements,

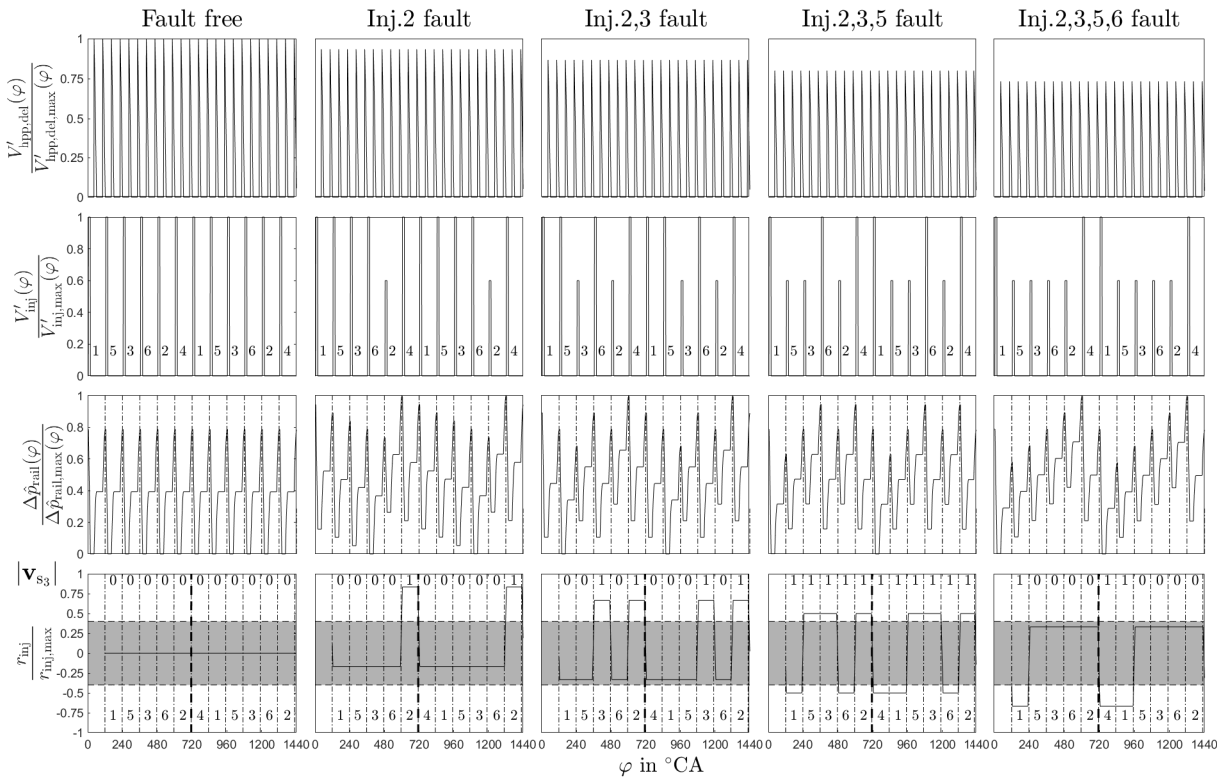

Fig. 7.11: Simulated RP signal and uniformity residuals for **column one:** A fault-free state, **column two:** F_6 an injector 2 fault (40% LF), **column three:** F_{19} an injector 2,3 fault (each 40% LF), **column four:** F_{20} an injector 2,3,5 fault (each 40% LF) and **column five:** F_{21} an injector 2,3,5,6 fault (each 40% LF).

the index(es) of the occurred element(s) in combination with the cylinder firing order point to the faulted injector number(s). See F_6 and F_{19} row four for the upper and lower index in Fig. 7.11.

For more than one injector fault the occurring sign of s_2 (r_2) in combination with the occurring sign of s_3 (s_{inj}) points to the injector quantity fault type (high or low flow). The root of the r_2 change is caused by a higher or lower injection fuel mass flow. This results in the actuation of the HPP fuel quantity closed loop control with an increased or decreased fuel delivery. For injector low flow faults with a decreased fuel delivery, see Fig. 7.11 row one.
For the case of three injector faults, the tendency of residual r_2 is important to choose the correct faulted injector numbers. For low flow faults the tendency with a negative sign of r_2 can already be seen in the decreased HPP volume flow delivery in Fig. 7.11 row one. In conclusion this means, that for low flow injector faults only the correlated cylinder firing numbers for a positive occurred r_3 (r_{inj}) are considered and vice versa for injector High Flow faults.

To separate multiple injector faults the following three additional symptoms $\sum_{x=1}^{3} s_{12,\mathrm{M}x}$ are developed

$$\sum_{x=1}^{3} s_{12,\mathrm{M}x} = \begin{cases} 1 & \text{for} \quad r_{12} = z(x) \\ 0 & \text{for} \quad \text{otherwise} \end{cases} \qquad \text{for } z = [1,2,6] \tag{7.4}$$

with the residual r_{12} calculated with the vector $\mathbf{v}_{s_3}$:

$$r_{12} = (1\ 1\ 1\ 1\ 1\ 1)^T \cdot |\mathbf{v}_{s_3}|. \tag{7.5}$$

$s_{12,\mathrm{M1}}$ occurs if only one injector fault occurs over one engine cycle, e.g. injector 2 low flow fault see Fig. 7.11 row four, column two. $s_{12,\mathrm{M2}}$ occurs if two injector faults ($r_{12} = 2$) and $s_{12,\mathrm{M3}}$ occurs if three injector faults ($r_{12} = 6$) occur over one engine cycle, see Fig. 7.11 row four, column three and four.

The calculation of the uniformity analysis has no plausibility check. Due to the calculation principle of the uniformity residual for the case of more than three injector faults, the faulted injectors seem to have the "fault-free" behavior for the calculated uniformity residual. This can be seen in Fig. 7.11 row four, column five. The occurrence of the residual r_{inj} (r_3) shows for four injector Low Flow faults (F_{21}) a negative sign and only two occurring injector fault numbers. This is usually only the case for two injector High Flow faults (F_{23}). Fault F_{21} is isolated from fault F_{23} with the sign of the r_2 (s_2) occurrence, see Table 7.5. Similar to two injector Low Flow faults, four injector Low Flow faults count only two injector fault numbers and symptom $s_{12,\mathrm{M2}}$ occurs. The counted injector fault numbers are the healthy injectors. Therefore for fault F_{21} the not occurring injector fault numbers are now the faulted injectors. The sign of residual s_3 (s_{inj}) in combination with the sign of the s_2 occurrence points to the underlying injector fault type, see Table 7.5. In conclusion for more than three injector faults, the inverse (not occurring) injector fault numbers must be considered for the isolation of the injector fault location.

Appendix A.3 shows an example for two and three injector Low Flow faults F_{19} and F_{20} inserted on the test bench. Comparing the measured residual r_3 in Fig. A.6 to the simulated residual r_{inj} in Fig. 7.11 shows a similar behavior for fault F_{19} and F_{20}.

Table 7.5 visualizes the overall investigated faults. This table also illustrates the unique pattern of each single and multiple injector fault, which proves the statement that up to five high and low flow injector quantity faults can be isolated. This means that the information of the exact type and location of each fault is provided, when injector fault numbers are considered.
Furthermore, Table 7.5 shows two groups of LP faults which can not be isolated directly. However, the LP faults F_{14} and F_{16} as well as F_{12} and F_{15} provide an identical symptom pattern. It was already mentioned in earlier sections, that the LP system can be actuated by a test signal without influencing the engine's OP. This gives the additional possibility of an active test, where only the LP setpoints are varied. These active tests have the benefit of better knowledge of the input signals and environmental conditions and can therefore generate a higher degree of system information, see next section.
Finally, looking at Table 7.5 all faults except F_{14}, F_{16}, F_{12} and F_{15} can directly be isolated.

Table 7.5: Fault symptom table for Overal LP/MP/HP faults

Faults	Description	s_1	s_2	s_3	s_4	s_5	s_6	s_7	s_8	s_9	s_{10}	s_{11}	$s_{12,M1}$	$s_{12,M2}$	$s_{12,M3}$
F_1	HPP one plunger chamber fault	0	+	0	0	0	d/c	d/c	d/c	**1**	d/c	0	0	0	0
F_2	HPP fails to build up RP	-	+	0	0	0	d/c	d/c	d/c	0	d/c	0	0	0	0
F_3	RP sensor High Offset	0	-	0	0	0	d/c	d/c	d/c	0	d/c	0	0	0	0
F_4	RP sensor Low Offset	0	+	0	0	0	d/c	d/c	d/c	0	d/c	0	0	0	0
F_5	PRV or HP leakage	-	+	0	0	-	d/c	d/c	d/c	0	d/c	0	0	0	0
F_6	Single injector Low Flow	0	0	+	+	0	d/c	d/c	d/c	0	d/c	0	**1**	0	0
F_7	Single injector High Flow	0	0	-	+	0	d/c	d/c	d/c	0	d/c	0	**1**	0	0
F_8	Engine misfire by compression loss	0	0	0	+	0	d/c	d/c	d/c	0	d/c	0	0	0	0
F_9	Primary fuel filter restriction	d/c	0	d/c	d/c	-	0	-	-	d/c	0	d/c	d/c	d/c	d/c
F_{10}	Secondary fuel filter restriction	d/c	0	d/c	0	0	+	-	0	d/c	0	d/c	d/c	d/c	d/c
F_{11}	Primary fuel filter inlet leakage	d/c	0	d/c	d/c	-	0	0/+	0	d/c	+/-	d/c	d/c	d/c	d/c
F_{12}	Secondary fuel filter outlet leakage	d/c	0	d/c	d/c	-	0	0	0	d/c	0	d/c	d/c	d/c	d/c
F_{13}	Leakage HCI dosing system	d/c	0	d/c	d/c	-	0	0	-	d/c	0	d/c	d/c	d/c	d/c
F_{14}	LP sensor High Offset	d/c	0	d/c	0	0	0	+	0	d/c	0	d/c	d/c	d/c	d/c
F_{15}	LP sensor Low Offset	d/c	0	d/c	d/c	-	0	0	0	d/c	0	d/c	d/c	d/c	d/c
F_{16}	Fuel return flow restriction	d/c	0	d/c	0	0	0	+	0	d/c	0	d/c	d/c	d/c	d/c
F_{17}	PCV High start angle Offset	0	-	0	0	0	d/c	d/c	d/c	0	d/c	**1**	0	0	0
F_{18}	PCV Low start angle Offset	0	+	0	0	0	d/c	d/c	d/c	0	d/c	**1**	0	0	0
F_{19}	Two injector faults Low Flow	0	-	+	+	0	d/c	d/c	d/c	0	d/c	0	0	**1**	0
F_{20}	Three injector faults Low Flow	0	-	+	+	0	d/c	d/c	d/c	0	d/c	0	0	0	**1**
F_{21}	Four injector faults Low Flow	0	-	-	+	0	d/c	d/c	d/c	0	d/c	0	0	**1**	0
F_{22}	Five injector faults Low Flow	0	-	-	+	0	d/c	d/c	d/c	0	d/c	0	**1**	0	0
F_{23}	Two injector faults High Flow	0	+	-	+	0	d/c	d/c	d/c	0	d/c	0	0	**1**	0
F_{24}	Three injector faults High Flow	0	+	-	+	0	d/c	d/c	d/c	0	d/c	0	0	0	**1**
F_{25}	Four injector faults High Flow	0	+	+	+	0	d/c	d/c	d/c	0	d/c	0	0	**1**	0
F_{26}	Five injector faults High Flow	0	+	+	+	0	d/c	d/c	d/c	0	d/c	0	**1**	0	0

7.7 Active test for LP system

In Table 7.5 it can be seen, that two fault groups, F_{14} and F_{16} as well as F_{12} and F_{15}, can not be isolated directly. Also, the separated propulsion structure of the LPP and the HPP gives the possibility to impress an active test. Especially with the help of the LP model from Sect. 6.3.7 and an active test, the dynamic behavior of the LP control can be monitored without influencing the engine's OP. Similar to Fig. 4.12 from Sect. 4.7.3 an active test for each fault F_{14}, F_{16} and F_{12},

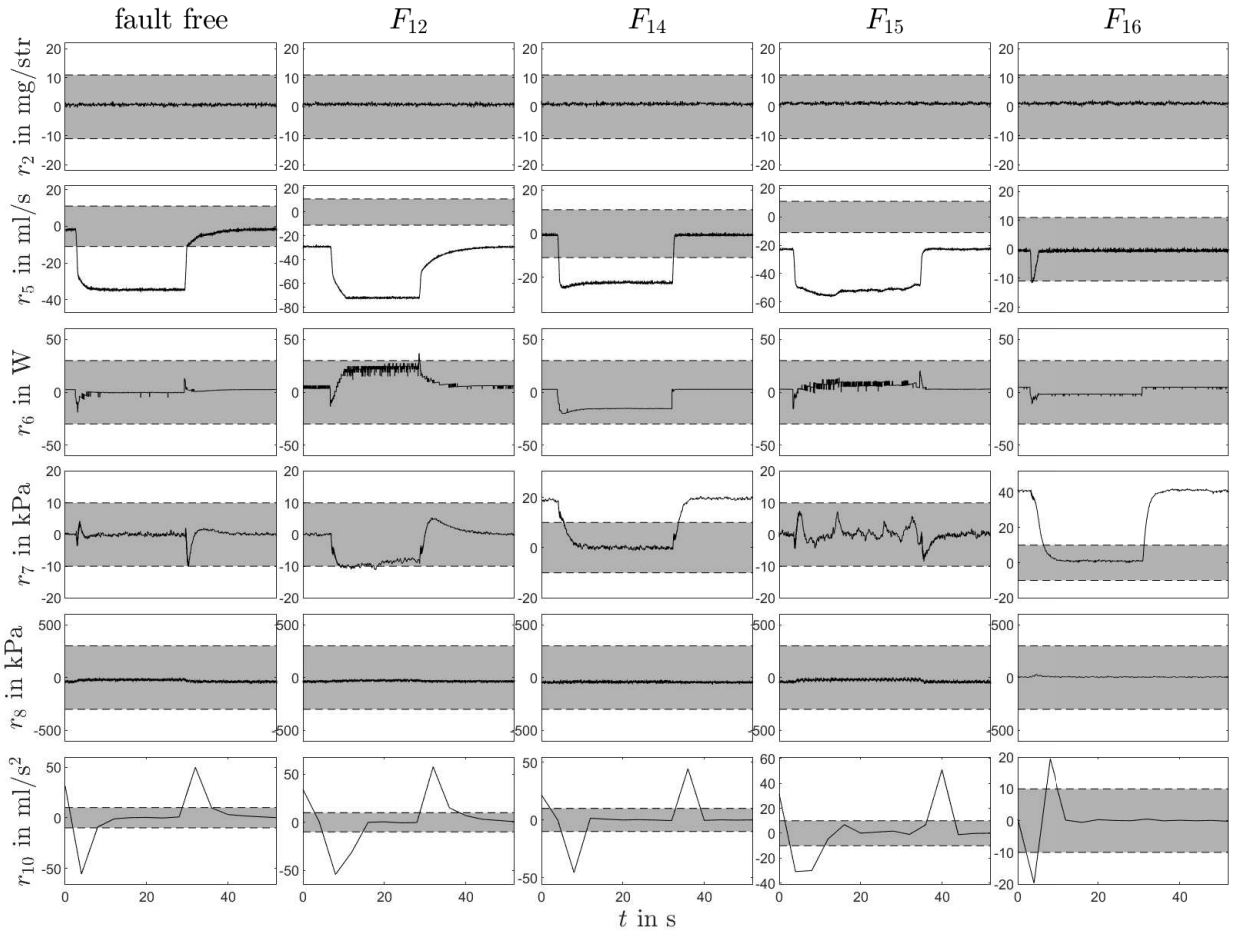

Fig. 7.12: LP residuals calculated from measured signals for the active tests (step signal for $\Delta p_{\mathrm{lp,sp}}$, OPs according to Table 7.6): F_{12}: Secondary fuel filter outlet leakage, F_{14}: LP sensor High Offset, F_{15}: LP sensor Low Offset and F_{16}: Fuel return flow restriction.

Table 7.6: OPs and important parameters

graphs	n_{eng}	M_{br}	$\hat{M}_{\mathrm{eng}}$	fault (parameter)	fault size in %
fault-free	803 rpm	34 Nm	41 Nm	-	-
F_{12}	801 rpm	35 Nm	43 Nm	Secondary fuel filter outlet leak.	-
F_{14}	800 rpm	35 Nm	45 Nm	LP sensor High Offset	10
F_{15}	801 rpm	34 Nm	45 Nm	LP sensor Low Offset	10
F_{16}	799 rpm	35 Nm	40 Nm	Fuel return flow restriction	33

F_{15} with a LP setpoint step signal from 20 kPa to 60 kPa is impressed. Then, due to the active test, the resulting residual behavior is visualized in Fig. 7.12.

The fault symptom pattern is shown in Table 7.7. With the new gained information of the active

Table 7.7: Fault symptom table for the LP step faults

Faults	Description	s_2	s_5	s_6	s_7	s_8	s_{10}
F_{12}	Secondary fuel filter outlet leakage	0	-	0	0	0	+/-
F_{14}	LP sensor High Offset	0	-	0	+	0	+/-
F_{15}	LP sensor Low Offset	0	-	0	0	0	+/-
F_{16}	Fuel return flow restriction	0	0	0	+	0	+/-

test, the fuel return flow restriction F_{16} can be separated from the LP sensor High Offset F_{14}. Also, the separation of the faults F_{12} and F_{15} seems to be possible with the supported information of the LP model r_7 and the active test. In detail the residual r_7 shows a reaction for the secondary fuel filter outlet leakage F_{12}, see Fig. 7.12. In the end, the chosen threshold causes that the symptom s_7 does not occur. However, the same symptom pattern for F_{12} and F_{15} in Table 7.7 show, that the faults can not be separated with the chosen threshold for r_7. But finally there is another possibility to separate F_{12} from F_{15} by a visual leakage inspection of the LP fuel lines on the engine.

7.8 HP fault detection in transient engine speed OPs

In the previous sections, only stationary HP OPs are considered. This is valid for all previously discussed faults (F_1 to F_{26}) and was primary driven by the usage of the engine (applications) and the calculation of the uniformity residuals, see Sect. 6.5. In this section transient states with quasi-stationary OPs are discussed. To finally complete the fault diagnosis an additional PRV fault F_{27} is implemented. As described in Sect. 6.3.1, the PRV is only active in transient OPs with a quick RP decrease caused, for example, by a quick engine speed decrease. In case of stationary OPs this reasonably results in the fact that a PRV activation fault can not be detected. To detect a PRV fault the static thresholds for the HP residuals can be transformed to adaptive thresholds with a fixed and variable component. The basis for this can be gathered from the adaptive thresholds, presented in Sect. 2.5.
The symptoms s_1, s_2 can be generated with a fix threshold value in combination with a variable threshold, developed with two high pass filters. One dependent on the RP setpoint and the other dependent on the RP (see first approach in Sect. 2.5). This has the benefit, that the adaptive thresholds are only updated in transient engine OPs, whereas they stay equal in stationary OPs.

The uniformity residual r_3 uses an approach relying on the residuals energy (third method in Sect. 2.5). With this approach only lower residual frequencies update the threshold, whereas in case of an injector fault, higher residual frequencies will not have a significant influence to update the threshold. Hence, it is possible to detect injector faults and to stay robust against RP setpoint changes in dynamic operation ranges.

In Fig. 7.13 adaptive thresholds for r_1, r_2 and r_3 are shown for a test run with a transient engine speed OP. All adaptive thresholds and the filter design are generated empirically on the engine's test bench. In the first step of this test run the engine was stable at 1200 rpm speed and 0 Nm

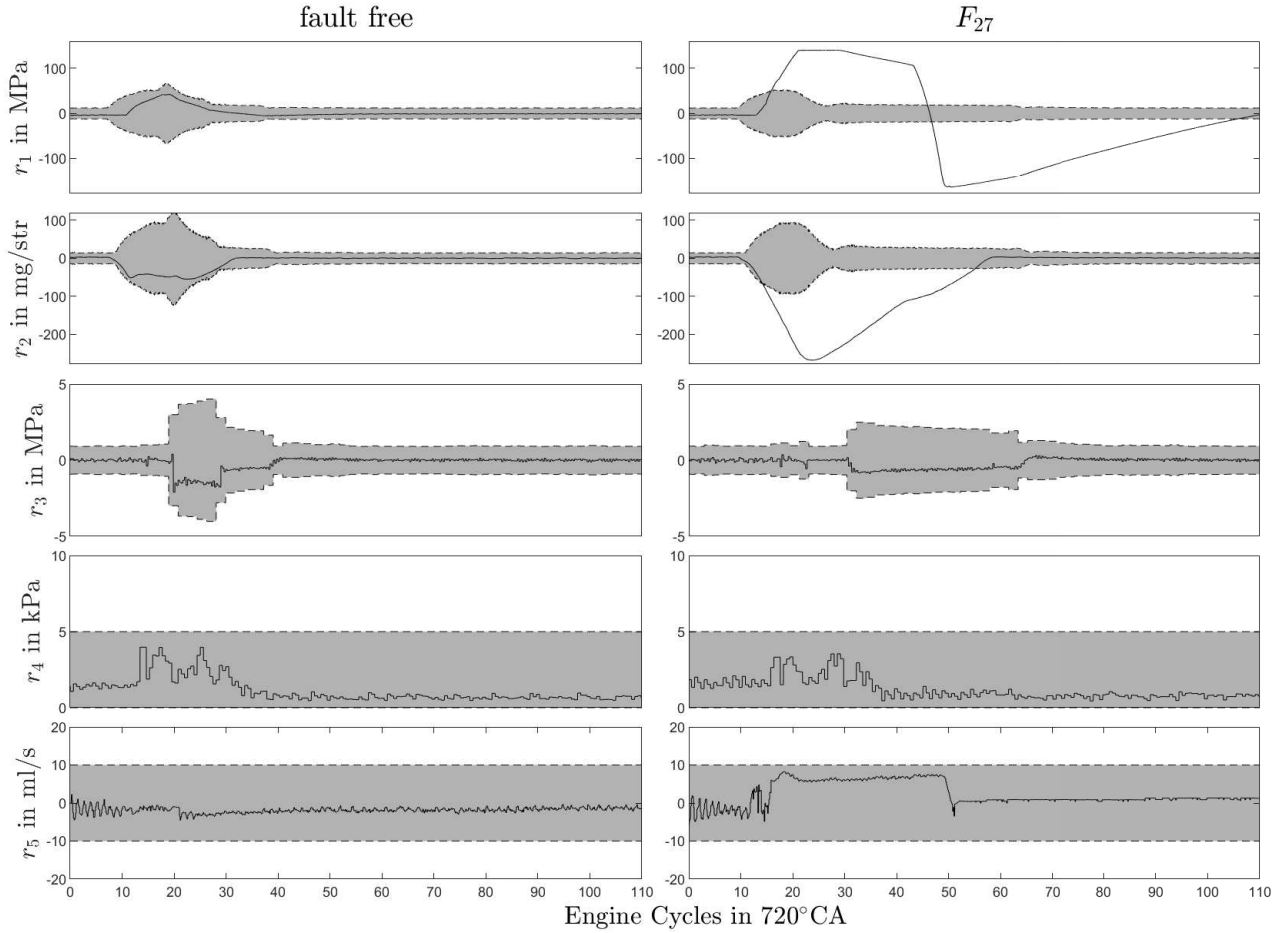

Fig. 7.13: Visualization HP residual calculated from measured signals with adaptive thresholds and a dynamic operation mode with fault-free and PRV fault F_{27} for engine speed setpoint change with steep ramp from 1200 to 800 rpm

torque. Then the engine speed was reduced with a steep ramp from 1200 rpm to 800 rpm. This causes a rapid RP setpoint change, which can not be fulfilled with only the HPP deactivation. Here, the PRV activation is needed to reduce the RP in a certain extent. In Fig. 7.13 this is done with a proper function of the PRV and with an unplugged power supply of the PRV. This disabled PRV reproduces the fault F_{27}.
It can clearly be seen, that the PRV fault F_{27} is detected in transient engine speed OPs.

7.9 Summary

In this chapter a new approach was discussed for an injector fault and cylinder misfire fault isolation with the uniformity analysis. With this new concept up to 5 injector High and Low Flow faults

with the fault type and location can be isolated, as well as the separation between an injector or a cylinder misfire fault. The simple structure, small calculation effort, robustness against system noise and small amount of application for different engine OPs show the benefit of this approach.

As the main topic of this chapter, an inference method-based fault diagnosis system was discussed. The derivation of this fault diagnosis system was made in the first step with a singular fault diagnosis for the most important faults and an extension with all additional multiple faults. Therefore, different symptoms were generated on the basis of the residuals from Chap. 6. Further on, symptom tables visualized the different fault patterns and the development of the inference method-based diagnosis with fault trees was shown.

The fault dependency on different engine OPs was shown pointing to the area of validity for the implemented fault diagnosis. In the next step the overall fault diagnosis system with all additional variations of faults, especially multiple injector faults, was discussed. Up to four injector Low Flow faults were shown and analyzed with the type and location for the injector fault isolation. Some LP faults have shown the same fault symptom pattern, which made it impossible to isolate these faults without additional information. The independent drive of the HP and LP system gave the possibility to gather this additional information, to separate these LP faults with an active test for the LP system.

Finally it was shown in Table 7.5, that all 26 inserted faults were detected with the chosen 14 symptoms. With the help of an active test for the LP system it was furthermore possible to isolate or diagnose nearly all 26 faults, except for the faults F_{12} and F_{15}.

To finally complete the fault diagnosis, adaptive thresholds for the HP system were described. This gives the possibility of fault detection in transient engine OPs. It is necessary for fault detection of components which are only active in transient engine OPs, like the PRV. Note, that this was only exemplary shown for the PRV fault. To keep the expense small the other 26 faults weren't tested in this dynamical environment.

8 Diesel engine fuel system fault management for injector faults

This chapter provides a short overview of fault management strategies. A fault compensation strategy for injector fuel quantity faults, based on the exact type and location information, is gained from the fault diagnosis.

8.1 General fault management structure

The evaluation of fault diagnosis such as fault type, size and location are the basis of fault relevant classification for the fault management system. The comfort-, legislation- or safety-relevant fault classification further decide the need for actions during the current occurred fault. Depending on the fault, the technical system is reconfigured to quickly react and compensate for the fault. Or the fault occurrence is reported to the operator including a need for maintenance. Especially safety relevant faults require quick actions to prevent personal or material damages. Also, every fault is stored in the ECU for an inspection at the next workshop maintenance visit. Fig. 8.1 illustrates an overall described fault management system.

The two primary topics of this thesis are fault detection and fault diagnosis. The additional characteristic information, gained from Chap. 7 for the occurred faults, helps to define further steps to maintain the performance of the engine. With the new concept of the uniformity analysis isolation from Sect. 7.2, the information of the exact type and location of an injector fault is provided.

8.2 Fault compensation strategy for injector faults

In this section, a concept of a possible fault compensation strategy for injector faults is discussed. An occurred injector fault can be compensated by a parameter reconfiguration in the ECU for the faulted injectors. This gives the possibility to quickly adjust the underlying fault, to keep the full engine functionality running until the system gets repaired. The importance of this possibility is obvious for heavy-duty engines due to the reduction of machine downtime, which in turn results in high productivity and delivery losses.

The procedure for injector fault adjustment is visualized in Fig. 8.2. First of all, an injector fault is detected, identified and isolated in the fault diagnosis. With the information of fault type and

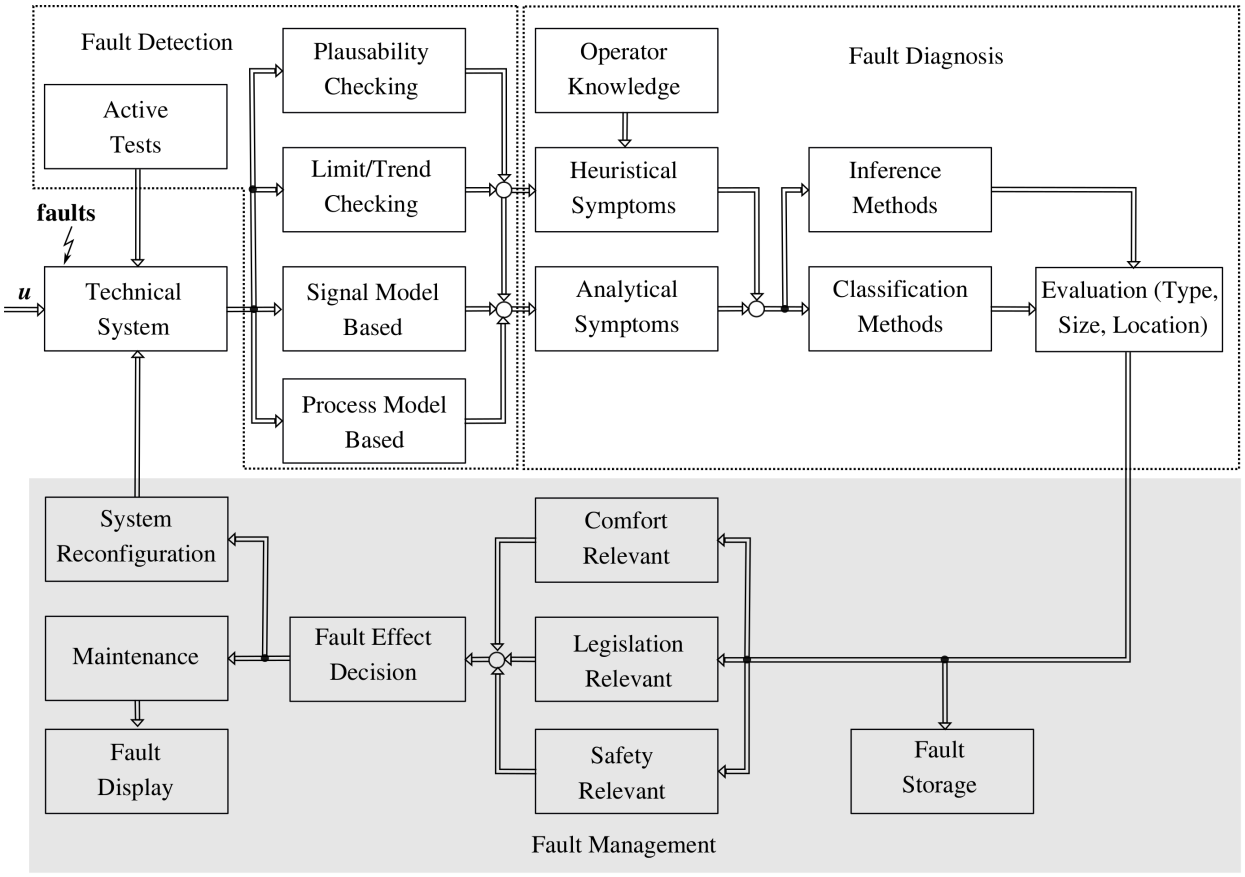

Fig. 8.1: Overall diagnosis structure with the main focus on fault management system, according to [58]

location, the fault compensation system can adjust the fault by a reconfiguration of the fuel injection duration. The longer or shorter period of fuel injection is adapted for each faulted injector in the ECU. Since the fault size is not known, this adjustment must be done iteratively until the fault disappears. This iterative software reconfiguration also has an inherent advantage of estimating the fault size.

For proper implementation of this strategy, it has to be ensured that the injector fault is classified correctly and that the compensation structure reconfigures the underlying fault properly. This means, that the classification of the detected injector fault has to be observed over a few engine cycles. Also, the reconfiguration has to be monitored for unexpected increase of the fault (size) as opposed to decrease. Furthermore, investigations need to be performed on how the compensation influences the combustion, which primary varies the torque generation and the emissions.

8.3 Summary

This chapter briefly described a possible fault management structure focusing on the need for action, driven by comfort-, legislation- or safety-relevant regulations.

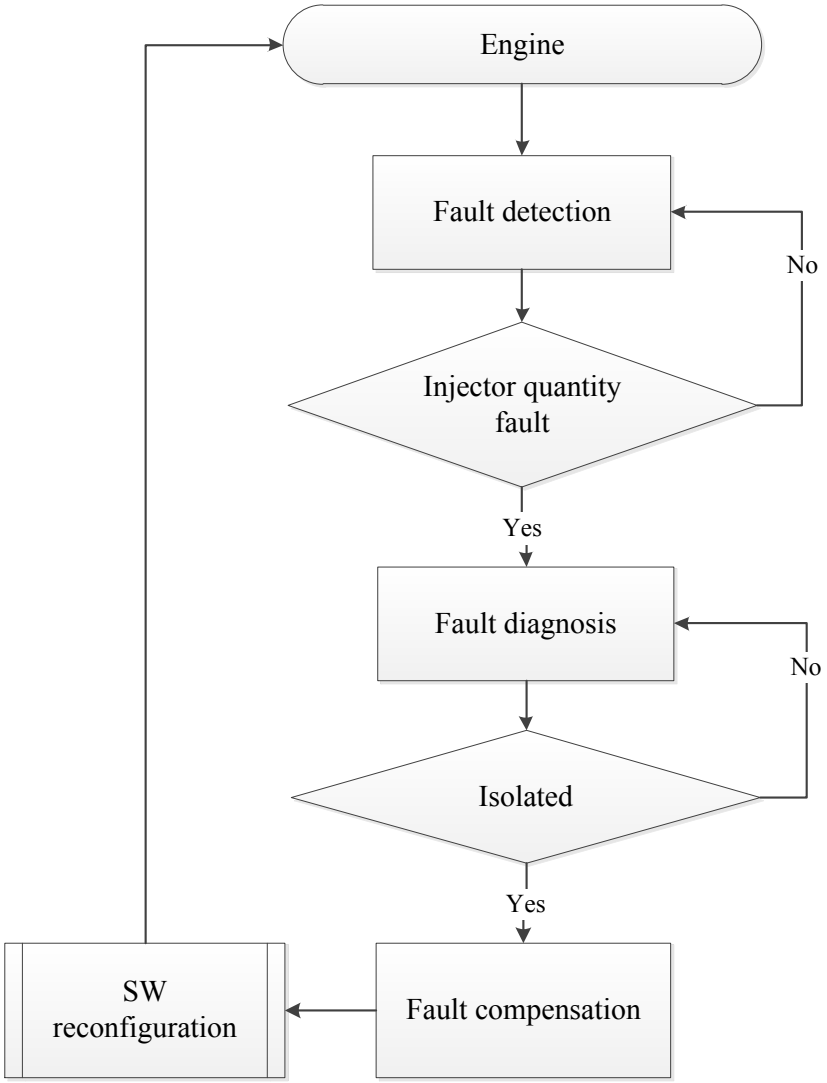

Fig. 8.2: Injector fault compensation structure

A fault compensation strategy for injector faults was discussed, primary relying on the uniformity isolation concept from Sect. 7.2. This strategy gives the possibility to improve the robustness of the engine fuel system diagnosis in case of an injector fault. This can in turn significantly improve the engine's reliability and reduce downtime cost for the customer.

9 Conclusion and outlook

9.1 Conclusion

The continuous improvement of engine development towards tighter efficiency and compliance with legislation requiring tougher emission standards significantly increases the complexity of modern engines. This leads to a particular attention for OBD development, where conventional methods reach their limit. Hence, in this work advanced model-based approaches for the engine's fuel path diagnosis were discussed that could help overcome the above mentioned issues. As a result of these advanced methods, additional information is gained to develop an enlarged fault diagnosis system with the isolation of different fuel component faults.

This thesis offers approaches that help meet the requirements to develop a fuel path diagnosis in already existing production environment. Conventional used methods decrease the robustness and precision of the diagnosis system, due to missing additional integrated sensors for intermediate variable monitoring. Also, model uncertainties increase when only the integrated serial sensor, mostly having a smaller resolution, are used to estimate e.g. the engine position. In contrary to this disadvantage, the lower resolution has the benefit of less calculation effort caused by a decreased model update rate.

The developed fault detection algorithms are structured in process and signal model-based approaches augmenting conventional methods. With process model-based fault detection algorithms, it is possible to detect faults at an earlier stage, because the system's intermediate variables are already monitored (e.g. volume flow instead of pressure). Furthermore, the physical modeling also provides a deeper insight into the system and therefore generates higher system information giving the possibility for an extended fault identification or isolation.

The engine's LP and HP fuel path design has a separated propulsion structure. The LPP is electrically and the HPP mechanically driven. This forms the basis for the development of two independent process models for the same variable. An example for this are the physical volume flow models of the LPP and the MP inlet volume flow, extracting additional information for an enlarged diagnosis. With these process model-based algorithms, different kinds of fuel leakages in the LP, MP, inner leakages in the HP system, as well as filter restrictions can be detected.
Also, the physical rail pressure model is an important process model-based algorithm monitoring the engine's fuel system. Additionally, the intermediate variables, leading to this pressure model, provided useful information for deeper system knowledge. This helped to develop a simulation, useful in understanding the inner system behavior and the development of additional residuals to detect and isolate more system faults. E.g. single and multiple injector fault detection and isolation.
Another process model-based algorithm is the physical power model of the LPP using a hydraulic

and an electrical equation. With this algorithm, it is possible to detect and separate between primary and secondary fuel filter restrictions. Only these handful of algorithms show the advantages of process model-based development clearly resulting in an enlarged engine fuel system diagnosis.

The signal model-based approaches also provide additional information for the fuel system diagnosis. Specifically, the FFT is a strong approach in detecting faults in periodic systems, but the advantages of this method diminish with the highly variable crank angle synchronous calculated RP control. This RP control significantly changes the RP oscillations over different engine OPs, caused by the flexibility of the system. This makes it difficult for the FFT application. Hence, this issue is solved by the developed uniformity residuals, where the application part vanishes due to the calculation principle. A skillful choice of the residual's periodic as well as supervised angle period gave the possibility to directly isolate injector fuel quantity and cylinder misfire faults, by an observation of the RP and EMP signal. Also, with this new method, up to five injector High and Low Flow fuel quantity faults for a six-cylinder engine can be detected simultaneously.

An advanced fuel system diagnosis was implemented with all important faults, inserted on the engine test bench. The advanced diagnosis system was integrated with a MATLAB-Simulink model into a RCP system (the MABX), tested in real time on the test bench. With process and signal model-based approaches along with conventional methods all inserted faults were detected. An inference method-based fault diagnosis system was discussed for static OPs and a short introduction to dynamic OPs was provided. Tools for the inference system-based fault diagnosis, fault symptom tables and fault trees, were discussed. Also, a new signal model-based isolation concept for the injector fuel quantity and cylinder misfire faults was introduced. With this new isolation concept, up to five injector fuel quantity faults for a six-cylinder engine with a lower or higher injection rate can be isolated. It was not possible to isolate all inserted faults immediately and therefore an active test for the LP system was described, to separate some LP faults with identical symptom pattern. In conclusion, it was possible to identify and isolate nearly all inserted 26 faults.

Furthermore, a fault management system was discussed for the injection fuel quantity fault correction. With this injector fault management system, it is possible to adjust the individual fuel injection rates of the injectors in case of an injector fuel quantity fault. This significantly increases the reliability of the engine. The storage of the fault and the exact location support maintenance by reducing repair time and costs.

The conclusion is, that a combination of the process model as well as the new signal model-based approach for the injector and misfire isolation improves the fuel path diagnosis significantly. Additionally, an improvement of the fault detection in different engine OPs for 40% less fuel injections with over 75% detection rate was illustrated.

9.2 Outlook

In this section the possibility to further improve the developed engine diagnosis for the fuel system is discussed.

Detailed investigations have shown that multiple misfire faults could not be isolated in every path, caused by the EMP sensor position and the missing fault compensation structure. Further investigation needs to be carried out to solve this issue with an update of the EMP sensor position in combination with a skillful choice of the residual. This should be done similar to the RP system for the EMP signal and the additional residual UA-EMP-2 described in Sect. 7.2.2.

The combination of an overall engine diagnosis for different engine systems like the fuel, combustion, intake and exhaust system can be merged to improve the developed diagnosis system. This combination allows for a deeper fuel system diagnosis, because the systems are closely linked to each other. In detail, one component fault can influence various system variables.

Another area for improvement is on the test side. The test environment did not capture all influences such as:

- Change in environmental conditions.
- Long term effects due to wear.
- Transient engine OPs.
- Vibrations or noise, caused by different vehicle components.

This can lead to misclassification from a wrong occurrence of the developed symptoms. Hence, the diagnosis system has to be tested in field conditions to extract sufficient data for the improvement of the fuel system diagnosis and especially the fault isolation. This means, that all investigated faults should be implemented and tested long term on a vehicle, to ensure the proper functionality of the developed advanced fuel diagnosis system.

One more improvement could be a more accurate process model-based development, with e.g. an interpolation of the crank angle resolution for the (HP) physical rail pressure model. This results in less system noise or model uncertainties. With this improvement, smaller HP faults sizes can be detected dealing with the trade-off between small fault detection and misclassification. Furthermore, the MP/LP models could be updated with additional neglected system variables, for example the volume flow of the air bleed valve. This also leads to an earlier detection of faults, such as different leakage faults.

Finally, the injection fuel quantity correction in case of injector fuel quantity faults, discussed in the fault management Chap. 8, has to be tested for different engine OPs. This has to be done with an in-cylinder-pressure sensor, to ensure a proper combustion for an extended or shortened fuel injection duration.

Appendix

A.1 Engine test bench

In Fig. A.1 the engine test bench is visualized. Table A.1 gives an overview of the engine specifications. The engine as well as the test bench sensors are already described in Chap. 3. In this figure the test bench equipment can be seen. The engine is decelerated by a water swirl dynamo-meter (waterbrake) from Horiba called DT1200. With this brake it is possible to safely operate engines with less than:

- 1200 kW nominal power,
- 5500 rpm nominal speed and
- 7500 Nm nominal Torque.

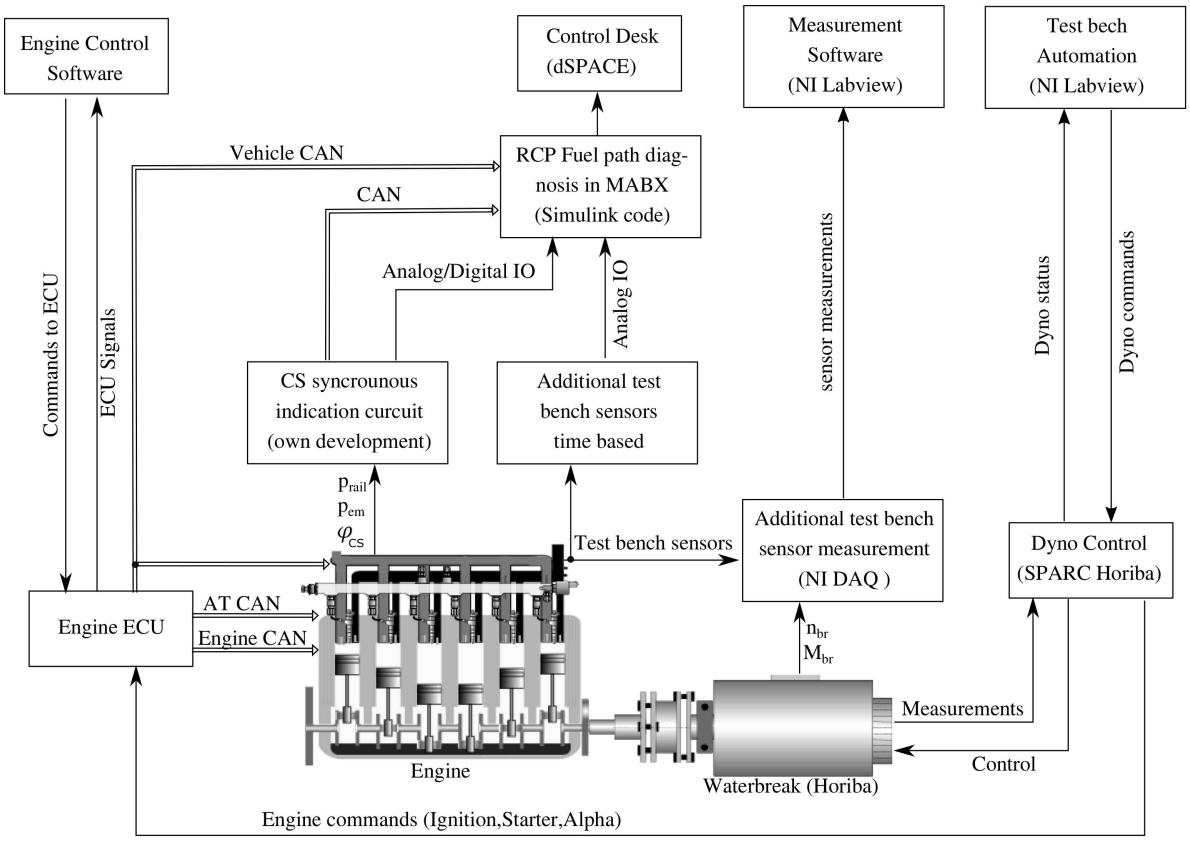

Fig. A.1: Engine test bench

The higher level control of the dynamo-meter is the SPARC controller from Horiba. In this work the engine is speed controlled by the engine ECU and the dynamo-meter is torque controlled by the SPARC controller. The SPARC controller was calibrated for the test bench engine.

Table A.1: Engine test bench specifications

Components, parameters	Descriptions, values
Number of cylinders	6
Cylinder displacement	9000 cm^3
Cylinder firing order	1-5-3-6-2-4
Number of valves	24
Maximum engine power	317 kW
Maximum torque value	1742 Nm
Fuel system	common rail system from Denso with HP6 pump and G4S injectors
Turbo charger	one fixed and one VGT turbocharger

The engine was fully integrated on the test bench. Therefore it was required to implement the following equipment:

- Crank shaft synchronous indication circuit. This circuit translates the analog signal of the inductive incremental encoder ($\varphi_{cs,serial}$, see Fig. 3.1) to a digital signal. Note that the digital signal is already available in the engine ECU, but the transmission of this data via CAN bus (from ECU to MABX) is not fast enough to guarantee a proper calculation of the crank angle-based signals, especially for higher engine speed values. Furthermore the circuit contains a galvanic isolation of the analog and digital signals to prevent hardware damage of the expensive RPC system (the MABX). Also a requirement of the RPC Hardware was, that the signal level of the digital signal should be held constant, when the analog signal vary with a factor of 10 dependent on the engine speed. The first version of the developed circuit is shown in Fig. A.2. [81] developed a second version in his Master thesis with a more advanced etched circuit board and signal processing via a micro-controller Cortex M7. This version of the crank shaft synchronous indication circuit can be seen in Fig. A.3 for a) the etched circuit board and b) the complete unit.

- Additional pressure and temperature sensors (see white shaded sensors in Fig.3.1) to monitor the test bench for critical engine situations. The Software was implemented in labVIEW from National Instruments on a separate PC.

- Volume flow sensors (see white shaded sensors in Fig.3.1) for the fuel system, to verify the developed models in Chap. 4. This also includes the software development (drivers) in MATLAB Simulink and sensor hardware integration into the MABX (from dSPACE).

- Creation and assembly of special test bench pipes and equipment for the air intake, cooling, aftertreatment and especially for the fuel system.

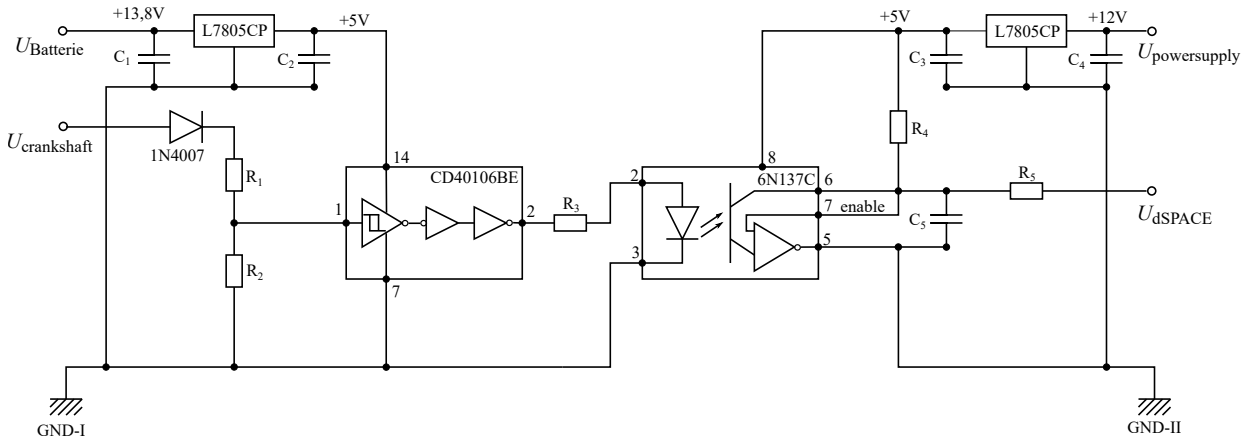

Fig. A.2: First version of the crank shaft synchronous indication circuit

- Build up the engine foundation including dampers, design and assembly of brackets for the engine, aftertreatment, cooling, fuel pipes and equipment.
- Wiring of the additional sensors, CAN communication, emergency stop infrastructure (electrical) with a shutdown of the engine. This includes a logic where the injector fuel flow is interrupted and the waterbrake activated, to decelerate the engine until standstill as quick as possible.
- An automated fill control for the fuel tank (fuel tank see Fig.3.1) when the fuel falls below a lower fuel level threshold.
- An integrated control for the intercooler to hold a specific temperature setpoint.
- Model-based fuel system engine diagnosis software in MATLAB Simulink in real time RCP system, the MABX from dSPACE. This includes also the visualization of all residuals, parameters and engineering modes, as well as the preparation to record all important parameters in Control Desk.
- [80] developed a GUI in MATLAB to visualize the in Control Desk recorded data in a crank angle and time-based domain. Furthermore with this GUI it is possible to post process all data and quickly implement new residual structures to speed up the development of the model-based fuel system engine diagnosis system. Fig. A.4 shows the possibility of the parameter visualization in the GUI dependent on the crank angle or time. This figure also shows the possibility of data post processing with the individual tabs like the implementation of additional residual in tab "Math Operations", monitoring of the actual developed residuals in tab "Residuals" and the visualization of the additional created residuals or math operations in MATLAB figures in the "Evaluation" tab.

The engine furthermore is calibrated by the engine manufacturer's developed engine control software. This software was also used to update the engine parameters for the fault insertion in this project.

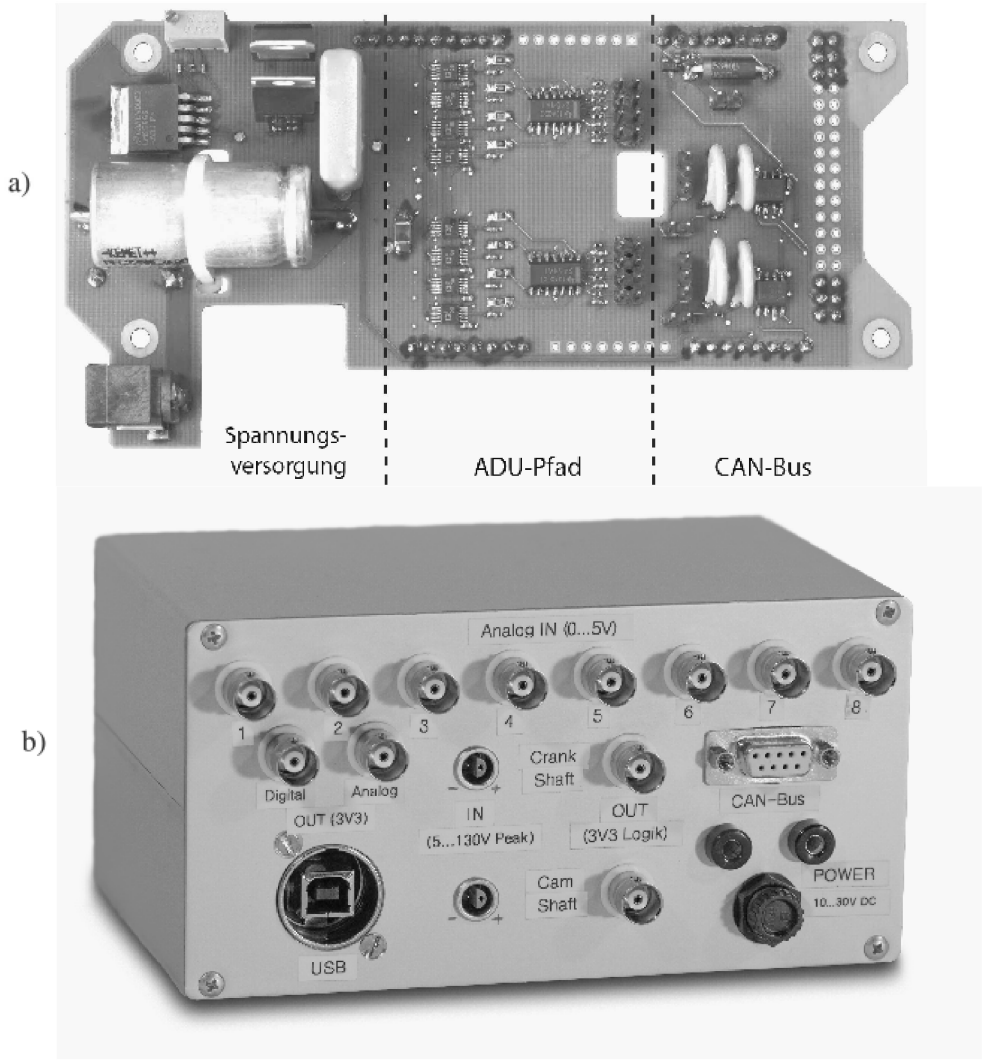

Fig. A.3: Crank shaft synchronous indication circuit (see [81]) with a) etched circuit board b) complete unit

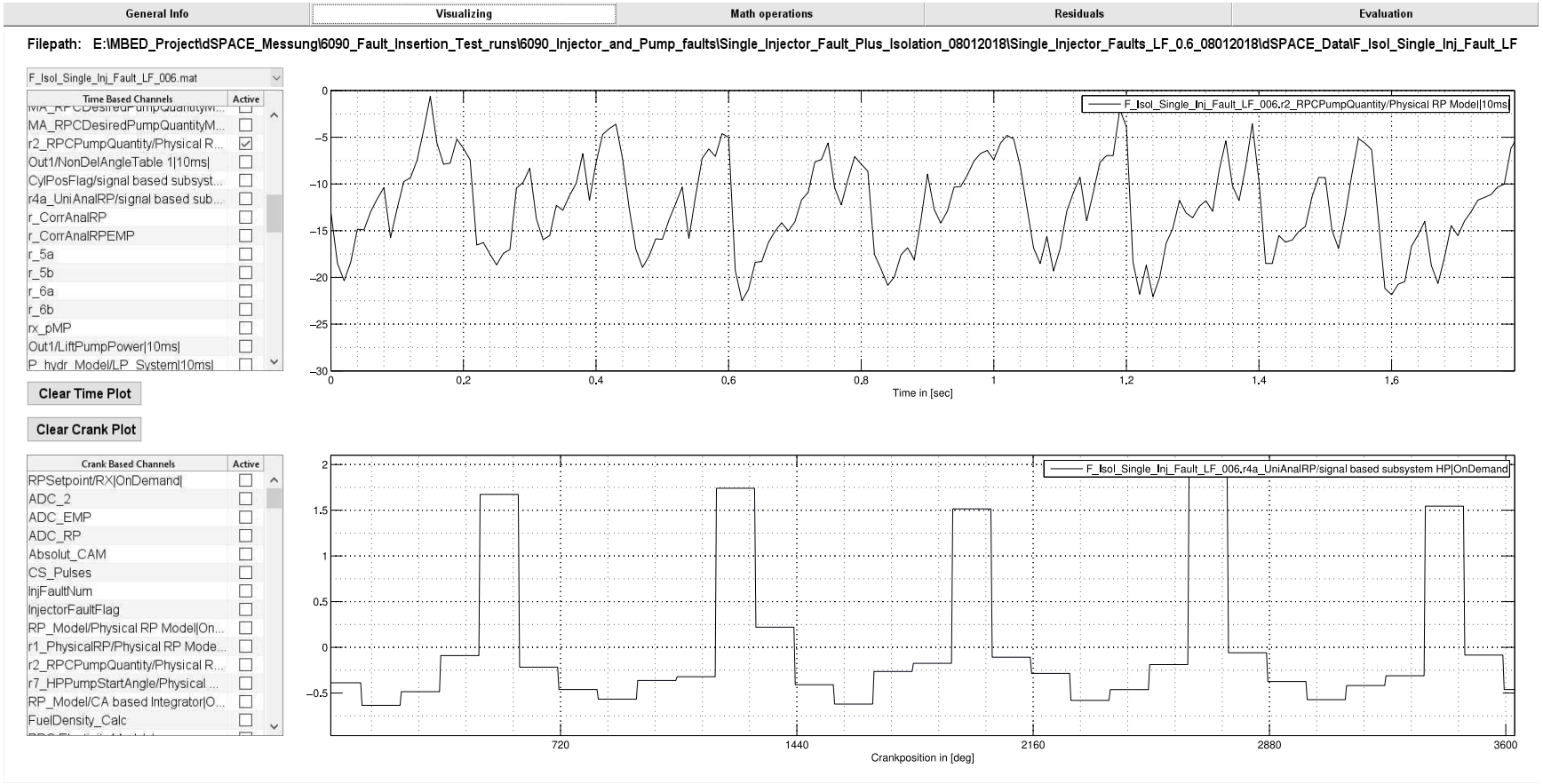

Fig. A.4: GUI design for visualization and post process of test bench recorded data from Control Desk

A.2 Gerotor pump schematic

In Fig. A.5 the gerotor pump schematic is visualized. In this example the inner teeth number of the pump is $z = 5$.

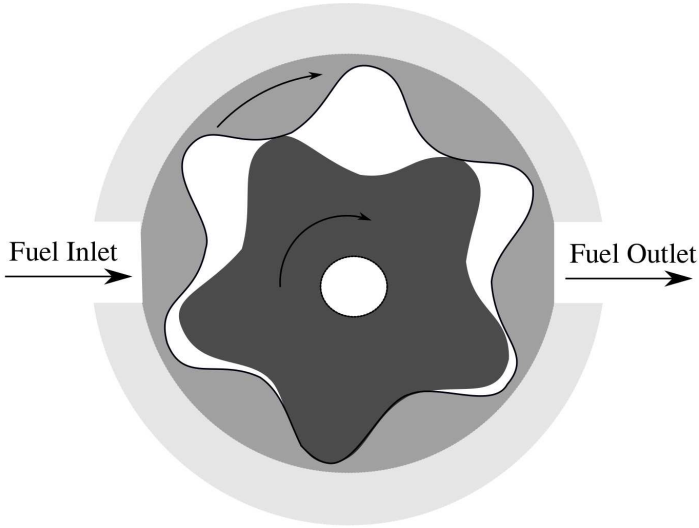

Fig. A.5: Gerotor pump schematic

A.3 Additional residual results

In Fig. A.6 a single injector Low Flow fault with only 20% fault size is visualized. Furthermore multiple low flow injector quantity faults with 40% less fuel injections for two and three injector faults are shown. Finally a misfire fault with the 20% less air is illustrated in the last graph.

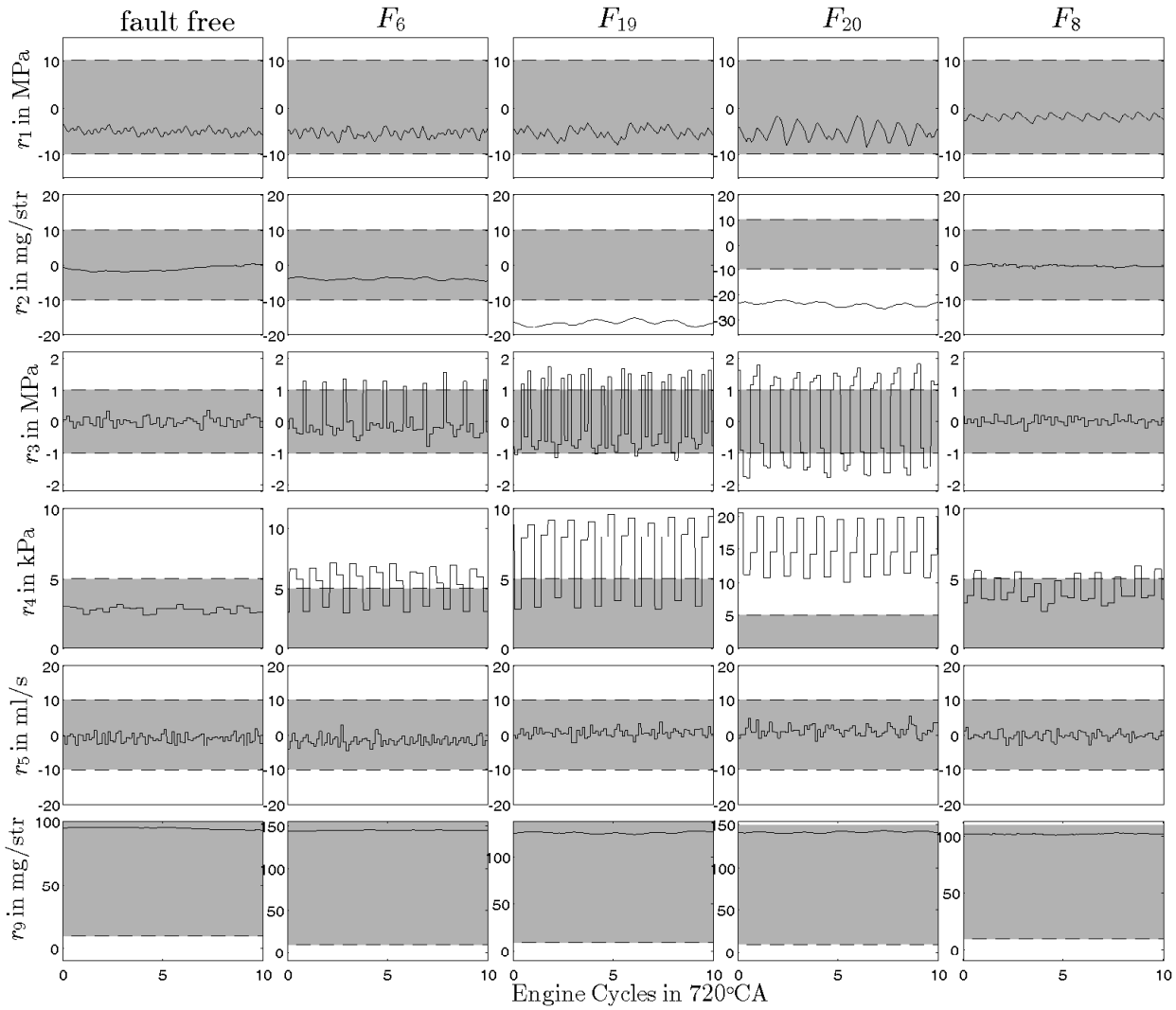

Fig. A.6: HP residuals calculated from measured signals for a fault-free state and with faults (OPs according to Table A.2): F_6: Less single injector mass flow quantity (Low Flow), F_{19}: Less two injectors mass flow quantity (Low Flow), F_{20} : Less three injectors mass flow quantity (Low Flow), F_8: Engine misfire by compression loss

Table A.2: OPs and important parameters

graphs	n_{eng}	M_{br}	$\hat{M}_{\text{eng}}$	fault (parameter)	fault size in %	fault size in Δ
fault-free	1604 rpm	799 Nm	776 Nm	-	-	-
F_6	1600 rpm	800 Nm	770 Nm	inj. 1 LF, q_{mi}	20	18,6 mg/str
F_{19}	1600 rpm	797 Nm	912 Nm	inj. 1,2 LF, q_{mi}	40	37,2 mg/str
F_{20}	1599 rpm	795 Nm	992 Nm	inj. 1,5,3 LF, q_{mi}	40	37,2 mg/str
F_8	1598 rpm	802 Nm	829 Nm	compression loss	20	80% air intake

A.4 Difference between investigated system and system in [67] for injector and HPP fault detection using uniformity residuals

Sect. 5.1 already described that the HPP and injectors cause specific pressure frequencies in the common rail. In the following paragraph the periodicity of the RP signal over the angle period of one engine cycle $\tau_{\text{eng,cycl}} = 720°\text{CA}$ is investigated, when only the HPP is delivering fuel into the rail (without injections), with a constant leakage of fuel out of the rail. This was already shown in the first test case in Sect. 5.1 in Fig. 5.1 where only the HPP is active. In general, there are two possibilities of HPP fuel delivery frequency compared to the engine cycle frequency in case of an HPP fault case (i.e. one or more elements do not supply fuel):

- **HPP fuel delivery frequency is a multiple integer of the engine cycle frequency** $f_{\text{eng,cycl}} = \frac{1}{720°\text{CA}}$, where the HPP delivers fuel with a harmonic frequency (multiple integer x) of the engine cycle frequency ($f_{\text{hpp,sec}} = f_{\text{eng,cycl}} \cdot x$) in spite of an HPP fault. This is the case for the investigated system. In an HPP fault case, where one plunger chamber doesn't supply fuel, the healthy chamber will compensate this fault by delivering the double amount of fuel. For the investigated system, due to the fuel system design, the second HPP period lines up with the main injector period $\tau_{\text{inj,main}} = \tau_{\text{hpp,sec}} = 120°\text{CA}$ (see Sect. 5.1). So the engine cycle period is a multiple integer of the second HPP period $\tau_{\text{eng,cycl}} = 6 \cdot \tau_{\text{hpp,sec}}$. Fig. A.7 illustrates the RP oscillation caused by the HPP fuel delivery in a) a fault-free case and b) fault in chamber 1. It can be seen that in a fault-free case and in an HPP fault case the RP signal remains periodic with the engine cycle period.

- **HPP fuel delivery frequency is a fraction number of the engine cycle frequency**, where in the case of a fault, the HPP delivers fuel without a harmonic frequency (fraction number) of the engine cycle frequency. The system in [67] follows this behavior, where the engine is a 4 cylinder with a 3 chamber radial piston HPP. The propulsion ratio of the HPP to the engine's crank shaft is 4:3. Here also one plunger chamber element has a fault. Instead of the first case, the second HPP period and the injector period doesn't line up: $\tau_{\text{inj,main,4cyl}} = 180°\text{CA}$ and $\tau_{\text{hpp,sec,4cyl}} = 540°\text{CA}$. However, the second HPP period is a fraction number of the engine cycle period $\tau_{\text{eng,cycl}} = \frac{4}{3} \cdot \tau_{\text{hpp,sec,4cyl}}$. Fig. A.8 illustrates the RP oscillations caused by a) the fault-free case and b) a fault in the third plunger chamber. Finally it can be seen that only in a fault-free case the RP signal remain periodic with the engine cycle period.

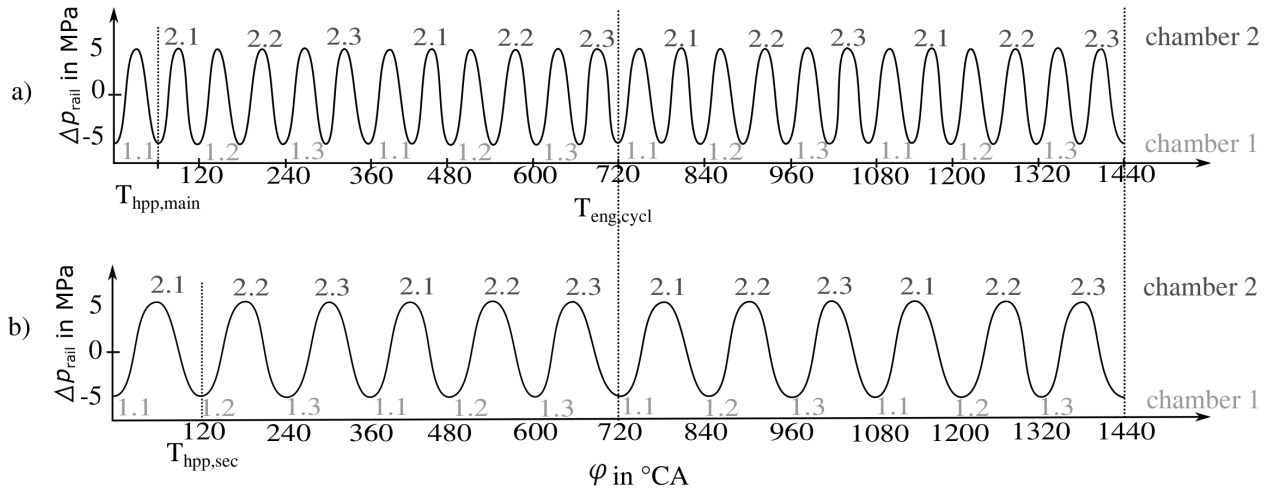

Fig. A.7: Simulated RP oscillation signal for a multiple HPP fuel delivery frequency to engine cycle frequency with
a) a fault-free case (the first number in the upper index show the pump element and the second number show the actual profile peak. The same holds true for chamber number one for the lower index) and
b) HPP fault in chamber 1, where RP oscillations caused by pump chamber 2 are visualized

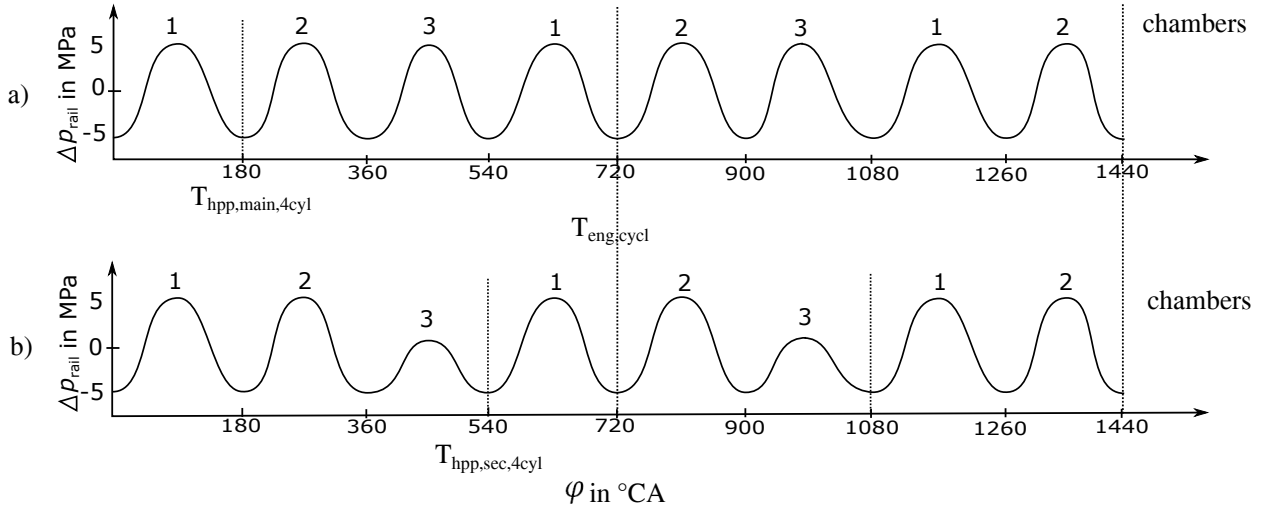

Fig. A.8: Simulated RP oscillation signal for a fraction HPP fuel delivery to engine cycle frequency with
a) a fault-free case and
b) HPP fault in chamber 3

The advantage of the first case is the additional possibility of the detection and isolation of injector faults with their exact location with and without HPP faults. For the injector fault location, it is important to mention that in case of an HPP fault this criteria is only satisfied if the fuel delivery frequency lines up or is an integer/multiple frequency of the injector activation frequency. This will be discussed in Sect. 7.2.1 for the investigated system and an example when this condition is not satisfied. The advantage of the second case, where the HPP fuel delivery frequency is a

fraction number of the engine cycle frequency, contains the detection and isolation of injector and HPP faults without identifying the injector or the HPP fault location. This was investigated in [67].

References

References

[1] Albarbar A., Gub F., and Ball A.D. “Diesel engine fuel injection monitoring using acoustic measurements and independent component analysis”. In: 2010.

[2] Jürgen A. *Fuzzy Logik, Neuronale Netze und Evolutionäre Algorithmen*. Tech. rep. Institut für Automatisierungstechnik, TU Darmstadt, 2015.

[3] Schiling A. “Model-Based Detection and Isolation of Faults in the Air and Fuel Paths of Common-rail DI Diesel Engine Equipped with a Lambda and Nitrogen Oxides Sensors”. PhD thesis. ETH ZURICH, 2008.

[4] Schwarte A. “Modellbasierte Fehlererkennung und Diagnose des Ansaug- und Abgassystems von Dieselmotoren”. Dissertation. Institute of Automation, TU Darmstadt, 2006.

[5] Sidorow A. “Model-based Fault Diagnosis of the Air and Turbocharger System of Diesel Engines”. Dissertation. Institute of Automation, TU Darmstadt, 2014.

[6] Parker Automation. *Pump Controller Technical Specification*. 2010.

[7] Welschof B. “Saugdrosselung - ein einfaches Prinzip zur Begrenzung des Fördervolumenstroms”. In: *O+P Ölhydraulic und Pneumatik* (1990).

[8] Welschof B. “Saugdrosselung - eine Phasenanschnittsteuerung in der Hydraulik”. In: *O+P Ölhydraulik und Pneumatik* (1992).

[9] Ahlin C. “Modeling of pressure waves in the Common Rail Diesel injection System”. TU Darmstadt, 2000.

[10] Ludwig C. “Modellgestützte Fehlererkennung für Turboaufladung und Einspritzung von Dieselmotoren”. Dissertation. Institute of automation, TU Darmstadt, 2000.

[11] Parker Hannifin Corporation. *RACOR 7683, Fuel Filter/ Water Separator Pump Systems*.

[12] Förstner D. “Qualitative Modellierung für die Prozeßdiagnose und deren Anwendung auf Dieseleinspritzsysteme”. Dissertation. Technische Universität Hamburg-Harburg, 2001.

[13] Förstner D., Weber R., and Lunze J. “Diagnose eines Diesel-Einspritzsystems mit ereignisdiskreten Modellen”. In: Automatisierungstechnische Praxis, 45. 2003, pp. 73–79.

[14] Füssel D. “Fault Diagnosis with Tree-Structured Neuro-Fuzzy Systems”. Dissertation. Institute of Automation, TU Darmstadt, 2002.

[15] Shane D. *Plug-and-Play Monitoring and Performance Optimization for Industrial Automation Processes*. Wiesbaden, Germany: Springer Vieweg, 2017. ISBN: 9783658159276.

[16] DieselNet. *United States: Heavy-Duty Onroad Engines, United States: Nonroad Diesel Engines, EU: Nonroad Engines, EU: Heavy-Duty Truck and Bus Engines*. 2020. URL: https://dieselnet.com/standards/.

[17] Chow E. and Willsky A. "Analytical Redundancy and the Design of Robust Failure Detection Systems". In: 29 (Aug. 1984), pp. 603–614.

[18] Shannon C. E. "Communication in the presence of noise". In: Proc. IRE. Vol. 37 No.1. 1949.

[19] Elamin F., Ball A., and Gu F. "Diesel Engine Injector Faults Detection Using Acoustic Emissions Technique". In: School of Computing and Engineering, University of Huddersfield, 2010.

[20] Kimmich F. "Modellbasierte Fehlererkennung und Diagnose der Einspritzung und Verbrennung von Dieselmotoren". Dissertation. Institute of Automation, TU Darmstadt, 2004.

[21] Posada F. and Bandivadekar A. "Global overview of On-Board Diagnostic (OBD) systems for Heavy-Duty Vehicles". In: (2015). URL: https://theicct.org/.

[22] Rasul M. G., Kamal Kahn M. M., and Hazrat M. A. "Lubricity Improvement of the Ultra-low Sulfur Diesel Fuel with the Biodiesel". In: Energy Procedia. Vol. Vol.75. 2015.

[23] de Graaf J. "Heavy duty OBD & Vehicle integration apects". In: SAE OBD Symposium. Turin, Italy, 2017.

[24] Niemann H. *Klassifikation von Mustern*. 2. edition. 2003. URL: http://aiweb.techfak.uni-bielefeld.de/files/Klassifikation-von-Mustern.pdf.

[25] Ortwig H. *Hydraulik Formelsammlung*. 2017.

[26] Press W. H., Teukolsky S. A., and Vetterling W. T. *The Art of Scientific Computing*. 1992.

[27] Späth H. *Cluster-Analyse-Algorthmen zur Objektklassifizierung und Datenreduktion*. 1975.

[28] Tschöke H. "9. Tagung Diesel- und Benzindirekteinspritzung". In: 2014. ISBN: ISBN 978-3-658-07650-4.

[29] Kolev N. I. *Multiphase Flow Dynamics 3*. Erlangen, Germany: Springer Verlag, 2007. ISBN: 978-3-642-09062-2.

[30] Chen J. and Patton R. J. *Robust Model-Based Fault Diagnosis for Dynamic Systems*. Springer US, 1999. ISBN: ISBN 978-1-4615-5149-2.

[31] Führer J., Sinsel S., and Isermann R. "Erkennung von Zündaussetzern aus Drehzahlsignalen mit Hilfe eines Frequenzbereichverfahrens". In: 13. Tagung Elektronik im Kraftfahrzeug. Haus der Technik Essen, Germany, 1993.

[32] Galindo J. et al. "Detection and Correction of injection failures in diesel engines on the basis of turbocharger instantaneous speed frequency analysis". In: Proceedings of the Institution of Mechanical Engineers, Part D: Journal of Automobile Engineering. 2005.

[33] Gertler J. J. *Fault Detection and Diagnosis in Engineering Systems*. Marcel Dekker Inc., New York, 1998.

[34] Gertler J. J. "Survey of Model-Based Failure Detection and Isolation in Complex Plants". In: 8. Vols. no. 6. IEEE Control Systems Magazine, 1988, pp. 3–11.

[35] Kerekgyarto J. "Ermittlung des Einspritzverlaufs an Diesel-Injektoren". PhD thesis. Fakultät Maschinenbau, Otto-von-Guericke-Universität Magdeburg, 2009.

[36] Korbicz J. et al. *Fault Diagnosis*. Springer Verlag, 2004. ISBN: 9783642621994.

[37] Owen J. "Cummins experience - Diesel Misfire Monitoring". In: SAE OBD Symposium. Turin, Italy, 2017.

[38] Kotzan J.M. "On-board diagnostic for emission control systems". In: Government/Industry Meeting. Washington,DC, USA, 1991.

[39] Mollenhauer K. and Tschöke H. *Hanbook of Diesel Engines*. Springer Verlag, 2010. ISBN: 9783540890829.

[40] Reif K. *Moderne Diesel-Einspritzsysteme*. Wiesbaden, Germany: Vieweg Teubner, 2010.

[41] Jiang L. "Sensor fault detection and isolation using system dynamics identification techniques". PhD thesis. Mechanical Engineering, University of Michigan, 2011.

[42] Jones H. L. "Failure Detection in linear systems". PhD thesis. Massachusetts Institute of Technology, 1973.

[43] Blanke M. et al. *Diagnosis and Fault-Tolerant Control*. Springer, 2006. ISBN: ISBN 978-3-540-35653-0.

[44] Braunschweig M. and Czarnecki T. "On-Board-Diagnose bei Dieselmotoren". In: *Motortechnische Zeitschrift (MTZ)* (2004).

[45] Leykauf M. "Modellgestützte Fehlerdiagnose eines DI-Benzinmotors". In: *Elektronisches Management motorischer Fahrzeugantriebe*. Isermann Rolf, 2010.

[46] Lujan J. M. et al. "Injection diagnosis through common-rail pressure measurement". In: Journal of Automobile Engineering. 2005.

[47] Münchhof M. "Model-Based Fault Detection for a Hydraulic Servo Axis". Dissertation. Institute of Automation, TU Darmstadt, 2006.

[48] Romijn M. and Kumar U. *California HD OBD program - Summary of 2018 amendments*. 2018. URL: https://dieselnet.com/news/2018/12obd.php.

[49] Stepper M. *On-board Diagnostics (OBD) for Heavy-Duty Diesel Engines, Hybrids, and Electric Vehicles*. 2020. URL: https://www.lhpes.com/blog/on-board-diagnostics-for-heavy-duty-diesel-engines-hybrids-and-electric-vehicles.

[50] Vogt M. "Support Vector Machines for Identification and Classification Problems in Control Engineering". Dissertation. Institute of Automation, TU Darmstadt, 2007.

[51] Willimowski M. "Verbrennungsdiagnose von Ottomotoren mittels Abgasdruck und Ionenstrom". Dissertation. Institute of Automation, TU Darmstadt, 2002.

[52] Willimowski M., Füssel D., and Isermann R. “Misfire detection for spark-ignition engines by exhaust gas pressure analysis”. In: *MTZ* (1999).

[53] Willimowski M. et al. “Zukünftige Diagnose in Motorsteuerungen”. In: 5. Symposium Steuerungssysteme für den Antriebsstrang von Kraftfahrzeugen. Berlin, 2005.

[54] Föllinger O. *Regelungstechnik: Einführung in die Methoden und ihre Anwendung*. VDE-Verlag, 2013. ISBN: 978-3-8007-4201-1.

[55] Montes de Oca S. and Puig V. *Adaptive Threshold Generation for Robust Fault Detection using Interval LPV Observers*. 7th IFAC Symposium. Universitat Politencia de Catalunya, 2009.

[56] Klee P., Knirsch M., and Willimowski M. “Herausfordernungen der Diagnoseentwicklung in der Motorsteuerung”. In: *Onboard-Diagnose Status der Gesetzgebung und Auswirkungen auf die Fahrzeugentwicklung*. 2005.

[57] Ceccarelli R. et al. “Model-based Adaptive Observers for Intake Leakage Detection in Diesel Engines”. In: 2009.

[58] Isermann R. *Combustion Engine Diagnosis*. Springer-Verlag, 2017. ISBN: 9783662494660.

[59] Isermann R. *Engine Modeling and Control*. Springer-Verlag, 2014. ISBN: 9783642399336.

[60] Isermann R. *Fahrdynamik Regelung. Modellbildung, Fahrerassistenzsysteme, Mechatronik*. Vieweg+Teubner Verlag, 2006. ISBN: 9783834801098.

[61] Isermann R. *Fault Diagnosis Applications*. Darmstadt, Germany: Springer Verlag, 2010. ISBN: 9783642127663.

[62] Isermann R. *Fault Diagnosis Systems*. Darmstadt, Germany: Springer Verlag, 2006. ISBN: 9783540241126.

[63] Isermann R. *Identification of Dynamic Systems*. Darmstadt, Germany: Springer Verlag, 2010. ISBN: 9783540788782.

[64] Isermann R. *Mechatronische Systeme*. Springer Verlag, 2008. ISBN: 9783540323365.

[65] Isermann R. “Modellgestuetzte Ueberwachung und Fehlerdiagnose Technischer Systeme Teil(2)”. In: *atp - Automatisierungstechnische Praxis 38* 38.2 (1996), pp. 48–57.

[66] Isermann R. *Überwachung und Fehlerdiagnose. Moderne Methoden und ihre Anwendungen bei technischen Systemen*. 1994.

[67] Clever M. S. *Model-based Fault Detection and Diagnosis for a Common Rail Diesel Engine*. Berichte aus dem Institut für Automatisierungstechnik und Mechatronik der TU Darmstadt. VDI-Verlag, 2011. ISBN: 9783185202087. URL: https://books.google.de/books?id=ueFctwAACAAJ.

[68] Clever M. S. “Modellgestützte Fehlererkennung und Diagnose für Common-Rail-Einspritzsysteme”. In: Isermann Rolf. *Elektronisches Management motorischer Fahrzeugantriebe*. Vieweg+Teubner, 2010. ISBN: 978-3-8348-0855-4.

[69] Clever M. S. and Isermann R. “Model-based fault detection and diagnosis for common-rail injection systems”. In: *MTZ worldwide* 71.2 (2010), pp. 32–39. ISSN: 2192-9114. DOI: 10.1007/BF03227006. URL: https://doi.org/10.1007/BF03227006.

[70] Keppeler S. “Common-Rail-Einspritzung für den direkteinspritzenden Dieselmotor”. Dissertation. Technische Hochschule Aachen, 1997.

[71] Matsumoto S. et al. “4th Generation Diesel Common Rail System: Realizing Ideal Structure Function for Diesel Engine”. In: *SAE Technical Paper*. SAE International, Apr. 2013. DOI: 10.4271/2013-01-1590. URL: https://doi.org/10.4271/2013-01-1590.

[72] Willsky A. S. “A survey of design methods for failure detection in dynamic systems”. In: *Automatica* 12.6 (1976), pp. 601–611. ISSN: 0005-1098. URL: http://www.sciencedirect.com/science/article/pii/0005109876900418.

[73] Höfling T. and Isermann R. “Fault Detection based on Adaptive Parity Equations and Single-Parameter Tracking”. In: *Control Eng. Practice Vol 4* (1996), pp. 1361–1369.

[74] Kiencke U. “Engine misfire detection”. In: *Control Engineering Practice*. ELSEVIER. 1999.

[75] Armin W. “Komponentenbasierte Fehlerdiagnose industrieller Anlagen am Beispiel frequenzumrichtergespeister Asynchronmaschinen und Kreiselpumpen”. Dissertation. Institute of Automation, TU Darmstadt, 2002.

[76] Vesely W. et al. *Fault Tree Handbook*. Systems and Reliability Research, Office of Nuclear Regulatory Research, U.S. Nuclear Regulatory Commission, 1981. ISBN: 9780160055829.

[77] Wikipedia. *Nächste-Nachbarn-Klassifikation*. 2018. URL: https://de.wikipedia.org/wiki/N%C3%A4chste-Nachbarn-Klassifikation.

[78] Ding S. X. *Model-based Fault Diagnosis Techniques*. Duisburg, Germany: Springer Verlag, 2007. ISBN: 9781447147985.

[79] Seykens X., Somers L., and Baert R. “Detailed Modeling of Common Rail Fuel Injection Process”. In: Journal of Middle European Construction and Design of Cars. 2005.

Supervized Student Thesises

[80] Bensinger A. “Entwicklung einer graphischen Benutzeroberflaeche eines Diagnosesystems fur den Kraftstoffpfad eines Dieselmotors”. BA thesis. Hochschule Karlsruhe - Technik und Wirtschaft, 2018.

[81] Riedmann O. “Konzept und Realisierung einer kurbelwellensynchronen prognosegestuetzten Sensordatenerfassung fur Verbrennungsmotoren”. MA thesis. Technical University of Kaiserslautern, 2017.

[82] Patel A. R. *Fault classification with a support vector machine approach for a diesel engine fuel diagnosis system*. Tech. rep. Technical University of Kaiserslautern, 2018.